Integration Mode Proton Imaging with a CMOS Detector for a Small Animal Irradiation Platform

Katrin Beatrix Schnürle

München 2024

Protonenbildgebung im Integrationsmodus mit einem CMOS-Detektor für eine Bestrahlungsplattform für Kleintiere

Katrin Beatrix Schnürle

Dissertation

an der Fakultät für Physik

der Ludwig-Maximilians-Universität München

vorgelegt von

Katrin Beatrix Schnürle

geboren in Herrenberg

München, den 22. Mai 2024

Erstgutachterin: Prof. Dr. Katia Parodi
Zweitgutachter: Dr. Joël Hérault, HDR
Tag der mündlichen Prüfung: 10. Juli 2024

Zusammenfassung

Die Protonentherapie ist eine vielversprechende Modalität in der Krebsbehandlung, da sie ermöglicht, einem Tumor hochkonforme Strahlendosen zu verabreichen und gleichzeitig das umliegende gesunde Gewebe zu schonen. Diese Präzision bietet das Potenzial für bessere Behandlungsergebnisse im Vergleich zur konventionellen Strahlentherapie mit Photonen. Die Protonen-Radiographie (pRAD) und Protonen-Computertomographie (pCT) versprechen eine Verringerung der Unsicherheit bei der Planung der Protonentherapie, welche mit der Umrechnung von Röntgen-Computertomographie (CT)-Zahlen, wiedergegeben in Hounsfield-Einheiten (HU), in das Protonenbremsvermögen relativ zu Wasser (RSP) verbunden ist.

Trotz des zunehmenden Einsatzes der Protonentherapie in der klinischen Praxis mangelt es noch immer an präklinischer Forschung zur Präzisionsbestrahlung von Kleintieren, zum Beispiel zur Ermöglichung eines besseren Verständnisses der strahlenbiologischen Wirkungen von Protonenstrahlen in Tumoren und gesundem Gewebe. Die Kenntnis dieser Effekte ist entscheidend für die Erprobung neuer Therapieansätze und die Gewährleistung optimaler Behandlungsergebnisse. Während für die Photonentherapie moderne Plattformen für die Forschung an Kleintieren kommerziell verfügbar sind, gibt es für die Protonentherapie noch keine kommerziell erhältlichen Systeme. Bildführung und präzise Bestrahlung sind von äußerster Wichtigkeit für eine sinnvolle onkologische Forschung an Kleintieren. Die Small Animal Proton Irradiator for Research in Molecular Image-guided Radiation-Oncology (SIRMIO)-Plattform wird an der Ludwig-Maximilians-Universität (LMU) München unter der Leitung von Prof. Dr. Katia Parodi entwickelt und durch das European Research Council (ERC) gefördert (Fördervertrag Nummer 725539). Die Plattform ist ein tragbares Prototypsystem zur bildgesteuerten Protonenbestrahlung von Kleintieren für die präzise präklinische Strahlentherapieforschung.

Protonenbildgebung ist in die SIRMIO-Plattform integriert, um eine exakte Positionierung des Kleintiers und eine genaue Bestrahlungsplanung zu erreichen. Zur Ermöglichung von Protonenbildgebung mit dem hohen instantanen Strahlfluss von Synchrozyklotron-basierten Protonentherapiezentren, wurde die Entwicklung und Implementierung der Bildgebung im Integrationsmodus verfolgt.

In dieser Arbeit wird die Bildgebung im Integrationsmodus mit einem Complementary Metal-Oxide-Semiconductor (CMOS)-Detektorsystem und der Variation der initialen Protonenstrahlenergie untersucht. In experimentellen Studien wurde die Bildgebung von Objekten in der Größe kleiner Tiere an isochronen Zyklotronanlagen untersucht und ein Proof-of-Concept-Experiment an einem klinischen Synchrozyklotron-Protonentherapiezentrum durchgeführt. Zu diesem Zweck wurden zwei Detektorsysteme im Hinblick auf ihre Eignung für den Betrieb in der SIRMIO-Plattform analysiert. Zur Unterstützung der experimentellen Studien wurden umfangreiche Monte Carlo (MC)-Simulationsstudien durchgeführt, zum Beispiel, um den Aufbau des bildgebenden Systems zu optimieren, zusätzliche Kalibrierdaten für eine genaue Bestimmung der wasseräquivalenten Dicke (WET) zu liefern und ergänzende Daten zu berechnen, die in den Experimenten nicht gewonnen werden konnten (zum Beispiel die deponierte Strahlendosis).
Zur Bestimmung der WET in der Protonenradiographie wurde die Methode der Bragg-Peak-Zerlegung verwendet. Zusätzlich wurden zwei rechnergestützte Monte Carlo (MC)-Methoden zur Reduktion der Bildunschärfe aufgrund von Protonenstreuung in den abgebildeten Objekten untersucht: Regularisierung der Lookup Table (LUT), die in der Bragg-Peak-Zerlegung zur Bestimmung der WET verwendet wird, und ein inverser Optimierungsansatz, der die Transmissionsprotonenbilder für mehrere Protonenstrahlenergien und MC-berechnete Streukerne verwendet, um die erwartete Streuung für eine gegebene WET vorherzusagen.

Es wurden verschiedene Lösungen für die Implementierung von Protonenradiographie im Integrationsmodus in die SIRMIO-Plattform untersucht. Es wurde festgestellt, dass die Protonenradiographie in einem optimierten Aufbau die Bestimmung der WET mit einer relativen Abweichung von 1% und einer räumlichen Auflösung im Submillimeterbereich ermöglicht. In den Experimenten wurde eine WET-Genauigkeit von besser als 1% mit einer Präzision von nahezu 1% bei Bildgebungsdosen von 10.6 mGy und 21.2 mGy für Phantom-Detektor-Abstände von 0 mm beziehungsweise 10 mm innerhalb einer Bildgebungsdauer von etwa 90 s erreicht. Auf der Grundlage der im Rahmen dieser Arbeit gewonnenen Erkenntnisse wurde berechnet, dass ein optimierter Bestrahlungsplan für das selbe Objekt und die selben Abstände zu einer Bildgebungsdosis von 7.8 mGy und 11.7 mGy innerhalb von 30 s führen kann. Darüber hinaus wurde gezeigt, dass die Protonenbildgebung im CMOS-Integrationsmodus in Synchrozyklotron-basierten Protonentherapieanlagen möglich ist. Das entwickelte Protonenbildgebungssystem ist benutzerfreundlich und robust im Betrieb, hat eine kompakte Größe und basiert auf einem kommerziell erhältlichen Detektorsystem, das eine industrielle Zuverlässigkeit verspricht.
Während der Ansatz der Protonenstreukorrektur durch Regularisierung der LUT vielversprechende Ergebnisse zeigt, sind Verbesserungen der räumlichen Auflösung bei zu großen Abständen zwischen Phantom und Detektor naturgemäß durch Multiple Coulomb Scattering (MCS) begrenzt.

Für die inverse Optimierungsmethode wurde ein Proof-of-Concept für die Streuungskorrektur erbracht, aber es bleiben Herausforderungen wie zum Beispiel die Minimierung der Rechenzeit und der algorithmischen Komplexität.

Zusammenfassend wurde ein kompakter Prototypenaufbau für Kleintierstudien zur Protonenbildgebung im Integrationsmodus mit einem CMOS-Detektorsystem und dessen Implementierung in die SIRMIO-Plattform optimiert. Mit diesem Aufbau ist Protonenradiographie mit hoher WET-Genauigkeit und räumlicher Auflösung auch bei dem in Synchrozyklotron-basierten Protonentherapieanlagen zu erwartenden hohen instantanen Protonenfluss möglich.

Abstract

Proton beam therapy is a promising modality in cancer treatment due to its ability to deliver highly conformal radiation doses to the tumor while sparing surrounding healthy tissue. This precision offers the potential for superior treatment outcomes compared to conventional photon radiation therapy. Proton Radiography (pRAD) and Proton Computed Tomography (pCT) promise to reduce uncertainty in proton therapy treatment planning inherent in the conversion of X-ray Computed Tomography (CT) numbers, expressed in Hounsfield Units (HU), to proton (relative to water) stopping power (RSP). Despite the increasing adoption of proton therapy in clinical practice, there is still a lack of pre-clinical precision small animal radiotherapy research, e.g., to enable a better understanding of the radiobiological effects of proton beams in tumour and normal tissue. Elucidating these effects is critical to the testing of new therapeutic approaches and to ensure optimal patient outcomes. Advanced small animal research platforms are commercially available for photon therapy, but there are no commercial options yet for proton therapy. Image guidance and precise irradiation are of utmost importance for meaningful small animal oncology research. The Small Animal Proton Irradiator for Research in Molecular Image-guided Radiation-Oncology (SIRMIO) platform is developed at Ludwig-Maximilians-Universität (LMU) Munich under the direction of principal investigator Prof. Dr. Katia Parodi with funding by the European Research Council (ERC) (grant agreement number 725539). It is a portable prototype system for image-guided small animal proton irradiation for precision pre-clinical radiation therapy research.
Proton imaging is integrated into the SIRMIO platform in order to achieve an accurate setup of the small animal and accurate treatment planning. To enable proton imaging with the high instantaneous beam flux of the synchrocyclotron-based proton therapy centers, the development and implementation of integration mode imaging has been pursued.

This work investigates integration mode imaging with a Complementary Metal-Oxide-Semiconductor (CMOS) detector system and variation of the initial proton beam energy. In experimental campaigns, imaging of small animal-sized objects was investigated at isochronous cyclotron-based facilities and a proof-of-concept experiment was performed at a clinical synchrocyclotron proton therapy center. For this purpose, two detector

systems were evaluated with respect to their suitability for operation within the SIRMIO platform. Extensive Monte Carlo (MC) simulation studies were carried out to support the experimental studies, e.g., to optimize the imaging setup, to provide additional calibration data for accurate Water-Equivalent Thickness (WET) determination, and to gather complementary data that were not obtained in the experiments (e.g., dose deposition).
The Bragg Peak Decomposition method was used to determine the WET in proton radiography. Additionally, two computational, Monte Carlo (MC)-supported methods were explored to reduce image blurring due to proton scattering in the imaged objects: regularization of the Lookup Table (LUT) used in the Bragg Peak Decomposition for WET determination and an inverse optimization approach utilizing the transmission proton images for multiple proton beam energies and MC-computed scatter kernels that predict the expected scattering for a certain WET.

Different solutions of integration mode proton radiography were investigated for implementation into the SIRMIO platform. Proton radiography in an optimized setup was found to enable WET determination with a relative WET error of 1% and sub-millimeter spatial resolution. In experimental campaigns, WET accuracy of better than 1% with precision close to 1% was achieved at imaging dose levels of 10.6 mGy and 21.2 mGy for phantom-to-detector separations of 0 mm and 10 mm, respectively, within an imaging duration of approximately 90 s. Based on insights gained in the course of this work, it was predicted that a refined imaging irradiation plan can result in dose levels of 7.8 mGy and 11.7 mGy for the same object and distances, respectively, within 30 s. Furthermore, CMOS integration mode proton imaging was shown to be feasible at synchrocyclotron-based proton therapy facilities. The developed proton imaging setup is user-friendly and robust in operation, has a compact size and is based on a commercially available detector system, which promises industrial-grade reliability in operation.
While the approach of proton scatter correction through regularization of the LUT demonstrates promising results, spatial resolution improvements are inherently limited by Multiple Coulomb Scattering (MCS) at too large phantom-to-detector distances.
For the inverse optimization method a proof of concept for scatter correction has been demonstrated, but challenges such as computational time constraints and algorithmic complexity remain.

In summary, a compact prototype setup for integration mode proton imaging using a CMOS detector system has been optimized for small animal studies and implementation in the SIRMIO platform. In that setup, proton radiography is achievable with high WET accuracy and spatial resolution, even at the high instantaneous proton flux expected at synchrocyclotron-based proton therapy facilities.

Contents

Table 1: Summary of constants and variables used in this thesis unless otherwise specified (Groom et al., 2020).

Symbol	Definition	Value or (usual) units
c	Speed of light	$299\,792\,458\,\mathrm{m\,s^{-1}}$
$m_e c^2$	Electron mass $\times$ c^2	$0.510\,998\,946\,1(31)\,\mathrm{MeV}$
r_0	Classical electron radius $e^2/4\pi\epsilon_0 m_e c^2$	$2.817\,940\,322\,7(19)\,\mathrm{fm}$
α	Fine structure constant $e^2/4\pi\epsilon_0\hbar c$	$1/137.035\ 999\ 139(31)$
N_A	Avogadro's number	$6.022\,140\,857(74) \times 10^{23}\,\mathrm{mol^{-1}}$
e	Elementary charge	$1.602\,176\,63 \times 10^{-19}\,\mathrm{C}$
ρ	Mass density	$\mathrm{g\,cm^{-3}}$
z	Charge number of incident particle	
Z	Atomic number of absorber	
A	Atomic mass number	$\mathrm{g\,mol^{-1}}$
I	Ionization potential	eV
Z	Atomic number	
ρ_e	Electron density	
β	Relativistic velocity divided by c	$\beta = \frac{v}{c}$
γ	Lorentz factor	$\gamma = {}^{1}/\sqrt{1-\beta^2}$

List of Figures

List of Tables

CHAPTER 1

Introduction

Proton therapy exploits the characteristic energy deposition of proton beams along their path through the patients body to achieve a better probability of tumor eradication and lower occurrence of normal tissue complications compared to conventional X-ray radiotherapy. The proton beam energy is chosen such that the protons stop in the tumor volume. To obtain the same dose within the tumor, proton beams will deposit less dose in healthy tissues than conventionally used X-rays and the stopping allows to protect radiation-sensitive organs.

There are further benefits of proton therapy in addition to the preferable energy deposition along the beam's path and stopping in the tissue: Proton irradiation is more effective in driving cancerous cells into cell death than high-energy X-rays for the same administered radiation dose, which is described and quantified through the *Relative Biological Effectiveness (RBE)* (Krämer et al., 2003; Amaldi et al., 2005). In clinical proton therapy, the spectrum of relevant physical interactions extends from proton energies of 3 MeV to 300 MeV (Gottschalk, 2012) considering both the initial beam energies and the energies attained in tissue after slowing down. Commonly, initial proton beam energies in the clinical application are in the region of 50 MeV to 70 MeV for ocular treatments and from 70 MeV up to 250 MeV for the treatment of tumors at different depths in the patient's body. Beams of higher energies are used to pass through the patient's body for imaging. Particles in this energy range set in motion other cell signaling pathways in the tumor tissue than photon irradiation (Durante, 2014).

To calculate the optimal initial proton beam energy that is needed to deposit the prescribed dose in a specific region in the patient, a map of proton stopping power in the patient's body is necessary. This map can be obtained by transmission imaging, where X-rays or particle beams pass through the patient and are detected after exiting the patient's body. The measured properties of the radiation leaving the patient (e.g., fluence for X-rays or kinetic energy for particles) are used to deduce on the three-dimensional distribution of

the (relative to water) proton stopping power (RSP). The RSP can most directly be determined by radiographic or tomographic imaging with proton beams of higher energy than used in treatment. As an example, 200 MeV suffice to image a human head and 250 MeV are deemed reasonable to image the lung region of most people (Johnson, 2018), although higher energies are needed to pass through the thickest parts of most patients.
There is still a lack of long-term clinical studies to demonstrate that the aforementioned physical advantages and radiobiological effects translate into better treatment outcomes and reduce the adverse effects of radiotherapy (Baumann et al., 2016). Random and controlled patient studies are subject to strict ethical considerations, are complex to implement and may take several decades, especially when the smaller occurrence of secondary cancers from dose to healthy tissue needs to be shown. As proton therapy is not widely available, it is difficult to publish studies with large patient cohorts. Through pre-clinical experiments, the biological understanding of potential benefits of radiotherapy modalities is advanced whilst minimizing or eliminating adverse effects. Small animal studies are a necessary step to transfer research findings into clinical practice. Accuracy of treatment planning is crucial in particle therapy due to the RBE effect as well as the sharp distal dose fall-off and the thereby implied increased sensitivity to inter- or intra-fractional anatomical changes or alterations in RSP. Therefore further (pre-clinical) research is particularly important in the field of particle therapy.
Several platforms for pre-clinical radiotherapy research with photon irradiation are in existence including commercially available systems, like the Small Animal Radiation Research Platform (SARRP) (Xstrahl, UK) (Deng et al., 2007) and the X-RAD 225Cx (Precision X-Ray Inc., USA) (Clarkson et al., 2011). First systems for pre-clinical proton irradiation are in development, but limited by passive beam shaping and image guidance based on X-ray Cone Beam Computed Tomography (CBCT) (Ford et al., 2017; Kim et al., 2019). The Small Animal Proton Irradiator for Research in Molecular Image-guided Radiation-Oncology (SIRMIO) project aims to build a platform for precise image-guided small animal irradiation that can be installed at existing proton therapy facilities (Parodi et al., 2019). The project is lead by principal investigator Prof. Dr. Katia Parodi and funded by the European Research Council under the European Union's Horizon 2020 research and innovation programme (grant agreement number 725539). This work focuses on one of the proton imaging modes that are used in the platform: integration-mode imaging with a commercially available Complementary Metal-Oxide-Semiconductor (CMOS) detector.

1.1 The SIRMIO Platform

The SIRMIO platform allows precise image-guided small animal irradiation and can be installed at horizontal beamlines of existing proton therapy facilities (Parodi et al., 2019). It is the first system with a dedicated beamline and treatment planning system that offer the possibility to form a narrow enough proton beam to precisely irradiate small animals.

The SIRMIO beamline is mounted in a box filled with helium and produces a focused, narrow proton beam ($\sigma \approx 1\,\mathrm{mm}$). The lowest proton beam energy of the facility where it is installed is reduced to the relevant range of 20 MeV to 50 MeV (Gerlach et al., 2020) for small animal irradiation (see figure 1.1). After the beam shaping elements, a monitor IC is installed for measurement of the particles before hitting the sterile shell that includes the mouse. For tumor detection, treatment planning, and positioning, ultrasound images (Lascaud et al., 2021a) will be co-registered to proton images, with the advantage that proton imaging will directly measure the Water-Equivalent Thickness (WET) (in radiography) or RSP (in tomography) needed for treatment planning (Poludniowski et al., 2015; Johnson, 2018; Krah et al., 2018). In-vivo range verification is provided by ionoacoustic measurements (Lascaud et al., 2021a) and an in-beam PET system (Lovatti et al., 2020; Lovatti et al., 2023) (see figure 1.2).

Proton imaging will be available in three different modes, adapted to the treatment center where the SIRMIO platform is mounted. The collimators and magnets used to shape the beam for treatment are removed from the beam's path with motorized stages before imaging. Instead, two imaging collimators are moved in the center of the beamline to limit the Field of View (FoV) and protect the components in the box and its back wall from stray irradiation (see figure 1.3). A Single-particle Tracking (SPT) tomography system is developed in-house, consisting of floating strip Micromegas front and rear trackers (Bortfeldt et al., 2016) to measure position and direction of each individual proton before and after the object, respectively and a Time-Projection Chamber (TPC)-based range telescope (see figure 1.4). Simulation studies with a realistic model of the Proton Computed Tomography (pCT) system foresee improved range predictions in treatment planning compared to conventional (X-ray) planning Computed Tomography (CT) (Meyer et al., 2020).

At proton therapy facilities where the beam is provided by a synchrocyclotron, the proton flux within the microbunches exceeds the readout electronics' rate capability of $7\,\mathrm{MHz\,cm^{-2}}$. Therefore, proton imaging based on single-particle dE-measurement with two Timepix detectors (Würl et al., 2020a) as well as integration mode imaging using a large-area CMOS sensor and energy stacking are developed in parallel to be used in the SIRMIO platform. Figure 1.5 shows the approaches with the Timepix and the CMOS detector, respectively.

Proton images acquired in integration mode can be used in small animal experiments for position verification. In addition, there are innovative methods that could exploit the radiographic images for specific Hounsfield Units (HU) to RSP conversion (Gianoli et al., 2020) of a previously recorded tomographic image (typically X-ray CBCT) or adapt a X-ray or proton CT based on Deformable Image Registration (DIR) to the daily anatomy as suggested by Palaniappan et al., 2023.

The CMOS detector's area is sufficiently large to image a mouse at once without moving

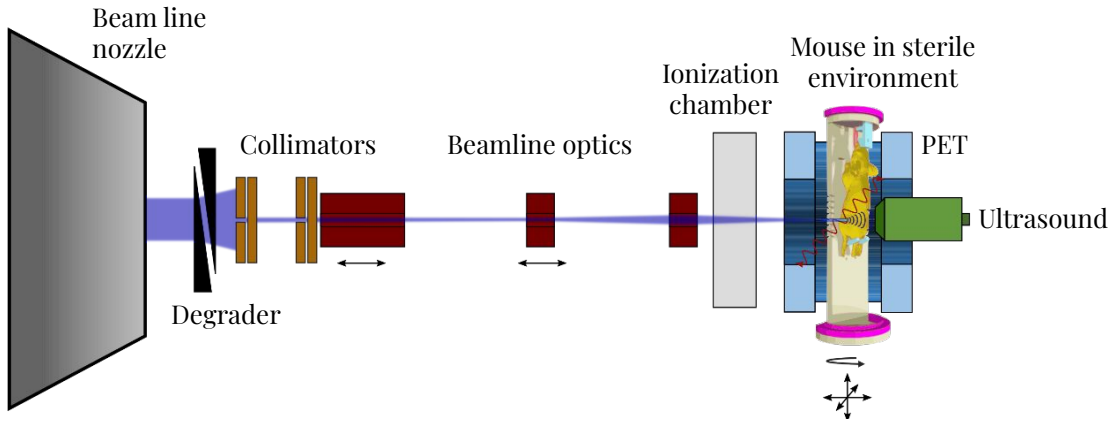

Figure 1.1: Schematic of the SIRMIO platform: After the nozzle of the proton therapy facility, the proton beam is degraded and shaped by a first set of degrader and collimators. Magnets are used to focus the beam of the proton therapy facility. A monitor Ionization Chamber (IC) is fixed in front of the mouse holder. During treatment, the Positron Emission Tomography (PET) system and the Ultrasound (US) system are in place. Image courtesy of Dr. Matthias Würl.

it or the detectors, which is advantageous compared to the Timepix detectors[1]. Relative to other proton imaging setups, integration mode setups are in general more compact and easier to operate. CMOS detectors provide the advantage of being commercially available, which entails increased confidence in reliable performance and lower cost as compared to a customized solution.

1.2 Aim and Outline of this Thesis

This work aims to thoroughly investigate different solutions of integration mode imaging with a CMOS detector system for implementation of small animal proton imaging in the SIRMIO platform. In the first chapter, the underlying physics of the interactions that take place when protons pass through matter and the basics of semiconductor detectors are recalled, along with the definition of necessary physical quantities and concepts. This chapter also introduces the general concept of Monte Carlo (MC) simulations. The following chapter explains the historical and technological development as well as the basic rationale of conventional and particle radiation therapy in general, and of proton imaging specifically.

Building on these introductory chapters, the successive two chapters outline the materials and methods used in this work. The first one introduces the computational methods and experimental materials that were used, including two different CMOS sensors. The second one describes the studies that were carried out to determine which CMOS detector meets the requirements for integration mode imaging and to devise the optimal setup of that

[1] The Timepix detectors are limited to 14 mm × 14 mm sensitive area at the time of writing and although multiple sensors can be tiled to form an array, this option results in considerable cost.

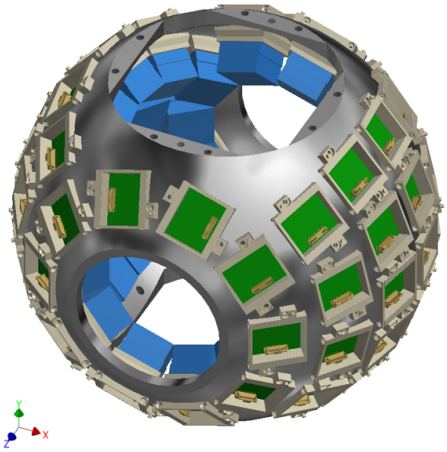

Figure 1.2: Schematic drawing of the dedicated in-beam SIRMIO PET scanner with the 56 crystal detector blocks arranged in spherical geometry. The openings in vertical directions allow to insert the mouse holder, while the openings in horizontal direction enable the beam to pass through. Reused with permission from (Nitta et al., 2021).

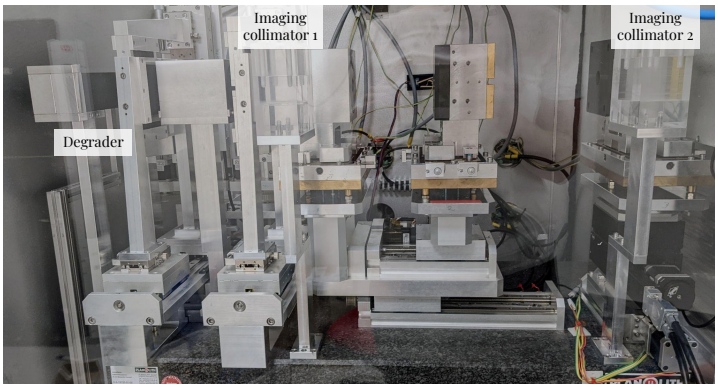

Figure 1.3: Photo of SIRMIO beamline box showing the degrader and the two imaging collimators in the front. In the back, the beam focusing elements (permanent quadrupole magnets and collimators) are visible.

detector.

The subsequent chapter *Integration Mode Imaging with a CMOS Detector* illustrates the principle of integration mode proton imaging with energy variation, which allows for imaging with a single CMOS sensor behind the imaged object. That chapter also explains how an image is produced from the acquired data and how the data were analyzed to optimize the imaging setup and workflow for application in the SIRMIO platform. Thereafter, the setups of different experimental campaigns are presented, including a description of how they were reproduced in MC simulations to complement the experiments. The last part of that chapter explains the data evaluation strategies which were used to combine the findings from the various experiments and MC studies into the main results, which are presented and discussed.

The following chapter *Scatter Correction Methods for Integration Mode Particle Imaging* introduces computational methods to deblur proton images by correcting for Multiple

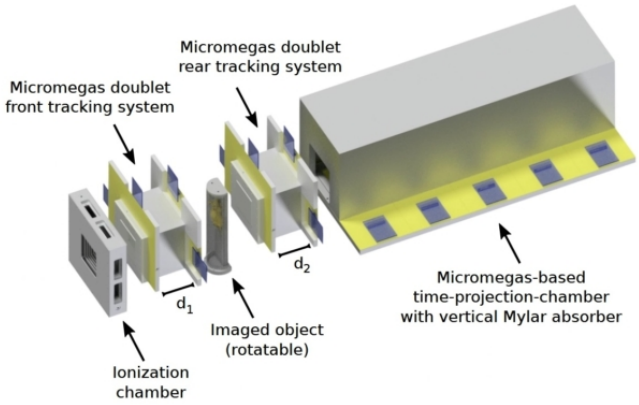

Figure 1.4: Schematic drawing of the SPT system with the monitoring IC, front and rear tracker pairs and the TPC. Reused with permission from Meyer et al., 2020.

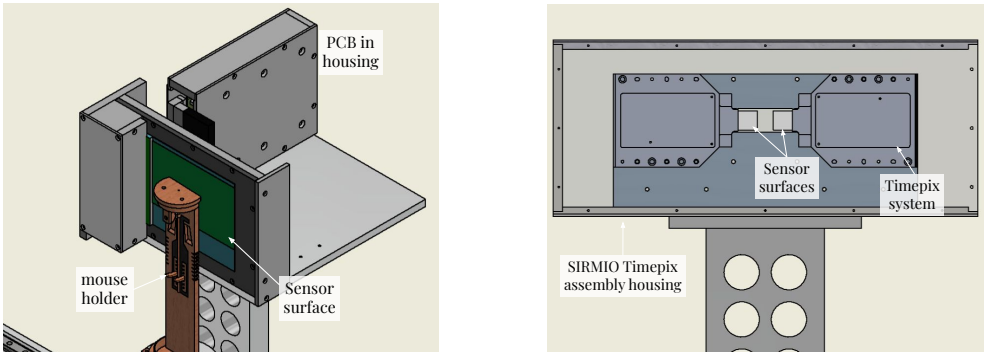

(a) **(b)**

Figure 1.5: Schematic drawings of (a) the CMOS integration mode detector system with the surface of the sensor placed immediately after the mouse holder and (b) the arrangement of the two Timepix detectors for imaging. The final proton images from the Timepix detectors have to be produced from several acquisitions to compensate for the limited sensor areas.

Coulomb Scattering (MCS) that were explored in the course of this thesis. First results exploiting these methods are shown and discussed.
Finally, the approach of integration mode proton imaging with a CMOS detector in general is critically reviewed and compared to SPT. Conclusions on the employment of integration mode proton imaging are summarized in the last chapter.

CHAPTER 2

Underlying Physics for Proton Beam Therapy and Imaging

Within the field of medical physics, ionizing radiation is used for the purposes of treatment and imaging. Charged particle irradiation for imaging and therapy research purposes as well as in clinical use is mostly considered in a scenario where a beam of accelerated particles, here called "projectiles", hits a fixed object, here called "target". The first section of this chapter will discuss the interactions that take place when a particle beam passes through matter and define the physical quantities that are relevant to understand the principles and discussions in the following chapters. As this work is within the field of proton imaging and all experiments were realized using proton beams, this chapter will firstly discuss the specific case of proton interactions.
The second section of this chapter will discuss the interactions of photons with matter, which are relevant in the course of this work, e.g., to understand the response of the detector in experiments with radioactive sources.
The third part of this chapter will introduce semiconductor particle detectors with an emphasis on CMOS technology.
The fourth part of this chapter introduces the general principle of MC simulations.

2.1 Principles of Proton Beam Interaction with Matter

If accelerated protons in the energy range that is relevant for clinical proton therapy pass through an object, they interact with the target atoms mainly in three physical processes that are schematically outlined in figure 2.1[1].

[1] Clinically relevant proton energies are usually considered from 3 MeV to 300 MeV (Gottschalk, 2012) consisting of both the initial beam energies and the energies during deceleration in the target.

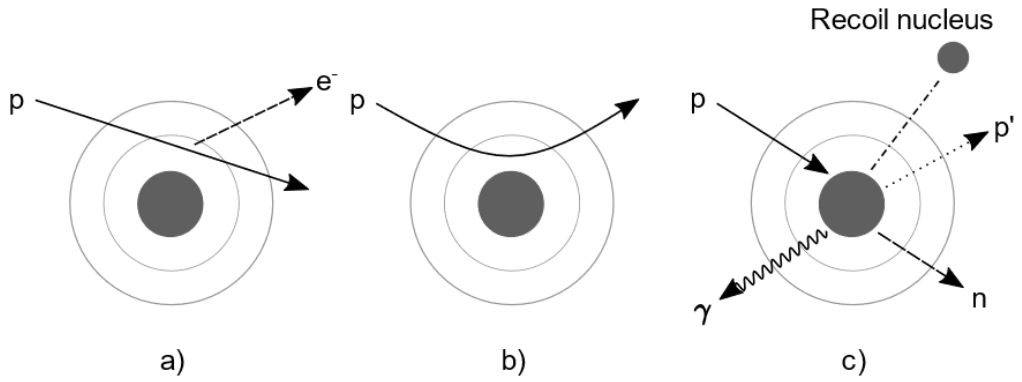

Figure 2.1: Proton interactions in matter most relevant to proton therapy[1]: a) Inelastic scattering with electrons, b) deflection from positive nuclei and c) nonelastic nuclear reactions and production of secondary particles.

Inelastic Coulomb Collisions of the projectile with atomic electrons, in which it transfers part of its kinetic energy to the electrons and therefore is slowing down, are the most likely interaction and cause excitation or ionization of the target's atoms.

Deflection of the projectile from its trajectory through the Coulomb field of the atomic nuclei is generally called Coulomb *scattering* and will laterally enlarge the beam size. Bremsstrahlung from this process can be neglected in the case of clinically relevant proton beam energies[1].

Nuclear reactions are collisions of the projectile with a target nucleus, which can happen either (quasi-)*elastic*, i.e., no or only a small amount of kinetic energy is transferred to the nucleus, or nonelastic. In the nonelastic case, the proton can set nuclear particles and light nucleon clusters into motion, so-called secondary particles. In those events, the secondary particles have much lower energy and larger scattering angles than the incident proton.

2.1.1 Energy Loss and Stopping of Protons in Matter

The stopping power S of a material is defined as the incremental energy loss per unit path length and given in $\mathrm{MeV\,cm^{-1}}$,

$$S = -\frac{\mathrm{d}E}{\mathrm{d}x} \ . \tag{2.1}$$

S consists of a component that is attributed to the energy lost in inelastic collisions of the proton with the orbital electrons of the target, the *collision stopping power* $S_{\mathrm{col.}}$, a second component due to elastic Coulomb collisions with the nuclei of the target, called the *nuclear stopping power* $S_{\mathrm{nuc.}}$, and a third component from bremsstrahlung emitted in the electric field of the target nuclei, the *radiative stopping power* $S_{\mathrm{rad.}}$. The nuclear

stopping power in water is relevant for proton energies below the region of 10 keV (see figure 2.2).

The collision stopping power $S_{\text{col.}}$ of ions can be approximated by the Bethe-Bloch equation (Bethe, 1930; Bloch, 1933). A version for relativistic particles including two important corrections is (Groom et al., 2020):

$$S_{\text{col.}} = -\left\langle \frac{dE}{dx} \right\rangle = 4\pi r_0^2 \, m_e c^2 \, N_A \rho \frac{Z}{A} \frac{z^2}{\beta^2} \left[\frac{1}{2} \ln \left(\frac{2m_e c^2 \gamma^2 \beta^2 W_{\max}}{I^2} \right) - \beta^2 - \frac{\delta(\beta\gamma)}{2} - \frac{C}{Z} \right] , \tag{2.2}$$

with $W_{\max}$ being the maximum energy transfer in a single collision:

$$W_{\max} = \frac{2m_e c^2 \beta^2 \gamma^2}{1 + 2\gamma m_e / M + (m_e/M)^2} \ . \tag{2.3}$$

Equation 2.2 is accurate to about 1% down to 1 MeV for protons (Groom et al., 2020). The properties of the target material enter the equation 2.2 with:

- $\boldsymbol{I}$ being the mean excitation potential of the target material, a quantity that also plays an important role in the MC simulations presented in this work.
- $\boldsymbol{Z}$ is the target material's atomic number.
- $\boldsymbol{A}$ corresponds to the atomic mass number.
- $\boldsymbol{\rho}$ is the mass density of the target.

Quantities describing the projectile are:

- $\mathbf{z}$ is the projectile's charge in multiples of the elementary charge e, which for protons is $z = 1$. Note that z is squared in equation 2.2, leading to a quadratic increase of the stopping power for ion species with higher charge (e.g., carbon ions) compared to protons.
- $\boldsymbol{\beta}$ is the projectile's velocity relative to the speed of light, v/c. It influences the energy loss proportionally to its inverse square, meaning that the slower the incident particle is, the higher the energy transfer to the target material is.
- $\boldsymbol{\gamma}$ the relativistic γ-factor $\gamma = (1 - \beta^2)^{-\frac{1}{2}}$.
- M being the particle mass.

The included corrections to the original version by Bethe are the **density correction** $\frac{\boldsymbol{\delta}}{\mathbf{2}}$ and the **shell correction** $\frac{\boldsymbol{C}}{\boldsymbol{Z}}$. The density correction $\frac{\delta}{2}$ takes into account the polarization

[2] NIST database. Available from: www.nist.gov/pml/data/asd.cfm

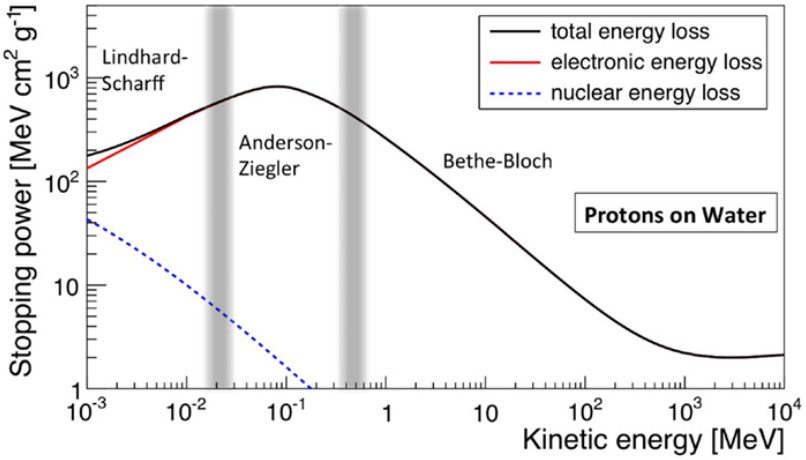

Figure 2.2: Stopping power $\frac{dE}{dx}$, in MeV cm^2 g^{-1}, for protons in water as function of kinetic energy. The total, electronic (collision), and nuclear stopping power are shown, as well as the characteristic regions. Made using NIST data[2]. Image from Kraan, 2015 reused under the Creative Commons Attribution License (CC BY).

of the target material, when a high energetic, charged particle is passing through it. Closer electrons are shielding the field of more remote ones, leading to a reduction in stopping power.

The shell correction $\frac{C}{Z}$ is relevant for low particle velocities. The uncorrected Bethe equation assumes free electrons, which is valid when the projectile's velocity (for protons about 10 MeV) is large compared to the atomic electrons.

Avogadro's number $\boldsymbol{N_A}$, the Bohr electron radius $\boldsymbol{r_0}$, the electron rest mass $\boldsymbol{m_e}$ and the speed of light in vacuum $\boldsymbol{c}$ are natural constants (see table 1).

$N_A\,\rho\,\frac{Z}{A}$ is the absorber's electron density ρ_e. The values of the electron density ρ_e and the mean excitation potential I of the target material are relevant for accurate calculation of the expected range. In the therapeutic energy range, the electronic part of the stopping power is almost equal to the total stopping power. The Bethe equation only provides the statistical expected value of collision stopping power for multiple particles in a thick absorber and is not suitable to predict the energy loss by a single particle.

The historic development of stopping power estimation, including the relevant corrections and extrapolations to energies below 1 MeV u^{-1} as well as different approaches to calculate them are outlined in Ziegler, 1999.

Protons in the therapeutic energy range are moderately relativistic, e.g., a proton beam with kinetic energy $E_1 = 3\,\text{MeV}$ to $E_2 = 300\,\text{MeV}$ has a relativistic velocity of $\beta_1 \approx 0.08$ to $\beta_2 \approx 0.65$, respectively.

The **mass stopping power** $\frac{S}{\rho}$ is the stopping power S divided by the materials mass density ρ and given in the units MeV cm^2 g^{-1}:

$$\frac{S}{\rho} = -\frac{1}{\rho}\frac{\mathrm{d}E}{\mathrm{d}x}\ . \tag{2.4}$$

2.1.1.1 Relative Stopping Power

As visible in figure 2.2, the lower the kinetic energy of the proton is, the higher is its stopping power within the validity range of the Bethe-Bloch formula. For kinetic energies lower than about 100 keV the stopping power decreases. Consequently, the energy loss per increment of depth of a proton that is traversing a material increases gradually, until it reaches a maximum and then rapidly drops, bringing the particle to a stop. Figure 2.3a shows the proton stopping power for different materials obtained from a FLUKA (Ferrari et al., 2005; Böhlen et al., 2014) MC simulation. Water is the reference material in medical physics as it is a first approximation to human tissue and the standard dosimetry material. Therefore, the Relative Stopping Power (RSP) of materials compared to water is a necessary quantity for proton therapy treatment planning.
It is defined from equation 2.2 without corrections as:

$$\mathrm{RSP} = \frac{\rho_{e,m}}{\rho_{e,w}} \times \frac{\ln(2m_e c^2\gamma^2\beta^2/I_m) - \beta^2}{\ln(2m_e c^2\gamma^2\beta^2/I_w) - \beta^2} \ , \tag{2.5}$$

with the electron densities $\rho_{e,m}$ and $\rho_{e,w}$ as well as the mean ionization potentials I_m and I_w for a specific material and water, respectively.

2.1.1.2 Dose

The imparted mean energy $\mathrm{d}E$ deposited in a finite volume V with mass $\mathrm{d}m$ is called the **absorbed dose** and expressed in units of Gray ($\mathrm{Gy} = {}^{\mathrm{J}}/_{\mathrm{kg}}$) (Podgorsak, 2005):

$$D[\mathrm{Gy}] = \frac{\mathrm{d}E}{\mathrm{d}m} \tag{2.6}$$

$$= 1.6 \times 10^{-10} \times \Phi \left[\frac{1}{\mathrm{cm}^2}\right] \times \frac{S}{\rho}\left[\frac{\mathrm{MeV\,cm}^2}{\mathrm{g}}\right] \ , \tag{2.7}$$

with Φ being the particle fluence.
The characteristic curve of energy deposition of ions as a function of material depth is called the **Integrated Depth Dose (IDD)** with its maximum at the position of the **Bragg peak** (see figure 2.3b). A mathematical parametrization of the Bragg peak curve is given by Bortfeld, 1997.

2.1.1.3 Proton Range

The **proton range** R describes the expectation value of pathlength traveled by a particle in a medium to its stopping point. It is defined for a beam of particles, i.e., a large number of particles with ideally identical initial energy and direction. In proton beam therapy, accurate prediction of the range in the patient is essential to precisely irradiate the tumor.

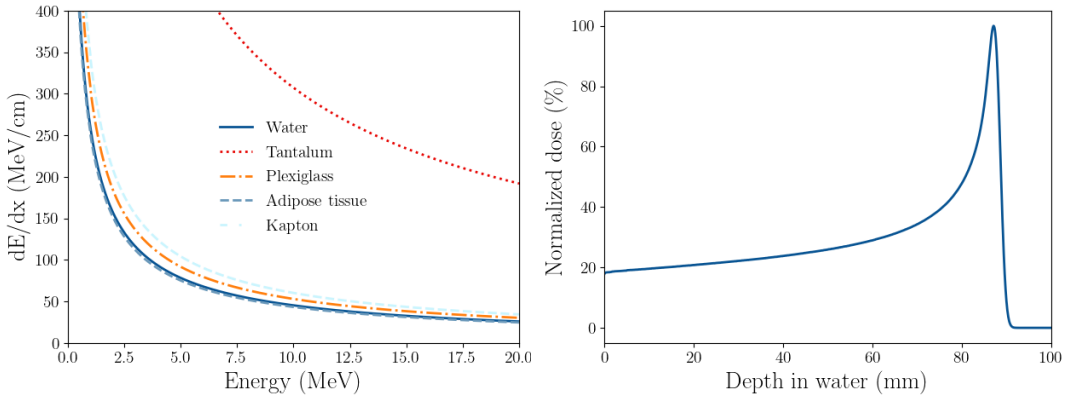

(a) **(b)**

Figure 2.3: (a) Comparison of the proton stopping power for different materials tabulated by the FLUKA MC code (Ferrari et al., 2005; Böhlen et al., 2014) for energies from 100 keV to 20 MeV. (b) Bragg peak curve of a 107 MeV proton beam in water, scored in a FLUKA MC simulation.

Charged particles passing through a material lose their kinetic energy mainly from numerous collisions with a small fraction of energy lost in each collision. In the **Continuous Slowing Down Approximation (CSDA)**, the energy loss is approximated to be continuous along the particle's track. The CSDA range R_{CSDA} of a proton beam with initial energy E_0 is defined as (Attix, 2004):

$$R_{\mathrm{CSDA}}(E_0) = \int_0^{E_0} \left(\frac{\mathrm{d}E}{\mathrm{d}x}\right)^{-1} \mathrm{d}E \ , \tag{2.8}$$

with R_{CSDA} given in cm. It is the path length along the proton's curved trajectory and does not represent penetration depth in beam direction.

The **mean projected range** R_{p} is the expectation value of the farthest penetration depth along the initial direction of the particle (Attix, 2004). Otherwise put, the mean projected range R_{p} is the depth in medium at which half of the incident particles that undergo only electromagnetic interactions have stopped (Gottschalk, 2012).

The ratio between the projected and CSDA range, the so-called *detour factor* $d = {}^{R_{\mathrm{p}}}/_{R_{\mathrm{CSDA}}}$, for protons and heavy ions is close to 1, meaning that the CSDA range is a close approximation to the projected range.

In clinical practice, the range is measured with an ionization chamber and expressed in terms of absorbed dose. The R_{80} is the depth distal, i.e., downstream, of the Bragg peak where energy deposition is reduced to 80 % of the maximum value. It was shown that the R_{80} corresponds closely to the mean projected range (Bortfeld, 1997; Berger, 1993). Other conventionally used values are the distal 90 % dose range R_{90} and the distal 10 % dose range R_{10}, e.g., to evaluate the steepness of the fall-of after the maximum, along with the distal and proximal 50 % of maximum dose to quantify the width of the Bragg peak.

In this work, *range* refers to R_{80} unless otherwise specified.

As the stopping power is proportional to $1/\beta^2$ and β^2 is approximately proportional to the kinetic energy of the particle, this indicates a power law formulation between the range and the initial beam energy E_0. This was proposed by Bragg and Kleeman (Bragg et al., 1905) and allows an analytical approximation of the range after:

$$\mathrm{R} = \alpha \cdot E_0^p \ , \tag{2.9}$$

where α is a constant of the target material given in $\mathrm{cm\,MeV}^{-p}$. The exponent p reflects the non-linear relation between range and initial beam energy. In the energy regime from 50 MeV to 250 MeV, the power p has been determined to $p \approx 1.7 - 1.8$ (Ulmer, 2007) and p is dimensionless if E_0 is given in MeV. For water, Bortfeld (1997) calculated $\alpha = 0.0022\,\mathrm{cm\,MeV}^{-p}$ from a fit of the range-energy table from the ICRU report 49 (Berger et al., 1993) to equation 2.9.

Due to the stochastic nature of the interaction processes, the single protons in a beam will each follow an individual path and suffer corresponding energy loss and therefore come to rest at various endpoints. The component of this spread longitudinal to the beam is described by the term **range straggling**. In addition, a proton beam produced in an accelerator will have an initial **energy spread** ΔE. Range straggling and energy spread determine the width of the Bragg peak in beam direction. For a beam consisting of many particles passing through a thick material layer, the statistical fluctuation in the energy loss allows to approximate the distribution of the particle range using a Gaussian function[3]. For protons in water, Bortfeld, 1997 determined the sigma of the range straggling to be:

$$\sigma_{RS} \approx 0.012 \times R^{0.935} \ , \tag{2.10}$$

where R and σ_{RS} are given in cm. σ_{RS} can be considered the minimal Bragg peak width taking into account the range straggling and is increased by the contribution σ_{beam} from the beam energy spread ΔE (Gottschalk, 2012).

2.1.1.4 Water-equivalent Thickness

An important concept in medical physics is the **Water-Equivalent Thickness (WET)** of an object. If a block of material with geometrical thickness in beam direction of t_m and mass density ρ_m is irradiated with a particle beam of initial energy E_i and the range in water R after the block is measured, then the Water-Equivalent Thickness is defined by the thickness of a hypothetical block of water t_w with density ρ_w replacing

[3]The approximation neglects multiple elastic scattering, which will lead to a slightly asymmetric distribution as it can only shorten the expected proton range.

the material that would result in the same range R:

$$t_w = t_m \frac{\rho_m}{\rho_w} \frac{\bar{S}_m}{\bar{S}_w} \ , \tag{2.11}$$

where $\bar{S}_m$ and $\bar{S}_w$ are the mean proton mass stopping powers of the material and water, respectively (Zhang et al., 2009).
Opposite to the calculation of the thickness of a hypothetical block of water, the measurement of the WET of a material can be used to estimate its mean RSP. As described in Grant et al., 2014 based on Schaffner et al., 1998, the Relative Linear Stopping Power (RLSP) is derived from the shift Δx of the Bragg peak in water from the introduction of a material with geometrical thickness t_m[4]:

$$\text{RLSP} = \frac{\Delta x}{t_m} \ . \tag{2.12}$$

A quantity closely related to the WET is the **Water-Equivalent Path Length (WEPL)**, which is defined for each proton as the path integral of the RSP along the individual trajectory of the proton. Averaging over many proton WEPL values that have passed through a material gives an estimate of the WET.

2.1.2 Multiple Coulomb Scattering

The lateral deflection of protons from their path through a medium is a random walk in angle, mostly caused by Coulomb interactions with the atomic nuclei (see figure 2.1b). Large angle scattering events can be neglected for radiotherapy purposes, as they only affect about 2 % of the protons in a beam (Gottschalk et al., 1993). At lower proton energies, more scattering events occur and the net displacement is higher. Molière's theory (Molière, 1948) of multiple Coulomb scattering of protons is regarded as the most elegant and accurate description of the scattering angle distribution. It includes generalizations to arbitrarily thick targets and compounds and mixtures as target materials, which are important factors for proton therapy treatment planning (Gottschalk, 2012). The net displacement from many additive small-angle events can be approximated through the Central Limit Theorem by a Gaussian distribution, as is done, e.g., in Highland's approximation (Highland, 1975). The root mean square (rms) width θ_0 of the projected angular distribution in this approximation is given by:

$$\theta_0 = \frac{13.6\,\text{MeV}}{\beta cp} z \sqrt{\frac{x}{X_0}} \left[1 + 0.038 \ln(\frac{x}{X_0})\right] \ , \tag{2.13}$$

[4]This equation applies to IDD measurements conducted in a vacuum. When employed in air, it serves as an approximation tailored for thin material slabs, ensuring that substituting the air in front of the water column with the material has negligible impact on the Bragg peak position.

where β, p and z are the relativistic beta function, the momentum, and the charge number of the projectile, c is the speed of light and x/X_0 is the thickness of the scatterer in radiation lengths. The numerical value of 13.6 MeV has been updated according to the value of the the Particle Data Group from Lynch et al., 1991.
The radiation length X_0 of a medium, given in $\mathrm{g\,cm^{-2}}$, is defined by the characteristic amount of matter traversed by high-energy electrons and photons. For high-energy electrons, bremsstrahlung is the predominant process of energy loss, while for high-energy photons, it is e^+e^- pair production. The radiation length is defined by both processes: (i) as the mean distance for an electron to lose all but $1/e$ of its energy through bremsstrahlung and (ii) for photons by $7/9$ of the mean free path for pair production (Tanabashi et al., 2018). It is determined using values calculated and tabulated by Tsai, 1974:

$$\frac{1}{X_0} = 4\alpha r_0^2 \frac{N_A}{A} \cdot \left[Z^2 (L_{rad} - f(Z)) + Z L'_{rad} \right] \ , \tag{2.14}$$

with mass number A given in $\mathrm{g\,mol^{-1}}$, atomic number Z, the fine structure constant α, the radiation logarithms L_{rad} and L'_{rad}. $f(Z)$ is the Coulomb correction to electron pair production that is estimated by:

$$f(Z) = a^2 \left[(1 + a^2)^{-1} + 0.020206 - 0.0369a^2 + 0.0083a^4 - 0.002a^6 \right] \ , \tag{2.15}$$

where $a = \alpha Z$ and α being the fine structure constant (Overbo, 1977).

2.1.3 Energy Loss in Thin Layers

The previous sections introduced the slowing down and lateral spread of multiple particles with similar incident energies passing through material. Another quantity of interest in this work is the amount of energy lost when protons pass through a particularly thin layer of material, e.g., a few µm of silicon in a sensor.
It is important to notice that the energy loss per particle fluctuates strongly. Figure 2.4 shows the measured distribution of pixel values (directly proportional to energy deposition) of protons in a 5.5 µm silicon detector. The energy loss probability follows the Landau-Vavilov distribution (Landau, 1944; Vavilov, 1957) with the most probable energy loss Δ_p given by Bichsel, 1988:

$$\Delta_p = \xi \left[\ln \frac{2mc^2\beta^2\gamma^2}{I} + \log \frac{\xi}{I} + j - \beta^2 - \delta(\beta\gamma) \right] \ , \tag{2.16}$$

where $\xi = (K/2)\langle Z/A \rangle z^2 (x/\beta^2)$MeV with thickness x in $\mathrm{g\,cm^{-2}}$, $K = 4\pi N_A r_0^2 m_e c^2$ and $\delta(\beta\gamma)$ being the density effect correction to the ionization energy loss. The most probable energy loss is preferable to the mean value when describing the energy loss by single particles in a detector. Rare high-energy-transfer collisions build the tail of the distribution, whereas 90 % of the collisions lead to an energy deposition below the mean value.

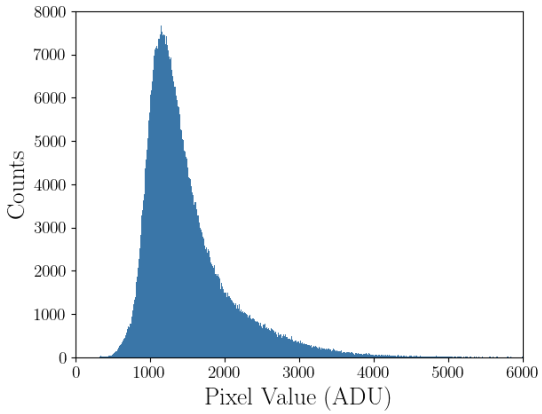

Figure 2.4: Occurence of measured pixel values in a 5.5 µm silicon detector from irradiation with 30 MeV protons and integration time of 100 ms.

2.1.4 Nuclear Reactions

Nuclear interactions of accelerated particles can be of elastic nature, i.e., without transfer of energy, or inelastic, where the kinetic energy of the projectile is not conserved, and nuclei may undergo fragmentation.

Nuclear inelastic interactions of protons with the target nuclei lead to the attenuation of the primary particle and can entail fragmentation of the target nucleus and thereby the production of secondary protons, deuterons, tritons, ^{3}He, ^{4}He, further ions, neutrons, as well as photon emission. These nuclear interactions impact the spatial dose distribution and the produced neutrons can also increase the risk for radiogenic late effects (Newhauser et al., 2015).

Those secondary emissions can also provide a means of *in-vivo* measurement of the proton range, e.g., by Positron Emission Tomography (PET) (Parodi et al., 2007b) or prompt gamma imaging (Polf et al., 2009).

2.1.5 Integrated Depth Dose Curves for Different Lateral Detector Sizes

Whether experimentally measured Bragg peak curves follow the "textbook" shape shown in figure 2.3 depends on the combination of the beam size, the beam's divergence and the detector geometry. For an optimal measurement of the IDD, the used detector's lateral extension should be large enough, such that all particles of the beam are collected along the depth of measurement. That is the reason why in clinical proton therapy practice, large diameter ionization chambers are used. If the detector is too small laterally, then the beam broadening with increasing depth in water will entail that less protons contribute to the measured energy deposition than compared to shallower depths.

Figure 2.5 shows the IDD of a 120 MeV annular proton beam with 5 mm radius in water for the scenarios of 0 mrad and 200 mrad divergence that was scored in a FLUKA MC simulation in detectors of different radii $r = 2$ mm, 5 mm, 8 mm, and 20 mm. The largest

detector radius of $r = 20\,\text{mm}$ captures all particles along the depth in water, including scattered ones. In figure 2.5a the change in the height of the Bragg peak is from fluence loss due to lateral scattering. The case of the $r = 2\,\text{mm}$ detector shows a detector that is smaller than the beam size at the entrance of the medium and therefore only captures a part of the proton beam. Figure 2.5b shows a scenario of divergence values that are not realistic for clinical treatments, but possible in experimental scenarios where the beam is broadly scattered on purpose. In this case more protons leave the detector area of measurement with increasing depth, leading to a decreasing slope in the Bragg peak region that is usually denoted as the "plateau region".

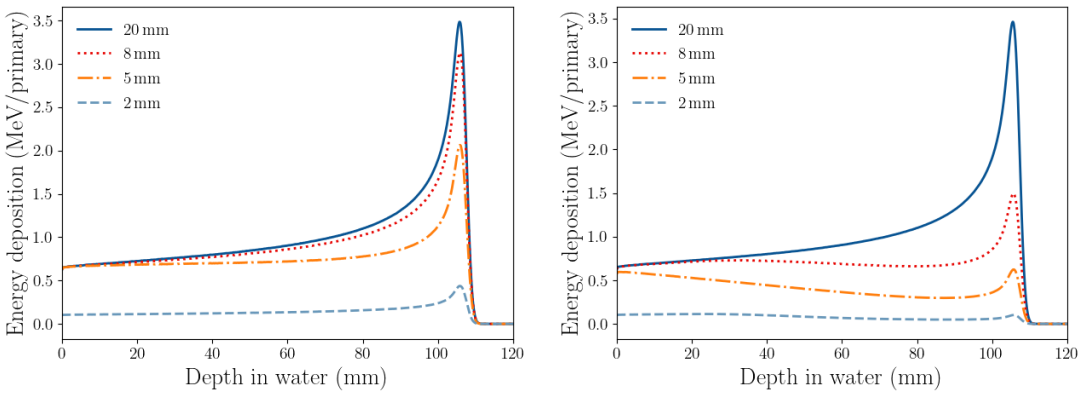

Figure 2.5: IDDs of a 120 MeV annular proton beam in water with 5 mm radius and obtained from a FLUKA MC simulation. The detector was set to a circular shape with radii of $r = 2$ mm, 5 mm, 8 mm and 20 mm. (a) Without any beam divergence. The reduced height of the maximum is a result of protons being scattered outside of the detector radius. (b) The extreme case scenario of 200 mrad divergence leads to a reduced proton number for increased depth in water.

2.2 Photon Interaction in Matter

The interaction processes of photons with matter are photoelectric absorption, Rayleigh scattering, Compton scattering, pair production, and photonuclear reactions. The relevant range of photon energy in this work and for medical applications is from a few keV to the commonly used 6 MV up to about 20 MV photon beams with an energy spectrum with 6 MeV and 20 MeV maximal energy, respectively. The physical interactions of photons that are most relevant in this energy range will be covered in this section. A comprehensive description of photon interactions including high-energy photons can be found in the literature, e.g., in Groom et al., 2020 or Podgorsak, 2005.

The probability for each process to occur depends on the photon energy $E_\gamma = h\nu$ and the target material's atomic number Z. Figure 2.6 shows the interaction probability for photons in silicon as a function of the photon energy.

The attenuation of a monoenergetic photon beam with initial intensity I_0 by a medium is described by the Beer-Lambert law[5]:

$$I(x) = I_0 e^{-\mu(E_\gamma, Z)x} \ , \tag{2.17}$$

[5]In the case of a polyenergetic beam, equation 2.17 needs to be modified to be: $I(x) = \int_0^{E_{\gamma,max}} I_0(E_\gamma)\ e^{-\int \mu(E_\gamma,Z)\mathrm{d}x}\ \mathrm{d}E_\gamma$.

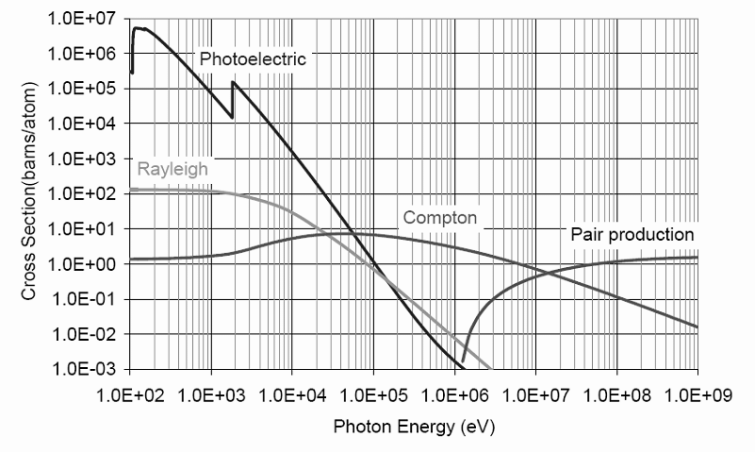

Figure 2.6: Partial cross sections for photon interaction in silicon. Reused with permission from Berghmans et al., 2008.

where $I(x)$ is the transmitted photon intensity after a depth x in a homogeneous material and μ is the *linear attenuation coefficient*:

$$\mu = \frac{\rho N_A}{A}\sigma_{\text{tot}} \tag{2.18}$$

which represents the fraction of attenuated incident photons per unit length traveled, e.g., in cm^{-1} if the thickness x is given in cm.
The *total cross section* σ_{tot} represents the probability of interaction of the photon with the atoms of the absorber per unit length with the length measured in nuclei cm^{-2} and is given by:

$$\sigma_{\text{tot}} = \frac{A}{\rho N_A}\mu \ , \tag{2.19}$$

with the unit of cm^2 per nucleus.
The *mass attenuation coefficient* μ_m is defined as:

$$\mu_m = \frac{\mu}{\rho} \ , \tag{2.20}$$

with the unit $\text{cm}^2\,\text{g}^{-1}$ such that for equation 2.17, the mass thickness $x\rho$ must be used, given in $\text{g}\,\text{cm}^{-2}$.

The *total attenuation coefficient* μ is the sum of the individual attenuation coefficients of photoelectric absorption τ, Rayleigh scattering σ_R, Compton effect

σ_C, and pair production κ[6]:

$$\mu = \tau + \sigma_R + \sigma_C + \kappa \ . \tag{2.21}$$

The *total mass attenuation coefficient* $\frac{\mu}{\rho}$ is the sum of the individual mass attenuation coefficients:

$$\frac{\mu}{\rho} = \frac{\tau}{\rho} + \frac{\sigma_R}{\rho} + \frac{\sigma_C}{\rho} + \frac{\kappa}{\rho} \ . \tag{2.22}$$

2.2.1 Photoelectric Absorption

At low photon energies and in high-Z media, the most relevant interaction process is photoelectric absorption, where a bounded electron in a material is ejected with maximum kinetic energy $K_{\max}$, if it absorbs the energy of a photon $E_\gamma = h\nu$ and gains more energy than its binding energy W:

$$K_{\max} = E_\gamma - W \ . \tag{2.23}$$

The photon is fully absorbed in this process. For $E_\gamma < 0.1\,\mathrm{MeV}$ where the effect dominates in water, the cross section $\sigma_{\text{p.e.}}$ can be approximated to be proportional to the atomic number Z and the photon energy following Z^4/E_γ^3 (Podgorsak, 2005).
Characteristic edges in the spectrum are according to the binding energies of electrons in specific atomic levels in the target material and called *absorption edges*.
The vacancies from ejected electrons are filled by rearrangement of the electronic shells or capture of free electrons, entailing characteristic X-ray or Auger electron emissions.

2.2.2 Rayleigh Scattering

Rayleigh scattering is the elastic scattering of photons with bound electrons that occurs predominantly for low photon energies. The cross section for Rayleigh scattering is proportional to Z^2/E_γ^2 and the scattering angle is inversely proportional to the photon wavelength. As there is no energy transfer, there are no secondary emissions.

2.2.3 Compton Effect

Compton scattering is the inelastic scattering of photons by an outer shell or free electron, resulting in a change of the photon's direction by the deflection angle θ. Part of the photon's initial energy $h\nu$ is transferred to the electron which is ejected, thereby ionizing the atom.

[6]Due to their low probability of occurrence in the relevant photon energy range for medical applications, photonuclear reactions are neglected in the total attenuation coefficients.

The lowered photon frequency $h\nu'$ after the energy transfer as a function of the scattering angle is derived from the conservation of energy and momentum to be:

$$h\nu' = h\nu \left(1 + \frac{h\nu}{m_e c^2}(1 - \cos\theta)\right)^{-1} . \tag{2.24}$$

The Compton effect is the dominant interaction mechanism for soft tissue in medical X-ray imaging and its cross section is proportional to Z and decreases for higher photon energies.
In the case of ionization, characteristic X-rays and Auger electrons are emitted.

2.2.4 Pair Production

Above a threshold energy of two times the rest mass of the electron $2m_e c^2 = 1.022\,\text{MeV}$, an electron-positron pair can be created in the vicinity of a nuclear Coulomb field.
The cross section increases with the photon energy until a saturation value due to electron screening of the nuclear field and is proportional to Z^2. A subsequent effect can be annihilation radiation.
This process of interaction is also possible for a photon in the field of an atomic electron, which is then ejected from the atom. As three charged particles emerge from this process, it is referred to as **triplet production**. The energy threshold is $4m_e c^2 = 2.044\,\text{MeV}$ and the ratio of triplet production compared to nuclear pair production is approximately $1/CZ$ with C being a function of the photon energy ($C = 1$ for $E_\gamma \to \infty$ and $C \approx 2$ for $E_\gamma = 5\,\text{MeV}$).

2.2.5 Photonuclear Reactions

In photonuclear reactions, a high energy photon is absorbed by the nucleus of the target material, and a proton ((γ,p) reaction) or neutron ((γ,n) reaction) is emitted and the nucleus is thereby transformed into a radioactive reaction product. Typical reaction thresholds are in the order of 10 MeV or higher (except for deuteron and ^{9}Be nuclei with $\sim 2\,\text{MeV}$) (Podgorsak, 2005). The contribution of photonuclear reactions to the total attenuation coefficient is only a few percent for energies above the reaction threshold and the probability of occurrence is much smaller than that of other photon interaction processes at clinically used photon energies. Neutron production from x-ray beams above 10 MeV energy leads to concerns about radioactivity induced in the treatment room.

2.3 Semiconductor Detectors

Particle detection generally relies on the measurement of the outcomes of the interactions that take place when a particle moves through matter. For the considered cases, these interactions are either ionization or excitation of the material's atoms, mainly from electromagnetic interaction. The role of a detector is to transform microscopic perturbations into a macroscopic phenomenon. As each particle leaves only a small signal when traversing a material, that signal must either be amplified or the detector has to be made from a material in that a large signal is created.
As this work is based on the utilization of a CMOS detector for proton imaging, this section will focus on semiconductor detectors.

2.3.1 The Band Model

In a solid material, the energy states that an electron can have are somewhat in between the cases of a free electron (the kinetic energy can have any value) and an atomic electron (with quantized energy states). In a crystal lattice, such as in silicon, the valence orbitals of neighboring atoms spatially overlap and split into different atomic levels that are energetically close to each other. As the number of close by energy levels is very large, they are forming a quasi-continuous energy band with finite width in energy. Between these conceptual bands are gaps of energy states that are not accessible to electrons, the so-called forbidden gaps (Spieler, 2005). The band formed by the outermost energy orbital of an atom is called the *valence band*. Electrical current can flow if electrons are excited from the valence band to the *conduction band*, where they have enough energy to move freely in the material. In a metal (a classical conductor), valence band and conduction band overlap and electrons move with little energy supply (small potential difference). In an isolator, the band gap is so large, that a prohibitively high energy influx would be necessary for electrons to move into the conduction band. This amount of energy is called the "breakdown voltage", as usually the isolator material is destroyed under such tension. Semiconductors are structurally similar to isolators, but the band gap is narrow with typical values of some eV, e.g., $E_{\text{gap}} = 1.12\,\text{eV}$ for silicon.

2.3.1.1 Doping

The conduction properties can be improved through the addition of a small quantity (concentrations in the range from $10^{12}\,\text{cm}^{-3}$ to $10^{18}\,\text{cm}^{-3}$ (Spieler, 2005)) of chemical elements, called "dopants". Dopants are either of the type donor (e.g., antimony with 5 electrons in the outer shell to dope silicon that has 4 valence electrons) or acceptor (e.g., boron with 3 valence electrons). The doped semiconductor is still electrically neutral. If for example antimony is added to a silicon lattice, a n-type semiconductor is formed with a quasi-free electron. These electrons occupy new energy levels just 0.05 eV below the conduction band.

The opposite case would be for example boron added as impurity, creating a p-doped semiconductor with a "hole", which is a not occupied electron energy state in a filled band. The holes are accessible to electrons from the valence band and are just 0.05 eV above it.

2.3.2 The p-n Junction

If a p-type and n-type semiconductor are juxtaposed, the electrons diffuse towards the p-doped region and recombine with the holes. At the same time, the movement of the charge carriers will cause that the charge from the fixed atomic nuclei are no longer compensated and the electric equilibrium is broken. This leads to an electrical field in opposite direction of the diffusion field. At the interface, a neutral region without free charge carriers, the depletion layer, is formed and there is no electrical current. The p-n junction is the elementary foundation for semiconductor diodes. If an external voltage is applied such that the positive terminal is connected to the p-doped region, called *forward bias*, electrons can flow from the n-type to the p-type semiconductor. If an external voltage is connected with the positive terminal to the n-type region, called *reverse bias*, the electrons are pulled away from the junction and the voltage barrier increases, so the p-n diode is behaving as an insulator.

2.3.3 Functional Principle of a Semiconductor Detector

The signal in a semiconductor detector is formed when ionizing radiation enters the depleted layer of the p-n junction. The energy deposition creates electron-hole pairs and the free charges will move according to the electric field lines. An electrical current that is proportional to the charges created by ionization events can be measured. In silicon, an electron-hole pair is created on average with an amount $w = 3.6\,\mathrm{eV}$ of deposited energy. The intrinsic number of charge carriers in silicon is quite large ($1.5 \times 10^{10}\,\mathrm{cm}^{-3}$ at 300 K) compared to the number of electron-hole pairs that can be created by a charged particle in the thickness of the detector. A minimum ionizing particle deposits around $4.6\,\mathrm{MeV\,cm}^{-1}$ in depth, creating $80\,\mu\mathrm{m}^{-1}$ electron-hole pairs (Spieler, 2005). To reduce the noise of the silicon, it needs to be emptied from the free charges. The depleted layer of the p-n junction is the so-called *sensitive volume* or *active volume* of a silicon detector. Through external voltage, the active volume can be enlarged.
The advantage compared to other types of detectors is the amount of excitation quanta that are created in a semiconductor detector when hit by an ionizing particle. For comparison, in a gas roughly 30 eV are required for each ionization (Hilke et al., 2020), and furthermore it exhibits a lower density than condensed matter, leading to lower interaction probability. Likewise, the required energy to produce a photon in a scintillating material is higher than the energy needed for one electron-hole pair in silicon, e.g., each photon produced in sodium iodide NaI(Tl) requires about 25 eV (Lecoq, 2020). The increased

statistics allows for a better energy resolution, that is even improved as compared to the known Poisson statistics by the Fano factor F (Spieler, 2005):

$$\Delta E_{\mathrm{FWHM}} = 2.35\, w \sqrt{F N_Q}\ , \tag{2.25}$$

with N_Q as number of created electron-hole pairs.
In addition, the time for collection of the generated electrons is 10 ns to 100 ns and therefore several orders of magnitude faster than that of ionization chambers, which leads to better time resolution of semiconductor detectors (Demtröder, 2017).
The explanations and examples in this section were all based on silicon, as this is the material of the detectors used in this work. Other materials for semiconductor detectors are for example germanium ($E_{\mathrm{gap}} = 0.66\,\mathrm{eV}$ and mean energy for electron-hole creation of $w = 2.9\,\mathrm{eV}$ at 300 K) and diamond ($E_{\mathrm{gap}} = 5.5\,\mathrm{eV}$ and $w = 13\,\mathrm{eV}$).

2.3.4 Active Pixel Sensors

First attempts to achieve spatial resolution with silicon detectors came with strip detectors, where many strip diodes with a readout channel for each were positioned on a wafer. Nowadays pixel detectors with sizes down to 15 µm × 15 µm have been built (Tiffenberg et al., 2017). Active pixel sensors have signal amplification and readout for every pixel. In a Monolithic Active Pixel Sensor (MAPS), the substrate of the wafer is also the detector material.

2.3.4.1 CMOS Detectors

CMOS technology is often used in active pixel sensors, therefore often called CMOS sensors. CMOS is the combination of a p- and n-type Metal-oxide-semiconductor Field-effect Transistor (MOSFET), as shown schematically in figure 2.7: in this example the wafer material is of type p. On top of the wafer, a lightly p-doped epitaxial layer is grown. Two n-type junctions are diffused into the epitaxial layer, forming two back-to-back p-n junctions. One of the n-type regions is the *source* and the other one is the *drain* of the transistor. To control the current between source and drain, a capacitor is build from a very thin dielectric layer (usually silicon oxide) between source an drain and another conducting layer on top of that, called the *gate*. This first part (belonging to the left side of figure 2.7) is a N-channel enhancement-mode Metal-oxide Semiconductor (MOS) Device (NMOS) (Lancaster, 1977). To build the P-channel Enhancement-mode MOS Device (PMOS), a larger region of the p-type substrate is doped n-type, forming the n-well and the transistor is built from two p-typed regions into the n-well. On top of the epitaxial layer is a passivation layer, mostly from silicon oxide, that holds the pixel architecture.

CMOS pixel sensors are used in particle physics to take advantage of their high spatial

resolution, readout speed, low material budget (sensitive thickness of few µm), relative radiation hardness (stable after 50 kGy with cooling to 0 °C (Beck et al., 2023)) and low power consumption. Signal processing in integrated circuits on the wafer allows for high throughput (around 10 GB s^{-1}) and there is practically no dead time (proportional to the number of pixels and pixel readout time). In the example of the LASSENA detector used in this work (see section 4.2.2) the dead time is about 10 µs, compared to the integration time in the order of some 10 ms. Furthermore, operation at room temperature is possible, the detector systems are not bulky, and the widespread use leads to manufacturing by multiple companies with industrial reliability and at reasonable cost.

2.3.5 Noise and Background

What is usually called the "background" signal of a measurement consists of several sources of noise that can be mitigated each on its own. Thermal fluctuations lead to the so-called *dark current* or *leakage current* which increases with radiation damage and can be reduced by cooling of the detector. In realistic measurement scenarios, also *ambient noise* is present. In the case of the measurement of the proton energy deposition with a CMOS detector, this source of noise is mainly from ambient light as the detector is sensitive to photons. Thorough light shielding is necessary to suppress the signal from ambient light. Dark current and the component of ambient noise that remains in spite of shielding in a given experimental setup can be measured and consequently subtracted from the measured signal. Naturally, *statistical fluctuations* in the proton interactions, in the beam current, and the charge collection in the detector are present, resulting in a minimum amount of protons to be measured per pixel for a targeted level of precision.

2.3.6 Radiation Damage in Silicon Detectors

One limitation to the lifetime of semiconductor detectors is damage from ionizing and non-ionizing interactions of radiation. One year at a standard radiotherapy facility will deposit around 30 kGy if every beam goes through the sensor (Beck et al., 2023). This damage can be classified in two categories: bulk damage and surface damage (Lutz et al., 2020).

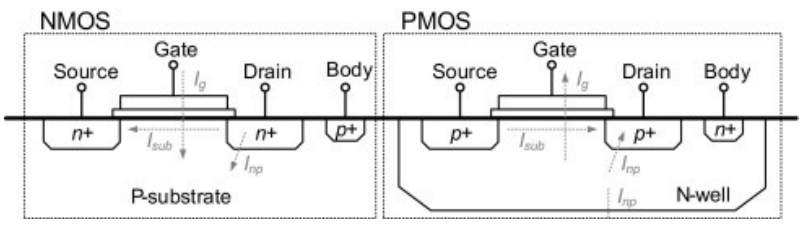

Figure 2.7: Cross-section of NMOS and PMOS Field-effect Transistors (FETs) fabricated in a CMOS process (reused with permission from Ha et al., 2021).

2.3.6.1 Bulk damage

Bulk damage comes from the atoms of the crystal lattice of the detector material being knocked-out of their place in a non-ionizing event that requires a minimum energy transfer of 25 eV in the case of silicon. Above 1 keV, the knocked-out silicon atom can itself knock out further atoms. These defects in the lattice add further energy levels in the band gap and can be of donor or acceptor type. At room temperature some of the defects can anneal. The consequences are an increased dark current, a reduced charge collection as signal charges could be trapped, and a change of the electric field in the region of charge collection. If the density of the introduced defects is larger than the doping density, this can result in a significant change of the electric field distribution in the detector, such that the n-type material can appear p-like ("type inversion").

2.3.6.2 Surface damage

Surface damage occurs from massive particles or photons that ionize atoms in the insulating layer (e.g., the SiO_2 for silicon sensors). Electron-hole pairs are produced in these ionization events. The electrons can diffuse, but the holes remain trapped at the interface between the Si sensitive area and SiO_2 passivation layer. Electrons in the silicon can accumulate at the interface, leading to short circuits or produce surface-generation currents, when an electric field is applied. Results can be breakdown after several days of operation, increased leakage current and noise, along with reduced charge collection.
At room temperature, significant annealing takes place. Surface-radiation effects can be mitigated by sensor design (Schwandt et al., 2013).

2.4 The Principle of Monte Carlo Simulations

Experimental campaigns need to be carefully prepared in advance, as the allocated time at proton therapy facilities is limited and expensive. The parameter space regarding the beam (employed beam energies, beam current, expected beam divergence), the detector settings, the phantoms to be used, and the detailed experimental setup (e.g., use of degraders, collimators, and scatterers) has to be explored as good as possible, so that only minor adaptations are carried out on-site. Also, dedicated hardware (e.g., degraders, phantom stands) needs to be manufactured or ordered. Besides analytical estimations, Monte Carlo simulations are a mighty tool to the physicist to estimate experimental outcomes and furthermore to complement experimental results by information that could either not be directly assessed (such as dose deposition in the imaged phantoms in the case of this work) or could not be obtained due to experimental time restrictions.

MC simulations are a statistical technique that was developed by physicists in the course of the nuclear weapons project at Los Alamos National Laboratory to sample the outcome of stochastic processes (Metropolis et al., 1949), for example the transport of neutrons and photons through matter. Physical laws and cross sections of particle-matter interactions are implemented and for each particle, the interaction process and its outcome is sampled step by step according to a sequence of (pseudo-)random numbers. When this is done for a large number of particles, the result can be considered a valid estimation of the real experiment, limited by the implemented physics models.
In particle therapy and imaging research, MC simulations are widely used, not only for dose calculation (Paganetti et al., 2008) and treatment planning (Parodi et al., 2012), but also to support almost any other aspect. This is nicely illustrated on the example of the SIRMIO platform (see section 1.1): MC simulations are used to predict irradiation-induced positron emitter distributions (Parodi et al., 2007a), to design the in-beam PET scanner (Lovatti et al., 2023), and optimize the setup of sensors in ionoacoustic measurements, to optimize Proton Radiography (pRAD) and pCT-systems (Meyer, 2019), to design the beamlines (Gerlach et al., 2020), and validate the treatment planning system (Zott, 2021).
The advantages are that the most sophisticated MC codes (e.g., FLUKA, see section 4.1) include physical phenomena from the lowest (keV) to the highest (e.g., cosmic ray) energies with high accuracy and the interactions can be modelled in realistic, 3D geometries, e.g., X-ray CT images. In medical physics, they are more accurate than analytical algorithms to predict dose deposition by particles, especially in heterogeneous media (Paganetti et al., 2008).
Compared to analytical calculations (Gianoli et al., 2019), MC simulations need significant computation resources and time.
To achieve accurate results in reasonable computing times, the physical processes taken into consideration in each simulation are chosen and limited by thresholds defined by the

user. State-of-the-art MC codes provide the flexibility to either follow the history of each particle, at the expense of higher computing resources, or to simulate the combined effects from many events on the basis of the statistical distribution that represents the physical stochastic effect, e.g., choosing between single scattering or MCS. Additionally, a given MC simulation setup needs to be validated against experiments to be used for reliable predictions.

During this work, the MC framework FLUKA (Ferrari et al., 2005; Böhlen et al., 2014) was used, which will be presented in section 4.1.

CHAPTER 3

Imaging and Tumor Therapy with Protons

This chapter outlines the beginnings of radiotherapy with X-rays and protons, along with the delivery of a proton beam therapy treatment to the patient, to explain the role of imaging in radiation therapy. Subsequently, the development and state-of-the-art of various modes of proton imaging are described.

3.1 Radiation therapy with X-rays and Particle Beams

Cancer is the illness where defect cells in an organism will not follow the path of controlled cell division until cell death, as in healthy subjects, but proliferate and eventually spread through the body.
Radiotherapy was developed along two fundamental fronts: nuclear radiation, i.e., radiation emitted in radioactive decays of nuclei, and radiation from extra-nuclear sources produced from electric devices. The accidental discovery of X-rays by Wilhelm Conrad Röntgen in 1895 and the discovery of of natural radioactivity by Henry Becquerel (1896) have rapidly been translated into medical applications. One prominent example is found in 1903 nobel laureates Marie and Pierre Curie, who in addition to fundamental research also developed solutions for medical imaging, e.g., cars equipped with X-ray tubes, and who provided the radium for the first brachytherapy in 1901 (Mayer et al., 2022).
When the first radiographic images were acquired, the skin of the patients showed irritations, which were the first hints of the biological effects of radiation on human tissue. These irritations were due to the characteristic dose deposition of X-rays with a maximum of dose deposited just below the skin and the long exposure times that were needed at that time to produce the images. The consideration of how the whole organism tolerates

radiation led physicians and physicists to design treatment schemes that are selective, focused and well dosed.

Radiotherapy in general is the medical specialization of using ionizing radiation as treatment agent with the objective to heal or reduce the complications of patients by inhibiting the cancer cells' capacity to reproduce. In its beginnings, radiotherapy was considered for multiple indications including benign diseases but has become an indispensable and effective means of treating cancer, in addition to other solutions among which the most important are surgery and chemotherapy.

Within a cell's nucleus, the amount and type of radiation-induced damage to the Deoxyribonucleic Acid (DNA) determine the activation of either the survival response network or cell death pathways. The DNA can either be damaged via direct hits of the DNA strands by ionizing radiation or indirectly, through the energy deposition in tissue (see section 2.1) that leads to ionization events either within the molecules of the cells or in adjacent water cells, releasing highly reactive free radicals that will damage the DNA. It was discovered by Puck et al., 1956 that cancerous cells are fast responding to radiation damage to the DNA (single and double strand breaks), which means that less cells survive an administered dose of radiation than late-responding healthy tissue cells[1]. In radiation therapy this difference in cell response is exploited to achieve the so-called "differential effect": a certain dose of radiation is applied to the tumor volume in several fractions distributed over a certain time, e.g., over several weeks with daily administration during the working weekdays of the hospital. During the breaks, more healthy tissue cells will regenerate as compared to the cancerous cells. When a cell's DNA is damaged too severely, it will eventually stop reproducing and activate the cell death pathway. The amount of dose and number of fractions are prescribed by the clinicians such that a maximum of the cancer cells will reach this threshold whilst reducing complications of the healthy tissue. The details are specific to the cancer type and site and are also a subject of current research. In this context, the possibility of reducing dose to critical structures has enabled new treatment regimens such as hypofractionation (i.e., the total prescribed dose is divided into fewer large doses and therapy is given over a shorter time than in standard radiation therapy), promising an improved biological effect and reduced time constraints to patients (Paganetti, 2017).

Radiation therapy as a cancer treatment modality was first attempted using X-rays in 1896 by Emil Grubbe[2] and first successfully conducted on a carcinoma by Senbeck and Sjögren in 1899 in Sweden (Berven, 1962). Radiation therapy with photons was continued until today, starting with X-ray tubes, then using ^{60}Co sources, including so-called Gammaknifes, and linear accelerators (commonly abbreviated as *LINAC*s).

[1] However, there are also normal cells that are fast responding to radiation, but typically less fast than tumor tissue.

[2] https://www.science.org/doi/abs/10.1126/science.125.3236.18

Similarly, the possibility to produce beams of accelerated heavy charged particles - enabled by the invention of the cyclotron by Ernest Lawrence in 1931 (Lawrence et al., 1932) - was rapidly linked to the envisioned application in radiation therapy by Robert Wilson in 1946 (Wilson, 1946). Wilson pointed out how the IDD of protons was suitable to irradiate a strictly localized region with lower skin dose as compared to X-rays (see figure 3.1). The SOBP in figure 3.1 is obtained from the superposition of multiple Bragg peaks to homogeneously irradiate the tumor volume in depth.

3.1.1 Proton Beam Therapy Treatment Delivery Modes

The proton beam shape and energy need to be adapted to the tumor size and localization in the patient's body. The volume that will be irradiated is defined by physicians with the help of medical imaging techniques, routinely with a X-ray CT scan and if beneficial complemented by Magnetic Resonance Imaging (MRI) and / or functional imaging such as PET or Single Photon Emission Computed Tomography (SPECT).
With the help of a Treatment Planning System (TPS), the optimal proton beam energies and angles to cover the tumor volume are calculated. The particular implementation of the beam delivery depends on the type of accelerator and the beamline design.

Before being modified in the treatment head, the proton beam from the cyclotron has an energy-dependent energy spread in the order of $\lesssim 1\%$ ($\Delta E/E$) and a Gaussian lateral beam profile with σ of a few millimeters (Paganetti et al., 2008; Paganetti, 2012a).

In **passive scattering**, the proton beam is first scattered laterally with high-Z materials and shaped to the lateral contours of the target volume by collimators, to achieve a homogeneous dose deposition in the target region and sharp dose-gradients at the edges. To cover the tumor volume in direction of the beam axis, the sharp Bragg peak of the monoenergetic beam from the accelerator needs to be spread, e.g., with a modulator

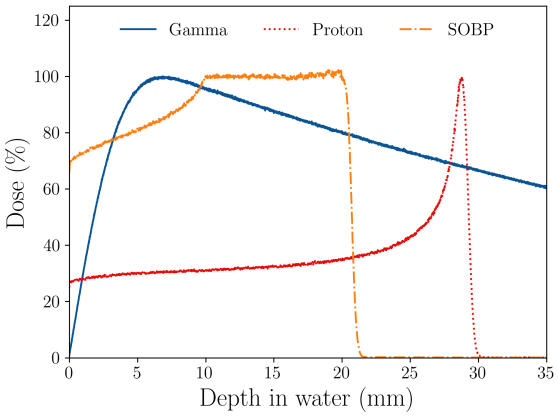

Figure 3.1: Comparison of the IDDs of a 18 MeV photon beam, a 226 MeV proton beam and a Spread-out Bragg peak (SOBP) with 20 cm range and 10 cm modulation (normalized to the 95% plateau dose).

wheel. Bragg peaks of different energies are irradiated each with a particle fluence that is optimized such that a flat dose region is obtained, the so-called Spread-out Bragg peak (SOBP). The distal contours of the irradiated area are adapted to the patient-specific anatomy and tumor shape with patient compensators (see figure 3.2).

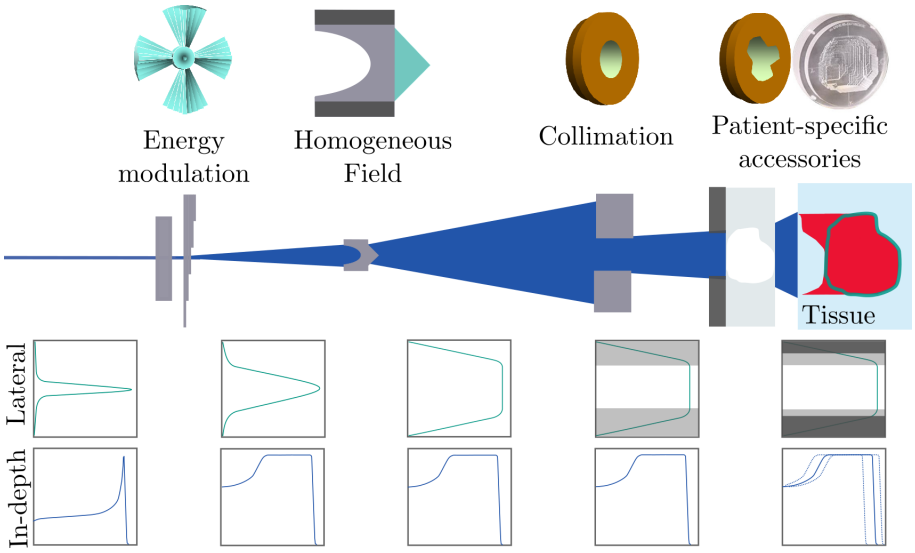

Figure 3.2: The dose deposition is shaped laterally through scattering and (patient-specific) collimators and in-depth by energy modulation (here illustrated by a modulator wheel) and a patient-specific compensator.

In **Pencil Beam Scanning (PBS)** or magnetic beam scanning the three-dimensional tumor volume is "painted" by scanning a narrow, quasi-monoenergetic pencil beam over several raster points to a slice of the tumor volume orthogonal to the beam direction. This is repeated for several slices in depth, where the depth is defined by the initial proton beam energy (see figure 3.3). The beam is steered by two pairs of magnets, one for each cartesian dimension orthogonal to the beam axis.

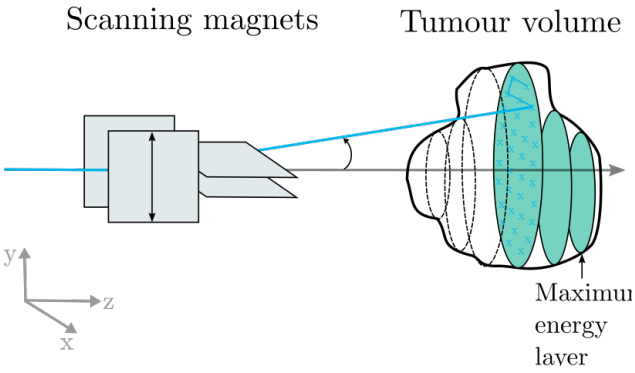

Figure 3.3: With the pencil beam scanning technique the energy is deposited in the tumor volume layer by layer by raster scanning a narrow beam of protons.

3.2 Proton Imaging for Particle Therapy

Visualizing the inside of the human body without operation has been a big advancement in medicine, which started with the discovery of X-rays in the end of the 19th century. Imaging is not only necessary for the initial treatment planning, but also for position correction during pre-treatment patient setup and for image-guided and adaptive radiation therapy.
In X-ray CT the photon attenuation in tissue is measured and the value in each voxel in a 3D grid is given in Hounsfield Units (HU), that are defined using the photon attenuation coefficient μ of the material relative to water (Hounsfield, 1973) (see section A.1).
As photons deposit their kinetic energy along the passage through matter very differently than protons (see figure 3.1), the conversion from HU to RSP for proton therapy treatment planning is inherently inaccurate (U. Schneider et al., 1996), translating to range uncertainties of on average 1-2 % of the proton range (Paganetti, 2012b). Direct measurement of the proton RSP promises improved proton range predictions and therefore treatment planning accuracy (R. W. Schulte et al., 2012; Meyer et al., 2020).
Proton imaging also allows to reduce the imaging dose to the patient (R. W. Schulte et al., 2005), especially when taking into account novel approaches like fluence-modulated proton CT (Dickmann et al., 2020).
A welcomed side-effect is the absence of artifacts from high-Z materials, e.g., titanium implants, after the pCT reconstruction (Oancea et al., 2018).

Cormack, 1963 firstly pointed out the possibility to use protons for imaging and Koehler, 1968 published a first radiography of an aluminum foil in a stack of absorbers using energetic protons from an accelerator and a photographic film.

The most direct way to determine the RSP is by measurement of the particles energy loss in an object. The approaches of proton imaging exploiting energy loss to deduce on the RSP can be divided into two categories: (i) concepts that aim to measure energy loss on a **single-particle** basis and (ii) cumulative measurement of the energy loss of multiple particles in **integration mode**.
Krah et al., 2018 have compared four proton imaging modes based on energy loss measurement, one based on SPT and three integration mode setups with beams provided either by passive scattering or PBS.
Comprehensive overviews on particle imaging including heavy ion imaging can be found in Parodi, 2014; Poludniowski et al., 2015; Johnson, 2018.

3.2.1 Single-Particle Tracking (SPT)

The measurement of the residual kinetic energy after traversing an object at known initial energy and taking into account the proton's path provides the most detailed data to infer

WET or RSP. The first radiography of an animal patient was done by U. Schneider et al., 2004, by imaging a dog. Generally, SPT is implemented through a pair of position-sensitive particle trackers to determine the particle position and angle in front and behind the object and a detector to measure the residual particle energy or range (R. Schulte et al., 2004; Penfold et al., 2011; Civinini et al., 2013; Scaringella et al., 2014; Taylor et al., 2016). Proton radiography systems already exist as prototypes, for example, the system built by ProtonVDA (DeJongh et al., 2022), the Proton Range Radiography 30× 30 cm^2 (PRR30) (Bucciantonio et al., 2013) or the Particle Residual Energy Detector And Tracker Enhancement (PREDATE) project (Presti et al., 2016). To obtain 3D pCT images, rotation of the detector system or the object is necessary. In the SIRMIO platform this is foreseen as described in Meyer et al., 2020. Established research projects for human-scale setups are for example the prototype built by the Proton Radiotherapy Verification and Dosimetry Applications (PRaVDA) consortium (Taylor et al., 2016), the phase-II scanner of the US pCT collaboration (R. Schulte et al., 2004; Giacometti et al., 2017; Johnson et al., 2016), the Bergen pCT project (Pettersen et al., 2017) and the Innovative Medical Protons Achromatic Calorimeter and Tracker (iMPACT) project (Mattiazzo et al., 2018). From the entry and exit trajectory of the particles and the remaining kinetic energy, an estimate of the most likely proton path in the object and thereby the WEPL along that path can be deduced. The uncertainties in that measurement stem from MCS in the object, initial energy spread of the beam and range straggling in the object and detector. The influence of the distance between the trackers and the object as well as the material budget of the trackers has been studied (Penfold et al., 2011; U. Schneider et al., 2012; Bopp et al., 2014). Additionally, the detectors have inherent limits in spatial and energy resolution.

3.2.2 Integration Mode

Proton imaging methods in integration mode use a single detector that measures either the residual energy for an ensemble of protons that have passed through the object or the energy loss in the object.

The energy measurement can be conducted with a range telescope, e.g., a multi layer ionization chamber (Rinaldi et al., 2013, 2014; Farace et al., 2016; Bentefour et al., 2016), or theoretically also with a calorimeter (Rescigno et al., 2016).

Otherwise a planar detector in combination with variation of the beam energy can provide the information necessary to determine the WET of the object. Energy variation is necessary as the difference in deposited energy in thin detectors does not vary significantly for different WETs of the object if the protons are not close to the stopping point after having passed through the object. Setups have been studied that employ diverse detectors such as for example charge-coupled devices (combined with scintillators) as in the first implementation of this approach by Zygmanski et al., 2000 and further systems (Ryu et al., 2008; Muraishi et al., 2009), diode arrays (Testa et al., 2013), CMOS sensors (Seco et al., 2011), amorphous-silicon detectors (Telsemeyer et al., 2012; Jee et al., 2017; Zhang

et al., 2019; Harms et al., 2020), dosimetric film (Amblard et al., 2019), and an ionization chamber (Lu, 2008). The energy modulation can be implemented with a modulator wheel as foreseen for passive scattering beam delivery, by dedicated degraders or from the energy selection system built into modern beamlines[3]. In the setups following this concept of a single planar detector and energy variation, as presented in this work, the WET is deduced from the beam energy for which the protons range out in the detector (Krah et al., 2018) or respectively, for which the particles do not traverse the sample and the signal on the detector is therefore zero, also called *dose extinction* (Doolan et al., 2015). Some of these setups measure the time-resolved energy deposition in the detector that is synchronized with the energy variation mechanism.
To deduce on WET of the object from the measured energy deposition, a calibration specific to the imaging system is necessary. In most of the presented setups, spatial information is obtained from position-sensitive detectors, although position information can also be approximated if a narrow pencil beam is used.

3.2.3 Proton Imaging for Small Animal Studies

The motivation for small animal studies is translational research using pre-clinical in vivo experiments to bridge scientific insights from in-vitro experiments, for example on cells, into clinical practice. Commonly, the term *small animals* describes mice, rats, or rabbits. Small animal studies allow for the observation of treatment effectiveness and treatment-related toxicity on a large number of almost identical whole organisms.
In small animal radiation therapy, sub-millimeter accuracy of imaging and radiation delivery is required due to the size of the tumors. Nonetheless, clinically realistic conditions should be reflected regarding the radiation fields, imaging, and treatment workflow.
To image the critical structures of e.g., mice, a resolution in the order of 100 µm is required which is achievable using specific imaging systems, for example, X-ray CBCT (100 µm - 200 µm), µ-CT (<100 µm), µ-MR (50 µm - 100 µm) and ultrasound (<100 µm) (Verhaegen et al., 2011). For small animal proton imaging there are no commercially available solutions yet and meeting the aforementioned requirement regarding the spatial resolution is even more difficult to achieve due to the enhanced scattering of low energy charged particles in matter.

[3]Given that the energy selection system's features as e.g., energy switching time suit the requirements of the experiment.

CHAPTER 4

Computational Methods and Experimental Materials

This chapter introduces the FLUKA Monte Carlo (MC) framework that was used for the simulations that were carried out in the course of this work.
Moreover, it describes the experimental environment, including a presentation of the two detectors that were used, the proton therapy facilities at which experiments were conducted and the imaged phantoms.
In the last section of this chapter, the quantities used for the evaluation of WET images in terms of image quality and feasibility for small animal imaging are defined.

4.1 The FLUKA Monte Carlo Code

4.1.1 FLUKA

FLUKA (short for FLUktuierende KAskade) is a MC code that enables the simulation of the interactions that particles undergo on their passage through matter (Ferrari et al., 2005; Böhlen et al., 2014). It is used in fields of physics as different as cosmic ray physics, radiation protection and - most relevant in the context of this work - medical applications such as dosimetry and hadron therapy (Battistoni et al., 2016). It was first developed from 1962 onwards to help in the design of shielding at the Conseil Européen pour la Recherche Nucléaire (CERN) (European Organization for Nuclear Research) Super Proton Synchrotron (SPS) project and in the following years was expanded and advanced "into a code which could handle most particles of practical interest and their interactions over the widest possible energy range"[1].

[1] www.fluka.org/fluka.php?id=history&mm2=1, as of 07.05.2022

The code that was used to obtain the simulation results presented in this work ranged from the version 2011.2x.2 to the version 2021.2.3 distributed by the Italian National Institute for Nuclear Physics (INFN).
The basic concept of such a MC simulation in FLUKA is to choose the incident radiation source and to describe the geometry and the media that it will travel through to retrieve the physical quantities that are to be observed (in so-called *scoring*). It is the responsibility of the user to select what models and thresholds for the transport and interaction calculations are deemed relevant for a particular application. For specific applications, collections of default settings are available. Most parameters are defined in an ASCII *input* file, where the composition of the simulation is given in a standardized format for each category (e.g., source, geometry, and transport), that is called a *card*. Furthermore the standard code can be linked to customizable, self-written FORTRAN 77 routines which enable to adapt the simulation to scenarios that are not covered by the standard options, so-called *user routines*.

The most relevant aspects to define a specific simulation framework are:

Source FLUKA enables calculations with about 60 particle species and heavy ions in a wide range of energies, e.g., from 1 keV to thousands of TeV for electrons and photons, and hadrons up to 20 TeV[2] (Ferrari et al., 2005). The particles are emitted as beams or from radioactive sources of numerous shapes, in any energetic, spatial or angular distribution that the user specifies in the pre-defined cards or in a **source.f** user routine. Also the possibility to read particle properties from an external phase space file is enabled by the **source.f** user routine.
A MC phase space file contains at least position and momentum information for a large number of particles at a particular point in the simulation geometry. For a specific set of beam modifying elements that stays constant for a number of experimental situations (e.g., the collimators and energy degraders of a certain beamline), the properties of the particles after passing through that setup can be written in a phase space file. In subsequent simulations, this phase space file can be used as source, e.g., for different phantoms or detector configurations, thereby saving computation resources. To obtain meaningful statistical distributions, such a phase space should be generated for a sufficiently large number of primary particles that depends on the particular simulation and the required precision.

[2]Simulations with hadrons are possible with energies up to 10 PeV by linking FLUKA with the Dual Parton Model and JETs (DPMJET) code.

Geometry Complex geometries can be built from geometric planes and bodies with combinatorial geometry to form so-called *regions*. Each region is assigned one material, either from the available standard library or defined by the user.
Especially interesting for medical physics applications is the possibility to import voxelized geometries, e.g., from a CT image (Parodi et al., 2007a; Parodi et al., 2007c). A voxel is a finite, small unit of a regular volumetric grid, analogous to a pixel in 2D imaging.

Transport In a MC simulation the primary and secondary particle histories are tracked step-by-step until the particle is absorbed, escapes the simulation geometry or its kinetic energy is lower than the transport threshold. At the endpoint, the remaining energy is either deposited in the current location (for electrons and photons) or ranged out in a simplified way in the surrounding (for hadrons and muons) (Ferrari et al., 2005). Low-energy neutrons are treated by a multigroup algortihm[3]. For charged particles, there are countless small energy loss events for the interactions with the electrons of the medium. Therefore a condensed history algorithm is adopted in FLUKA that treats ionization energy loss events differently, whether they are above or below the user-defined delta-ray production threshold T_δ. Explicit sampling of ionization loss and generation of delta rays is only done for energy transfers larger than T_δ. The combined effect of ionization and excitation losses smaller than T_δ in a step is handled as continuous energy loss along the step instead of explicit simulation to make the simulation more efficient in terms of Central Processing Unit (CPU) resources.
The PEANUT (Pre-Equilibrium Approach to Nuclear Thermalisation) model is implemented in FLUKA to handle hadron-nucleon interactions (Ferrari et al., 1993) in the range of ion energies that is used in proton therapy and imaging. A version of the Relativistic Quantum Molecular Dynamics Model (RQMD) (Sorge et al., 1989) handles nucleus-nucleus interactions from $0.1\,\mathrm{GeV\,u^{-1}}$ to few $\mathrm{GeV\,u^{-1}}$ and for lower energies the code switches to an event generator based on the Boltzmann Master Equation (BME) theory (Cavinato et al., 1996; Battistoni et al., 2016). At energies higher than $5\,\mathrm{GeV\,u^{-1}}$, cross sections for hadron-hadron, hadron-nucleus and nucleus-nucleus interactions are provided to FLUKA by the DPMJET III model (Roesler et al., 2001).
The MCS of protons is implemented following Molière's theory (Ferrari et al., 1992) (see section 2.1) and extended by a path length correction and a correlation algorithm. Those extensions ensure not only correlation of the lateral displacement of a particle with the scattering angle but also that the higher the scattering angle is, the lower the longitudinal simulation step is set. Accurate treatment of MCS is especially critical in the context of this work, when MC simulations are used to establish a scattering kernel, as described in section 7.1.2. Simulation of single scattering is possible and should be applied in situations where Molière's theory is not applicable (e.g., transport in gas or very thin geometries

[3] http://www.fluka.org/fluka.php?id=man_onl&sub=96

like wires), but is more demanding in terms of computing resources.
The FLUKA code has been extensively benchmarked regarding the transport of therapeutic proton and ion beams in matter (Parodi et al., 2012; Sommerer et al., 2006). The energy range that is relevant to this work is from 4 MeV to 110 MeV initial proton beam energy.

To facilitate the choice of interaction models and energy thresholds, there are **default** settings in FLUKA for different applications. In the course of this work, the default settings HADROTHE (for "hadron therapy" calculations) were used and complemented by explicitly setting step sizes in thin material slices. Adjusting the step size ensures that sufficient sampling is carried out in the respective region to avoid inaccuracies from lack of statistics.

Scoring Equivalent to a measurement in a real experiment, scoring is used in MC simulations. The scored quantities are sampled from statistical distributions and the variance is inversely proportional to the number of simulated particle histories. FLUKA is able to score numerous physical quantities such as energy deposition (and related quantities such as radiation dose), particle fluences, current, track length, and energy spectra.
User-defined scoring can be implemented with the **mgdraw.f** user routine to meet specific requirements by writing out particle trajectories and energy losses at each boundary crossing, particle step, energy deposition event or interaction.

The standard options that were predominantly used in this work for scoring are (i) scoring the amount of particles or energy deposition[4] in a defined volume with the USRBIN card and (ii) recording energy spectra of particles at a defined location in the geometry with the USRBDX card ("bdx" being an abbreviation for boundary crossing, because the particle's energy is read out when it passes from one region to the next).
The EVENTBIN option collects the energy deposition in a defined volume for each particle history.
User-defined scoring was mainly used in the context of this work to score phase spaces of the proton beam in the different simulation models of the experiments before impinging on the phantom.

[4]For increased accuracy, the USRBIN scoring option counts in every bin traversed by a simulation step a fraction of the observable (e.g., deposited energy) proportional to the track length in the bin.

4.1.2 FLAIR

FLUKA Advanced Interface (FLAIR) (Vlachoudis, 2009) is a graphical user interface to FLUKA that provides functionalities such as:

- Editing of the FLUKA input file while assuring the correct format is maintained and giving helpful explanations on the quantities and units to set.
- Graphical display of the simulation geometry and materials.
- Compilation of an executable and linking to the standard FLUKA library of user routines and external event generators, like the previously mentioned DPMJET and RQMD.
- Import of Digital Imaging and Communications in Medicine (DICOM) files, e.g., clinical X-ray CT images, and implementation as a FLUKA voxelized geometry (Kozlowska et al., 2019). Each voxel is assigned a tissue material based on a conversion of the voxel values (usually expressed in terms of CT numbers given in HU) to a FLUKA material with respective elemental composition. The standard stoichiometric calibration is based on U. Schneider et al., 1996 and W. Schneider et al., 2000.
- Running the simulation and tracking the progress.
- Data processing and plotting.

4.2 CMOS Detectors

Two detector systems based on CMOS technology were used for the proton imaging studies that are presented in this work, the CM49 (Teledyne Dalsa, Canada) and the LASSENA (Nordson, USA).

4.2.1 Teledyne CM49 DST

The CM49 DST by Teledyne Dalsa, Canada is a 114 mm × 65 mm CMOS sensor (see figure 4.1) with 49.5 µm pixel pitch. The three-transistor (3T) pixels allow for high sensivity, low dark current, low noise (Hynecek, 2006) and are capable of handling high charges, therefore the CM49 is classified as a radiation hard detector (Teledyne Dalsa, 2014). It is sold in the Shad-o-Box 3K HS detector system with different scintillator options for industrial, biomedical and scientific X-ray applications (Teledyne Dalsa, 2021). Table 4.1 summarizes the technical characteristics of the sensor.
First experience with the detector system was collected during proton irradiation experiments at the Tandem accelerator of the Maier-Leibnitz-Laboratorium (MLL) of the Ludwig-Maximilians-Universität (LMU) Munich and the Technische Universität München (TUM), and with laser-accelerated ions at the Centre for Advanced Laser Applications

(CALA) in Garching (Reinhardt, 2012; S'ng Ming Hao, 2019; Hartmann, 2022; Englbrecht, 2022). Furthermore, its large sensor area, which is sufficient for the imaging of a mouse, made this detector a reasonable candidate for application in the SIRMIO project. During the experiments to characterize laser-accelerated ions, the premounted plastic scintillator was removed from the sensor. In addition, the 11 cm flat ribbon cable that connects the sensor to the Printed Circuit Board (PCB) was elongated by 24.5 cm to enhance the distance of the PCB from the active area in order to avoid radiation damage to the sensor electronics, which were by default mounted directly behind the active area. For light shielding, a 15 µm-thick aluminum foil was installed with an air gap of 3 mm to the pixel surface.

4.2.2 Nordson LASSENA

The LASSENA vm2428 detector was developed for medical and scientific X-ray imaging by the CMOS Sensor Design Group at the Rutherford Appleton Laboratory (Sedgwick et al., 2013) (now licensed by Nordson X-ray technologies, USA). It has a 120 mm × 140 mm sensitive area (see figure 4.2) with 2400 × 2800 pixels, corresponding to 50 µm pixel pitch. The pixel design is based on the 3T pixel and enclosed layout transistors were used to achieve radiation hardness (Snoeys et al., 2000). The sensor consists of a 750 µm silicon wafer and a 5.5 µm epitaxial layer. Table 4.2 outlines the technical specifications of the LASSENA detector.

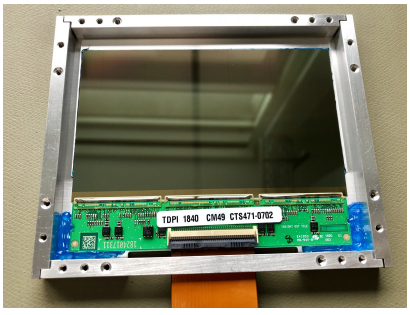

Figure 4.1: The CM49 sensor surface and the PCB containing the Analog-to-Digital Converter (ADC) units (from Englbrecht, 2022).

Table 4.1: Technical specifications of CM49 detector according to Teledyne Dalsa, 2014

Specification	Value	Unit
Chip size	114.06 × 69.24	mm^2
Active image area	114.05 × 65.04	mm^2
Total number of rows × columns	2304 × 1314	$pixels^2$
Pixel pitch	49.5	µm
Sensitive thickness	n.a., (≈2-10)*	µm
Fill factor	79	%
Maximum frame rate	20	Hz
Dynamic range	2×10^{14}	bits
Operating temperature	10-50	°C
Network interface	Gigabit Ethernet	
PCB-sensor connection	Flat ribbon cable, 80 connectors	
Data Transfer	Ethernet Cat6e	

*Estimate from the work of Englbrecht, 2022.

Table 4.2: Technical specifications of the LASSENA detector according to Sedgwick et al., 2013 and Flynn et al., 2022.

Specification	Value	Unit
Chip size	120 × 145	mm^2
Active image area	120 × 140	mm^2
Total number of rows × columns	2400 × 2800	$pixels^2$
Pixel pitch	50	µm
Sensitive thickness	5.5	µm
Maximum frame rate	20	Hz
Dynamic range	2×10^{14}	bits
PCB-sensor connection	4 flat ribbon cables: 0.5 mm pitch, type A same-side contacts, 40 circuits	
Data Transfer	Fibre optic cable: LC-LC, OM4	

The LASSENA was deemed a viable candidate to be used in the SIRMIO platform as the technical specifications fulfill the requirements. Furthermore, the availability of published data on and studies with the detector allowed to accurately model the LASSENA detector in MC simulations.

The sensor was glued on a 5 mm plastic plate for stability, with a rectangular window of 60 mm × 120 mm area to allow irradiation from both sides (see figure 4.2). An aluminum foil of 15 µm thickness was used to cover the wafer and the pixel surface of the detector for light shielding.

In parallel to this work, other groups explored applications with proton beams, for example, the possibility of monitoring pencil beam scanned proton beams was shown by

Flynn et al., 2022, who were able to track the delivery of planned spots and measure the spot-to-spot separation correctly.
The following chapter 5 reports on the experiments conducted to test the linear relation of the signal to energy deposition by various radiation sources and assess the temperature stability of the sensor.

4.3 Proton Therapy Facilities and Experimental Beamlines

4.3.1 Rinecker Proton Therapy Center (RPTC)

Patients were treated at the Rinecker Proton Therapy Center (RPTC) in Munich (Borchert et al., 2008) from 2009 until 2019. It was equipped with the first clinical isochronous cyclotron for particle therapy by Varian Medical Systems, Inc. (Palo Alto, California, formerly ACCEL) (Krischel et al., 2007; Krischel, 2012). Cyclotrons provide a quasi-continuous beam of fixed energy and are appreciated for their simplicity and reliability of operation, which are extremely important for medical accelerators. One disadvantage compared to a synchrotron is that beam energy has to be degraded - in the case of the ACCEL cyclotron with graphite wedges - leading to increased energy spread and activation (Silari, 2011).
The superconducting cyclotron and beamline with automatic energy switching system delivered protons in arbitrary energy steps within 75 MeV to 245 MeV and with a switching time of about 4 s to four dosimetrically equivalent treatment rooms with gantries that allow for 360° rotation around the patient (Borchert et al., 2008).
The treatment plan is delivered by PBS (see section 3.1.1) and spot size in terms of the standard deviation σ of a Gaussian lateral spot profile in air at isocenter ranges from $\sigma_x = 5.1\,\text{mm}$ and $\sigma_y = 4.1\,\text{mm}$ at 80 MeV beam energy to $\sigma_x = 5.0\,\text{mm}$ and $\sigma_y = 3.4\,\text{mm}$ at 230 MeV (Weick-Kleemann, 2013).

4.3.2 Centre Antoine Lacassagne (CAL)

The Mediterranean Institute of proton therapy at the Centre Antoine Lacassagne in Nice, France, hosts two cyclotrons for medical purposes: The 65 MeV cyclotron Medicyc for the treatment of ocular tumors and the 230 MeV S2C2® as part of the Proteus®ONE system (IBA, The Netherlands) to treat deep-seated tumors.

4.3.2.1 Medicyc

Medicyc was the first proton cyclotron in France and also delivered the first proton therapy treatment in France in 1991. The isochronous cyclotron was designed and built in collaboration by the CERN and the cyclotron laboratory of Centre Antoine Lacassagne (CAL). The cyclotron accelerates negatively charged H^- ions which are then extracted using a carbon foil as stripper. The beam is then transported along the 35 m beamline to the

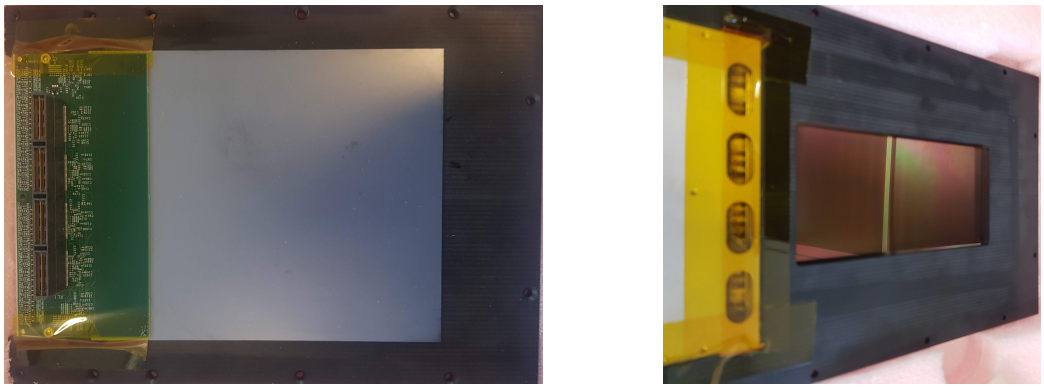

(a) (b)

Figure 4.2: The LASSENA sensor glued on a plastic plate for stability. Shown are: (a) The silicon wafer side, the Field Programmable Gate Array (FPGA) and connector. (b) The cut-out of the plastic plate and the exposed pixel surface.

treatment room. Formerly, proton and neutron therapy treatments were foreseen (Mandrillon et al., 1989). At the moment of writing, the beam is delivered to one treatment room and one experimental room (Hofverberg et al., 2022) and is adapted in-depth and laterally by passive scattering. The beam in the clinical treatment room that was used for the proton imaging investigations of this work has a remaining kinetic energy of 62.3 MeV at beam exit. The lateral beam profile is a flat field of up to 60 mm diameter and is customized with brass collimators to fit the tumor shape (Hofverberg et al., 2022).

4.3.2.2 Proteus®ONE

The Proteus®ONE built by IBA PT, Belgium, is the first system with the compact, superconducting synchrocyclotron S2C2® (Pearson et al., 2013; Kleeven et al., 2013; Van de Walle et al., 2016) and a rotating gantry. Between injection and extraction, the synchrocyclotron Radio Frequency (RF) is lowered from 93 MHz to 62 MHz to compensate for relativistic effects. The modulation of the RF is created by a rotating capacitor with 1 kHz repetition rate to which the proton pulse frequency is synchronized. The pulse width was measured with a scintillator in the beam to be 2.5 µs to 3.7 µs Full Width at Half Maximum (FWHM) depending on the charge per pulse (Lehrack et al., 2017).
The available beam energies range from 100 MeV to 226 MeV and are adjusted by the *energy selection system*. The beam is then steered towards the target by PBS with spot size in air at isocenter of $\sigma_x = 6.1$ mm and $\sigma_y = 6.0$ mm at 100 MeV to $\sigma_x = 3.3$ mm and $\sigma_y = 3.2$ mm at 226 MeV.
The air filled nozzle contains two beam monitor chambers that measure the delivered proton charge in Monitor Units (MU) (Van De Walle et al., 2014). The charge per pulse at 97 MeV beam energy ranges from 1.98×10^{-3} pC to 1.0 pC or alternatively 1.24×10^4 up

to 6.24×10^6 protons per pulse[5]. The high instantaneous proton fluxes require an adapted irradiation scheme to deliver the prescribed dose precisely: with the "blind golfer" algorithm, the spots are delivered to a two-dimensional energy layer in three to four consecutive bursts. The largest part of the dose is deposited in the first burst and based on control measurements by the monitor chambers, the remaining dose is delivered in an iterative manner.

4.3.3 Danish Centre for Particle Therapy (DCPT)

The Danish Center for Particle Therapy (DCPT) in Aarhus, Denmark, is a clinical proton therapy center in operation since January 2019 and as a part of Aarhus University hospital, also the Danish platform for particle therapy research. It is the only facility for particle therapy in Denmark and treats approximately 1000 patients each year. The center has three gantry treatment rooms and one fixed beamline room dedicated to research activities. A Varian ProBeam system equipped with an isochronous cyclotron delivers proton beams of energies from 70 MeV to 244 MeV in PBS technology and with faster energy switching as compared to Rinecker Proton Therapy Center (RPTC). Spot size in air at isocenter in terms of σ ranges from $\sigma_x = 4.5$ mm and $\sigma_y = 3.6$ mm at 70 MeV to $\sigma_x = 3.6$ mm and $\sigma_y = 2.8$ mm at 244 MeV. The available beam current ranges from 0.5 nA to 15 nA. DCPT also has a dedicated in vivo and in vitro laboratory available to visiting scientists.

DCPT owns an in-house developed prototype µ-CT based on a Hamamatsu microfocus L9421-02 X-ray source that was set to 60 kVp and 133 µA. The detector model is the 0505A (Rayence, Korea) with 1176 × 1104 pixels and 49.5 µm pixel pitch. The acquisition mode that was used for the images shown in this work were 360 projections acquired over 360° and image reconstruction used a Feldkamp–David–Kress (FDK) algorithm from the *Tigre*[6] *python*-package[7].

4.3.4 Helmholtz-Zentrum Berlin for Materials and Energy (HZB)

The Helmhotz-Zentrum Berlin (HZB) was established in 2009 from the merger of the Hahn Meitner Institute Berlin in Wannsee and the Berlin Electron Storage Ring Society for Synchrotron Radiation (BESSY) in Adlersholf. It is predominantly engaged in fundamental research in the field of structure and function of matter as well as solar energy. It also runs a cyclotron facility for research on radiation hardness testing.

HZB provides its proton accelerator to the Charité hospital for proton therapy treatment of ocular tumors.

The cyclotron at HZB produces a 68 MeV beam for therapeutic and industrial applications.

[5] Measured by IBA, March 2019

[6] https://github.com/CERN/TIGRE

[7] Private communication with Prof. Jasper Nijkamp, Aarhus University

It is possible to degrade the initial beam energy with aluminum plates to 50 MeV and 30 MeV remaining kinetic energy (Denker et al., 2013).

4.4 Phantoms

4.4.1 SMART Calibration Phantom

A µ-CT calibration phantom (SmART scientific solutions B.V., The Netherlands) was imaged in all proton radiography experiments for quantitative evaluation in terms of WET accuracy and spatial resolution. The baseplate has the shape of a truncated cylinder and is made out of water-equivalent material of 9.940(7) mm thickness and 30 mm diameter. It holds ten cylindrical inserts of Gammex® materials that have 3.5 mm diameter and 16 mm length (see table A.1). For the imaging experiments, the direction of irradiation is set along the long side of the inserts to remove uncertainties due to their round shape. The elemental composition by relative weight, effective atomic number Z_{eff}, mass density ρ_{ref} and relative-to-water electron density ρ_e^w are given by the vendor[8] (see figure 4.3). The RSP of the insert materials was measured for bigger samples of the same vendor in carbon ion beams[9] (Hudobivnik et al., 2016) with an uncertainty of 0.2 %. In addition, Dual-Energy CT (DECT) images of the phantom calibrated to RSP (Niepel et al., 2020) were used as consistency checks, paying attention to partial volume effects. The ground truth WET of the phantom inserts is calculated by multiplication of the measured RSP values with the geometrical insert length (see table A.1).

[8] SMART Scientific Solutions B.V., Routine Preclinical CT Calibration Phantom, Promotional Leaflet (2016)

[9] The RSP of materials is independent of the ion species.

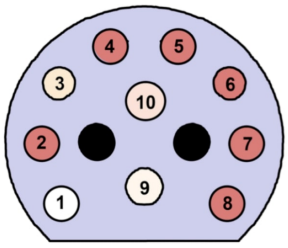

(a)

Tissue insert	No.	Z_{eff}	ρ_e^w	ρ_{ref}	H	C	N	O	P	Cl	Ca	RSP
Adipose	5	6.21	0.93	0.95	9.06	72.29	2.25	16.27	0.00	0.13	0.00	0.94
Breast	7	6.93	0.96	0.98	8.59	70.10	2.33	17.90	0.00	0.13	0.95	0.97
Solid Water	4	7.74	0.99	1.02	8.00	67.29	2.39	19.87	0.00	0.14	2.31	1.00
Brain	10	6.09	1.04	1.05	10.83	72.54	1.69	14.86	0.00	0.08	0.00	1.06
Liver	8	7.74	1.06	1.10	8.06	67.01	2.47	20.01	0.00	0.14	2.31	1.08
Inner Bone	6	10.42	1.09	1.13	6.67	55.65	1.96	23.52	3.23	0.11	8.86	1.09
B200 Bone	2	10.42	1.10	1.15	6.65	55.51	1.98	23.64	3.24	0.11	8.87	1.10
CB2-30%	3	10.90	1.28	1.33	6.68	53.47	2.12	25.61	0.00	0.11	12.01	1.28
CB2-50%	1	12.54	1.47	1.56	4.77	41.61	1.52	32.00	0.00	0.08	20.02	1.43
SB3 Cort. Bone	9	13.64	1.69	1.82	3.41	31.41	1.84	36.50	0.00	0.04	26.80	1.62

(b)

Figure 4.3: Depiction of µ-CT calibration phantom and the tabulation of its related properties according to the manufacturer (SMART scientific solutions, The Netherlands): effective atomic number Z_{eff}, relative-to-water electron density ρ_e^w, mass density ρ_{ref} and elemental composition by relative weight as well as the RSP measured by Hudobivnik et al., 2016 for each tissue mimicking material.

4.4.2 Multimodal Mouse Phantoms

To image a more realistic case of a small animal, 3D-printed mouse phantoms were fabricated in-house to compare multiple imaging modalities, namely x-ray, proton, ultrasound, and ionoacoustic imaging (Lascaud et al., 2022). In the experiments, two different versions of the multimodal mouse phantom were used:

Generation 1 This version of the multimodal mouse phantom uses silicone rubber (Elastosil 601, Wacker Chemie AG) as shell in which organ mimicking structures from polylactic acid (PLA, Ultimaker), bony structures from a mixture of granite and polyactic (grey Stonefil, Formfutura) and tumor surrogates as well as intestines from another silicone rubber (Elastosil M4601, Wacker Chemie AG) were placed (see figure 4.4a). The shape of the anatomical structures was extracted from a X-ray CBCT image of a real mouse acquired with the SARRP (X-Strahl, UK) that is installed at LMU hospital.

Generation 2 The shape of the second generation mouse phantom was derived from a X-ray CBCT acquisition in the same manner as was done for the first one and the bony structures, organ mimicking structures and the encapsulating shell were made out of the same materials. An improved production process made a more accurate reproduction of the skin contour possible, leading to reduced maximum thickness of the phantom compared to the first generation model and also closer to the realistic dimensions of real mice that will be imaged and irradiated in the SIRMIO platform (see figure 4.4b). This second generation version also contains an air cavity that can be filled with contrast agents.

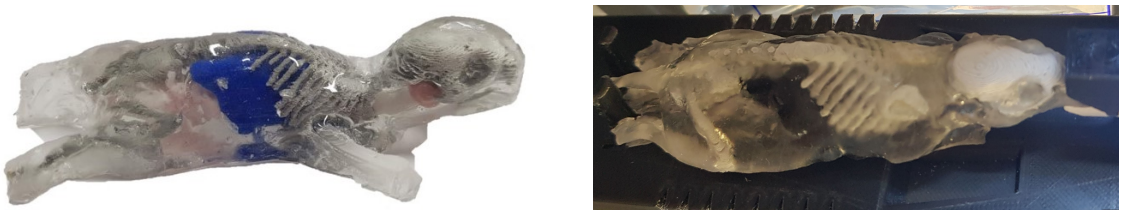

(a) **(b)**

Figure 4.4: Multimodal mouse phantoms fabricated in-house that were imaged in integration mode proton imaging: (a) first generation as described in Lascaud et al., 2022 and (b) second generation in the SIRMIO mouse holder with nose clamp.

4.5 Quantitative Image Evaluation

The image quality of proton radiographies is given by the WET accuracy and precision as well as the spatial resolution. For the feasibility of the imaging mode on living specimens also the dose deposition during imaging and the imaging time are to be considered.

4.5.1 WET Accuracy and Precision

The WET of the Gammex material inserts of the µ-CT calibration phantom depicted in the proton radiographies was compared to experimentally determined RSP values from Hudobivnik et al., 2016, multiplied by the geometrical length in beam direction of the insert (see figure 4.3 and table A.1). Regions-of-interest (ROIs) in the center of the inserts with a margin to the interface were chosen to evaluate WET accuracy independent of range mixing (see fig. 4.5a). The size of the margin is chosen depending on the blurring that is present in the image and the related spatial resolution. To evaluate WET accuracy and precision, the average WET $\overline{\mathrm{WET}_i}$ and standard deviation σ_i of the pixels within this region is computed for each of the $n = 10$ inserts individually and compared to the ground truth $\mathrm{WET}_{\mathrm{GT},i}$. The index i denotes the different tissue-equivalent material inserts, $i \in 1, 2, ..., 10$. The relative WET error $\mathrm{E}_{\mathrm{rel}}$ is defined as:

$$\mathrm{E}_{\mathrm{rel,\ i}} = \frac{\overline{\mathrm{WET}_i} - \mathrm{WET}_{\mathrm{GT},i}}{\mathrm{WET}_{\mathrm{GT},i}} \,. \tag{4.1}$$

The relative WET error $\mathrm{E}_{\mathrm{rel}}$ is negative, if the WET is underestimated, and positive if overestimated.
The WET accuracy is defined as the arithmetic mean of the absolute of the relative WET error, similar to the MAPE used in (Dickmann et al., 2021):

$$\mathit{Accuracy} = \frac{1}{n} \sum_i |\mathrm{E}_{\mathrm{rel,\ i}}| \,. \tag{4.2}$$

The precision is defined as the arithmetic mean of the standard deviations σ_i relative to the ground truth WET:

$$\mathit{Precision} = \frac{1}{n} \sum_i \frac{\sigma_i}{\mathrm{WET}_{\mathrm{GT},i}} \,. \tag{4.3}$$

The absolute value is chosen to avoid that over- and underestimation compensate each other and falsely improve the resulting WET accuracy.
Choice of the Region of Interest (ROI) margin such that pixels with range mixing are not included is important to evaluate WET accuracy decoupled from the spatial resolution (see figure 4.5b).

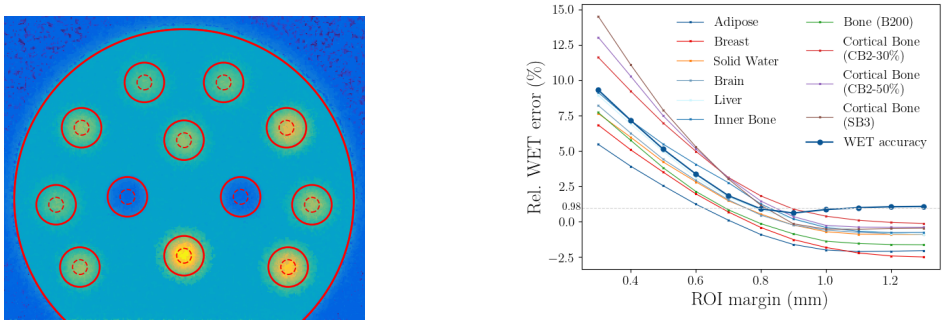

(a) **(b)**

Figure 4.5: (a) Margins from the insert edge (continuous circle) to the ROI (dotted circle inside) to evaluate WET accuracy and precision in a homogeneous region in the center of the insert. (b) Relative WET error E_{rel} for the ten material inserts and average of the absolute values for the radiography done at RPTC with 13 mm air gap as a function of the margin chosen to the ROI at the material interface to disentangle WET accuracy from spatial resolution. In this example the WET accuracy is considered independent of the choice of margin starting from a margin of 1.0 mm or higher.

4.5.2 Spatial Resolution

The interfaces between each insert to the solid water baseplate were used to quantify the spatial resolution (see fig. 4.6a). These image regions can be approximated to a slanted edge, neglecting the curvature of the 3.5 mm insert radius in a single 100 µm pixel. Thus, the Edge Spread Function (ESF) method described in Mori et al., 2009 can be used with some adaptations, with the aim to sample the intensity profile over the edge independently from the pixel size. Data points from nine rows around the center of the insert (see fig. 4.6b) were aligned to get a composite, oversampled edge profile. A fit of a sigmoid function to this edge profile provides the Edge Spread Function (ESF) (see fig 4.6c). From the sigmoid shape of the ESF follows that the Line Spread Function (LSF), which is the derivative of the ESF, can be approximated by a Gaussian function. The full width at half maximum (FWHM) of this Gaussian LSF is the difference between the positions at 75% and 25% of the maximum of the Edge Spread Function (ESF) (see fig. 4.6d) (Seco et al., 2013).
The spatial resolution limit is commonly chosen from the Modulation Transfer Function (MTF), which describes the loss of contrast that is inherent to the image of an object compared to the contrast of the actual object. In each imaging system, there is a loss of high spatial frequencies which is perceived as blurring. In the case of integration mode proton imaging, this loss of contrast is dominated by multiple Coulomb scattering in the object and the lateral displacement of protons between the object and the detector. The MTF is calculated by taking the Fourier transform of the LSF and normalizing to the point where the frequency is zero (see fig. 4.6e). The frequency where the MTF is reduced to 10 % was calculated for each of the ten inserts and the average value and standard deviation value, given in parentheses, are reported in chapters 5, 6 and 7.

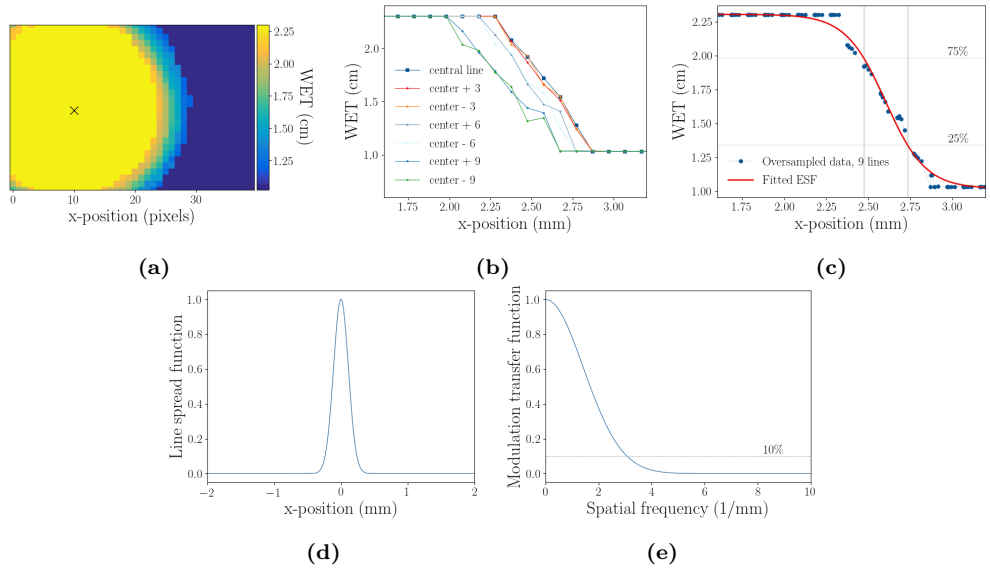

Figure 4.6: (a) Example of edge between insert and baseplate in a proton radiography. The 'x' marks the center of the insert. (b) Edge profile of the pixel row along the center of the insert and 3, 6, and 9 pixels above and below the central line. (c) The Edge Spread Function obtained from a sigmoid fit to the oversampled insert edge. (d) The normalized Line Spread Function. (e) The Modulation Transfer Function which is the Fourier transformation of the LSF.

4.5.3 Imaging Dose

Direct measurement of the imaging dose was not possible in the given experimental setups. To obtain an estimate of the imaging dose, FLUKA simulations were used in which the phantom was modelled in the simulation frameworks for each experiment with its geometric dimensions and material parameters as stated in figure 4.3. The dose was scored in a voxelized grid of 100 µm voxel size in the radiography plane and 1 mm slice thickness.
The incident particle number for dose estimation was retrieved either from the proton fluence at nozzle exit measured with the respective facility's instrumentation and the irradiation time for each probing energy or directly from the beam records, if available.

4.5.4 Imaging Time

The imaging time is given as the total time of data acquisition for each radiography or tomography, including the time needed to change between probing energies.
If a hypothetical low-dose reconstruction was obtained from a subsample of the acquired data and no beam records were available, then the period of the imaging time that is related to the beam-on part was reduced accordingly, but the energy switching time was assumed to be constant and independent of the irradiated charge for each energy step.

CHAPTER 5

Preliminary Studies with CMOS Detectors

In this chapter, the MC simulations and the experiments performed to assess the suitability of the CM49 and the LASSENA detector systems for integration mode imaging are presented. This section also describes the commissioning measurements of the LASSENA detector conducted at the HZB.

5.1 Assessment of Suitability of the CM49 and LASSENA Detector Systems for Proton Imaging

The technical specifications of the Teledyne CM 49 and Nordson LASSENA detectors were introduced in the previous chapter. Relevant considerations for the use of a CMOS detector in integration mode imaging experiments are the control of data acquisition, the linear relationship between the energy deposition by protons and the height of the detector's signal, radiation hardness and temperature stability.

5.1.1 Teledyne CM49 DST

Data acquisition was controlled with the software *Sapera CamExpert* and a console based interface described in S'ng Ming Hao, 2019, that ran on a notebook with a second ethernet port. Checks regarding the data transfer during proton imaging experiments conducted with the CM49 revealed that in continuous acquisition mode at a frame rate of 10 Hz, random image frames were not stored and no frames were saved for times up to 1 s (see figure 5.1). The frames before and after these bad events were not corrupted, i.e., were reliably acquired with the predefined integration time, as was tested and confirmed in the laboratory.

The **linear relationship** between the detector"s signal and the energy deposition in the sensitive volume was confirmed in experiments that used optical photons, alpha particles from radioactive sources, and protons (S'ng Ming Hao, 2019). The response to proton beams as well as the radiation hardness were tested at the MLL with a Tandem accelerator that made proton beams of up to 22 MeV. For the linearity test with protons, initial beams of 22 MeV and 10 MeV were degraded with a degrader wheel with segments of variable thickness to produce protons from approximately 3 MeV to 22 MeV. The degrader wheel material was the rigid transparent photopolymer AR-M2 (Würl, 2018). Additionally, measurements with a radioactive source consisting of ^{239}Pu, ^{241}Am and ^{244}Cm, with dominant α-lines at 5.16 MeV, 5.49 MeV, 5.80 MeV respectively, were carried out. The expected energy deposition of the individual protons and the alpha particles was calculated with FLUKA MC simulations. A linear relationship between the pixel value in Analog Digital Unit (ADU) PV(ADU) and the energy deposition dE was found to be:

$$\mathrm{PV(ADU)} = 6.38\frac{\mathrm{ADU}}{\mathrm{keV}} \cdot \mathrm{d}E(\mathrm{keV}) + 2.16\mathrm{ADU} \tag{5.1}$$

(S'ng Ming Hao, 2019).

The tests for **radiation hardness** were done with a 10 MeV beam and the detector showed remaining damage and 7 pixels constantly at maximum ADU value after receiving a total proton fluence of $1 \times 10^{13}\,\mathrm{protons\,cm^{-2}}$. The radiation damage healed partly (Englbrecht, 2022; S'ng Ming Hao, 2019).

Also the **Temperature stability** of the detector was tested with the result that with an aluminum housing acting as a heat sink, the temperature of the detector components stays within the operating temperature, even in continuous readout for 10 min (Englbrecht, 2022; S'ng Ming Hao, 2019).

The exact **pixel architecture** was not disclosed by the vendor and also could not be reconstructed from experimental data (Englbrecht, 2022; S'ng Ming Hao, 2019). According to details shared by the vendor, there is a first passivation layer of silicon nitride and a second one made out of silicon oxide in front of the sensitive layer, which itself is estimated to be between 2 µm and 10 µm of silicon (Englbrecht, 2022). An exact modelling of the detector in MC simulations was therefore not possible.

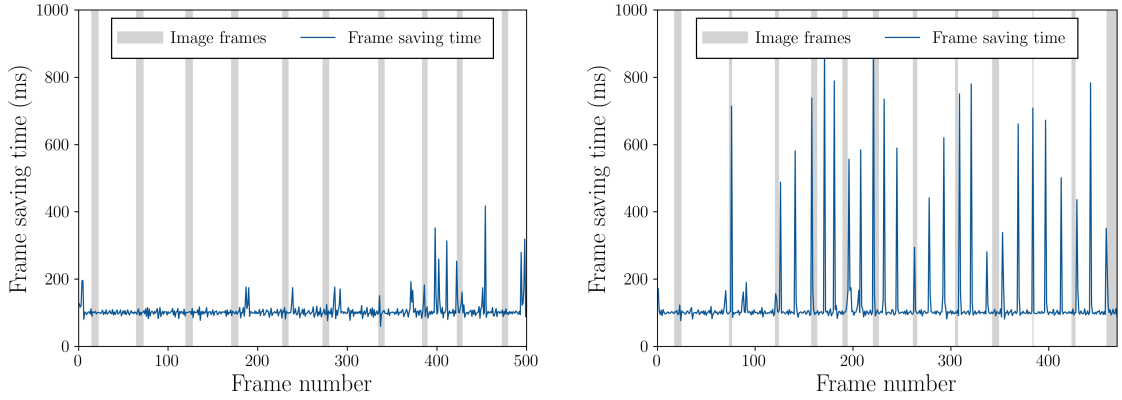

Figure 5.1: Illustration of problems in saving images from the CM49 detector: The grey bars show the frames where the cumulated pixel value shows that the beam was on, the blue line indicates the difference between two image timestamps, which should be equal to the set integration time of 100 ms. (a) "Successful" radiography: Although there are some corrupted frames, the regular pattern of beam-on and beam-off shows that data were acquired for each probing energy and the set of data can be used for WET determination. (b) The time for saving images rises up to over 1 s for some frames during which the sensor is idle. Therefore data are missing and a correct WET determination is not possible. The data were collected during an experimental campaign at the RPTC.

5.1.2 Nordson LASSENA

5.1.2.1 Data Acquisition

The LASSENA detector is distributed with a Graphical User Interface (GUI) (formerly vivaMOS Imaging Tool, now Neutrino) with functions for image processing, visualisation, sensor information and image capture. During proton imaging experiments, the detector was controlled with a python-script for the robust acquisition and storage of up to 2000 frames at integration time of 40 ms. A personal computer with a dedicated module for the data transfer via fibre optic cable was used.

5.1.2.2 Linearity of Pixel Value to Energy Deposition

Experiments to investigate the linear relationship between the detector's response to the energy deposition of optical photons, X-rays from a ^{55}Fe source and protons of 30 MeV, 50 MeV, and 68 MeV were performed to assess the detector's suitability for proton imaging.

Optical Photons Similar to the experiments described in Würl, 2018, first linearity tests were carried out with a 650 nm laser diode (Laserfuchs, Germany) and several Neutral Density (ND) filters (Thorlabs, USA) with combined optical density (OD) of 0.1, 0.2, 0.3, 0.4, 0.5, 0.6, 0.7, 0.8, 0.9. The OD is defined as

$$\mathrm{OD} = -\log(I/I_0)\ , \tag{5.2}$$

with I being the intensity of the transmitted light through the filter and I_0 the initial intensity. The intensity of the detector signal from illumination with the laser after the different filters is expected to be reduced by the factor $1/10^{\mathrm{OD}}$. As a cross-reference, the laser beam was divided by a 50/50 beam splitter and the intensity was also measured by a commercial photodiode (DET10A/M, Thorlabs, USA) (see figure 5.2a), which was read out with an oscilloscope (HMO3004, Rohde & Schwarz HAMEG, Germany). To measure the detector response, the pixel values of the LASSENA in the region exposed to the laser beam were accumulated. The intensity recorded by the photodiode and the LASSENA detector for each optical density were divided by the respective value without a filter and a linear function was fitted to the data points (see figure 5.2b).
The slope of the fit result was $m = 1$ and the y-axis intercept $c = -0.01$ with goodness of fit $R^2 > 0.999$, which demonstrates very good linear behavior for optical photons.

X-rays from ^{55}Fe Source To perform a measurement, where the detector response to single X-ray photon hits in the detector pixels can be compared to a known energy deposition, a ^{55}Fe source was mounted in front of the detector. ^{55}Fe decays by electron capture to ^{55}Mn and the main emissions are 5.19 keV Auger electrons and X-rays of 5.90 keV (16.2 % probability), 5.89 keV (8.2 % probability) and 6.49 keV (2.8 % probability). Taking into account that the detector is not expected to resolve differences in energy deposition lower than 100 eV, the source is considered as a quasi-monoenergetic source of 5.9 keV X-rays in this experiment. In the silicon sensitive volume of the CMOS, the dominant interaction at this photon energy is via photoelectric effect (see figure 2.6). In case of interaction by the photoelectric effect, the photon energy is transferred to the electron which is ejected from the atomic shell if the transferred energy is higher than the electron's binding energy. The integration time was set to 320 ms so that most pixel hits corresponded to single photon interactions. The most probable pixel value for single and double photon hits, 252(19) ADU and 484(37) ADU (corresponding to 5.9 keV and 11.8 keV energy deposition, respectively) were extracted from a Gaussian fit to the peaks occurring in a histogram of the pixel values.
These values confirm linear behavior of the detector response for low energy X-ray photons according to

$$\mathrm{PV(ADU)} = 41.0\frac{\mathrm{ADU}}{\mathrm{keV}} \cdot \mathrm{d}E(\mathrm{keV}) + 3.3\mathrm{ADU} \ , \tag{5.3}$$

with goodness of fit $R^2 > 0.999$.

Protons First tests of the detector with charged particles were performed at the HZB cyclotron facility, which provides a 68 MeV proton beam that can be degraded with aluminum plates down to 50 MeV and 30 MeV remaining kinetic energy.
For the experiments regarding linearity of the detector response, the proton beam's current

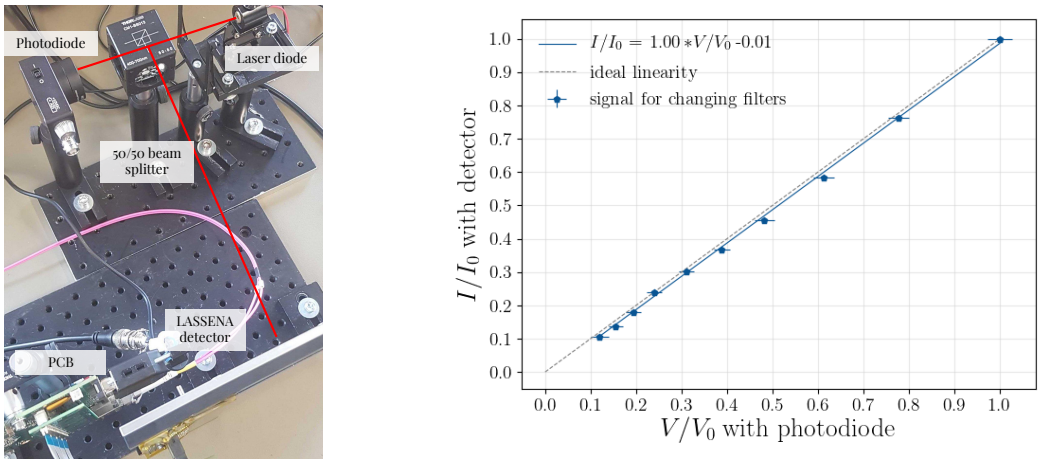

(a) **(b)**

Figure 5.2: (a) Experimental setup of linearity test with the laser that is directed by the beam splitter on the LASSENA detector and a photodiode as reference. (b) The recorded intensities relative to the signal without ND filters for the LASSENA detector as a function of the reference photodiode's signal, showing linear behaviour.

was set to a value in the order of 10^4 protons s^{-1} [1], which allowed to distinguish individual proton hits. Frames were acquired with 40 ms integration time in direct on-pixel irradiation and irradiation through the wafer. In each of the two configurations, measurements were done for the three above-mentioned energies.

In order to conclude on the relationship between detector response and energy deposition, the most probable detector pixel value for a proton hit had to be determined with a method correcting for *charge sharing*. In post-processing, the first step was to subtract an average dark frame from each frame with proton signal to discard dark current and background noise for each pixel (in the following referred to as "background subtracted"). Then, the frames are corrected for charge sharing similar to the procedure described in Mathieson et al., 2002: A "hit threshold" is set and all pixels with values larger than the threshold (e.g., 200 ADU for 68 MeV protons) are considered as proton hits. Also, a "low energy threshold" is set to three times the standard deviation of the mean dark value of all pixels, to discard pixel values higher than zero that stem from fluctuations in the background noise. For each hit pixel, its pixel value and the pixel values of the eight direct neighbour pixels that are higher than the low energy threshold are summed up and assigned to the position of the hit in the corrected image (see figure 5.3a to 5.3c). To obtain the most probable pixel value for single and double proton hits, a superposition of two landau distribution functions was fitted to the corrected histograms (see figure 5.3d).

The detector response was compared to the expected energy deposition in the sensitive layer, determined in a MC simulation of the experiment in front and back illumination (see blue marks in figure 5.4 and table 5.1).

[1] At beam currents below 10^6 s^{-1}, the beamline diagnostics can not measure the current accurately.

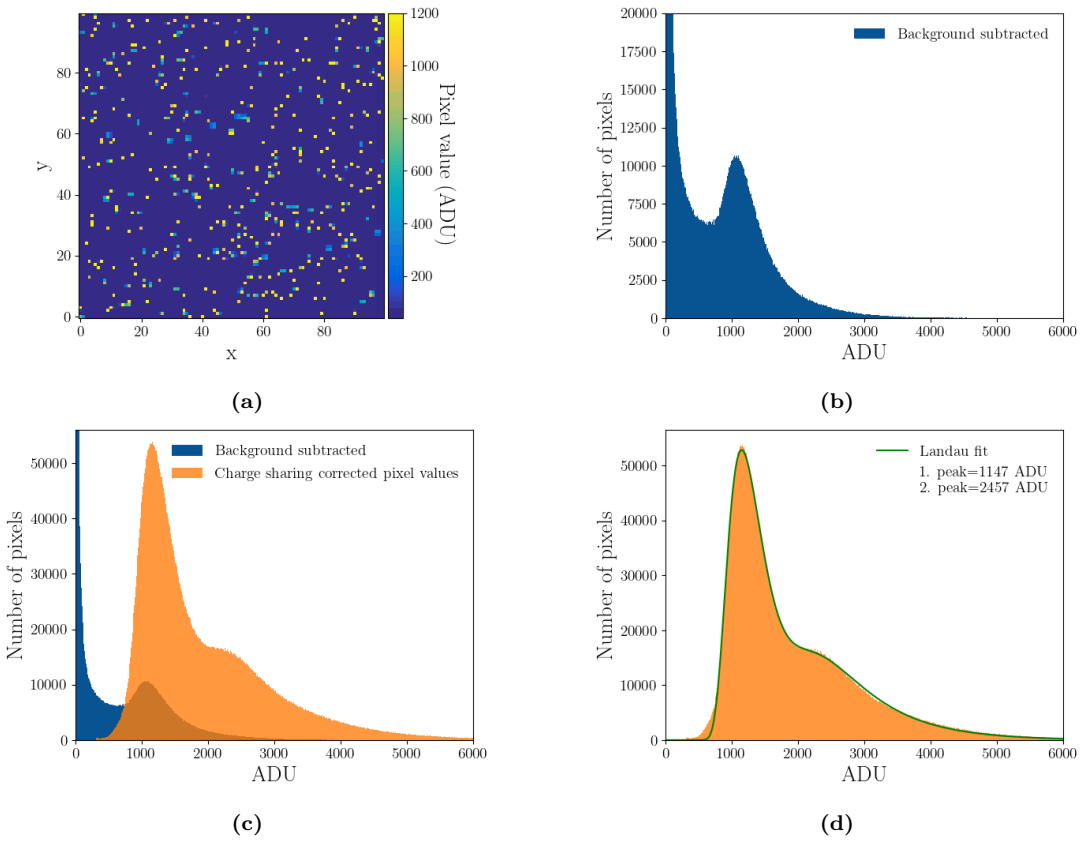

Figure 5.3: (a) Background subtracted image region of 100 × 100 pixels acquired for irradiation with a 30 MeV beam at HZB with 1000 ms integration time. For this configuration, charge sharing over 2-4 pixels in most cases is clearly visible. (b) Histogram of the background subtracted pixel values. Note the high occurrence of low pixel values due to charge sharing and fluctuations in noise. (c) Comparison of histograms of background subtracted pixel values with and without correction for charge sharing. In each of the corrected values corresponding to a hit pixel (PV > 200 ADU), the low-ADU pixel values of neighbor pixels from charge sharing are included. (d) Fit of superposition of two Landau distributions to the charge sharing corrected pixel values.

Also for the energy deposition from protons, a linear relation of

$$\mathrm{PV(ADU)} = 76.3\frac{\mathrm{ADU}}{\mathrm{keV}} \cdot \mathrm{d}E(\mathrm{keV}) - 15.3\mathrm{ADU}\ , \tag{5.4}$$

to the intensity of the detector signal was found with goodness of fit $R^2 > 0.999$.

While the detector response is perfectly linear as a function of the calculated energy deposition for both, the proton and the X-ray source, it is striking, that the detector response to proton irradiation seems to be twice as high (see figure 5.4). In correspondence with the manufacturer, these results were discussed and attributed to the different mechanism of energy deposition. The detector was originally designed for X-ray applications, so the depth of the interaction layer is not as relevant, as long as all created charges from an interaction are collected. In the LASSENA detector, charges are not only collected from the few µm silicon layer that is deemed the "sensitive layer" but also from the bulk silicon underneath. And as protons deposit energy all along their path through the detector, a higher detector response compared to X-rays is the expected outcome. The mechanism of energy deposition also explains the difference in standard deviation between the X-ray and the proton measurement: while the energy distribution from the ^{55}Fe source is relatively sharp, the energy deposited by protons depends on the path the protons take through the detector.

5.1.2.3 Temperature Stability

The detector system has temperature sensors at two different positions: The PCB and the FPGA, which is connected to one of the short sides of the sensor. The temperature was recorded every 5 min for 70 min with the detector continuously acquiring images with exposure time set to 320 ms to limit the amount of generated data. It was observed that the measured temperature stabilizes after 20 min at 35(2) °C and 65(2) °C, for the PCB

Table 5.1: Energy deposition from X-rays and protons in the 5.5 µm silicon sensitive layer of the LASSENA detector model estimated in MC simulations and corresponding measured detector response.

Case	Expected energy deposition (keV)	Detector response (ADU)
Fe-55 X-ray, single hit	5.9	252(19)
Fe-55 X-ray, double hit	11.8	484(37)
68 MeV protons, front irradiation	6.4	461(102)
68 MeV protons, back irradiation	6.5	475(110)
50 MeV protons, front irradiation	8.5	621(118)
50 MeV protons, back irradiation	8.8	654(128)
30 MeV protons, front irradiation	13.9	1058(190)
30 MeV protons, back irradiation	15.3	1157(200)

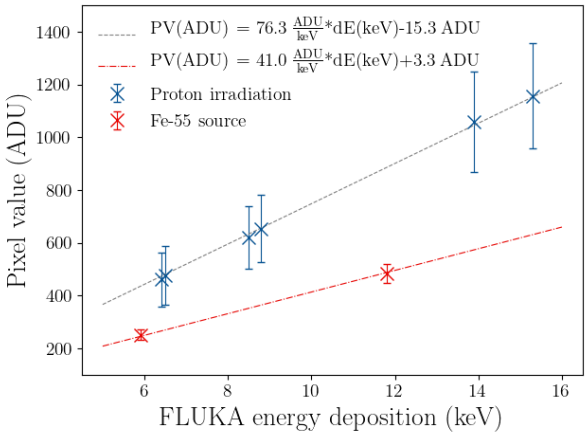

Figure 5.4: Average and standard deviation of detector response to proton and photon hits compared to MC determined energy deposition, assuming a 5.5 µm sensitive thickness for charge collection.

and FPGA, respectively (see figure 5.5a).

To obtain information on the spatial heat distribution, a thermal camera (T450sc, FLIR, USA) was used to observe the temperature variation over the sensor surface during a second set of measurements. In this measurement, the temperature was recorded in intervals of 2 min for 50 min, and 200 images were acquired with an exposure time of 80 ms every interval. The region on the sensor with about 10 mm distance from the FPGA ("upper right corner" and "lower right corner" in figure 5.5b) heats up to 29 °C in the first 20 minutes and remains constant afterwards (see figure 5.5). From that edge, the temperature declines continuously along the long edge to an observed temperature of 27 °C at the opposite edge ("upper left corner" and "lower left corner" in figure 5.5b). To evaluate the noise level during heat up, dark images were acquired in continuous acquisition with exposure time of 320 ms and the average and standard deviation of the pixel values were calculated. Figure 5.6a shows that the noise level fluctuates during heat up and stabilizes at 1202(10) ADU

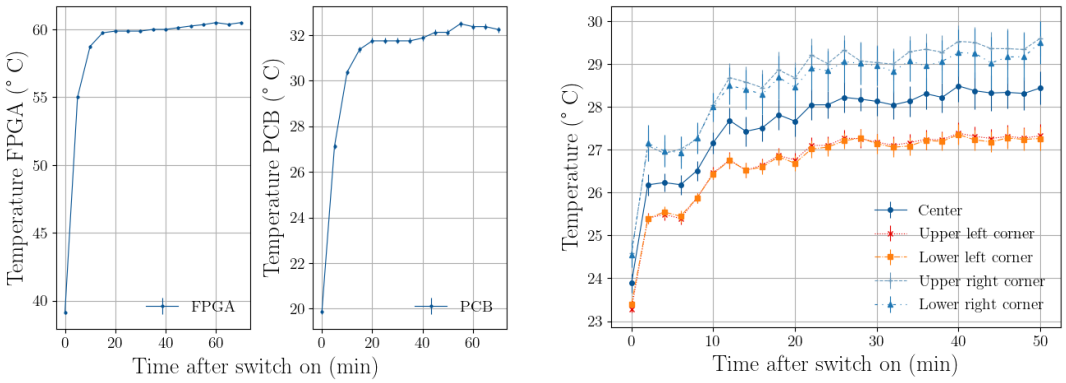

(a) **(b)**

Figure 5.5: Temperature of the FPGA and PCB and for five different regions on the detector in the time after switching on.

when temperature stays constant afterwards. The detector response during heat up was observed using a ^{55}Fe source and the pixel value is not influenced by the temperature raise (see figure 5.6b). As the noise level of the detector is temperature dependent, it is advised to start acquisition of images (including the *dark images* for pixel-wise background correction) 20 min after connecting the detector to the power supply.
Active cooling of the LASSENA detector is not necessary for the purpose of proton imaging. In addition, the aluminum casing of the detector acts as heat sink.

5.1.2.4 Radiation Hardness

The radiation hardness of the sensor to non-ionizing radiation was tested to be in the order of $< 1 \times 10^{13}\, n_{\mathrm{eq}}\mathrm{cm}^{-2}$ (Deveaux et al., 2011)[2].
In other experiments, the performance of the LASSENA sensor was tested up to 50 kGy of energy deposition from protons. It was observed that leakage current increases with dose, but can be limited with cooling. To be more specific, at ambient temperature of 20 °C, up to 20 kGy of continuous irradiation are tolerated before the sensor is saturated by increased leakage current. By active cooling to 0 °C, the lifetime can be increased to up to 50 kGy (Beck et al., 2023).

[2]The 1 MeV *equivalent neutron fluence* is the fluence of 1 MeV neutrons producing the same damage in a detector material as induced by an arbitrary particle fluence with a specific energy distribution (Bock, 1998).

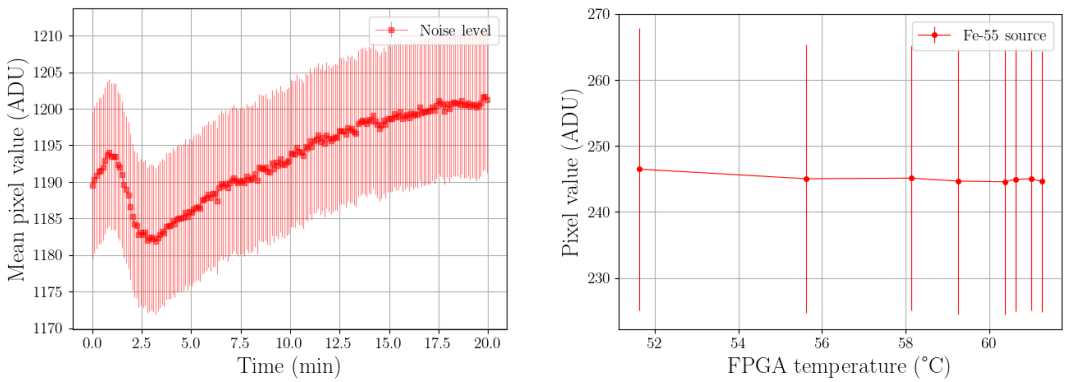

(a) **(b)**

Figure 5.6: (a) Noise level extracted from dark images during heat-up of the detector. (b) Average and standard deviation of pixel values from photons of a ^{55}Fe source during heat-up of the detector.

5.2 Study on CMOS Detector Setup for Integration Mode Imaging

This section addresses the optimal way to set up the CMOS sensor. More specifically, it was investigated which configuration is to be favored for imaging purposes among the two options to mount the sensor. The sensor can be mounted either with the pixel surface (referred to as "front irradiation") or with the wafer (referred to as "back irradiation") directed towards the proton source. It was hypothesized that the back irradiation would reduce blurring in the proton images at material interfaces, as more energetic, less scattering protons can be chosen to image the desired object (with a gain of energy equal to the amount that is lost in the wafer). The left panel in figure 5.7 illustrates how in a chosen imaging setup (5.7a) proton beams with the chosen range of probing energies pass through the phantom and the lateral beam profile is broadened through MCS in the phantom. In the right panel, another setup (5.7b) shows that higher probing energies are needed to produce the same desired energy on the sensor when traversing additional material in front of the detector. In that second scenario, MCS angles in the phantom are lower, but scattering will occur in the introduced degrader material. The wafer of the detector acts as additional degrader of fixed width without air gap to the sensitive volume. To understand whether the introduction of a material in front of the pixel surface can be helpful specifically in integration mode imaging with energy variation, it is sufficient to focus only on the lowest probing energy used for imaging that will just reach the detector. Protons of this probing energy are close to their stopping point and therefore have a high gradient of $\mathrm{d}E/\,\mathrm{d}x$ (which makes them the most relevant for WET contrast) and their mean scattering angle is high (as it is inversely proportional to β as explained in section 2.1.2). If the protons are measured after the wafer, the ones that have been slowed down the most in the phantom and/or scattered at a large angle are stopped in the wafer. This effect is only observable as long as the reduction of protons with large lateral displacement in the imaged object is not counteracted by the additional scattering in the silicon layer.[3] The following two subsections describe, firstly, the MC simulations, and secondly, the experiments, that were carried out at HZB and CAL to study the optimal configuration.

5.2.1 Monte Carlo Study on CMOS Irradiation through the Wafer

MC simulations were performed to test whether irradiation through the 750 µm silicon wafer of the LASSENA reduces scattering angles in two configurations: Firstly, the irradiation of a simple object composed of two materials with the interface along the direction of the irradiation using a monoenergetic beam and secondly, the more realistic

[3] In an experimental setup with an additional (variable) degrader mounted between phantom and detector, further air gaps between phantom, degrader and detector would eliminate the benefits of higher probing energies and increase the complexity of the setup.

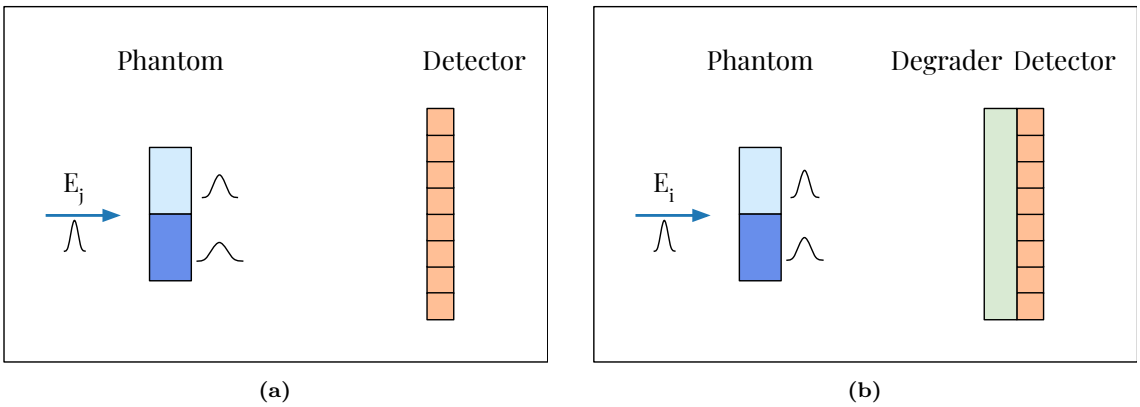

Figure 5.7: Illustration of two scenarios for initial probing energy and degrader used: Whilst passing through the phantom, the protons undergo multiple Coulomb scattering and the lateral beam profile enlarges. The phantom is composed of two materials with unequal atomic number Z, hence scattering angles are different. (a) The phantom is irradiated with a sequence of probing energies E_j. The energy values are selected to enable WET determination for the given phantom. (b) If a material slice is introduced between phantom and detector, the energy values of the probing energies E_i in that scenario can be chosen higher as in (a). Therefore, the mean scattering angle for protons that pass through the phantom is reduced. Additional scattering will occur in the homogeneous degrader material.

case, using a clinical beam model and a phantom considered for small animal studies.

In the first simulation, the lateral displacement of individual protons in a transversal interface region and while traversing the wafer and sensitive volume was tracked stepwise with a user-defined mgdraw.f routine. Figure 5.8 shows the lateral positions (here the y-direction was chosen) of 60 protons with an initial energy of 87 MeV that pass through an interface region between simulated solid water and bone material (as described in 4.4.1) at $y = 0$. The proton position was recorded at entrance and exit of the 1 cm thick phantom and every 75 µm in the silicon wafer and sensitive volume. The wafer and sensitive volume of the detector are both made from silicon and are modeled as one block (see figure 5.8). To simulate front irradiation, the proton radiography is formed from the per-pixel accumulated energy depositions at the entrance of the detector. Likewise, to simulate back irradiation, the proton radiography is constructed from the energy deposition of protons that have passed through the wafer. Protons that have passed through both phantom materials were flagged and are shown in blue. If the marker is at the right hand side of the detector the protons either stop in the rear 75 µm of the wafer or pass through the sensor. It is visible in figure 5.8 that the average lateral displacement of protons in the interface region is larger at the entrance of the detector (depth in wafer 0 µm) as compared to after the silicon wafer (depth in wafer 750 µm). In front irradiation, the proton image would therefore be more blurred at interface regions than the image acquired in back irradiation. This phenomenon is relevant to integration mode imaging, as large-angle scattering events can not be excluded from the data that are used for image reconstruction.

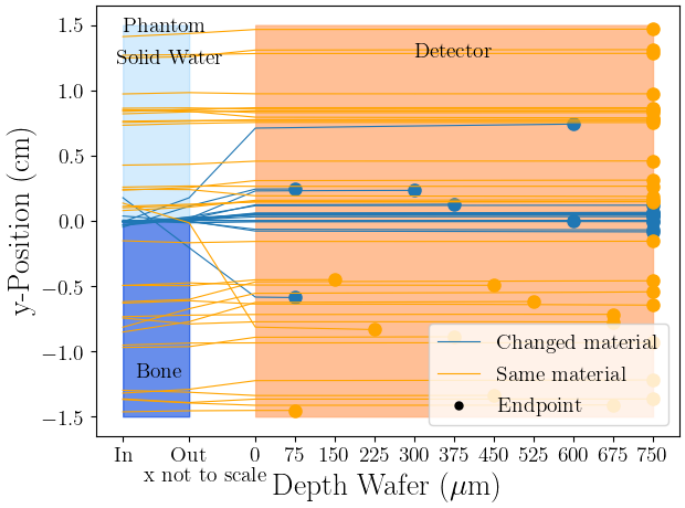

Figure 5.8: Example of proton tracks in the phantom, the air gap and the detector for an initial beam energy of 87 MeV. The wafer and sensitive volume of the detector are both made out of silicon and are simulated as one block. Part of the protons that have been scattered at large angles or lost significantly more energy than average in the phantom are stopped in the wafer.

In a second set of simulations, a more complex scenario taking into account realistic conditions was evaluated. Two phantom geometries were used in the simulation: 1) A cylindrical phantom of 30 mm diameter of solid water material with inserts of cortical bone (SB3), adipose, liver, and bone (B200) material of 6 mm diameter each and thickness of 10 mm for the phantom was chosen to evaluate WET accuracy (see figure 5.9a and 5.9b). 2) A cylindrical phantom of 30 mm diameter of solid water material and a quadratic insert whose sides are tilted at 2° angle from the main axes of the simulation (referred to as *slanted-edge phantom*), and therefore the scoring grid, for evaluation of the spatial resolution (see figure 5.9c and 5.9d).
The chosen beam model for irradiation was the experimentally validated MC model of the proton beam at RPTC (Englbrecht, 2014), and the central axis of the respective phantom cylinder was aligned with the beam axis.
The evaluation of WET and spatial resolution is done as outlined in section 4.5 and a margin of 0.3 mm inside the inserts was chosen to define the ROI for the WET evaluation that is summarized in table 5.2.
As shown in table 5.2, WET accuracy is better in the "back irradiation" configuration of the MC simulation, which is due to less range mixing at interfaces. The same holds true for the spatial resolution, that is quantified to be 0.48 mm for the front irradiation and 0.32 mm for the back irradiation.

Conclusion

MC simulations were carried out for the case of a monoenergetic beam and a simplistic phantom composed of two materials as well as a more realistic case using an experimentally validated beam model to irradiate two cylindrical phantoms: one for evaluating

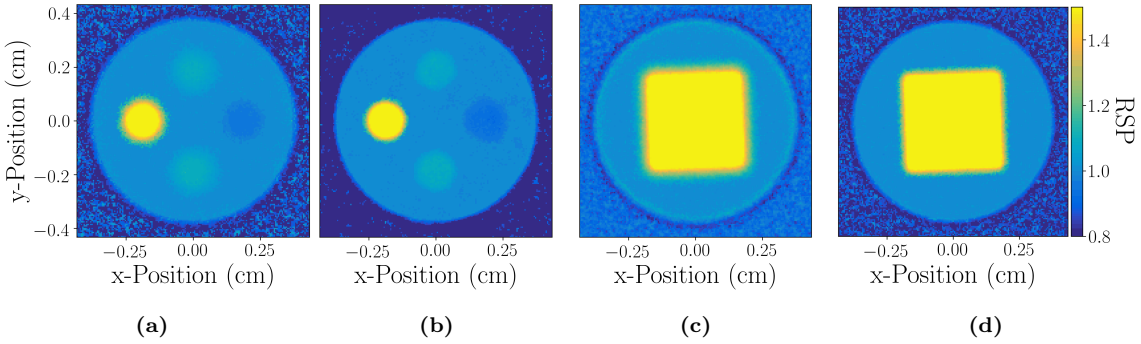

Figure 5.9: Images of phantom with cortical bone (SB3), adipose, liver, and bone (B200) materials in (a) front and (b) back irradiation of the detector. Images of the slanted edge phantom for evaluation of the spatial resolution in (c) front and (d) back irradiation.

Table 5.2: WET accuracy of phantom with cortical bone (SB3), adipose, liver and bone (B200) mimicking materials in front and back irradiation.

Insert		Front irradiation		Back irradiation	
	Ground truth WET	WET	Difference (%)	WET	Difference (%)
Cortical bone (SB3)	1.64	1.62	3.29	1.65	1.85
Adipose	0.95	0.98	2.90	0.97	2.82
Liver	1.08	1.08	1.50	1.08	1.32
Bone (B200)	1.10	1.10	0.74	1.10	0.48

the WET accuracy and a slanted-edge phantom to evaluate the spatial resolution. It was indicated that for the investigated setups, irradiation through the 750 µm silicon wafer improves spatial resolution in integration mode imaging. Through the reduction of blurring at interfaces, also WET accuracy in homogeneous regions of the image is improved.

5.2.2 Experiments on CMOS Irradiation through the Wafer

Dedicated measurements at HZB and CAL were performed to examine if the advantage of the irradiation through the wafer found in MC simulations also proves to be true in experiments or if unknown aspects, e.g., in the pixel architecture, corrupt this apparent advantage.

In the experiments at HZB, a Polymethyl Methacrylate (PMMA) step phantom with 4 mm steps and a total thickness of 10 mm was irradiated with a fixed proton beam energy of 50 MeV in order to study the blurring at the interfaces between the steps. The three phantom thicknesses forming the 4 mm steps were 2 mm, 6 mm, and 10 mm. The step phantom was placed central to the beam axis, directly in front of the detector with the steps oriented along the vertical direction (see figure 5.10). The detector was mounted in such a way, that it was possible to change from front irradiation to back irradiation without altering any other element of the setup. In this combination of beam energy and phantom step thicknesses the alteration of energy loss in the phantom steps

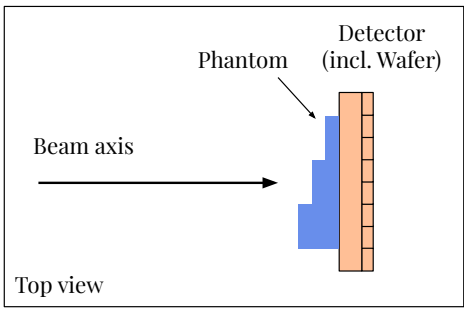

Figure 5.10: Schematic drawing of the irradiation geometry for the experiments using step phantoms at HZB and CAL as seen from above (not to scale).

is considerable, so that the individual steps are visible in a transmission image (see figure 5.11a) and the beam is not stopped in one of the phantom steps.

Measurements in integration mode were done at CAL to assess if additional homogeneous material layers in front of the 750 µm wafer would further reduce the amount of protons, that were scattered at a large angle in the imaged object, reaching the pixel surface. A second step phantom with thicknesses of 1 mm, 2 mm, 3 mm, and 4 mm was used as well as additional absorber material placed in between the detector and the step phantom. The absorber material foils were one of 0.5 mm thickness made from PMMA and a second one of 0.7 mm thickness made out of Mylar. The irradiation geometry was similar to the geometry shown in figure 5.10 with the difference that the phantom-to-detector distance was 10 mm. The experimental setup, beam characteristics, and calibration are described in (see section 6.2.8).

The contrast at the step edges in the transmission image was quantitatively evaluated using the ESF method described in section 4.5.2.

5.2.3 Results

Figure 5.11 shows the averaged pixel values of the LASSENA image of the 4 mm step phantom along the step edges. It is visible to the eye that in irradiation through the wafer (back irradiation), the slope at the edges is steeper. For each step, the spatial resolution was quantified and irradiation through the wafer was always beneficial for proton imaging (see table 5.3).

If additional degrading material is placed in between the step phantom and the wafer at a phantom-to-detector distance of 10 mm, spatial resolution evaluated from the step phantom remains unchanged considering the uncertainty of the measurement, as summarized in table 5.4. It is concluded that the chosen thicknesses of the additional materials has no significant effect on the spatial resolution.

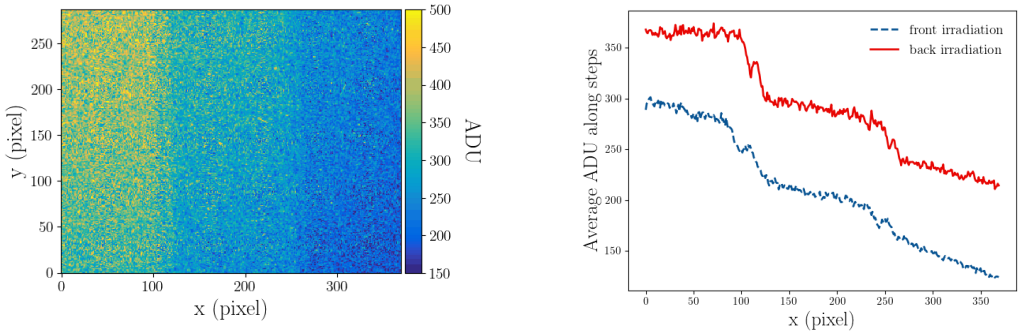

(a) **(b)**

Figure 5.11: (a) Transmission image of the 4 mm step phantom with 2 mm, 6 mm, and 10 mm step thickness irradiated with a 50 MeV proton beam. (b) Averaged pixel values along the edges of the 4 mm step phantom in front (dashed line) and back (solid line) irradiation with the 50 MeV beam at HZB.

Table 5.3: Spatial resolution at the edges of the a 4 mm step phantom irradiated with 50 MeV beam energy. The three phantom thicknesses forming the 4 mm steps were 2 mm, 6 mm, and 10 mm.

	Front irradiation	Back irradiation
Step 6 mm-10 mm	1.2 mm	0.5 mm
Step 2 mm-6 mm	1.5 mm	0.8 mm

Table 5.4: The average value of the spatial resolution given in mm evaluated at the edges of the step phantom with thicknesses of 1 mm, 2 mm, 3 mm, and 4 mm. For each step edge, the spatial resolution was calculated for ten ROIs along the step edges (standard deviation in parentheses).

	Spatial res. (mm)		
Irradiation scenario	Step 1 mm-2 mm	Step 2 mm-3 mm	Step 3 mm-4 mm
Wafer	0.20(1)	0.25(1)	0.30(1)
+ 0.5 mm PMMA	0.20(1)	0.24(1)	0.28(1)
+ 0.7 mm Mylar	0.21(1)	0.23(2)	0.30(3)

5.3 Discussion

For proton imaging with the LASSENA detector, this work thoroughly investigated through MC simulations and measurements how the spatial resolution is affected by the orientation of the detector with respect to the beam, namely whether protons pass through the wafer first (back irradiation) or directly impinge on the pixel surface (front irradiation).
Additional considerations for the setup are in the handling and light tightness: The distance between the imaged object (e.g., the mouse holder) and the detector surface should be reduced but an undesired collision with the pixel surface would possibly damage the detector. Such collisions are prevented by mounting the detector with the wafer towards the object. Furthermore, the wafer is almost opaque and with an additional aluminum foil fixed directly on the wafer, the influence of ambient light on the background signal can be eliminated. In comparison, the holder for the CM49 had to be designed with an additional air gap of 3 mm between aluminum foil and pixel surface, as well as a special cable pass. In the case of damage to the aluminum foil it is a cumbersome procedure to change it.
It was tested in experiments if adding additional material in front of the wafer could further improve the spatial resolution in interface regions of proton images. The results for the cases under investigation were inconclusive. It is assumed that for the used beam energies, scattering in the surplus material cancels out the stopping of some protons that were scattered at a large angle in the object.

5.4 Conclusion

CM49 Due to the issue of non-reliable data acquisition described in the first part of this chapter, the CM49 was deemed not suitable for proton imaging in the SIRMIO platform. The random idle times of the detector already compromised WET determination in test conditions, where delivery of one probing energy took several hundreds of milliseconds. To reach the lowest possible imaging dose at the same beam current, the irradiation time is supposed to be minimized, which increases the importance of the reliable operation of the detector.

LASSENA Based on an in-depth MC simulation and experimental study, the preferable configuration to mount the LASSENA detector was found with the wafer mounted toward the proton source, such that protons pass through the wafer before entering the detector's sensitive volume. Due to these findings, this configuration (back irradiation) was used in all subsequent imaging experiments with the LASSENA detector.

CHAPTER 6

Integration Mode Imaging with a CMOS Detector

This chapter begins with describing the principle of how to achieve imaging with energy variation and a CMOS sensor and how to retrieve a quantitative WET image from the measured data.
Secondly, the experimental campaigns at the previously introduced proton therapy facilities are presented, including the description of the general experimental setup and how MC simulations were used to prepare the experimental campaigns, refine WET calibration and support more accurate WET retrieval.
Building upon those previous steps, it is outlined how data from the experiments are used to draw conclusions on the factors that influence image quality and practicability in integration mode imaging with a CMOS sensor for small animals.

6.1 Principle of Integration Mode Imaging with a CMOS Detector

The key to determine the WET of an object is to deduce the energy loss in the object (see section 3). In this specific work that employs a CMOS sensor in integration mode, energy loss is indirectly determined by irradiation of the object with a sequence of probing energies E_i (here called *probing energies*) and recording the respective detector signal (see figure 6.1a). By measuring which initial proton beam kinetic energies stop in the object (and vice versa, at which beam energies the protons pass through the object and reach the detector) the WET of the object can be assessed. This approach is similar to other integration mode setups outlined in section 3.2.2 with the refinements of using a CMOS detector, a more robust method of WET determination and the application to small animal research. Early phase MC studies were carried out by Carriço, 2018 and Esslinger,

2019. Spatial resolution is achieved through a pixelated detector with pixel size that is small compared to the proton beam size.

The utilized CMOS sensor measures the accumulated energy deposition E_d of an unknown number of protons in its sensitive layer during the exposure time. The height of this signal as a function of probing energies $E_d(E_i)$ can be correlated to a value of WET in the object. The sequence of probing energies that is necessary to scan an object depends on the WET values that are of interest to be retrieved from the measurement. The higher the maximum kinetic energy impinging on the object is, the higher the maximum WET that can be determined. In the case of small animal irradiation, maximum WET values of 4 cm are expected, which requires a maximum proton beam energy of up to 70 MeV. The minimum applied in the experiments contributing to this work was about 4 MeV as structures of lower WET, e.g., mouse ears and claws, are of minor interest. The number of different probing energies to be used for imaging has to be chosen as a compromise between dose exposure of the object and granularity of measurements to achieve high accuracy in the WET determination.

6.1.1 Determination of the Water-equivalent Thickness

In the following it is explained how the WET value for each image pixel is determined from the raw data, starting from the general formalism of signal Bragg Peak Decomposition and then expanding on the WET calibration and processing of the raw detector data.

6.1.1.1 Bragg Peak Decomposition

For each pixel, the detector signal is the accumulated energy deposition of protons during the integration time. These pixel values are displayed as a function of the irradiated probing energies (see figure 6.1c).

To illustrate the principle of Bragg Peak Decomposition, the example shown in figure 6.1 assumes a phantom, where the WET varies in direction lateral to the beam, but that is homogeneous along beam direction. In the interface regions of such an object, protons will pass through several materials (and accordingly WET values) due to their lateral scattering and initial beam divergence. The accumulated signal from multiple protons in a sensor pixel therefore contains not only the energy deposition of protons that went through the part of the object which is in a straight line upstream of the sensor pixel, but also scattered-in components from surrounding materials (see figure 6.2). The most relevant WET contribution therefore might differ from the maximum of the measured signal.

In the simplistic case of two interfacing materials, the range mixing will lead to a E_d versus E_i curve that shows the superposition of two Bragg peaks (see figure 6.3a), with the detector signal denoted as the vector $\vec{b}$ with size n corresponding to the number of probing energies:

$$\vec{b} = x_1 \cdot \vec{c}_1 + x_2 \cdot \vec{c}_2 \,, \tag{6.1}$$

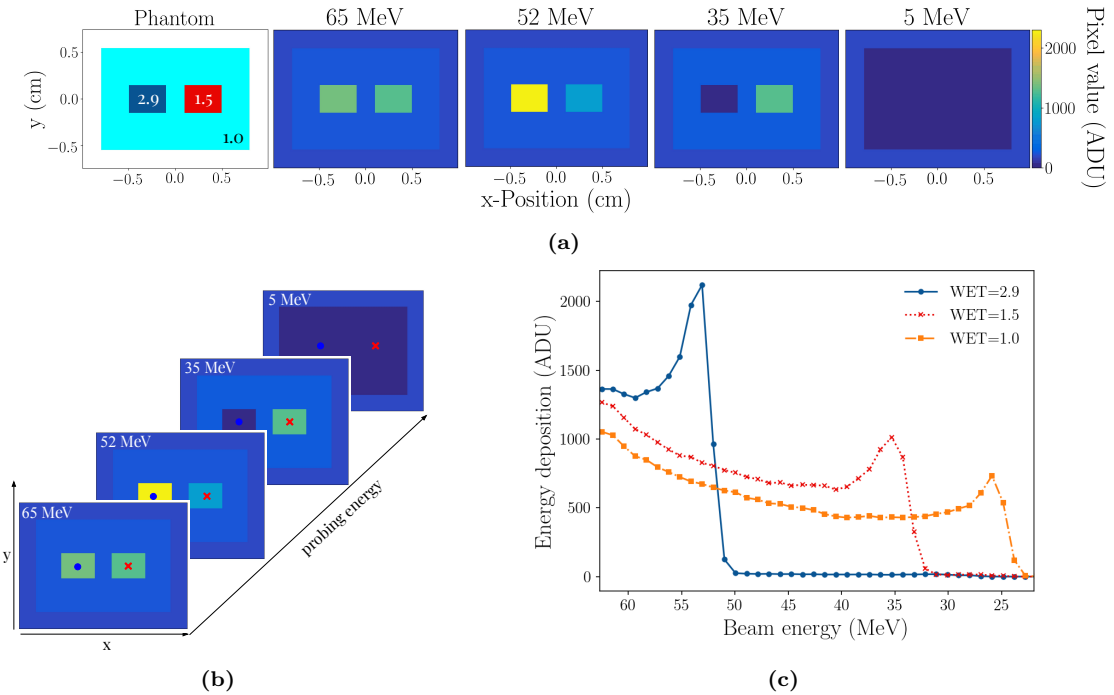

Figure 6.1: (a) Hypothetical phantom and detector signal. From left to right: Geometrical outline of the phantom baseplate with WET = 1 and two material inserts of higher WET values, $\mathrm{WET_A} = 1.5$ and $\mathrm{WET_B} = 2.9$ and detector signal in arbitrary ADU values for four different probing energies. (b) The acquired images are stacked into a three-dimensional matrix. (c) The detector signal as a function of the probing energies in two pixels behind the inserts corresponding to two different materials of the phantom and one pixel behind the phantom baseplate. The lines are to guide the eyes only.

with x_1 and x_2 denoting the respective weights of the two Bragg peak contributions $\vec{c}_1$ and $\vec{c}_2$.

To recover the WET of the object in each image pixel from the measured signal, a reference of this detector's signal for well-known WET values is needed. This reference is used to set up a Lookup Table (LUT), which is an $m \times n$ matrix of the energy deposition in the detector pixels for each of the m reference WET values and n initial beam energies. The Bragg Peak Decomposition method is able to retrieve the individual weights of the WET components in the signal measured in a detector pixel. The measured signal $E_d(E_i)$ is a vector $\vec{b}$ with size n. The solution vector $\vec{x}$ (size m) will contain the respective weight x_j of each WET component j in the measured signal $\vec{b}$. This solution is found by the linear combination of calibration curves, i.e., rows in the LUT A, that best reproduces the signal. This corresponds to minimizing the difference between the superposition of Bragg peaks in A and the measured signal $\vec{b}$, which is formulated as the following bounded-variable linear least-squares problem:

$$\min_{\vec{x}} \frac{1}{2} ||A\vec{x} - \vec{b}||_2^2 \; for \; 0 \leq x_j \leq 1 \; \forall j \,, \tag{6.2}$$

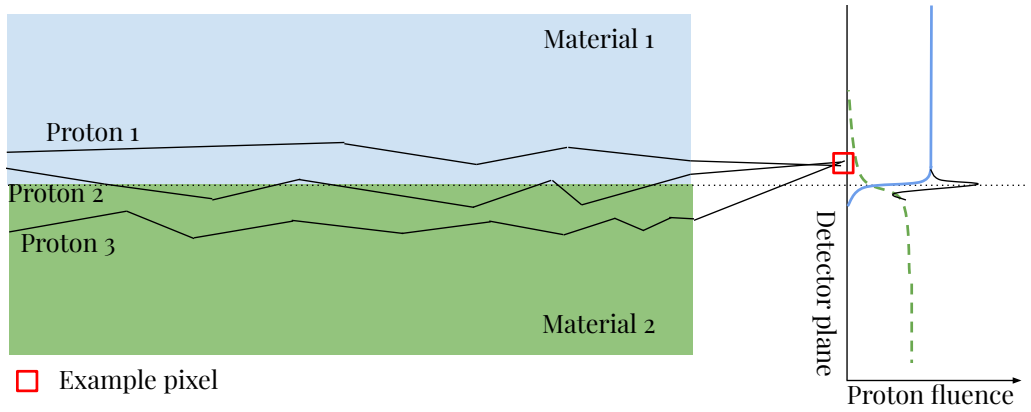

Figure 6.2: Simplified depiction of signal from interface region between two materials. Through scattering in the object, protons that have gone either through only one of the materials (Proton 1 and 3) or both (Proton 2) could all strike the detector in the same pixel close to the interface. The proton fluence after the material is a superposition of the proton fluence after attenuation and scattering from material 1 (blue line) and material 2 (green dashed line).

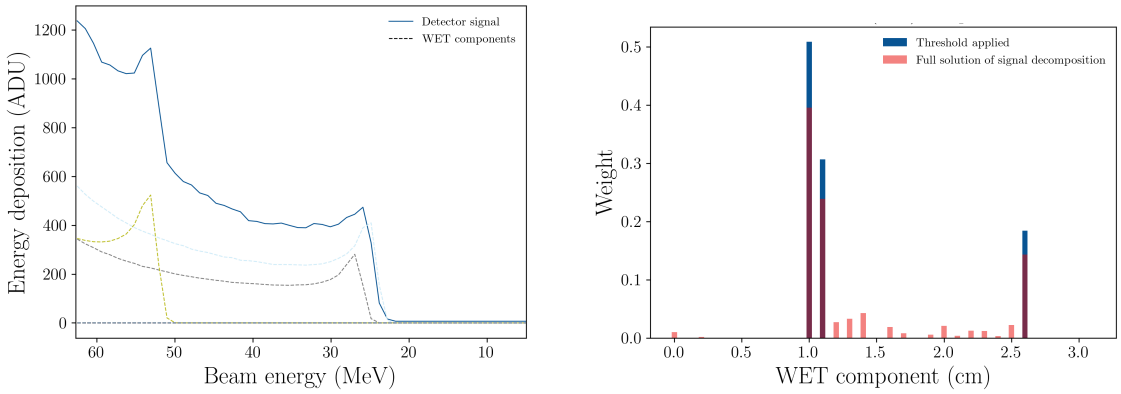

(a) **(b)**

Figure 6.3: Example of signal decomposition algorithm for a detector pixel behind an interface region between the Cortical bone (SB3) insert and the baseplate, leading to range mixing. (a) Detector signal in a pixel with range mixing. The mixed WET components are indicated as dashed lines. (b) WET components found as solution corresponding to the signal in (a).

analog to the methods described in Meyer et al., 2017 and Krah et al., 2015.
In the example of two components contributing to $\vec{b}$ as in Fig. 6.3a, the algorithm will find the solution in the basis of the WET components in the LUT A. In figure 6.3b it can be observed that (i) *artifact* WET components are present in the solution $\vec{x}$ and (ii) the solution gives the weights of the discrete WET components in the LUT and the true value could lie in between (e.g., the right peak in figure 6.3a stems from a WET in front of the detector that is between 1.0 and 1.1).
The artifact WET components with small weight (see "Full solution" in figure 6.3b) can occur because the solver will strictly find the mathematical optimum and has no limit of non-zero values in the solution, i.e., no prior knowledge how many WET values can be present in the signal through the geometry of the object. Albeit such small WET contributions could be present in the object, they are often only a consequence of statistical fluctuations in the measured signal for each pixel. To exclude unwanted contributions, a threshold is applied (in the example of figure 6.3b it is 10 % of the total of WET components) and the remaining components are re-normalized, so that the sum of the weight of all WET components identified in a pixel equals one. The fluctuation in the measured detector signal arises partly through varying proton number arriving on a given pixel for consecutive probing energies. In general, the current of the proton beam in an experiment can fluctuate to a certain degree depending on the facility where experiments are conducted. Also the heterogeneous object being present itself instead of a homogeneous calibration material will slightly change the proton number hitting each single pixel for changing probing energy (West–Sherwood effect (West et al., 1973)). Additionally, the energy deposition of protons in the sensitive layer varies following a Landau distribution. Moreover, the detector has limited energy resolution and there is variation in the detector's dark current as well as ambient noise.
In order to identify the WET value that will be assigned to an image pixel, the found WET components in the solution $\vec{x}$ can be combined or used separately. Common practice is to either choose the mode of the solution vector (most likely component) $\mathrm{WET}_{\mathrm{max}}$ or to calculate the weighted mean to obtain an image of $\mathrm{WET}_{\mathrm{mean}}$ (Gianoli et al., 2019). Choosing $\mathrm{WET}_{\mathrm{mean}}$ gives the possibility to reconstruct the image with a finer WET resolution than tabulated in the LUT, but at the cost of degraded spatial resolution. The blurring at interfaces in the $\mathrm{WET}_{\mathrm{mean}}$ image shows the lateral deviation of protons through scattering in the object and drift in the air gap to the detector and allows evaluation of the magnitude of the detrimental effect of scattering on spatial resolution.
In this work, the minimization to find the WET values is carried out with a *python*-script (python version 3.8) that uses the function *lsq_linear* in the *scipy.optimize* package (scipy version 1.8.0) with the parameter defining the optimization method set to *bvls*[1] as described in Stark et al., 1995 to solve the linear least-squares problem in Equation 6.2.

[1] https://docs.scipy.org/doc/scipy/reference/generated/scipy.optimize.lsq_linear.html

6.1.1.2 Data Processing

To generate one radiography, a series of images with fixed integration time is acquired for each probing energy. Each image represents the energy deposition in the 2D pixel grid. The images are either acquired in one continuous acquisition for all probing energies or for one probing energy after the other ("step and shoot"). The raw data for one radiography are then used to form a 3D array with the spatial information on energy deposition in two dimensions and probing energy as third dimension. Figure 6.1b shows schematically how images are stacked to give the 3D data used as input for the algorithm for WET determination.

Background Correction In one 3D array of raw data frames, there will be *dark images* without signal from the proton beam and the here called *image frames* containing the detector signal for the probing energies. The dark images contain the background signal, e.g., from ambient light in the event of imperfect light shielding, and the detector's dark current.
In a first step as preparation for the Bragg Peak Decomposition, the image frames for each probing energy are identified from the acquired sequence (see figure 6.4). For each subset of images belonging to one probing energy, the first and the last frame are discarded to not take into consideration frames that received signal for only part of the integration time. As second step, the dark images are used to subtract the background noise from the image frames.

Filtering and Downsampling As all the experiments were conducted with a relatively low beam current ($\mathcal{O}(0.1\,\mathrm{nA})$ at the nozzle, that was further reduced through scattering and a drift space to the detector, there is a relatively high statistical fluctuation of the number of proton hits in between pixels. A median filter with a kernel size of 5 pixels was applied to decrease the fluctuation between pixel values of the raw images. To further smoothen the acquired images they are downsampled to an artificially larger pixel size, i.e., the average of a given number of neighbouring pixels is calculated. If not stated otherwise, all images in this work were evaluated with downsampled images of 2×2 pixels, resulting in 99 µm pixel size for the CM49 detector and 100 µm pixel size for the LASSENA detector.

Choice of Image Number and Probing Energies for WET Determination If beam current (for each probing energy) is constant, the number of particles giving rise to the signal in each image frame in the subset is the same. Based on the desired WET accuracy and imaging dose, a certain number of image frames is chosen and the average value for each pixel is calculated.
Also the number of probing energies that are used in the WET determination can be varied. The granularity in probing energies determines the WET contrast that can be

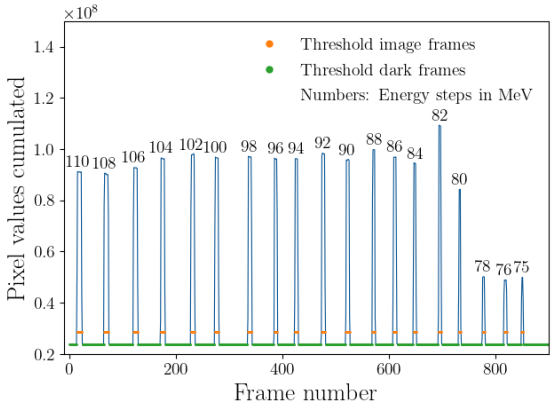

Figure 6.4: Sum of energy deposition in detector units for each frame for the measurement of the µ-CT phantom (see section 4.4.1) conducted at RPTC, showing beam-on and energy switching phases during the irradiation of the treatment plan. The orange bars show the threshold for choosing frames for the proton image, frames with a cumulated value lower than the dark threshold were used to subtract the background noise from the frames with signal.

achieved.
The chosen images are stored in the order of highest to lowest selected probing energy as input for the Bragg Peak Decomposition. An illustration of how this input to the solver for one pixel changes with the averaging of a different number of frames is shown in figure 6.21a and for the choice of probing energies in figure 6.21b.

Implementation Sorting the raw data along with background subtraction and filtering is done in a dedicated python-routine. For filtering the function *median_filter* from the *scipy.ndimage*-package is used.

6.2 Experimental Campaigns

In this work, results from experimental campaigns using the beam from four proton beamlines are presented. During each of these campaigns, several experiments were performed to address distinctive research questions. Some experiments were repeated at another facility, to be able to draw more general conclusions independent of specific experimental settings.

In the first part of this section, the experimental implementation of energy variation in the imaging workflow is presented, followed by a general overview of the experimental routine and method to use MC simulations to support WET determination. Thereafter, the details on beam energy variation, WET calibration, which detector was used and the respective settings, the phantoms, and type of measurement for each proton imaging experiment are outlined. In this section, also the simulation models corresponding to the respective experiments are presented.

How the acquired data from several experimental campaigns were combined to investigate factors impacting the image quality in integration mode imaging and optimize the setup for implementation in the SIRMIO platform is presented in the following section 6.3.

6.2.1 Energy Variation in Experiment

At most proton therapy facilities (e.g., at the RPTC described in sec. 4.3.1), to treat deep-seated tumors, the beam delivery system includes a mechanism for automatic energy switching and Pencil Beam Scanning which is used by default for therapy. The energy switching can be exploited to produce the probing energies by generating a treatment plan that will be executed for every radiography that is captured.
The lowest beam energy available at such clinical facilities is typically in the range of 70 MeV to 100 MeV, which is too high compared to the necessary probing energies. As solution, a fixed thickness of material can be inserted into the beam to degrade all the energies listed in the treatment plan before reaching the imaged object, similar to a range shifter employed in ion beam therapy. An appreciated side-effect is that the use of this degrader material (in this study: PMMA) also broadens the beam. This beam broadening is exploited by choosing a large distance between detector and range shifter as compared to the distance between range shifter and beam exit to obtain a more homogeneous and parallel illumination of the FoV (similar to the passive scattering beam delivery approach described in section 3.1.1).
The advantages of the method using the energy switching system of the beamline are the simplicity and short time duration of 45 s to 90 s per radiography.
Alternatively, in particular at facilities without automated energy switching, a custom made energy degradation system can be inserted in the beam path between nozzle and object. Material slabs of known WET are moved into the beam by motorized linear and rotation stages as indicated in figure 6.5.

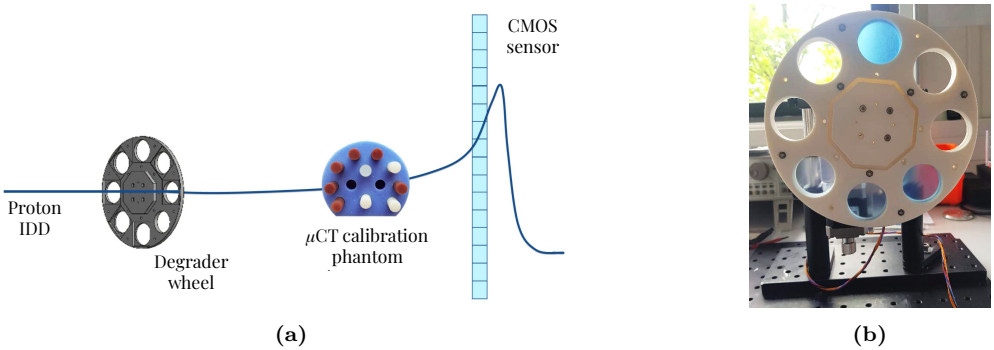

Figure 6.5: (a) Schematic drawing of the experimental setup including a degrader wheel, the μ-CT calibration phantom and the CMOS detector. A variable degrader like the depicted wheel is needed when there is no automatic energy layer switching. (b) Degrader wheel used to generate probing energies at beamline with fixed proton beam energy, in this case adapted to the beam exit of the Medicyc beamline at CAL.

In this thesis work, an energy degrader wheel was porduced specifically to be used in the experiments at the beamline of the Medicyc cyclotron at CAL, which delivers a fixed proton beam energy of 62.3 MeV. The wheel holds seven PMMA layers with thickness ranging from 0.5 mm to 3.5 mm in a 3D-printed frame. The circular cutouts that hold the layers have a diameter of 34 mm each, adapted to the size of the collimator at the beam exit of the Medicyc cyclotron at CAL. The wheel is turned by a motorized rotation stage. Up to seven PMMA-slabs of 4 mm can be inserted manually in an additional holder directly behind the wheel at the height of the beam exit, such that the available range in PMMA thickness is from 0 mm to 31.5 mm in steps of 0.5 mm. The RSP of this specific PMMA, in this work, referred to as $\text{PMMA}_{\text{Wheel}}$, was measured to be 1.147 using 107 MeV and 125 MeV proton beams at Heidelberg Ionenstrahl Therapiezentrum (HIT) and the PeakFinder water column (PTW, Germany) (see section A.3).

6.2.2 General Measurement Procedure

Dark images The first set of images that is acquired are dark images without any beam. The detector is in its place in the experimental setup. These dark images are used to compute an average dark image that will be subtracted from all measured images to diminish ambient noise. Depending on the specific experimental plan, dark images are acquired regularly throughout the experiment to control that the ambient conditions remain stable.

Open field Open field images are plain images of the degraded and scattered (and if applicable also collimated) beam in the detector's FoV for each probing energy. The same exposure time and beam current as for the calibration and the imaging of phantoms are chosen. Those measurements provide the beam position with respect to the FoV and the proton fluence distribution on the detector surface, i.e., spot shape and size, for each probing energy.

Calibration Images with material slices of known WET were acquired as calibration measurements of the detector signal for each probing energy to set up the facility-specific LUT. The RSP of these materials was independently measured in a water column at HIT (see section A.3). These images give a reference for a certain value of WET in the given experimental setup specific to the detector.
The result of this WET calibration is a LUT with WET and beam energy as measured (see figure 6.6a), which will then be complemented through Monte Carlo simulations (see figure 6.6b and section 6.1.1).
These measurements also provide the basis to precisely adjust MC simulations mimicking the experimental setting, as it is necessary for the WET determination and estimation of the imaging dose.

Phantom images Images of different phantoms are acquired, depending on the aim of the study. For comparison amongst experimental setups, a radiography of the SMART µ-CT calibration phantom (see section 4.4.1) was acquired each time with a distance of 10 mm between the back of the phantom and the light shielding aluminum foil, which is the minimum distance that an object can have to the detector surface.

6.2.3 Monte Carlo Simulations for WET Determination

For every experimental configuration, a detailed MC simulation was set up to reproduce the geometry and materials of all elements in the beam path. These details contain the distances between beam exit, degrader (and scatterer if applicable), phantom and detector as well as the geometrical dimensions and material parameters (e.g., atomic composition, mass density, ionization potential).
These simulations are first fine tuned to reproduce the open field measurements, then compared to the further calibration measurements and in the last step used to generate the experiment-specific LUT.

6.2.4 Overview of Experimental Campaigns

In order to obtain the data necessary to investigate integration mode proton imaging, several experimental campaigns were carried out with the beam of clinical proton therapy facilities. Table 6.1 lists the respective experimental campaigns, the detector that was used, the proton beam delivery method, and the phantoms imaged.
First proof-of-feasibility experiments with the CM49 detector were conducted at the RPTC in Munich, Germany, followed by a more comprehensive set of experiments with the same detector at the Medicyc cyclotron at CAL in Nice, France. The first proton imaging experiments with the LASSENA detector were performed at the DCPT in Aarhus, Denmark. Further proton imaging experiments with the LASSENA detector were carried out at the

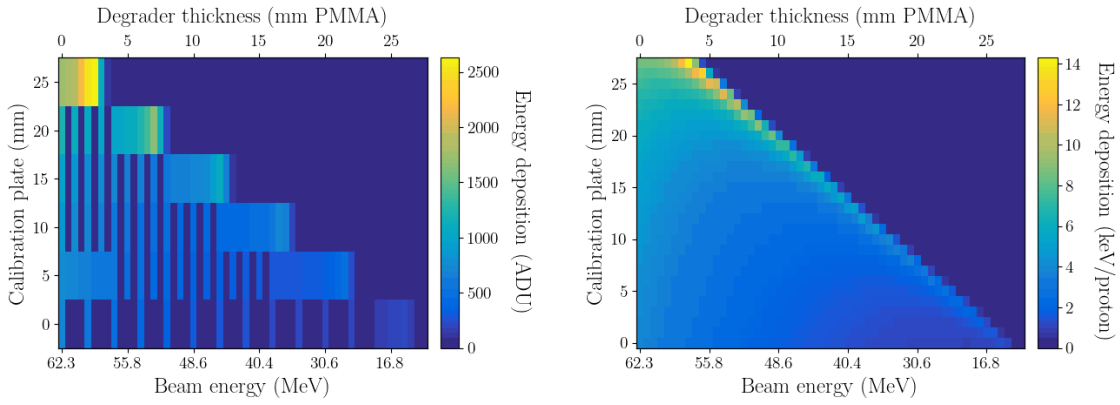

(a) **(b)**

Figure 6.6: LUTs (a) from calibration measurements with PMMA plates and (b) FLUKA MC simulations.

Medicyc cyclotron of the CAL and the first integration mode proton radiography with the pulsed beam of the synchrocyclotron was acquired at the CAL's Proteus®ONE.

Table 6.1: Overview of the experimental campaigns carried out to investigate integration mode proton imaging.

Facility (year)	Detector	Proton beam delivery mode	Objects imaged
RPTC (2019)	CM49	PBS + 35 mm PMMA as degrader and scatterer (see section 6.2.5)	µ-CT calibration phantom
Medicyc, CAL (2020)	CM49	62.3 MeV beam energy + custom degrader wheel (see section 6.2.6)	µ-CT calibration phantom Multimodal mouse phantom Plexiglas cylinder
DCPT (2021)	LASSENA	PBS + 1.5 mm tantalum scatter foil + 30 mm PMMA degrader (see section 6.2.7)	µ-CT calibration phantom Multimodal mouse phantom Mouse (post-mortem)
Medicyc, CAL (2021)	LASSENA	62.3 MeV beam energy + custom degrader wheel (2^{nd} version) (see section 6.2.8)	Step phantoms: (min.-max. thickness, step size) 2 mm-10 mm, $\Delta = 4$ mm 1 mm-4 mm, $\Delta = 1$ mm
Proteus®ONE, CAL (2021)	LASSENA	PBS + 0.5 mm tantalum scatter foil + 60 mm PMMA degrader (see section 6.2.9)	µ-CT calibration phantom

6.2.5 First Test of Feasibility of Integration Mode Proton Radiography at RPTC, 2019

Conducted measurements A radiography of the SMART µ- CT phantom (see section 4.4.1) was acquired with distance between phantom and sensor surface of 13 mm.

Setup The degrader and detector were mounted on the treatment table (see figure 6.7). The degrader consisted of two blocks of PMMA with combined thickness of 35 mm. They were placed in the treatment isocenter, thus reducing the clinical energies to the suitable energy range to image the µ-CT phantom. The RSP of the two pieces of PMMA building the degrader, referred to as *Degrader Block*, was measured to be 1.166 at the HIT (see section A.3). The optimal proton fluence for imaging would be homogeneously distributed over the FoV and the direction of protons in the beam would be parallel to each other and orthogonal to the detector surface. To fulfill these conditions as best as possible and have reduced proton fluence on the detector, the degrader and the detector were separated by a drift space of 220 cm.

To estimate the flux and the angular distribution of protons hitting the detector, a thorough MC model of the experimental setup was produced, including the geometry and materials of all elements in the proton beam path. Proton flux on the detector was estimated in MC simulations to be $9.2 \times 10^5\,\mathrm{cm}^{-2}\,\mathrm{s}^{-1}$ and the FWHM of the angular distribution of protons hitting the detector was 1.4° in x-direction and 1.6° in y-direction for a probing energy of 84 MeV initial beam energy (corresponding to 39.05 MeV on the detector).

Beam energy variation The probing energies were produced with an adapted treatment plan that contained energy layers from 76 MeV to 96 MeV in steps of 2 MeV. Beam position was set to one single raster point in the center and the beam current was adapted to be 0.12 nA at the nozzle exit for each energy layer. The probing energies were changed by automatic energy switching from the beamline system for a total irradiation time of 94 s, including switching time between the energies of 4 s. The remaining kinetic energy after the 35 mm of PMMA was calculated to range from 20 MeV to 65 MeV in MC simulations of the exact experimental setting (see section 6.2.5.1).

Calibration Due to time constraints, no separate calibration measurements were done using reference phantoms of known RSP. As replacement, the measured signal behind the baseplate of the µ-CT phantom was used for calibration. Five different circular regions (see figure 6.8a) in the baseplate part with 3 mm diameter each and separated from material interfaces in the phantom to exclude influence of scattered-in protons were evaluated and compared to MC simulations (see section 6.2.5.1).
Comparison of the $E_d(E_i)$ curves for the five different circular regions that were evaluated in the measured data showed negligible difference in peak-to-plateau ratio or distal fall-off, which is due to the homogeneous illumination of the FoV in this experiment (see figure 6.8b). The average calibration curve for the five evaluated regions is therefore assumed to be valid for the whole FoV.

Detector and settings The CM49 sensor (Teledyne Dalsa, see section 4.2.1) was used with 100 ms exposure time for each frame. During the irradiation of the treatment plan, the

Figure 6.7: Experimental setup at RPTC with a PMMA block as energy degrader on the left and the CMOS detector in its housing on the right.

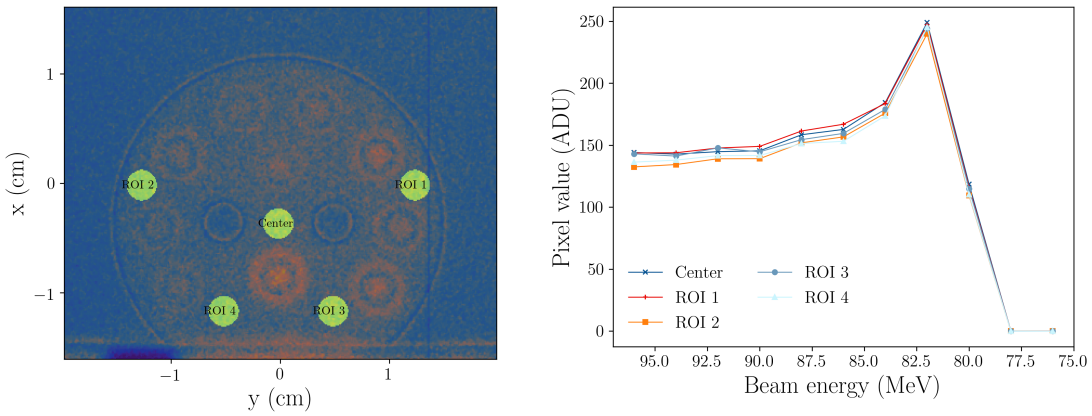

(a) **(b)**

Figure 6.8: (a) Overlay of a raw image frame from the experiment at RPTC for 96 MeV with the ROIs used for the calibration with the baseplate of the µ-CT calibration phantom. (b) Measured pixel values for the five circular regions in figure (a).

sensor was continuously acquiring frames (see figure 6.4). The frames that were recorded during the beam-off time for energy switching were used to subtract the dark current of the detector from the beam-on frames.

6.2.5.1 Simulation Model of the Experiments at RPTC

Beam source In previous thesis works at our chair, a FLUKA source model was developed for the RPTC proton beam. This model alters the beam properties for each energy and explicitly includes the elements in the nozzle such as vacuum window, Multi-strip Ionization Chamber (MSIC) and Transmission Ionization Chamber (TIC) (Englbrecht, 2014; Würl, 2014) (see figure 6.9). The calculated dose distributions from the model showed excellent agreement to measurements and calculations from the TPS (Würl et al., 2016). This simulation model was based on reference measurements in 2012 and 2014, while measurements carried out in 2019 for 75 MeV showed that there had been a shift in the mean beam energy from 75.1 MeV to 74.5 MeV at isocenter (Gerlach et al., 2020), while the energy spread remained unchanged. A FLUKA source was set up in this work, based on the existing model with adapted mean beam energies, that were obtained using the detector signal behind the baseplate of the µ-CT calibration phantom as reference, as described below.

Adjustment to open field measurement In the open field setting, there was no characteristic Bragg peak curve measured as the lowest initial beam energy of 75 MeV at the RPTC still reached the detector after passing through the degrader and the drift space. A comparison of the MC simulated and measured energy deposition as a function of probing energy $E_d(E_i)$ with the aim of adjusting the initial energy of the MC beam source was carried out using the data from the calibration measurement instead.
The 2D distribution of the proton beam over the FoV was evaluated from the open field

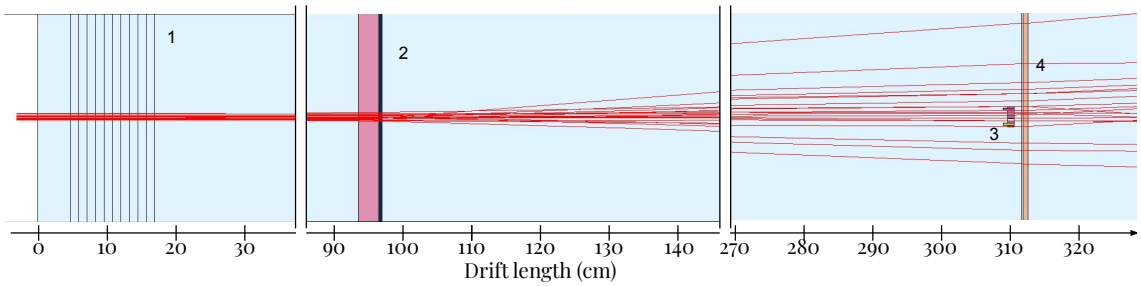

Figure 6.9: Simulation geometry of the experimental setup at RPTC including (1) the explicit modeling of the nozzle, (2) the plexiglas degrader placed in the isocenter, (3) the simulation model of the µ-CT phantom and (4) the CM49 detector. For illustration purposes the air drift spaces have been cut before and after the isocenter. The trajectories of 20 protons are shown to demonstrate the broadening of the beam from the source to the detector.

measurements. The measured and simulated beam size on the detector as standard deviation σ of a Gaussian fit to the data was large compared to the image FoV of 40 mm in x-direction and 35 mm in y-direction (see table A.3). Although the absolute difference between simulated and measured beam size on the detector was up to 9 mm (15 %), the relevant consideration for accurate WET determination is that the simulated $E_d(E_i)$ corresponds to the measurement. The difference in spot size results in less than 1 % difference between measured and simulated energy deposition in the edge of the FoV for each of the probing energies.

To generate the LUT, the energy deposition was scored in the simulated detector model in a 3D grid with lateral binning of 49.5 µm × 49.5 µm with the USRBIN card in FLUKA, which stores the accumulated energy deposition in each pixel, equivalent to an integrating detector. The thickness of the silicon layer in the simulated detector was set to 2.5 µm as a surrogate for the unknown exact design of the layers in the sensor. The simulated WET was varied from 0 mm to 30 mm in steps of 1 mm.

Comparison to calibration measurement To achieve proton energy deposition in the simulation FoV similar to the measurement behind the baseplate of the µ-CT calibration phantom, the energy deposition in the detector model after a water column of 0.994 cm was scored. The density and ionisation potential of the water column used were adapted to reflect measurement conditions at RPTC and therefore set to $\rho_w = 0.997\,\mathrm{g\,cm^{-3}}$ and $I_e = 73.5\,\mathrm{eV}$ (Englbrecht, 2014). Figure 6.10 shows the energy deposition normalized to the three first points in the plateau region for the ROIs in figure 6.8a. The difference between the simulated and measured Bragg curve was estimated assuming that the possible location of the Bragg peak x_{BP} is uniformly distributed between the measurement points for the 80 MeV and the 82 MeV probing energy, corresponding to 38.5 MeV and 35 MeV remaining kinetic energy on the detector. The variance of a continuous uniform

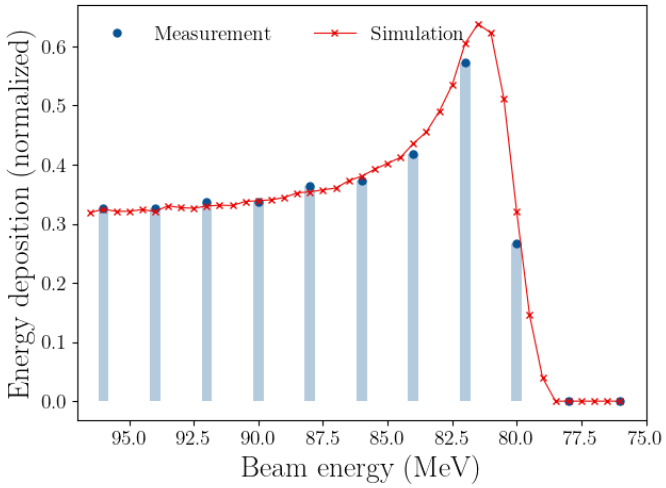

Figure 6.10: Comparison of simulated and measured energy deposition in five circular regions behind the baseplate of the µ-CT phantom.

distribution of x in the interval a to b is given by:

$$V(x) = \frac{(b-a)^2}{12} \tag{6.3}$$

$$\sigma(x) = \sqrt{\frac{(b-a)^2}{12}} \tag{6.4}$$

$$\sigma_{x_{\mathrm{BP}}} = \sqrt{\frac{(38.5-35)^2}{12}}\ \mathrm{MeV} \tag{6.5}$$

$$= 1.01\,\mathrm{MeV}\ , \tag{6.6}$$

which was used to calculate the uncertainty in kinetic energy of protons hitting the detector. In the next step, the WET t_w that yields the same energy loss as $\sigma_{x_{\mathrm{BP}}}$ is calculated from equation 6.8 (corresponding to equation 2.20 in Paganetti, 2012a) and is therefore considered the uncertainty in WET estimation:

$$t_w = \int_{E_{\mathrm{initial}}}^{E_{\mathrm{final}}} \left(\frac{\mathrm{d}E}{\mathrm{d}x}\right)^{-1} \mathrm{d}E = \int_{E_{\mathrm{initial}}}^{E_{\mathrm{final}}} \frac{\mathrm{d}E}{S(E)} \approx \frac{\Delta E}{S_{\mathrm{E,final}}} \tag{6.7}$$

$$t_w = 0.67\,\mathrm{mm}\ . \tag{6.8}$$

In this case, $\Delta E = \sigma_{x_{\mathrm{BP}}}$ and as approximation the stopping power value $S_{\mathrm{E,final}}$ for the highest of the possible kinetic energies $E_{\mathrm{final}} = 38.5\,\mathrm{MeV}$ was used to generate an upper limit of the error estimate.

The systematic uncertainty from this calibration approach is the combined uncertainty from the measured RSP (0.2%) of the baseplate material, the thickness measurement of the phantom baseplate (0.007 mm) and the difference between simulated and measured proton range of 0.67 mm. The combined systematic uncertainty in WET determination

with the MC model of the experiments at RPTC is therefore 0.67 mm or 6.7 % of the calibration WET of 9.940(7) mm.

6.2.6 Experiments with the CM49 Detector at the Medicyc Cyclotron at CAL, 2020

Conducted measurements To quantify the improvement in WET accuracy and precision through a properly performed calibration measurement, the SMART µ-CT calibration phantom was measured with 13 mm air gap to the sensor surface. Radiographies of the same phantom were also carried out for different phantom-to-detector distances and proton radiographies of the first generation multimodal mouse phantom (see section 4.4.2) were acquired. Furthermore, a plexiglas cylinder with a diameter of 20 mm was imaged with the central axis of the cylinder in vertical direction and perpendicular to the beam axis, in order to collect data to be used in the development of a method for proton scatter correction (see chapter 7).

Setup The diameter of the collimator at the beam exit at Medicyc was chosen to be 34 mm. The degrader wheel described in section 6.2.1 was installed directly afterwards (see figure 6.11a).
Between the beam exit and the detector there was a drift space of 125 cm. The resulting proton flux on the detector was estimated in MC simulations to be $4.6 \times 10^6\,\mathrm{cm}^{-2}\,\mathrm{s}^{-1}$. The FWHM of the angular distribution in the detector's FoV was estimated to be 1.8° in x-direction and 1.7° in y-direction for 16 mm degrader thickness (corresponding to 38.5 MeV beam energy on the detector).

Beam energy variation Due to the fixed beam energy of 62.3 MeV, a dedicated degrader wheel was used (see fig. 6.5a). The proton beam energy after degradation was estimated with a FLUKA MC simulation to be in the range from 5 MeV to 62 MeV (see

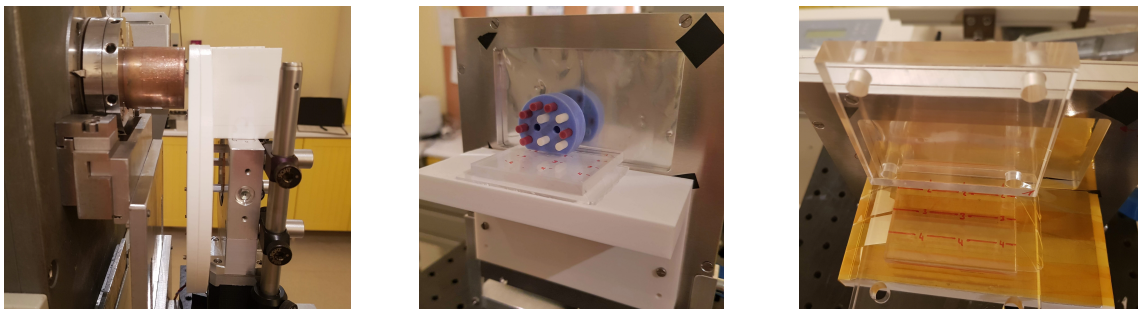

(a) (b) (c)

Figure 6.11: (a) 3D-printed degrader wheel mounted directly after the collimator at beam exit. (b) Detector and SMART µ-CT calibration phantom. The black patches block light from entering through screw holes that lie underneath. (c) Detector and 10 mm-thick PMMA slab for calibration.

section 6.2.6.1). The beam current at the beam exit was deduced to be 0.1 nA from a measurement at the stripper of the cyclotron.
To acquire the raw data for all probing energies, which is needed to generate one full radiography, the beam had to be started and stopped manually to change the configuration of the degrader wheel, which resulted in 15 min time for one radiography.

Calibration Homogeneous PMMA plates bigger than the FoV were used for a per-pixel WET calibration (see figure 6.11c). Three plates, one with a nominal thickness of 5 mm, referred to as *Calib5*, and two with 10 mm thickness, referred to as *Calib10a*, were combined to provide calibration thicknesses of 5 mm, 10 mm, 15 mm, 20 mm, and 25 mm.
The mass density ρ of the PMMA slabs was measured to be $\rho_{\text{Calib5}} = 1.190\,\text{g}\,\text{cm}^{-3}$ and $\rho_{\text{Calib10a}} = 1.188\,\text{g}\,\text{cm}^{-3}$ with a density scale (EMB-V, KERN & SOHN, Germany). The RSP of the PMMA was determined to be 1.163 for both of the Calib10a pieces and 1.165 for the Calib5 piece in measurements at the HIT (see section A.3). With this information the material can be modeled in FLUKA MC simulations. Calibration data were acquired with impinging probing energies degraded with coarser steps of 2 mm degrader wheel thickness in the plateau region of the $E_d(E_i)$-curve and with 0.5 mm steps in the Bragg peak region.

Detector and settings The CM49 sensor was used with 100 ms exposure time. For each probing energy, a fixed number of 40 image frames was acquired. A set of dark frames was acquired before and after each measurement series.

6.2.6.1 Simulation Model of the Experiments at the Medicyc Beamline

Beam source The particle source for the simulation of the Medicyc beamline was based on a phase space that was scored from a detailed simulation of the beamline geometry as described in Carnicer et al., 2012 and Carnicer et al., 2013 with the MC code MCNPX Pelowitz, 2011 (see figure 6.12). The phase space contains information on momentum, position and direction of 5.95×10^7 protons in a plane perpendicular to the beam direction at the final brass collimator at the beam exit (C4 in figure 6.12).
These protons were read in input and further transported in the FLUKA simulation with a customized source.f user routine. The beam shape at a perpendicular plane with respect to the beam axis sampled at the isocenter (7 cm behind the beam exit) was compared to measurements performed with a type N silicon diode detector (BP104F, OSRAM, Germany), as described in Carnicer et al., 2013.
A horizontal and vertical line profile, averaged over the 1 mm central part of the beam in simulation was compared to the measurement (see figure 6.13a). To reproduce the diode measurement in the MC simulation, the energy deposition was scored in a silicon block with the geometrical dimension of 2.2 mm in beam direction and lateral to the beam.

Figure 6.12: MCNPX geometry of the Medicyc beamline elements in the patient room: (1) Kapton vacuum window, (2) range shifter and modulator wheel, (3) mylar foils in the (4) two parallel-plate ionization chambers and (C1-C4) several brass collimators. With permission from (Carnicer et al., 2012).

The differences between the line profile's lateral edges in MC simulation and diode measurement are well within the deviation of 0.4 mm (see table 6.2) on either side given in Carnicer et al., 2013, who also noticed that the MC lateral slopes are slightly softer than the measurement. For MC aided calibration and evaluation of the proton imaging setup, the differences were deemed negligible as the degrader wheel and the air gap of 125 cm will smear out the edges of the beam profiles, so that on the detector only small deviations are expected between MC simulated and measured beam shape that will not detriment the WET determination (see figure 6.14).

Adjustment to open field measurement The reference open field measurements done with the degrader wheel were used to adjust the simulated beam energy to reproduce the remaining kinetic energy of the beam on the detector with the required accuracy. To generate the IDD, the sum of the energy deposition in three regions on the detector (the whole field of view, 40 × 40 pixels in the center, 40 × 40 pixels in the corner) for all thickness values of the degrader wheel was compared in simulation and measurement (see figure 6.15). A slight reduction of the initial beam energy by 0.4 MeV reached best agreement in the distal fall-off with 0.3 mm difference at 80 % of the maximum value for all three investigated regions of the image. Agreement in the distal fall-off is most relevant for reliable WET determination if the calibration measurements are supplemented by MC

Table 6.2: Beam width of the Medicyc beam: At the beam exit, this was assessed at 80 % and 10 % of the maximum from measured and simulated line profiles in x- and y-direction. On the detector, it was determined as σ of a Gaussian fit to the data (see figure 6.13).

Beam exit	x, 80%	y, 80%	x, 10%	y, 10%
Measured width (mm)	33.2	33.2	35.7	35.7
Simulated width (mm)	32.7	32.8	36.4	36.3
Detector	σ_x	σ_y		
Measured width (mm)	20.6	21.0		
Simulated width (mm)	20.5	20.8		

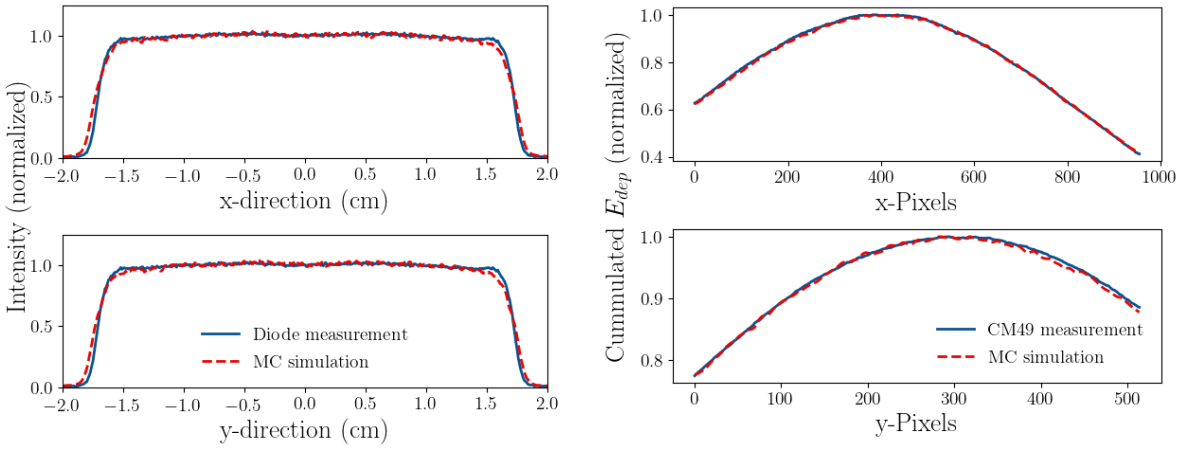

(a) **(b)**

Figure 6.13: Comparison of the MC-obtained energy deposition to measurements at the Medicyc at CAL: (a) Compared to the measured intensity by a BP104F silicon diode (OSRAM, Germany) placed at isocenter. Simulated values represent a horizontal and vertical 1 mm central line profile, all values are normalized to the average of the central 20 pixels in the plateau. (b) Compared to the 2D distribution on the CM49 detector. Shown are projections of the respective energy depositions for a degrader wheel thickness of 4 mm, normalized to the maximum value (see table 6.2).

simulations.

To reproduce the measured signal for every thickness of the degrader wheel, the exact geometry of the degrader wheel steps and the air gaps in between of 1.912(5) mm was reproduced. As in the simulation model for RPTC, the thickness of the silicon layer in the simulated detector was set to 2.5 µm.

The average point-to-point difference between MC simulated and experimental energy deposition in the three regions on the sensor surface was:

$$\Delta_{pp} = \frac{\sum_i^N (\mathrm{d}E_{measurement} - \mathrm{d}E_{simulation})}{N} = 2.4\%$$

for the $N = 56$ degrader wheel thickness values.

The difference in the distal 80 % from the maximum energy deposition is 0.03 mm in PMMA degrader thickness, corresponding to 0.035 mm WET uncertainty from the simulation model of the experiments at Medicyc. The difference in beam size was within $\Delta_{\sigma,x} = 1$ mm and $\Delta_{\sigma,y} = 2$ mm (see figure 6.13b) for all degrader thicknesses, except for the measurements close to the end of the range, where the low number of protons hitting the detector did not allow for a valid evaluation of the beam size.

Comparison to calibration measurement The calibration measurements described in section 6.2.6 were simulated and the resulting difference in proton range on the detector was evaluated to conclude on the uncertainty in WET determination (see figure 6.16a). The maximum difference between measured and simulated proton beam range was 0.11 mm

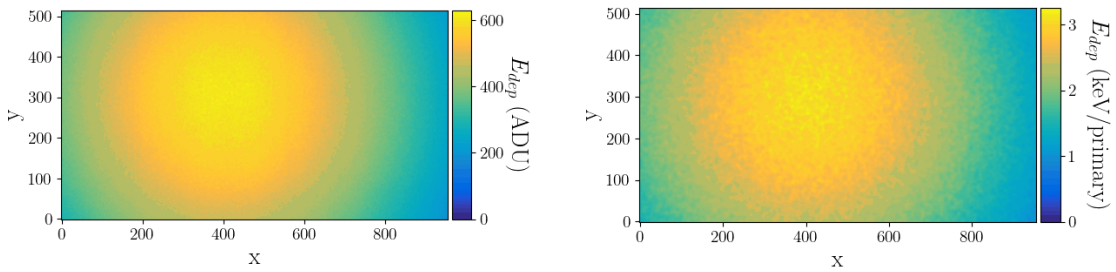

(a) **(b)**

Figure 6.14: Comparison of (a) measured and (b) MC simulated image of the beam spot on the CM49 detector after 4 mm degrader thickness at the Medicyc at CAL.

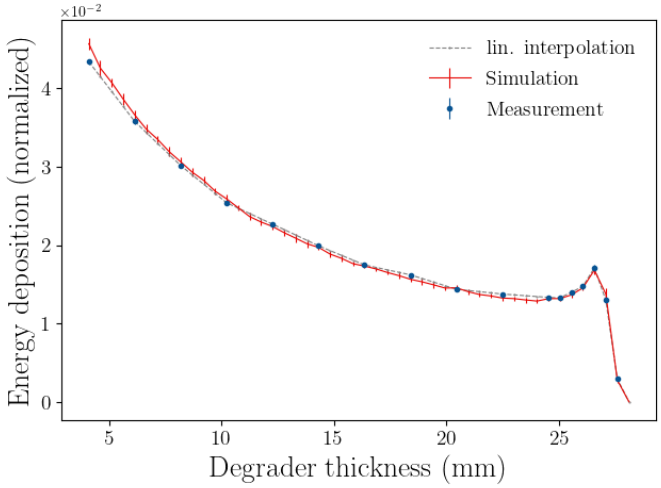

Figure 6.15: Comparison of measured and MC simulated energy deposition as a function of probing energies $E_d(E_i)$ at the Medicyc at CAL as a function of degrader thickness for the 40 × 40 pixels in the center of the beam, normalized to the sum of all values.

for all calibration measurements (see figure 6.16b), which leads to a combined WET uncertainty of 0.118 mm for the experiments at Medicyc.

6.2.7 Experiments with the LASSENA Detector at DCPT, 2021

Conducted measurements Radiographies of the µ-CT phantom at different phantom-to-detector distances were acquired to compare to data that were obtained previously at CAL. Sparse angle tomographies of the µ-CT phantom, the second generation of the multimodal mouse phantom and a dead mouse were performed (see sections 6.3.6 and 6.3.7).

Setup The experiments were conducted in the fixed beam room of DCPT. The initial spot size for the beam energies relevant to this experiments ranges from $\sigma_x = 4.5$ mm

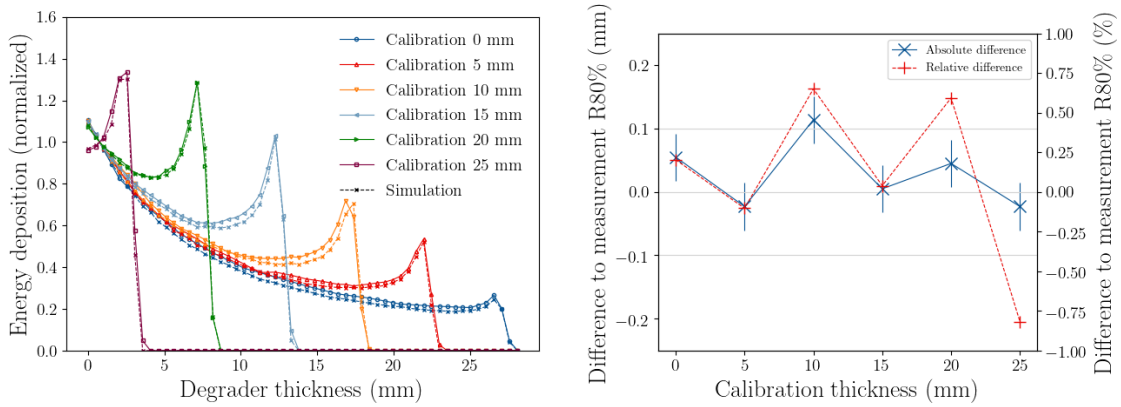

(a) **(b)**

Figure 6.16: (a) Comparison of measured and simulated energy deposition in the experiments at CAL in the FoV for the six different calibration pieces, normalized to the average of the first three measurement points. (b) Absolute and relative difference between measured and simulated 80 % range in water, the errorbars show the uncertainty propagated from the PeakFinder WET assessment of the PMMA pieces and the simulation model.

and $\sigma_y = 3.6\,\text{mm}$ at 70 MeV to $\sigma_x = 3.8\,\text{mm}$ and $\sigma_y = 3.1\,\text{mm}$ at 110 MeV. The proton beam was additionally broadened with a 1.5 mm scatter foil of tantalum placed at 39.5 cm after the beam exit. At a location set to 20 cm downstream of the scatter foil, a PMMA collimator of 50 mm length in beam direction and 8 mm diameter opening was used to select the central part of the scattered beam (see figure 6.17).

In between scatterer and collimator, a PMMA block of 30 mm thickness and 10 cm × 10 cm lateral size was placed to adapt the beam energies for the imaging of small animals and similar objects. The LASSENA detector was installed with a distance of 138.5 cm to the collimator. Proton flux on the detector was estimated in MC simulations to $2.5 \times 10^5\,\text{protons}\,\text{cm}^{-2}\,\text{s}^{-1}$ and the FWHM of the angular distribution in the

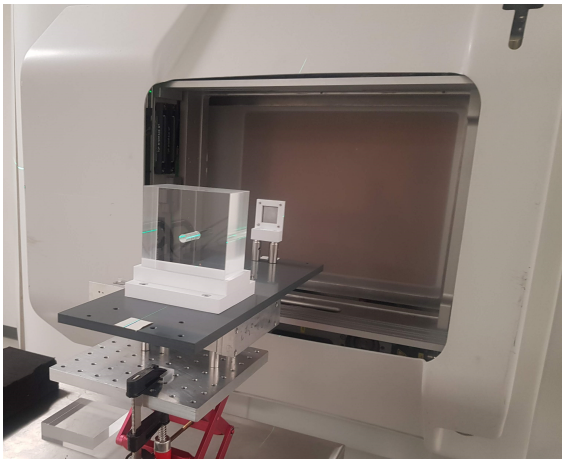

Figure 6.17: Tantalum scatter foil and PMMA collimator in front of the beam exit at DCPT.

FoV was 1.6° in x-direction and 1.3° in y-direction for 90 MeV initial beam energy (corresponding to 38.4 MeV beam energy on the detector).

Beam energy variation The probing energies were produced from a treatment plan with energies from 75 MeV to 108 MeV in 1 MeV steps. Using the PMMA block, the planned beam energies were degraded to a range from 4 MeV to 67 MeV remaining kinetic energy on the detector.
Due to issues of the beam delivery system to irradiate a low-current proton beam, the proton current at nozzle exit in the treatment plan was increased twice during the conducted experiments. The first version of the treatment plan (TP1) was used for radiographies of the µ-CT phantom and had a beam current of 0.2 nA at nozzle exit for all probing energies and was irradiated in 87 s. The second version (TP2) was used for the tomography of the same phantom and had different beam current for the energies, from 0.2 nA for 75 MeV to 0.3 nA for 108 MeV at nozzle exit and was irradiated in 50 s. The third treatment plan version (TP3) was used during imaging of the mouse phantom and the real mouse. The beam current in the third treatment plan varied from 0.2 nA for 75 MeV to 0.6 nA for 108 MeV and had an irradiation time of 44 s. For each experiment the respective beam log files were used to calculate the dose exposure.

Calibration Plates of 5 mm, 10 mm and 20 mm thickness, referred to as *Calib5*, *Calib10b*, and *Calib20*, respectively (see section A.3), were placed in front of the detector separately and also in combination to obtain measurements for 15 mm, 25 mm, 30 mm, and 35 mm thickness. Table A.2 shows the thickness, the density that was measured with a density scale (EMB-V, KERN & SOHN, Germany), and the RSP of the single plates.

Detector and settings The LASSENA detector was set to acquire image frames continuously during the irradiation of the treatment plan. The dark frames acquired before and after the irradiation sequence and during the energy switching were used for background subtraction (see section 6.1.1.2 and figure 6.4). The integration time was set depending on the beam current at the nozzle. The first treatment plan was used with 80 ms integration time, for the other two plans the integration time was reduced to 60 ms due to the higher beam current.

6.2.7.1 Simulation Model of the Experiments at DCPT

Beam source For the simulations of the experiments at the DCPT, a beam model was available that describes the protons' energy spectrum as a Gaussian distribution and the lateral spread as a spatial angular bi-Gaussian distribution 50 cm upstream of the isocenter. For each nominal energy E_{PB}, the mean beam energy E_{mean} and energy spread σ_{E} as well as the three Fermi-Eyges moments angular variance $\sigma^2_{\mathrm{x'},\mathrm{y'}}$, covariance $cov(x, x')$, and

positional variance $\sigma^2_{\mathrm{x,y}}$ are given (Trock Laegdsmand, 2020).
As the beam energy in the imaging experiments was only varied between 76 MeV and 108 MeV, the energy spread σ_E as percentage of the mean beam energy E_{mean} was calculated from a linear function

$$\sigma_{\mathrm{E}}(E_{\mathrm{PB}}) = -0.00453 E_{\mathrm{PB}} \% \,\mathrm{MeV}^{-1} + 1.49 \,\% \,, \tag{6.9}$$

as described in Trock Laegdsmand, 2020.

Adjustment to open field measurement The first element in the beam's path was the tantalum scatterer of which the WET was not known a priori. With a material thickness of 1.62 mm for the simulation model of the scatterer, the open field calibration measurement that was carried out with the LASSENA detector was reproduced in the simulation of the experimental setup with a remaining error of 0.2 % in the proton beam range as deduced from the $E_d(E_i)$ curve.
The simulated beam size on the detector was larger than the measurement for all probing energies, especially for the lower beam energies. The difference in 2D fluence distribution for consecutive probing energies translates to differences in peak-to-plateau between measured and simulated $E_d(E_i)$ (see figure 6.18), which could lead to high WET components found in the least squares optimization. But the resulting difference in energy deposition in the edge of the FoV is below 5 %, which means that wrongfully found WET components would be filtered out by the threshold applied in the algorithm (see section 6.1.1.1). Possible reasons for this discrepancy are discussed in section 6.5.1.

Comparison to calibration measurement The highest difference in the Bragg peak position in $E_d(E_i)$ between simulation and the experiments described in section 6.2.7 is 0.25 MeV, corresponding to an additional WET of 0.24 mm, which is therefore considered the systematic uncertainty for the proton images from the experiments at DCPT. Figure 6.18 shows the experimental and simulated energy deposition versus probing energy of the calibration measurements.

6.2.8 Experiments with the LASSENA Detector at the Medicyc Cyclotron at CAL, 2021

Conducted measurements Proton radiographies of a step phantom with thicknesses of 1 mm, 2 mm, 3 mm, and 4 mm were done at different phantom-to-detector distances and with additional material in front of the wafer to assess the change in spatial resolution (see section 5.2.2).

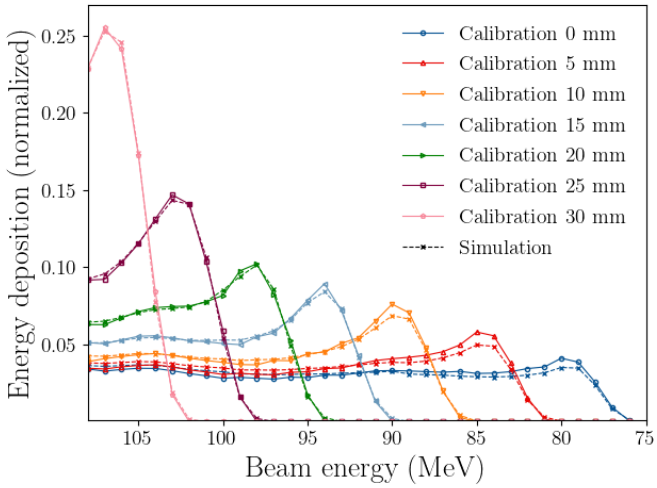

Figure 6.18: Comparison of the measured and MC simulated energy deposition as a function of probing energies $E_d(E_i)$ at DCPT in the FoV of the detector for the different PMMA calibration pieces, normalized to the sum of all energy depositions for better visibility.

Setup The setup was similar to the description in section 6.2.6. The presented degrader wheel (see section 6.2.1) was complemented by a PMMA staircase and fully motorized. The LASSENA detector was placed at a distance of 145.2 cm to the degrader wheel.

Beam energy variation Probing energies were produced with a fully motorized PMMA energy degradation system. This system consists of the previously introduced degrader wheel and a staircase of seven 4 mm thick PMMA plates, which was mounted on a motorized linear stage (see figure 6.19). The RSP of the plate material, referred to as $PMMA_{Stair}$, was determined to be 1.162 in experiments at the HIT (see section A.3).
Compared to the previous experiments at the Medicyc, this allowed to perform the measurements without entering the treatment room. Nevertheless, the beam had to be started and stopped manually. The imaging time for one radiography was 5 min to 7 min.

Calibration Three PMMA slabs of 10 mm out of the *Calib10a* (see section A.3) batch were used. The slabs were combined to have calibration measurements for 10 mm, 20 mm, and 30 mm thickness.

Detector and settings The LASSENA detector was started with each manual beam start to acquire 100 frames with 60 ms integration time.

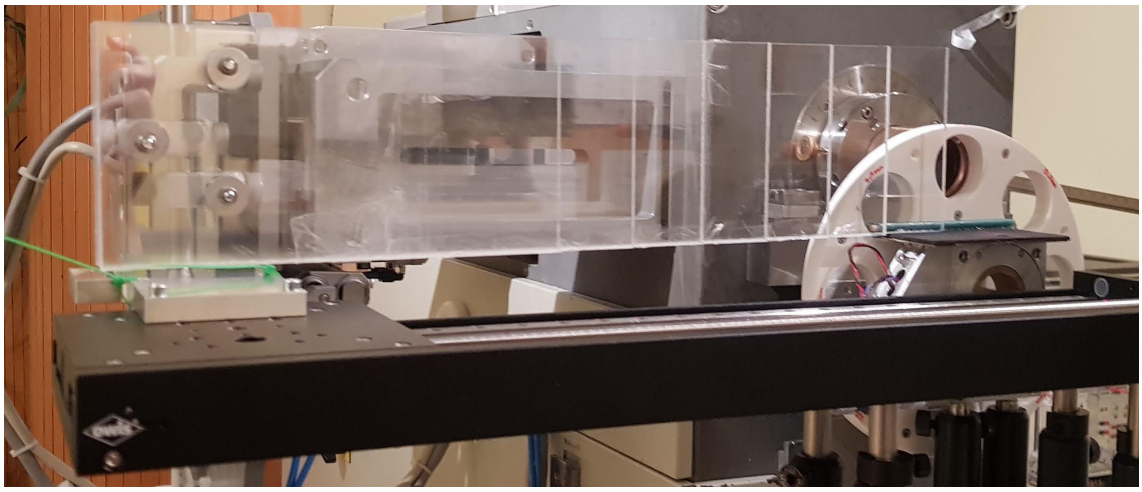

Figure 6.19: Fully automated version of the degrader wheel used at the Medicyc beamline. A linear motor moves additional PMMA plates of 4 mm in front of the rotating wheel.

6.2.9 Proof of Feasibility of Integration Mode Proton Imaging with the Beam from the Proteus®ONE

Conducted measurements The aim of this experiment was to show the feasibility of integration mode proton imaging at a synchrocyclotron, which was done through acquisition of a proton radiography of the µ-CT calibration phantom.

Setup As in the experiments at DCPT, the beam was scattered and collimated close to the nozzle. A 0.5 mm thick Tantalum scatter foil was used in combination with the PMMA collimator of 8 mm diameter. Six pieces of the *Calib10a* PMMA (see section A.3) of 10 mm thickness each were placed between scatterer and collimator to degrade the beam energies (see figure 6.20). The scatter foil was placed at isocenter. The distance from the the used scattter foil to the detector was 210.5 cm.
The FWHM of the angular distribution was 1.4° in x-direction and y-direction for 106 MeV initial beam energy (corresponding to 38.6 MeV beam energy on the detector). Due to the pulsed beam and the subsequent delivery using the so-called blind golfer algorithm (see figure 6.24 and section 4.3.2.2), the instantaneous proton flux on the detector varies by up to a factor of 10 in this experiment between the first and last of three to four bursts per beam energy layer. The instantaneous proton flux on the detector for a single pulse of the beam is not accessible due to the short pulse duration of 2.5 µs to 3.7 µs FWHM per pulse (Lehrack et al., 2017) compared to the integration time of the detector of 60 ms. The average proton flux on the detector was estimated to be 3.1×10^6 protons cm^{-2} s^{-1} from MC simulations and the number of MU irradiated. Since the beam for 106 MeV initial beam energy was detected in 5 frames, the total charge for the energy was delivered in a maximum time of 300 ms, thus implying that the instantaneous particle flux on the detector was at least 10^7 protons cm^{-2} s^{-1}.

Beam energy variation Energy variation was done with a so-called *spot list*, a sequence of spot positions and energies that is irradiated from a machine operation mode for research and Quality Assurance (QA). This list contained spots in the central position for energies from 100 MeV to 110 MeV in steps of 1 MeV and from 112 MeV to 129 MeV in steps of 2 MeV. This spot list was chosen to cover all necessary imaging energies, whilst at the same time reducing imaging dose and time. After degradation in the PMMA, these correspond to proton beam energies of 23 MeV to 78 MeV on the detector. Duration of the irradiation was 122 s.

Calibration Due to restricted access to the beam, calibration measurements were possible only for 10 mm and 30 mm PMMA thickness, conducted using three slabs of the *Calib10a* PMMA with RSP = 1.163 and with 10 mm thickness each.

Detector and settings The LASSENA detector was operated continuously during the irradiation of all probing energies, which led to the acquisition of 2000 image frames with integration time of 60 ms each.

6.2.9.1 Simulation Model of the Experiments at the Proteus®ONE

Beam source A pencil beam scanning MC simulation model of the beam at the Proteus®ONE in the Geant4-based framework GATE was available and already validated against measurements (Schnürle, 2018). The GATE beam model provides the spatial, angular and energy distribution of protons for each nominal beam energy between 100 MeV and 226 MeV.
A FLUKA source.f routine was developed that samples from this distributions to initiate the particles at a virtual source point in the nozzle, 45 cm upstream of the isocenter.
In FLUKA, the proton beam range in water for the relevant energies from 100 MeV to 120 MeV assessed in commissioning measurements was reproduced within 1 mm difference. The spot size agreement in air at isocenter in terms of σ is within 0.2 mm in x- and y-direction.

Adjustment to open field measurement The simulated beam size on the detector differed at maximum 2 mm from the measurement.
However, the lowest probing energy of 100 MeV was not stopped in the degrader, the air of the drift space or in the wafer and therefore a range agreement can not be evaluated for the open field configuration. The consistency in beam energy after the scatterer and degrader between simulation and measurement had to be verified with the calibration measurements. The RSP of the *Calib10a* PMMA of the degrader plates was assessed at HIT and the thickness of the tantalum scatter foil was adjusted and verified with the data acquired at DCPT.

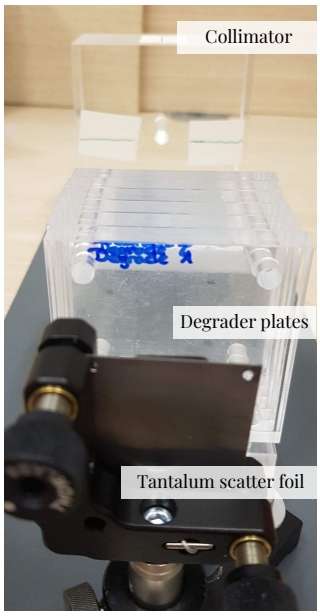

Figure 6.20: Setup in front of the beam exit to scatter, collimate and degrade the beam at the Proteus®ONE. The degrader slabs were labelled such that precise modelling of the experimental setup in MC simulations is possible.

Comparison to calibration measurement As described in section 6.2.8, calibration measurements were done for 10 mm and 30 mm thick PMMA pieces. Range difference in $E_d(E_i)$ was 0.06 MeV and 0.30 MeV for 10 mm and 30 mm, respectively. The 0.30 MeV uncertainty in $E_d(E_i)$ translates into an uncertainty in WET of 0.48 mm from the calibration.

6.3 Data Evaluation Strategies

This section classifies the investigations that were done in integration mode proton imaging with a CMOS detector, with emphasis on addressing their scientific aims and the factors that either improve or detriment WET accuracy and spatial resolution.

6.3.1 Proof of Feasibility

Scientific aim: To provide first quantitative proton radiography of a small animal sized object at a clinical proton therapy facility. Secondarily, to collect experimental data supporting the optimization of the experimental setup, the acquisition settings and routine as well as data processing.

A radiography of the µ-CT calibration phantom was acquired at RPTC with distance between phantom and detector of 13 mm. The WET was determined as described in section 6.1.1 using the calibration obtained by MC simulation of the experimental setup. The threshold in the Bragg Peak Decomposition algorithm to filter out small WET contributions was set to 15 % (see section 6.1.1.1). The selection of a 15 % threshold was derived

empirically, as it reduced the number of WET components within individual pixels to a number that was considered realistic from knowledge of the geometry of the µ-CT phantom. For consistency, this value is employed in all Bregg Peak Decompositions throughout this work, unless specified otherwise. WET accuracy was evaluated with a margin for the ROIs of 1.1 mm, to evaluate WET accuracy independent of range mixing (see section 4.5).

6.3.2 Calibration Specific to Detector Region

Scientific aim: To investigate the extent to which a calibration specific to the detector region improves accuracy in WET determination in proton radiography.

Radiographies of the µ-CT calibration phantom from the experiments at RPTC and CAL with equal phantom-to-detector distance of 13 mm were compared. In addition, the radiography acquired with the LASSENA detector at DCPT for 10 mm separation was analysed.
The difference in the method of calibration was that in the case of the radiography acquired at RPTC, only a calibration for some regions behind the phantom baseplate was available, whereas in all other experiments, calibration measurements for each pixel in the FoV were performed using pieces of PMMA with lateral size bigger than the FoV. These measurements were used to produce 4D LUTs, with a value of expected energy deposition for each probing energy, traversed WET and pixel on the detector. To assess the improvement in WET determination from such a calibration with extended targets, the achieved WET accuracy and precision of the radiographies including statistical and systematic uncertainties were compared.

6.3.3 Imaging Dose

Scientific aim: To explore the correlation between imaging dose to the phantom and WET accuracy. It is desired to reduce imaging dose as much as possible whilst maintaining the necessary level of image quality.

For the radiographies of the µ-CT calibration phantom from the experimental campaign at DCPT, different dose levels were reconstructed in post processing. This is possible either through the variation of the number of image frames averaged for each probing energy, i.e., changing the proton statistics in each image pixel (see figure 6.21a), or by changing the number of probing energies taken into account, which is altering the number of supporting points in the WET determination algorithm (see figure 6.21b).
To evaluate how the proton statistics in each pixel, which is proportional to the dose level, influences the WET accuracy, radiographies were reconstructed at pretended dose levels of 5.3 mGy, 15.9 mGy, 26.5 mGy, 31.8 mGy, 37.1 mGy, 42.4 mGy, 47.7 mGy and 53 mGy (corresponding to one to ten averaged image frames for each probing energy) for

phantom-detector separations of 0 mm and 10 mm, respectively, and including all probing energies foreseen in the treatment plan for measurement (see tables A.4 and A.5).
By changing granularity in probing energy, proton radiographies were constructed with 5.3 mGy, 2.7 mGy, 1.8 mGy and 1.4 mGy dose (corresponding to 1 MeV, 2 MeV, 3 MeV and 4 MeV between probing energies) for the data set belonging to a separation of 0 mm phantom-detector distance and using one image frame. For this configuration, also a reconstruction that averages between two, three and five frames was produced (see table A.6).
The threshold on WET components in the solution vector was set to 15 % and the margin to evaluate WET accuracy to 1 mm.

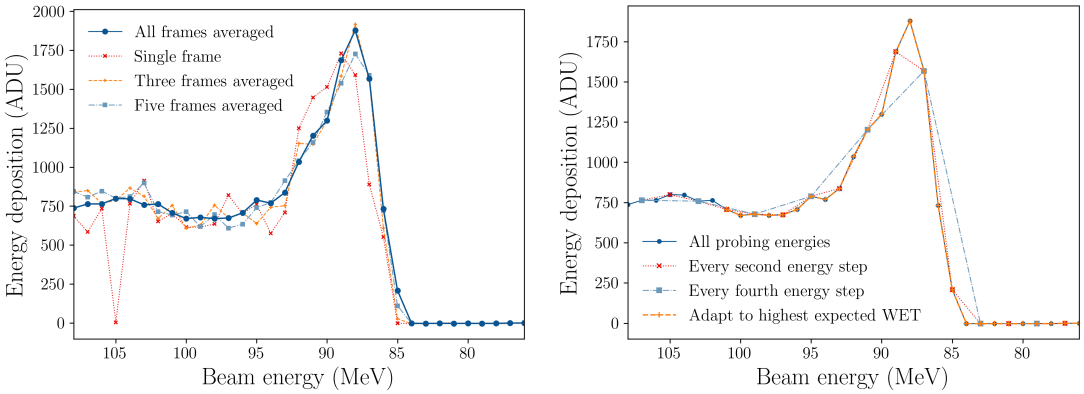

(a) **(b)**

Figure 6.21: (a) The energy deposition as a function of probing energy $E_d(E_i)$ in one pixel of the LASSENA detector behind the phantom baseplate for different numbers of imaging frames. In the curve denoted as "all frames averaged" the maximum amount of image frames is different for each probing energy, due to varying beam current. (b) The $E_d(E_i)$ for different choices of granularity in probing energy. As shown in the case of "adapted to highest expected WET" it is beneficial to estimate the expected values of WET before the imaging (e.g., from CBCT images converted to RSP) and omit unnecessarily high or low probing energies instead of choosing coarser energy steps.

6.3.4 Impact of Scattering in Correlation with Phantom-to-Detector Separation

Scientific aim: To investigate the relation between the image quality and the phantom-to-detector distance in order to determine what distances can be tolerated in the realistic case of the SIRMIO platform.

Experiments on the image quality as a function of the air gap between detector and object were done in the course of the experimental campaigns at CAL and DCPT with the SMART µ-CT phantom. At CAL, proton radiographies were acquired with phantom-detector distances of 3 mm, 13 mm and 33 mm and at DCPT with 0 mm, 10 mm, 20 mm and 30 mm, while all other parameters in each of the imaging experiments remained unchanged. Additional experiments were conducted with a PMMA step phantom with

thicknesses of 1 mm, 2 mm, 3 mm, and 4 mm at CAL. The phantom-to-detector separations were 0 mm, 5 mm, and 10 mm and the achieved spatial resolution was evaluated.
All proton radiographies of one experimental campaign were reconstructed at the same dose level (identical probing energies and number of frames) to ensure a valid quantitative comparison between the acquired images. The radiographies of the µ-CT phantom obtained at CAL were reconstructed at a dose level of 143 mGy, which corresponds to one image frame for each of the acquired 56 degrader wheel thicknesses. For the images from DCPT, the imaging dose was 53 mGy, for ten averaged frames and all probing energies. The threshold in the WET determination was set to 15 % and the margin chosen for the ROIs in the inserts to evaluate WET accuracy was 1 mm to separate the evaluation of the WET accuracy from the spatial resolution.
The combined data from both experimental campaigns allow for an overall evaluation concerning the degradation of image quality as a function of the air gap.

6.3.5 Impact of Angular Dispersion on Spatial Resolution

Scientific aim: To determine to what extent a more parallel alignment of protons hitting the FoV, quantified by the angular dispersion, benefits the spatial resolution of the conducted proton imaging experiments.

The angular dispersion of protons in the FoV of the radiographies of the µ-CT phantom perpendicular to the beam axis was estimated in the MC frameworks of the respective experimental setups. The initial beam energy and, in the case of the experiments at CAL, degrader thickness, were chosen such that the remaining kinetic proton beam energy was similar for all experimental campaigns and in the plateau region of the Bragg peak to not be in the region of high gradient of $\mathrm{d}E/\,\mathrm{d}x$. A mgdraw.f user routine (see section 4.1) was used to extract the direction cosine values of individual protons hitting the simulated detector model in the FoV that was relevant for the images of the µ-CT phantom.
A comparison was done for the radiographies with 13 mm phantom-to-detector distance available from the experiments at RPTC and CAL, and with 10 mm separation at DCPT. For WET determination, a threshold of 15 % was used in all three cases. To obtain the angular distribution, the extracted values of direction cosine were arranged into a histogram showing the proton number as a function of the direction cosine (see figure 6.30). The FWHM and the maximum occurring angle of the angular distribution is reported and related to the spatial resolution of the proton radiographies.

6.3.6 Murine and Murine-like Objects

Scientific aim: To show WET images of murine(-like) objects obtained in realistic measurement conditions of integration mode imaging in the SIRMIO-platform. Furthermore, to demonstrate the feasibility of position correction of the mouse using 2D-3D registration.

The multimodal mouse phantom of Lascaud et al., 2022 was imaged in its first version in the experiments at CAL in 2020 and in the second version at DCPT. Additionally, images of a dead mouse were acquired at DCPT in 2021.
The first version of the multimodal mouse phantom was imaged in coronal and sagittal projection with the CM49 detector (see figure 6.22).
The second generation multimodal mouse phantom and a dead mouse were mounted in different experiments on the in-house developed mouse holder[2] which is coupled to a rotation stage to enable tomographic acquisitions. In each experiment, radiographies in multiple angles were acquired (see figure 6.23b).
The distance between the imaged object and the detector was given by the dimension of the mouse holder and was therefore already corresponding to the realistic scenario of integration mode imaging in the SIRMIO platform.
The proton images of the mouse phantoms were registered to Digitally Reconstructed Radiographs (DRRs) produced from the SARRP CBCT images described in Lascaud et al., 2022. The SARRP pixel values were converted to RSP using a special calibration adapted to low-energy X-rays (Liubchenko, 2021).
For the real mouse (post-mortem), a µ-CT volumetric image of the prototype scanner at DCPT from the same day was availabe (see section 4.3.3). The voxel values of the µ-CT were not given in the usual CT number scale of HU values, and therefore the conversion to RSP was not possible. For the registration to the proton image, relative voxel values were used. For image registration, the function *phase_cross_correlation* of the *scikit-image* package (version 0.19.3)[3] was used with python in version 3.8.

(a) **(b)**

Figure 6.22: Multimodal mouse phantom (version 1) mounted in front of the CM49 detector for (a) sagittal and (b) coronal projection. The tumor surrogate in the head and neck region is visible.

[2] https://www.med.physik.uni-muenchen.de/research/3rd_party_funds/sirmio/integration/index.html, date accessed 24.04.2024
[3] https://scikit-image.org/

6.3.7 Tomography

Scientific aim: To evaluate whether tomographic image acquisition and reconstruction would be achievable in the SIRMIO platform in integration mode.

In the experimental campaign at DCPT, sparse angle tomographies of the µ-CT phantom, the second generation multimodal mouse phantom and a dead mouse were conducted with each object mounted on the mouse holder of the SIRMIO platform (see figure 6.23).

Acquisition: The µ-CT phantom and multimodal mouse phantom were imaged in 36 radiographic projections in steps of 10° (see figure 6.23).
The dead mouse was imaged in 45 radiographic projections in steps of 8° plus the coronal and sagittal views. For the tomography of the µ-CT phantom, treatment plan TP2 was used (see section 6.2.7) with a detector integration time of 80 ms. To image the multimodal mouse phantom and the dead mouse, TP3 was used with 60 ms integration time.

Reconstruction: The acquired data for each projection were first converted to a WET image using the calibration produced with the simulation model of DCPT (see section 6.2.7). For all tomographic reconstructions the implementation of Simultaneous Algebraic Reconstruction Technique (SART) (Dössel, 2016) for *python* from the *skimage.tranform.iradon_sart* was used[4].
The tomography of the µ-CT phantom was separated into the solid part and the inserts surrounded by air. Tomographic reconstructions were obtained without the use of prior information, with a ground truth first guess, and with a SARRP CBCT of the same phantom. The ground truth prior was produced from knowledge of the phantom geometry and the ground truth WET values (see section A.2). The slice thickness utilized was 2.5 mm, which was possible as the µ-CT phantom is homogeneous in the z-direction.
The tomographic image of the multimodal mouse phantom was reconstructed with slice thickness of 0.3 mm and compared to a SARRP CBCT images.
The **dead mouse** tomography was reconstructed with 0.3 mm slice thickness and the central slices in the sagittal and coronal plane were qualitatively compared to images from the prototype µ-CT scanner at DCPT.

The threshold in the Bragg Peak Decomposition was set to 15 %. A quantitative assessment of the µ-CT phantom images was conducted for a slice reconstructed utilizing the ground truth prior and another slice reconstructed employing the CBCT prior. As blurring at interfaces was considerably reduced compared to the other ex-

[4] https://scikit-image.org/docs/stable/api/skimage.transform.html

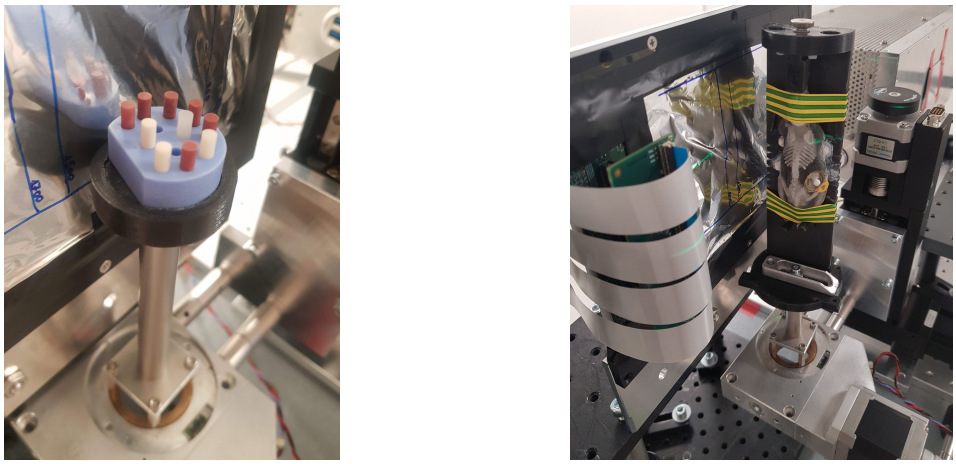

(a) **(b)**

Figure 6.23: (a) µ-CT phantom in a 3D printed holder and (b) multimodal mouse phantom (version 2) on the in-house manufactured mouse holder and a rotation stage foreseen for the SIRMIO platform, each mounted in front of the LASSENA detector for tomographic acquisitions.

periments, WET accuracy was assessed with a margin for the ROIs of 0.6 mm, with the advantage of incorporating more pixels.

6.3.8 Feasibility of Integration Mode Proton Imaging with the Pulsed Beam from a Synchrocyclotron

Scientific aim: To show the feasibility of integration mode imaging with the pulsed beam from a clinical synchrocyclotron facility.

A proton radiography of the µ-CT phantom was acquired at the synchrocyclotron Proteus®ONE system without air gap between phantom and detector.
The procedure for WET determination differed from the approach detailed in section 6.1.1.2 as each probing energy was delivered in three to four bursts (see figure 6.24). The fraction of the dose that is delivered within a burst is not known[5] and cannot be deduced from the integrated signal. Furthermore, the dose fraction in each burst will slightly differ for each radiographic acquisition, i.e., be different for the calibration measurements and the acquisition with the µ-CT phantom. Hence, the only possibility for reliable WET determination is to sum the pixel values that correspond to one probing energy. This is possible as the detector has practically no dead time.
The threshold in the Bragg Peak Decomposition was 15 %. The image was evaluated regarding WET accuracy and spatial resolution with a ROI margin of 1 mm to the insert edges. Furthermore, imaging time and dose were assessed.

[5]The so-called *spot list* for the integration mode imaging experiments was delivered in a special module of the beam control and delivery system for research and QA which does not produce log-files of the delivery.

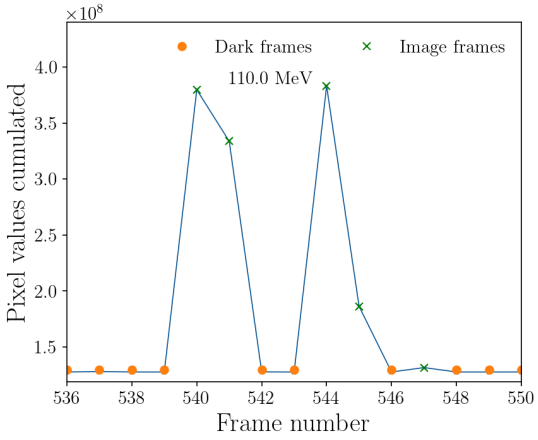

Figure 6.24: Example of intensity on detector (cumulated over the sensitive area) at the Proteus®ONE for one initial beam energy of 110 MeV that is delivered with the blind golfer algorithm in three bursts.

It was concluded whether imaging at synchrocyclotron-based facilities would be feasible with integration mode imaging in the SIRMIO platform.

6.4 Results

6.4.1 Proof of feasibility

Figure 6.25 shows the radiography acquired as proof of feasibility at RPTC with the CM49 detector. Imaging time at RPTC was 94 s for the irradiation of the pre-defined treatment plan.

The measured WET accuracy over all inserts was 0.98 % with 1.0 % statistical uncertainty and 6.7 % systematic uncertainty derived from the calibration as explained in section 6.2.5.1. The margin from the insert edge to the ROI chosen for evaluation of the WET accuracy was 1.1 mm (see section 4.5). Values for all inserts can be found in table 6.3.
The spatial resolution of the proton radiography from RPTC with a phantom-to-detector distance of 13 mm is 0.31(3) mm.
In this case the WET determination was done with one image frame for each energy step, resulting in a total imaging dose of 8 mGy.

6.4.2 Calibration Specific to Detector Region

The radiographies from all experiments could be obtained with similar WET accuracy between 1 % and 2 %. The systematic uncertainty in determination of the WET in the first experiments without pixel-specific calibration was 6.7 % (as explained in section 6.2.5.1). In the experiments that used a region-specific calibration, the systematic uncertainty was reduced to 0.6 % and 1.3 %, for CAL and DCPT, respectively.

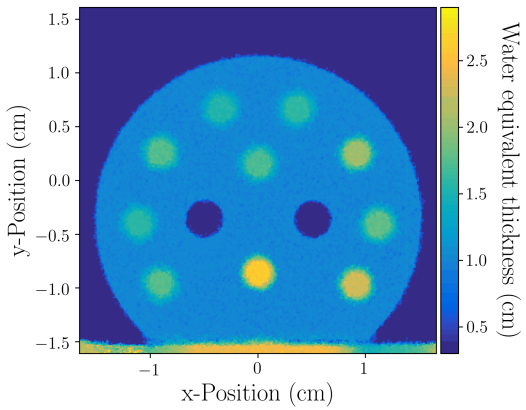

Figure 6.25: Radiography of µ-CT calibration phantom in first feasibility experiment at RPTC.

Table 6.3: WET accuracy in feasibility experiments at RPTC with 13 mm phantom-detector separation: Comparison of the experimentally determined WET WET_{exp} to the ground truth WET (see table A.1).

Insert material	Ground truth WET (cm)	WET_{exp} (cm)	Relative difference (%)	Std. deviation (cm)	Stat. uncertainty (%)
Adipose	1.51	1.54	2.11	0.01	1.43
Breast	1.55	1.59	2.22	0.01	1.13
Solid Water	1.59	1.61	0.89	0.01	0.68
Brain	1.70	1.71	0.76	0.01	1.06
Liver	1.72	1.73	0.64	0.01	1.31
Inner Bone	1.74	1.75	0.62	0.01	0.99
B200 Bone	1.76	1.78	1.55	0.01	0.85
CB2-30%	2.04	2.04	−0.09	0.01	1.04
CB2-50%	2.29	2.30	0.40	0.01	0.74
SB3 Cort. Bone	2.60	2.61	0.54	0.01	0.80
Average of absolute difference			0.98		1.00%

6.4.3 Imaging Dose

In the comparison of different proton statistics in each pixel, a WET accuracy better than 1 % with precision close to 1 % is achieved with doses of 10.6 mGy or higher for the 0 mm separation (see table A.4) and 21.2 mGy for 10 mm separation (see figure 6.26a and table A.5). This corresponds to a minimum flux requirement of 10 protons and 20 protons per pixel of 100 µm × 100 µm pixel size and detector integration period, respectively.
From the variation of the granularity in probing energy, the (1 ± 1) % accuracy level is only achieved with 1 MeV and 2 MeV increment in probing energies. Reduction of the number of probing energies by using a 2 MeV step size does not lead to dose reduction compared to a 1 MeV step size, as averaging between at least five frames is necessary for the required accuracy (see figure 6.26b and table A.6).
The optimum dose level assuring a defined WET accuracy can be found through estimation of the highest and lowest probing energy from knowledge on the imaged object and preparatory MC simulations including the experimentally used beamline. Based on the required WET accuracy and statistical precision, the irradiation charge at nozzle exit (translating to proton number in each pixel) and granularity in probing energy steps can be planned. For the considered measurements at DCPT and the (1 ± 1) % WET accuracy target, this optimized new plan would foresee probing energies from 76 MeV to 101 MeV in 1 MeV steps and an irradiated planned charge of 40 pC and 60 pC for 0 mm and 10 mm phantom-detector-distance, respectively. The imaging dose for such a hypothetical scenario would be 7.8 mGy and 11.7 mGy for each radiography.
As the presented experimental studies were research for the SIRMIO project and not routine imaging, higher proton statistics and a wider range of probing energies were used. It is discussed in 6.5.4 which adaptations are necessary to deliver the probing energies, such that only the specified dose level is deposited.

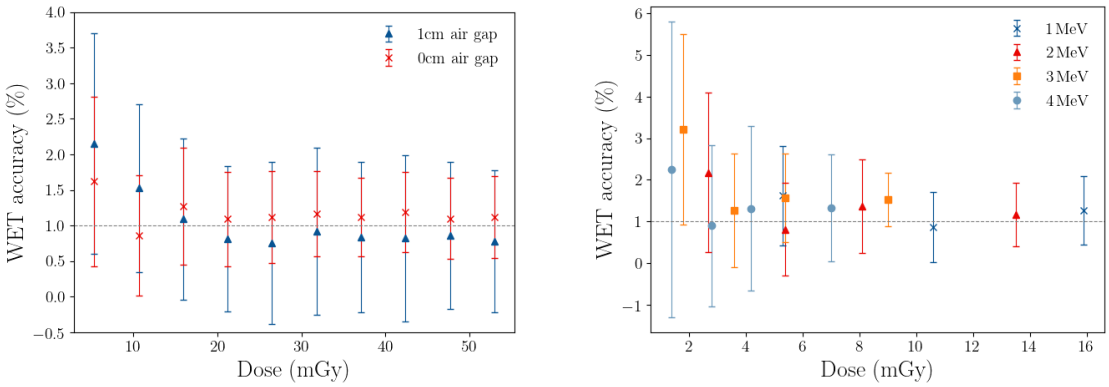

(a) **(b)**

Figure 6.26: WET accuracy and precision as a function of dose. The dose reduction is achieved by variation of (a) the number of averaged image frames for 0 mm and 10 mm phantom-detector distance (see tables A.4 and A.5 in the appendix) and (b) the granularity in probing energy steps for one, two, three and five averaged image frames. The values are tabulated in table A.6 in the appendix.

6.4.4 Impact of Scattering in Correlation with Phantom-to-Detector Separation

Figure 6.28a shows how the WET accuracy obtained in the radiographies of the µ-CT phantom at CAL and DCPT deteriorates with the phantom-to-detector distance. Figure 6.27 shows the radiographies obtained in the experimental campaign at CAL with 3 mm, 13 mm and 33 mm phantom-to-detector separation.

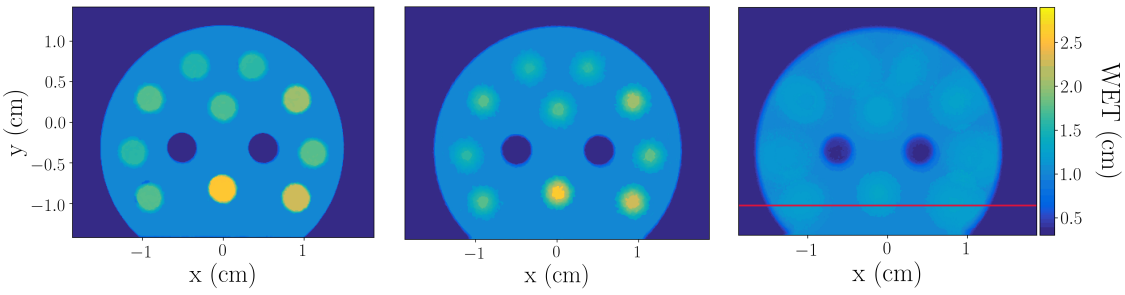

(a) **(b)** **(c)**

Figure 6.27: (a-c) WET radiographies from the experimental campaign at CAL with 3 mm, 13 mm and 33 mm phantom-to-detector distance (left to right). The red line in the plot on the right marks the position of the line profiles in fig. 6.29.

Separations of up to 13 mm allow for 1 % accuracy in this scenario with an object that represents a range of WET values similar to small animals. For larger separations, WET accuracy deteriorates to values of 14 % for 20 mm air gap and about 30 % for 30 mm and 33 mm.

Spatial resolution evaluated from the radiographies of the µ-CT phantom at CAL and DCPT (see figure 6.28b) as well as the step phantom imaged at CAL (see figure 6.28c) deteriorates with increasing phantom-to-detector distance. In addition, the blurring of

edges is increased through scattering in the phantom, which is also visible in figure 6.28c: The spatial resolution evaluated from the radiographies of the step phantom is worse, the higher the amount of traversed material is.

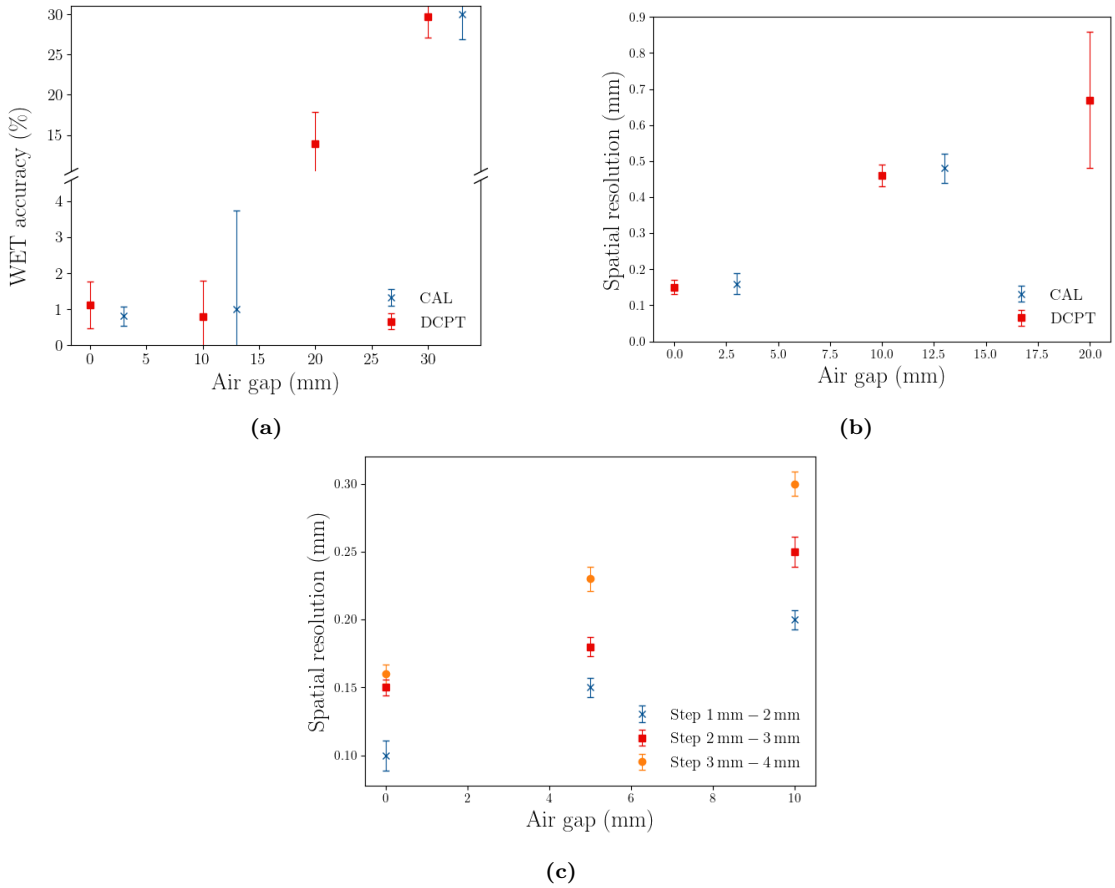

Figure 6.28: (a) WET accuracy for the evaluated phantom-detector separations between µ-CT phantom and detector from the experiments at CAL with the CM49 detector and DCPT using the LASSENA. (Note that the CM49 has a minimum distance of 3 mm between phantom and detector due to the design of the housing.) (b) Spatial resolution for the cases as described in (a). For air gaps > 30 mm the spatial resolution could not be evaluated, as the blurring over the edge is larger than the radius of the insert. (c) Spatial resolution evaluated on the step phantom with thicknesses of 1 mm, 2 mm, 3 mm, and 4 mm imaged with the LASSENA detector at CAL for varied distance to the detector.

Table 6.4 and 6.5 show the WET values and spatial resolution for the evaluated radiographies. In the radiography for the largest air gaps, the evaluation of the spatial resolution is not possible, as the blurring over the edge is larger than the insert radius of 1.75 mm.

Table 6.4: WET accuracy and spatial resolution of in the radiographies of the µ-CT phantom imaged at CAL and DCPT. The air gap is measured as the distance between the detector's pixel surface and the back of the phantom.

Experiment	Air gap (mm)	WET accuracy (%)	Spatial resolution (mm)
DCPT	0	1.1(6)	0.17(3)
CAL	3	0.8(3)	0.16(3)
DCPT	10	0.8(10)	0.47(4)
CAL	13	1.0(27)	0.48(7)
DCPT	20	13(4)	0.67(20)
DCPT	30	29(3)	n.a.
CAL	33	30(3)	n.a.

Table 6.5: Spatial resolution evaluated at the three edges of the step phantom irradiated with the CM49 at CAL. The steps in thickness were from 1 mm-2 mm, from 2 mm-3 mm, and from 3 mm-4 mm.

	Spatial res. (mm)		
Air gap (mm)	1 mm-2 mm	2 mm-3 mm	3 mm-4 mm
0	0.10(1)	0.15(1)	0.16(1)
5	0.15(1)	0.18(1)	0.23(1)
10	0.20(1)	0.25(1)	0.30(1)

Figure 6.29 shows profiles in the radiographies for the three different air gaps along a line through two cortical bone (CB-SB3 and CB-50%) and the liver tissue-equivalent insert (see line indicated in fig. 6.27 on the right and table A.1 for ground truth values).

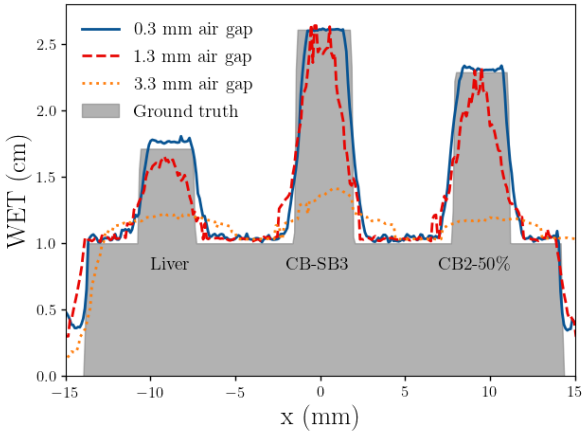

Figure 6.29: Line profiles through the liver and two cortical bone (CB-SB3 and CB-50%) inserts along with the ground truth (line position indicated in fig. 6.27) for the radiographic acquisitions obtained at CAL with the CM49 detector and with phantom-to-detector distances of 3 mm (solid line), 13 mm (dashed line), and 33 mm (dotted line).

6.4.5 Impact of Angular Dispersion on Spatial Resolution

The angular distribution of protons in the FoV of the simulated detector surface was evaluated from the direction cosine extracted from the MC simulations of the respective experimental setups (see figure 6.30). Table 6.6 shows the maximum occuring angle and FWHM of the angular distribution in the lateral directions and the spatial resolution evaluated over the edges of the µ-CT phantom in the respective direction.
The beam was almost perpendicular to the detector surface and less divergent in the experiments at RPTC as compared to CAL, where the maximum occuring angle was as well close to 90° but the width of the angular distribution was larger. In contrast, at DCPT, the FWHM was similar to RPTC, but the protons were hitting the detector under an angle.
The radiography acquired at RPTC shows less blurring at interfaces compared to the other two radiographies which is consistent with a more parallel and perpendicular illumination of the FoV. Although this sparse set of data does not allow to conclude on a function that calculates spatial resolution from the angular distribution, it provides a means to estimate boundary conditions to achieve a certain value of spatial resolution.

6.4.6 Murine and Murine-like Objects

6.4.6.1 First generation mouse phantom imaged with the CM49 detector

The WET images of the first generation multimodal mouse phantom obtained in the experimental campaign with the CM49 detector at CAL and the corresponding DRR from X-ray CBCT are shown for the coronal and the sagittal projection in figure 6.31. A 2D-3D image registration of the integration mode proton images to the volumetric CBCT was possible with 13° and 3° rotation of the xy-plane coronal and yz-plane (sagittal), respectively. It is not meaningful to give a translation value, as the images were obtained in

[6]This file is made available under the Creative Commons CCO 1.0 Universal Public Domain Dedication, https://commons.wikimedia.org/wiki/File:Direction_cosine_vector.svg (downloaded 06.10.2022)

Table 6.6: The maximum occurring angle and the FWHM of the angular distribution in x- and y-direction of protons hitting the detector FoV for the experiments conducted at RPTC, CAL and DCPT. The beam is propagated along the z-direction.

Experiment	Direction	Maximum occurrence (°)	FWHM (°)	Spatial resolution (mm)
RPTC	x	90.2	1.4	0.27(4)
	y	90.2	1.6	0.25(8)
CAL	x	89.8	1.8	0.48(4)
	y	90.1	1.7	0.47(3)
DCPT	x	90.5	1.6	0.46(3)
	y	88.2	1.3	0.45(4)

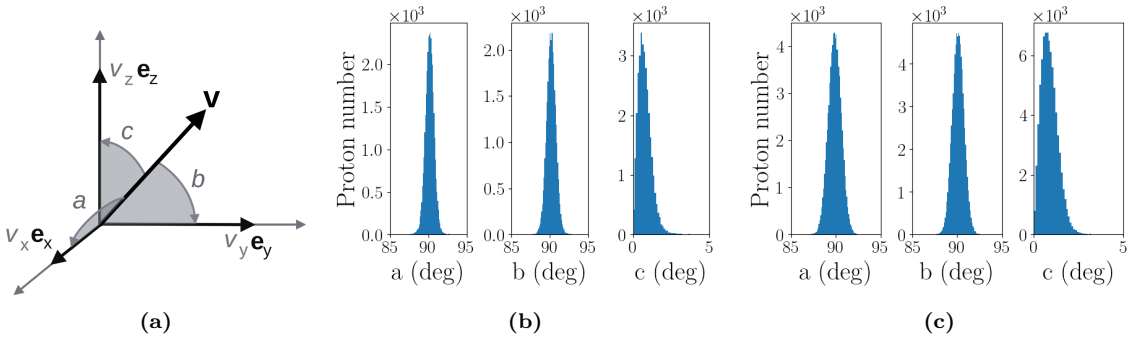

Figure 6.30: (a) Definition of direction cosines for three-dimensional Cartesian coordinates[6]. (b) Angular distribution of protons hitting the FoV evaluated in MC simulations for 1×10^6 primary particles and with 0.1° bin width in the experiments at RPTC and (c) at CAL.

different experimental setups.
A quantitative pixel-to-pixel comparison of the images was not feasible due to the considerable discrepancy in the values of the background of the DRRs and the proton radiographies, which were acquired in different experiments.

6.4.6.2 Second generation mouse phantom with LASSENA detector

The images acquired with the LASSENA detector at DCPT of the second generation multimodal mouse phantom were registered to the respective DRRs with 0° rotation in the xy-plane and 2° in the yz-plane (see figure 6.32).
As the DRRs and the proton radiographies were produced from different experimental setups and the mouse holder was only present in the acquisition of the proton radiographies, a quantitative per-pixel comparison was not possible.

6.4.6.3 Post-mortem imaged mouse

The integration mode proton images acquired with the LASSENA detector for the dead mouse are shown in figure 6.33. Image registration to the µ-CT images was feasible with 1° rotation of both, the xy-plane (coronal) and the yz-plane (sagittal). The width of the lower abdomen of the mouse exceeded 3.7 cm WET, such that for the sagittal projection even protons of the highest probing energy of 108 MeV, corresponding to 67.7 MeV after scatterer and degrader, could not pass through the mouse and no signal was received on the detector (see 0 cm WET region in the abdomen in figure 6.33d). The X-ray CT images of the mouse show three special low-density markers (Localizers Localization Markers 210, Beekley Medical, USA) that were put on the mouse holder to facilitate image registration in experiments performed by other groups.

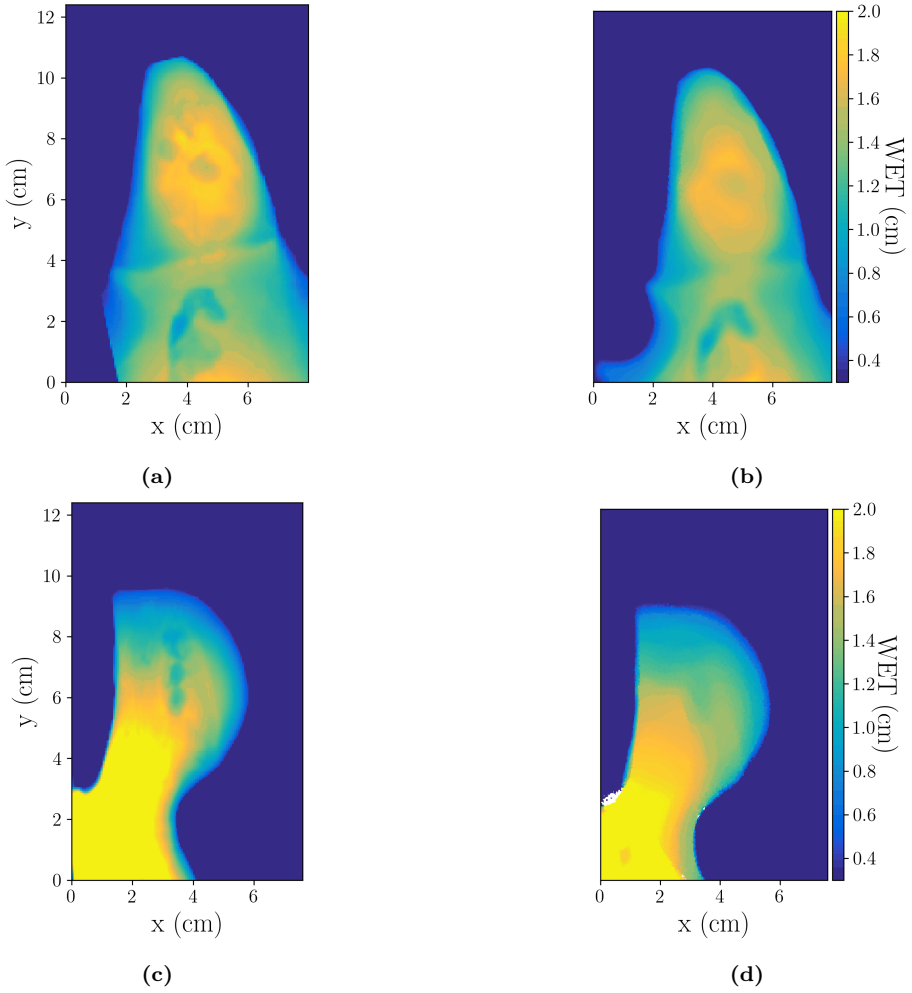

Figure 6.31: Radiographic projections of the first generation multimodal mouse phantom: Coronal (a) and sagittal (c) DRR from X-ray CBCT and corresponding (b and d, respectively) integration mode proton images acquired with the CM49 detector.

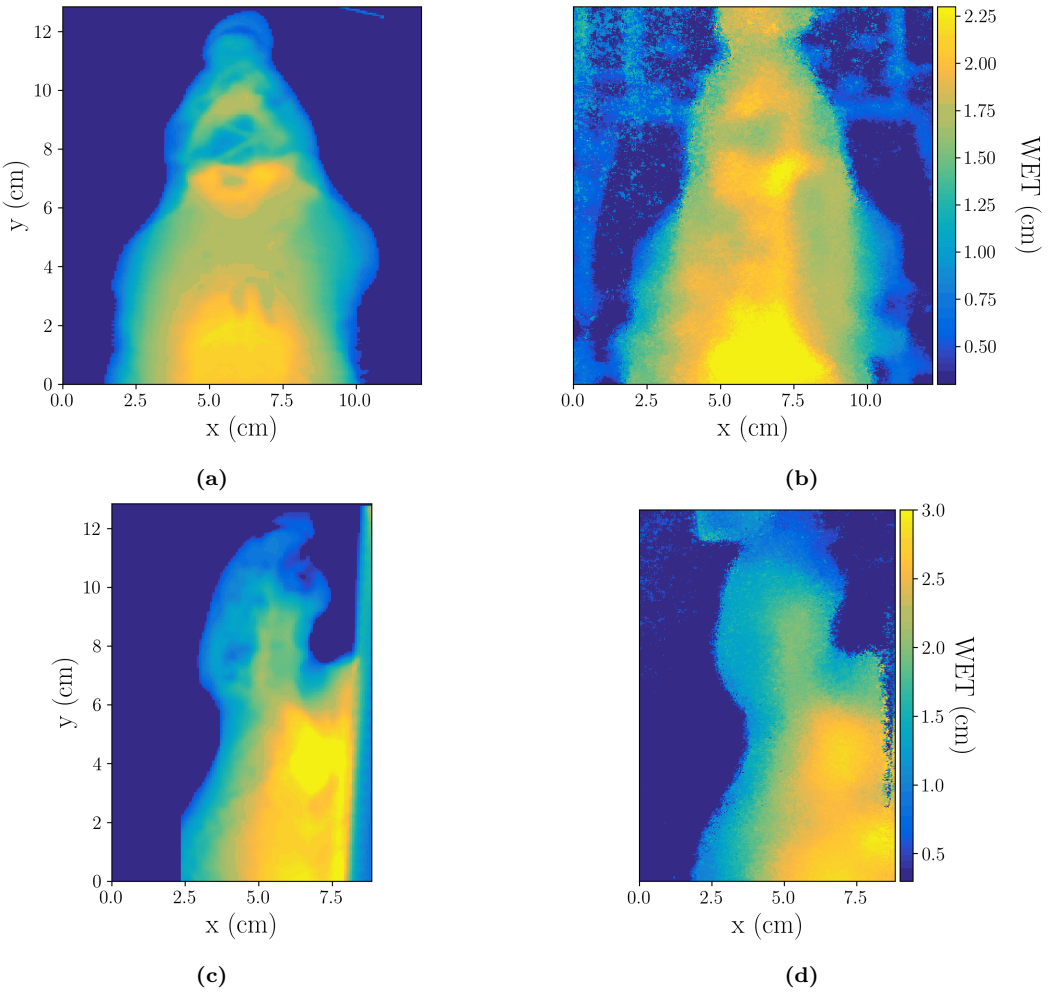

Figure 6.32: Radiographic projections of the multimodal mouse phantom in second generation: Coronal (a) and sagittal (c) DRR from X-ray CBCT and corresponding (b and d, respectively) integration mode proton images from the LASSENA detector. In image (b), the thicker parts of the mouse holder on which the phantom was mounted are visible.

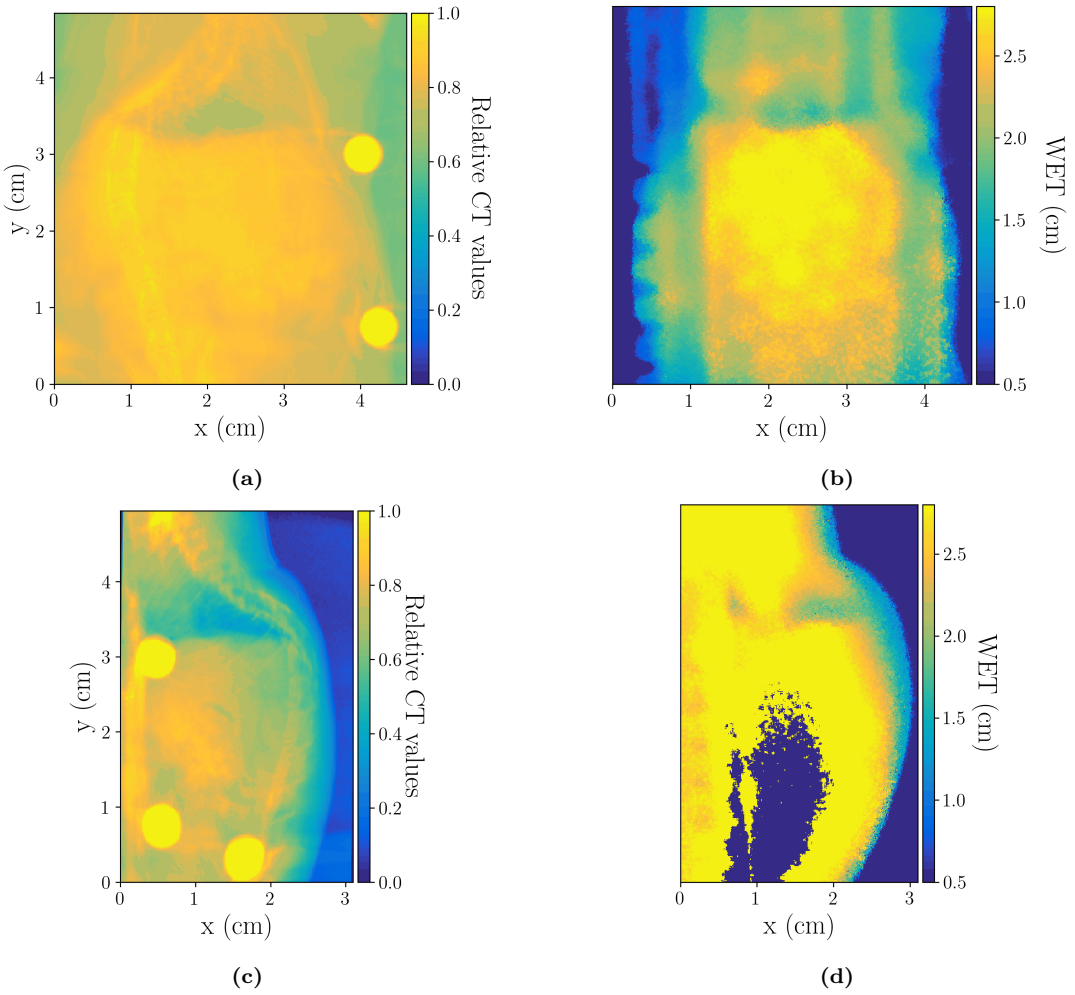

Figure 6.33: Radiographic projections of the post-mortem imaged mouse: Coronal (a) and sagittal (c) DRR from X-ray µ-CT and corresponding (b and d, respectively) integration mode proton images from the LASSENA detector. Note that for the thickest part of the mouse in the lower abdominal region, no protons are reaching the detector. In a) and c), three special low-density markers (Localizers Localization Markers 210, Beekley Medical, USA) for X-ray CT are visible.

6.4.7 Tomography

µ-CT phantom: Figure 6.34 shows the results obtained for the sparse angle tomography of the µ-CT phantom acquired at the DCPT with the LASSENA detector. The images of the baseplate part (figure 6.34e - 6.34h) show that it is not possible to achieve RSP contrast between the baseplate ($RSP_{base,\ GT} = 1.0$) and the inserts ($RSP_{adipose,\ GT} = 0.94$ to $RSP_{CB2\text{-}50\%,\ GT} = 1.43$) except for the insert with the highest RSP ($RSP_{SB3,\ GT} = 1.62$) if no prior knowledge is used.
If prior knowledge is used as first guess in the SART reconstruction, RSP contrast is achieved for all inserts. With a ground truth prior, RSP accuracy evaluated for the inserts in the baseplate deviates from an underestimation of $-20.9\,\%$ for the CB2-50% material insert to 35.3 % overestimation for the adipose tissue equivalent material (see table 6.7 for all results). With prior knowledge from CBCT, the largest underestimation is again found for the CB2-50% insert with $-24.6\,\%$ and the adipose material's RSP was overestimated by 32.9 % (see table 6.8).

Imaging time for the sparse angle tomography of the µ-CT was in total 95 min, of which 52 min (36×87 s) can be attributed to irradiation of the treatment plans (TP1, see section 6.2.7) for each radiographic projection and the remaining time was necessary for movement of the phantom as well as manual restart of the treatment plan. The calculated dose for the images that are presented is 115 mGy for each of the 36 radiographic projections, resulting in a total dose of 4.1 Gy for the sparse angle tomography.

Multimodal mouse phantom: Comparison of the sparse angle tomography of the multimodal mouse phantom to X-ray CBCT images show that qualitatively, regions with increased RSP and cavities can be identified (see figure 6.35), but the edges of anatomical structures are smeared due to MCS.
Imaging time for the tomography of the multimodal mouse phantom was 75 min, of which 26 min (36×44 s) were irradiation of the treatment plans (TP3, see section 6.2.7). The calculated dose for the images that are presented is 82 mGy for each of the 36 radiographic projections, resulting in a total dose of 3.0 Gy for the sparse angle tomography.

Post-mortem imaged mouse: The sparse angle tomography of the mouse allows to match the contours of the mouse to the µ-CT images, e.g., for positioning, and to identify sharp contrasts in RSP, e.g., for the lungs (see figure 6.36). As the mouse was thicker than expected beforehand, no protons reached the detector for the abdominal region and the Bragg Peak Decomposition reached no result, such that the WET was set to WET = 0, as is visible from comparison to the µ-CT images. Imaging time for the sparse angle tomography of the dead mouse was 74 min, of which 34 min (47×44 s) was due to irradiation of the treatment plan (TP2). The dose for the images that are presented is 82 mGy for each of the 47 projections, resulting in a total dose of 3.9 Gy.

Table 6.7: RSP obtained from the sparse angle tomography of the inserts in the baseplate of the μ-CT phantom using the ground truth RSP image as a prior information. Evaluated with 0.6 mm margin to the edge of the inserts.

Insert material	Ground truth RSP	RSP exp.	Relative difference (%)	Std. deviation
Adipose	0.943	1.28	35.3	0.06
Breast	0.973	1.28	31.6	0.04
Solid Water	1.0	1.27	26.8	0.06
Brain	1.064	1.16	8.8	0.05
Liver	1.079	1.33	23.3	0.04
Inner Bone	1.092	1.46	34.0	0.06
B200 Bone	1.10	1.24	12.9	0.09
CB2-30%	1.279	1.39	8.6	0.06
CB2-50%	1.434	1.13	−20.9	0.03
SB3 Cort. Bone	1.623	1.56	−3.8	0.06

Table 6.8: RSP obtained from the sparse angle tomography of the inserts in the baseplate of the μ-CT phantom using the CBCT as a prior information. Evaluated with 0.6 mm margin to the edge of the inserts.

Insert material	Ground truth RSP	RSP exp.	Relative difference (%)	Std. deviation
Adipose	0.943	1.25	32.9	0.07
Breast	0.973	1.20	23.7	0.04
Solid Water	1.0	1.17	16.8	0.07
Brain	1.064	1.16	8.8	0.04
Liver	1.079	1.21	12.4	0.05
Inner Bone	1.092	1.36	24.3	0.06
B200 Bone	1.10	1.16	5.2	0.05
CB2-30%	1.279	1.28	0.3	0.06
CB2-50%	1.434	1.08	−24.6	0.03
SB3 Cort. Bone	1.623	1.54	−4.9	0.07

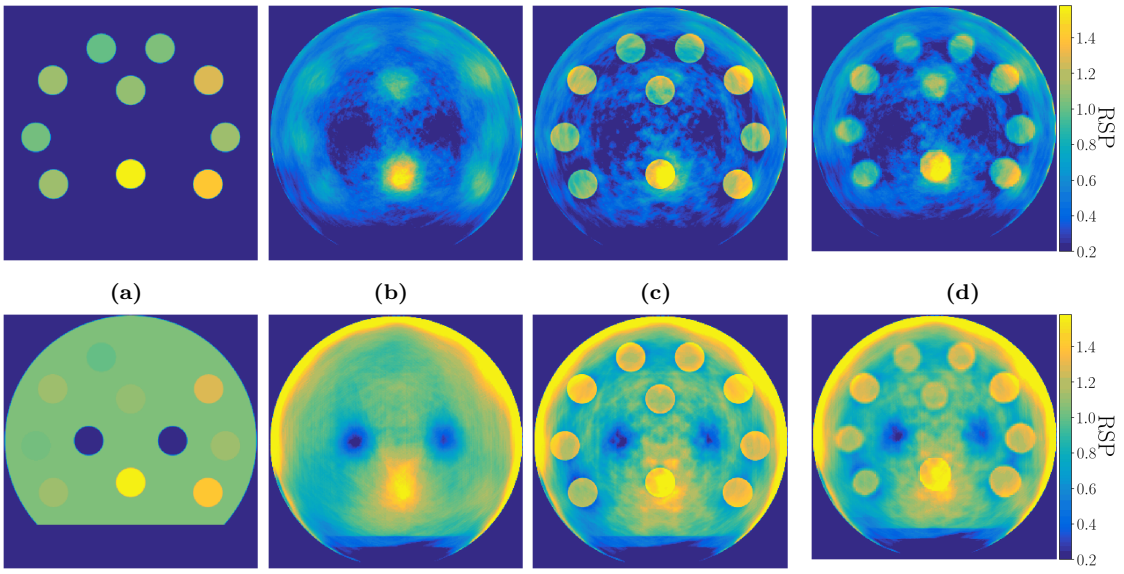

Figure 6.34: Images obtained with SART from the sparse angle tomography (36 projections with 10° separation) of the µ-CT phantom for the inserts in air and in the baseplate, respectively: (a), (e) Ground truth RSP (b), (f) results obtained without using prior information, (c), (g) results with ground truth as first guess, (d),(h) results with prior from a CBCT converted to RSP.

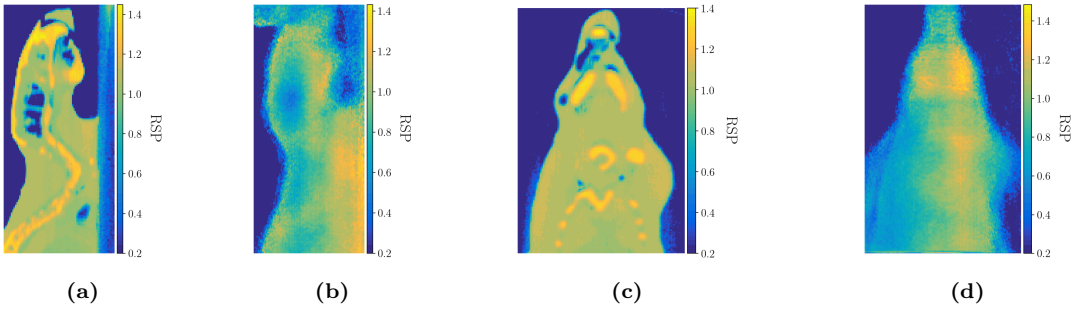

Figure 6.35: Central slices in the sagittal (a) and coronal (c) plane of the X-ray CBCT of the multimodal mouse phantom compared to the respective slices extracted from the sparse angle tomography acquired with the LASSENA detector at DCPT (b and d, respectively).

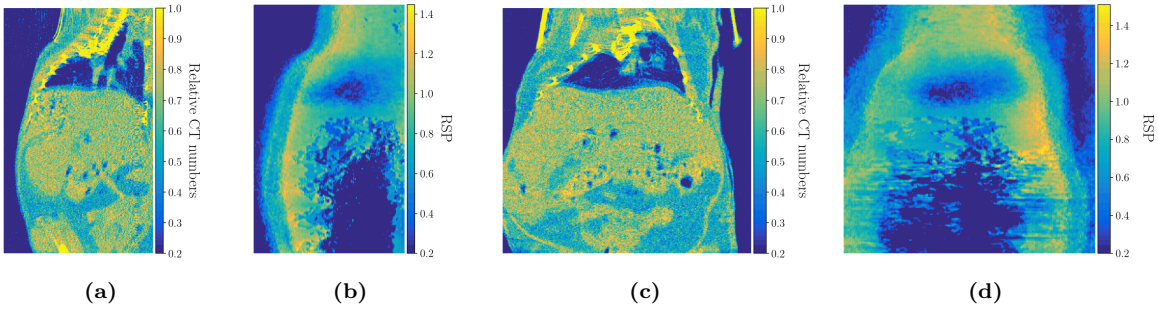

Figure 6.36: Central slices in the sagittal (a) and coronal (c) plane of the µ-CT of the real mouse compared to the respective slices extracted from the sparse angle tomography acquired with the LASSENA detector at DCPT (b and d, respectively). In the lower abdomen, the region with WET = 0 is where the mouse was wider than expected before and no signal was reaching the detector.

6.4.8 Feasibility of Integration Mode Proton Imaging with the Pulsed Beam from a Synchrocyclotron

In the proof-of-feasibility radiography at the Proteus®ONE system with the beam from the S2C2 synchrocyclotron, the WET of the ten inserts of the µ-CT phantom was measured with an average accuracy of $(1.97 \pm 0.60)\,\%$ and the spatial resolution was determined to be 0.16 mm for a phantom-detector separation of 0 mm. Imaging time was 122 s and the dose estimation obtained from MC simulation was 55 mGy.
The results indicate that the LASSENA detector is capable to operate reliably in the high instantaneous flux from the synchrocyclotron. Furthermore, the results demonstrate that WET determination using Bragg Peak Decomposition is possible in the case of a beam delivered by the blind golfer algorithm.

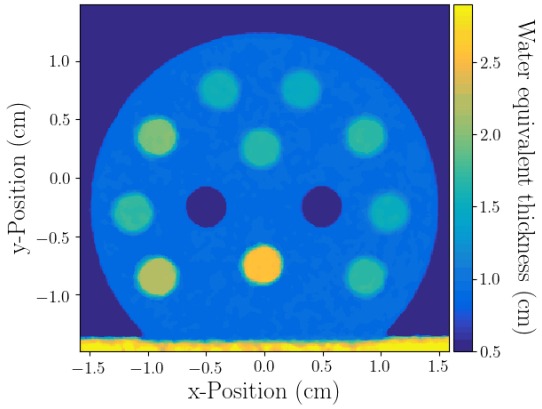

Figure 6.37: Radiography of µ-CT calibration phantom in proof-of-feasibility measurement at the Proteus®ONE.

6.5 Discussion

This discussion is structured to first provide a series of considerations, followed by suggestions for improvement where deemed appropriate.

6.5.1 Beam position instability and spot size discrepancy in experiments at DCPT

To reduce the beam current at the nozzle, an out-of-field spot at lateral position $x = 0$ and $y = 100\,\text{cm}$ with low requested charge (2 MU-4 MU) was added to each energy layer in the treatment plan that was used for energy variation. This low-MU spot forced the whole energy layer to be delivered at reduced current. This extreme position switch is supposed to be the cause of an observed instability of the beam position on the detector with a maximum deviation of 12.7 mm in x-direction and 15.7 mm in y-direction. The position shift was constant for each probing energy and was taken into account in the generation of the LUT specific to DCPT.

The reasons for the discrepancy between measured and MC simulated spot sizes for the experiments at DCPT could stem from one or more of several sources: (i) The MC beam model is based on measurements in one of the gantry treatment rooms and the true beam parameters could differ for the experimental room in which the proton imaging experiments were conducted. (ii) The scattering power of the tantalum foil assumed in FLUKA differs from the real value. Through the large separation between scatter foil and imaging detector, small dissimilarities potentially have considerable impact. (iii) The instability in the beam position at isocenter leads to a fraction of the beam selected by the collimator in the measurements that is different from the simulation. (iv) The collimator in the measurement was aligned with the laser coordinate system of the experimental room. Slight position shift and/or tilt with respect to the position indicated by the lasers could add to the discrepancies measured after the 138.5 cm of drift space.
To estimate the angular distribution of the protons with 90 MeV probing energy hitting the detector (see section 6.3.5), the simulation geometry was changed, setting an artificial radius of the collimator hole of 0.19 mm to obtain agreement in simulated and measured spot size on the detector. From the simulation as described in section 6.2.7.1 with an overestimation in spot size, the proton angle on the detector would be underestimated. This artificially adapted value would lead to worse agreement in spot size for all other probing energies and is only used for the evaluation of the angular distribution.

6.5.2 Proof of feasibility

The large systematic uncertainty in this first proof-of-principle measurements emphasizes that more precise knowledge of any object in the beam path enables to produce a more

meaningful calibration. A beam model of the RPTC that had been validated against experiments (Englbrecht, 2014) was available before the experimental campaign of this thesis, as well as the measured density of the degrader block. These pieces of information did not enable to overcome the lack of a dedicated calibration measurements. It was possible to determine the WET of the degrader block independently at HIT, but the imaging experiments could not be repeated as the RPTC stopped operation in December 2019. The experience from this first measurements led to adaptation of the experimental routine in all subsequent experimental campaigns.
The granularity in probing energy of 2 MeV was in the reasonable range for imaging of the µ-CT phantom, as is shown by the statistical uncertainty of 1 %, but was too coarse to enable a more precise calibration (see figure 6.10).

6.5.3 Calibration Specific to Detector Region

In general, a spatially independent calibration with the same two-dimensional LUT used in each image pixel can achieve satisfactory results, if the illumination of the FoV is homogeneous and (near-)parallel. Another possibility to work with a two-dimensional LUT would be to use information on the fluence distribution in the FoV for each probing energy in order to do a flat field correction for all acquired images. In the case of the acquired experimental data, such a correction has shown to be extremely error-prone, as the intended low-current irradiation of the FoV also leads to a) fluctuations in the proton statistics between neighboring pixels, and b) many pixels without signal, especially in the corners.
The reproduction of the beam shape and size on the detector was not only beneficial to obtain a spatially resolved LUT, but also necessary for each individual experimental setup to produce valid estimations of the imaging dose and proton flux in the FoV.
For DCPT, a region-specific calibration was essential for precise WET retrieval through the instability in the beam position.

6.5.3.1 Possible Improvements

In the calibration procedure foreseen for the final version of the SIRMIO platform, a pixel-specific calibration $E_d(E_i)$ curve is acquired for several WET values from a motorized step phantom made out of PMMA. For future applications in small animal radiography and tomography, variable water columns similar to the setup proposed by Selzner, 2021 with low material budget entry window might provide an accurate and time-efficient calibration procedure.

6.5.4 Imaging Dose

As mentioned in section 6.4.3, certain prerequisites need to be met to achieve the mentioned lowest dose in each experiment:

- The setup must be modified to deliver a short burst ($\mathcal{O}\left(100\,\mathrm{ms}\right)$) of a low current ($\mathcal{O}\left(0.1\,\mathrm{nA}\right)$) beam for all probing energies. Therefore the particle current needs to be reduced below the clinically used value of a few nA. This can be implemented either from the beamline by using an irradiation mode foreseen for QA and experiments along with designing a treatment plan with a low MU spot or after the beamline through scattering and collimation. The first option is favorable with regards to minimizing the stray dose that will be deposited in the surrounding equipment, possibly including sensitive electronic parts. Since the presented experiments were conducted only once, the treatment plans were calculated with additional MU per spot to ensure sufficient statistics for the WET determination.

- In general, a dose reduction can be achieved by optimizing the probing energies used and proton charge irradiated, e.g., with MC simulations, based on knowledge of the expected range of WET values of the object, e.g., retrieved from a CBCT of the object.

- The lowest detector integration time should be used for the sake of averaging the signal for one pixel over a few frames. If the LASSENA detector is running continuously, the dead time is around 10 µs per frame and negligible in comparison to the integration time of as low as 30 ms for a full frame (Sedgwick et al., 2013).

6.5.4.1 Possible Improvements

If the CMOS detector is triggered from an external signal, the irradiation system could be actively turned off as soon as a sufficient amount of data is collected. Furthermore, the beam could be turned off if the beam does not reach the detector, e.g., if the probing energy is too low to traverse the object, thereby avoiding unnecessary dose from low probing energies employed. In future implementations of the imaging setup within the SIRMIO system, the beam could also actively be switched off from the IC that is installed at the exit of the beamline box. Consequently, the fluence on the LASSENA pixels for each probing energy would be precisely controlled, resulting in lower dose to the imaged object.

6.5.5 Impact of Scattering in Correlation with Phantom-to-Detector Separation

Multiple Coulomb scattering of particles in the object and air around is the reason for worse performance of integration mode particle imaging systems in comparison to single

particle tracking setups (Meyer, 2019; Gianoli et al., 2019; Krah et al., 2015). The acceptable average lateral deflection is also depending on the pixel size and the aspired spatial resolution of the reconstructed WET image.
The experiments using the µ-CT phantom did reveal the problems that arise if small structures in a heterogeneous object should be imaged when the phantom-to-detector distance is large.
The objective for the design of the imaging setup is to mount the object such that it is as close as possible to the detector, e.g., using a motorized stage that moves along the beam axis.

6.5.5.1 Possible Improvements

As explained in section 7, the detrimental effect of proton scattering on image quality can be reduced through scatter correction methods with prior information from another imaging modality or without prior information. Several concepts for proton scatter correction are introduced in this work and presented as well as discussed in chapter 7.

6.5.6 Impact of Angular Dispersion on Spatial Resolution

If the SIRMIO platform is switched into integration mode imaging configuration, the variable energy degrader made out of boron carbide is exploited to degrade and broaden the initial beam.[7] This setup generates a low divergence and perpendicular illumination of the FoV. Through the low angular dispersion of the protons hitting the phantom, average lateral scattering angles are reduced and thereby spatial resolution might be improved as compared to the preparatory studies presented in this work.
If incoming beam angles and initial beam divergence are precisely known before the experiments, this information can be implemented into the models used for scatter correction.

6.5.7 Murine and Murine-like Objects

The possibility for position correction through 2D-3D registration of a µ-(CB)CT image of a mouse with proton radiographies acquired in integration mode proton imaging with a simulated CMOS detector model was shown in a MC study (Schnürle et al., 2019).
The imaging experiments with the mouse phantoms and the post-mortem imaged mouse have shown feasibility of 2D-3D registration to X-ray CBCT images.

[7] The experiments presented in this work were carried out using prototype proton imaging setups, not including the beamline box containing the final set of beam shaping and degrading elements of the SIRMIO platform (see section 1.1).

6.5.7.1 Possible Improvements

1. The 3D images from CBCT or µ-CT should be in HU values or a procedure to obtain a reasonable estimate in the correct range of HU should be developed and validated such that the image can be converted to RSP in order to facilitate the registration process to WET.

2. The murine specimen or phantom should be mounted for the 3D image as for the irradiation to simplify the registration procedure.

3. Palaniappan et al., 2023 demonstrate that with DIR it is possible to quantify and compensate for anatomical changes in the case of small animal imaging with a realistic detector model.

6.5.8 Tomography

Sparse angle tomography using SART showed the contours of the phantoms and the mouse, but lacked sufficient RSP accuracy to be used in treatment planning. More robust approaches to obtain treatment planning images are volumetric images from small-animal X-ray CBCT and µ-CT converted to RSP or direct RSP assessment from single particle tracking pCT.
The tomographic images also show the loss in spatial resolution from proton scattering in the object. Increasing the number of tomographic projections is expected to improve image quality and compensate part of the noise in single radiographies. Also improvements in the radiographic domain, e.g., through scatter correction are expected to improve spatial resolution in the tomographic domain.
The imaging dose of more than 3.0 Gy for 36 projections in the presented experiments is similar to the dose of a treatment fraction and therefore considered too high for imaging. While acknowledging the need for minimal dose exposure, it must be emphasized that the conducted first experiments were not specifically optimized to this purpose.

6.5.9 Feasibility of Integration Mode Proton Imaging with the Pulsed Beam from a Synchrocyclotron

The presented results of the integration mode proton image acquired at the Proteus®ONE system are encouraging in terms of WET accuracy and spatial resolution. Due to the irradiation of the probing energies by the blind golfer algorithm, i.e., in three to four bursts, the detector signal for these bursts was added up resulting in $E_d(E_i)$ curves similar to the calibration measurements, thereby allowing reliable WET determination.
Imaging time can be significantly reduced if the sequence of probing energies is adapted to the energy switching time of the machine. In the case of the Proteus®ONE, a prescription (i.e., the *spot list*) should be written such that irradiation is executed starting from the highest probing energy. The presented experiments were not optimized for imaging time

and the probing energies were irradiated from lowest to highest.

6.5.9.1 Possible Improvements

It remains to be investigated if the blind golfer algorithm for irradiation can be bypassed in a special mode for QA and experiments.

6.5.10 Imaging Time

Differences in imaging time are mainly introduced from the beam delivery systems at the respective proton therapy facilities.
Imaging times for radiographies at lowest possible dose in each experiment were compared. The crucial difference in the radiography experimental routine influencing the imaging time was in the variation of the probing energy: In experiments where only one fixed beam energy is provided by the facility, a self-built mechanism was needed to degrade the beam to the required energies. Energy switching time is therefore either dependent on the energy switching system of the facility or the motor stages in the degrader wheel.
In addition, the computing time for WET determination is evaluated, under the assumption that a pre-calculated LUT for the experimental setup is available.

As shown in table 6.9, the imaging time of maximum 2 min from a treatment plan irradiation using the beamline's energy switching was always lower than the time needed to switch probing energies with self-built systems. Without further development, energy switching from the beamline is the only option that makes radiography in several projections of a living small animal possible in an acceptable timeframe.

Computation time for the WET determination of a radiography with 300 pixels × 400 pixels is 90 s.

During the development of the prototype integration mode imaging system for SIRMIO, optimization of the imaging time was not prioritized. In future developments, reduction of

Table 6.9: Mode of beam energy switching and imaging time for one radiography in the different experiments.

Experiment	Mode of energy switching	Imaging time
RPTC	Beamline energy switching	94 s
Medicyc 2020	Partly automated degrader wheel	15 min
DCPT	Beamline energy switching	87 s
Medicyc 2021	Automated degrader wheel	5 min
Proteus®ONE	Beamline energy switching	122 s

the imaging time can be achieved. The imaging time is limited by the maximum amount of time that the murine specimen can be under anaesthesia (estimated up to 60 min in total including irradiation[8]) subtracted by the duration that is needed for the delivery of the therapeutic proton irradiation.
The imaging time of 94 s at RPTC was dominated by the 4 s needed for each of the 18 energy switches. Newer facilities are considerably faster than the first ProBeam® proton therapy system (Varian Medical Systems, Inc., Palo Alto, California) that was installed at RPTC.
The degrader wheels employed to change probing energies were helpful tools for the research phase for the SIRMIO project and were also used in other experiments in combination with an optical detector to measure the range of protons.
The times shown in table 6.9 are from experiments in the research phase for SIRMIO and realistic times will be lower, as the irradiated charge will be limited to the amount necessary for sufficient imaging quality.

6.5.10.1 Possible Improvements

In addition to the use of the beamline's energy switching mechanism, the irradiation plan used for imaging can be optimized to reduce the imaging time. As a realistic scenario, the proposed optimized treatment plans for experiments at DCPT with 7.8 mGy and 11.7 mGy (see section 6.4.3) for a radiography at 0 mm and 10 mm phantom-detector-distance correspond to imaging times of 27 s and 29 s imaging time, respectively.

[8] Non-published communication by Prof. Dr. Lauber, LMU

6.6 Conclusion

Integration mode radiography allows for proton imaging at high (instantaneous) flux as it is the case at synchrocyclotron facilities. In the presented setup for the SIRMIO platform with a CMOS detector and energy variation, radiographic imaging can be achieved for small animals or similar objects in realistic experimental conditions.
Aaccurate WET retrieval with 1% accuracy and sub-millimeter spatial resolution is possible, if the air gap between object and detector is limited and careful calibration is performed.
WET accuracy better than 1% with precision close to 1% was obtained in the experimental campaigns with estimated dose levels of 10.6 mGy and 21.2 mGy for 0 mm and 10 mm phantom-to-detector separation, respectively in an imaging time of about 90 s. A proposed optimized irradiation scheme for the same object, based on the experience gathered in the course of this work, predicts a dose level of 7.8 mGy and 11.7 mGy for 0 mm and 10 mm phantom-detector distance, respectively, in 30 s imaging time.

The most relevant factors in the experimental implementation are the minimization of the distance between object and detector to reduce blurring through MCS of protons in the object, and the homogeneous illumination of the FoV with a (near-)parallel beam to ensure sufficient proton statistics in each pixel while at the same time limiting the dose exposure. If these conditions are only partially met, imaging in integration mode remains challenging, as individual particles that have been scattered at large angles can not be excluded from the measurements.

The compact setup and ease of operation enable imaging at various proton therapy facilities and in different beam delivery modes.

Tomography in integration mode with energy variation is possible with limited performance, besides being unreasonable for a living specimen regarding imaging dose and acquisition time.

CHAPTER 7

Scatter Correction Methods for Integration Mode Particle Imaging

Computational methods can be used in manifold ways to improve medical images. For proton imaging in integration mode, proton scattering has considerable impact on image quality. In the course of this work, different methods were investigated, to determine how the measured pixel information can be used in combination with data from MC simulations for proton scatter correction.

Image quality in integration mode proton imaging is strongly affected by MCS. Prior information, e.g., from CBCT images, can be employed to improve proton radiographies. A particular possibility of removing signal from scattered-in protons from pixels arises for the imaging approach used within this work of achieving WET contrast by energy stacking. The measured images for each of the single probing energies can be exploited to remove scattered-in WET components based on an inverse, analytical approach.

Proton images For the investigations regarding scatter correction, the proton images of the SMART µ-CT phantom (see section 4.4.1) acquired at CAL using the CM49 detector with phantom-to-detector distances of 13 mm and 33 mm (see section 6.2.6) were used. In addition, the method of scatter correction with a regularized LUT was used to improve images of a plexiglas cylinder with 20 mm diameter and the first generation multimodal mouse phantom acquired in the same experimental campaign.

7.1 Methods for Scatter Correction

In this chapter, a concept for scatter correction based on prior information and regularization will be presented firstly. Secondly, an analytical method for scatter correction without prior information is outlined.

7.1.1 Scatter Correction by Regularization of the LUT

The general idea of this regularization approach is to determine the WET in a similar manner as presented in section 6.1.1, but to alter the LUT with information from a priori imaging or MC simulations to make the linear least-squares solver assign more weight to WET components that are more likely to be present, according to the prior image.

7.1.1.1 Prior Information

Two different prior WET images were created to support the scatter correction algorithm: An ideal prior based on the RSP and geometrical measurements of the phantom that were used to define the ground truth WET (see table A.1), and a realistic case on the basis of CBCT imaging where the ground truth geometry is not known.
In the former realistic case, the prior information was obtained from a CBCT image of the µ-CT phantom acquired with the SARRP at 60 kVp tube voltage and 0.26 mm pixel size, that was adapted to the 99 µm pixel size of the CM49 measurement, using the function *resize* from the python implementation of *OpenCV*[1]. The SARRP pixel values were converted to RSP using a special calibration adapted to low energy X-rays (Liubchenko, 2021). The RSP from the CBCT image was integrated along the beam direction in the proton imaging experiments to achieve a prior image in terms of WET.
Both prior images were registered to the measured proton radiographies.
As an option for the condition that no prior information is available, the regularization approach was finally also tested with a radiography obtained via a Bragg Peak Decomposition that uses a non-regularized LUT as first guess.

7.1.1.2 Modification of the WET determination algorithm

To include the prior information into the WET determination, the employed LUT was modified such that the least-squares minimization in a given pixel favours WET values close to the prior, whilst keeping enough flexibility to find a different solution, in case the measured signal is different from the WET components suggested by the prior.
In practice, this means including a penalty in the LUT depending on which WET components are less likely to be giving rise to the signal in a given pixel $\vec{b}$, so that the altered

[1] https://docs.opencv.org/4.x/index.html

LUT A' multiplied by solution $\vec{x}$ reproduces the detector signal $\vec{b}$:

$$A'\vec{x} = \vec{b} \ . \tag{7.1}$$

To account for uncertainties in the pixel values of the prior information and remaining position uncertainty after image registration, the penalty function was chosen to be in the form of a Gaussian function

$$G(x, a, x_0, \sigma) = a \cdot e^{\frac{-(x-x_0)^2}{2\sigma^2}} \ , \tag{7.2}$$

which is then used to construct a Gaussian window $G_w(\mathrm{WET})$ around the predicted component $\mathrm{WET_p}$, with s as a user-definable factor to give the algorithm more or less flexibility to take into account WET components around the prior, i.e., to adjust the width of the Gaussian window (see figure 7.1)

$$G_w(\mathrm{WET}, a, \mathrm{WET_p}, s \cdot \mathrm{WET_p}) \ . \tag{7.3}$$

The width of the window scales linearly with the expected WET component $\mathrm{WET_p}$ as larger mean scattering angles of the protons are expected on the detector after passing trough higher thickness of the object.
As the penalty should suppress components outside of this window, $a = 1$ and the LUT entries for one constant value of WET (i.e., row in the LUT) are multiplied by

$$p(\mathrm{WET}) = 1 - G_w(\mathrm{WET}) \ . \tag{7.4}$$

The LUT entries with WET close to $\mathrm{WET_p}$ are therefore multiplied by a value close to zero (see figure 7.2), which will lead to a higher relative weight in the solution vector $\vec{x}$ assigned to these components in the linear signal decomposition than the penalized ones (see figure 7.3).

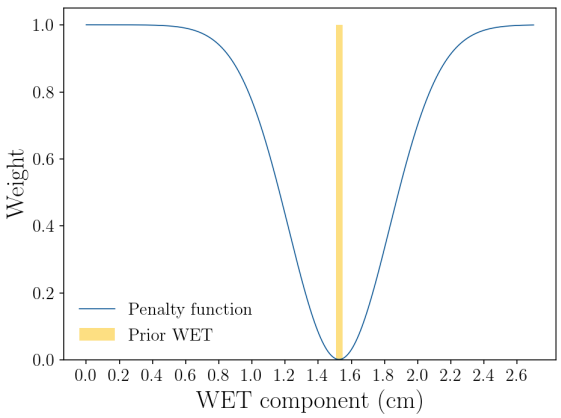

Figure 7.1: Example of Gaussian window $p(\mathrm{WET})$ around predicted WET $\mathrm{WET_p}$ for a pixel in the region behind the phantom insert with brain-like material ($\mathrm{WET_{GT}} = 1.70\,\mathrm{cm}$) and s chosen to be $s = 0.2$.

A small increment of 0.001 is finally added to each p(WET) to assure that there will not be a row of zeros in the LUT that would corrupt the WET determination.
This approach has the advantage that the full LUT is used for signal decomposition and also a WET value different from $\mathrm{WET_p}$ can be determined from the measured signal (see figure 7.3).

7.1.1.3 Iteration

To further improve the scatter correction, the regularized WET determination was repeated over several iterations. The updated initial guess WET components for each new iteration are set based on the previous image of $\mathrm{WET_{mean}}$. The stopping criterion for the iterative process is set based on the Root Mean Square Error (RMSE) between the outcome of subsequent iterations (see figure 7.4).

7.1.1.4 Test cases

The approach of scatter correction with a regularized LUT was tested with proton radiographies of several objects. The proton images were acquired at CAL using the CM49 detector.
The imaged objects were:

- the µ-CT calibration phantom with phantom-to-detector distances of 13 mm and 33 mm
- a plexiglas cylinder with 20 mm diameter
- the first generation multimodal mouse phantom

7.1.2 Inverse Optimization for Scatter Correction

Another approach for scatter correction that is not based on prior information makes use of the fact that with integration mode imaging and energy stacking, an image of the object for every probing energy is available. In each of these radiographies, proton scattering for that specific beam energy and the the imaged object is included. Vice versa, general knowledge about the anticipated proton scattering for a given beam energy and material thickness allows for inference on the WET of the object from the recorded signal.
This method is not a modification of the already used algorithm for WET determination, but a different technique to retrieve the WET from the measured data already accounting for the expected proton scattering. The images for the probing energies $E_{i,\dots,n}$ are used in a similar manner to multichannel film dosimetry (Micke et al., 2011). The inverse optimization of the calculated total energy deposition or dose from several pencil beams at different lateral positions is analogous to particle therapy treatment planning (Krämer et al., 2000).

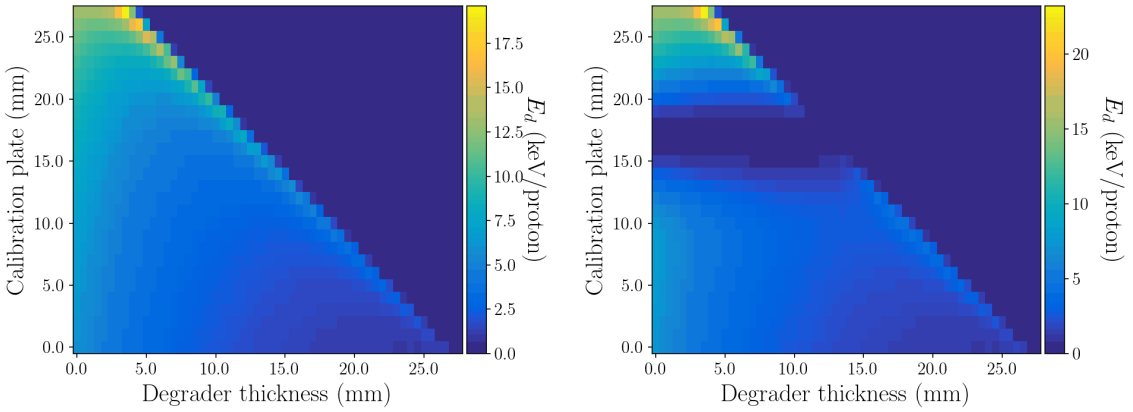

Figure 7.2: (a) LUT for the example pixel and (b) manipulated LUT using the penalty function shown in figure 7.1.

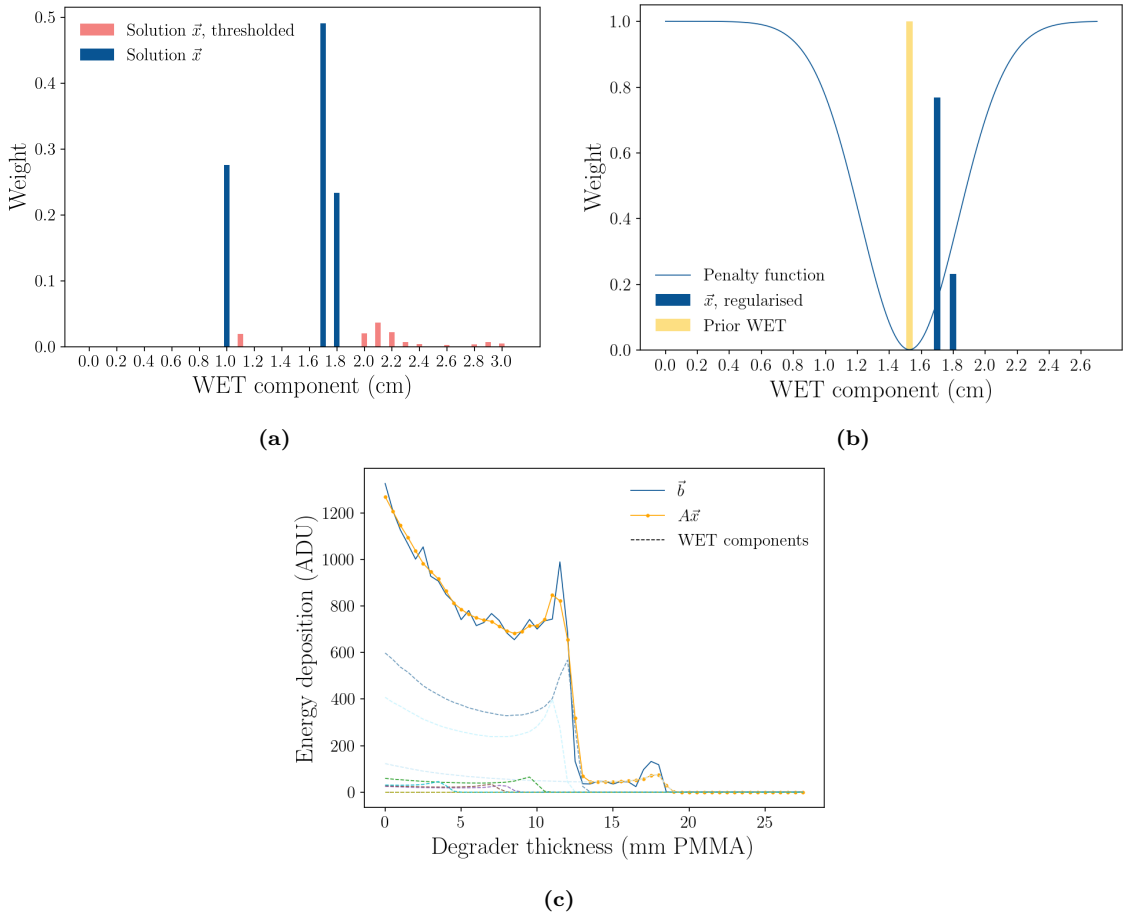

Figure 7.3: (a) Solution found by standard Bragg Peak Decomposition: Small WET components are thresholded, but the component of the baseplate ($\mathrm{WET}_{\mathrm{GT,base}} = 1.0\,\mathrm{cm}$) that is scattered in from all around the insert is not suppressed. (b) Solution with regularized LUT: The correct components are found, even though they are not equal to the prior value. Note that the prior value from the CBCT is not at the ground truth value of $\mathrm{WET}_{\mathrm{GT,brain}} = 1.7\,\mathrm{cm}$. (c) Solution obtained with regularization $\vec{x}$ multiplied with the regularized LUT

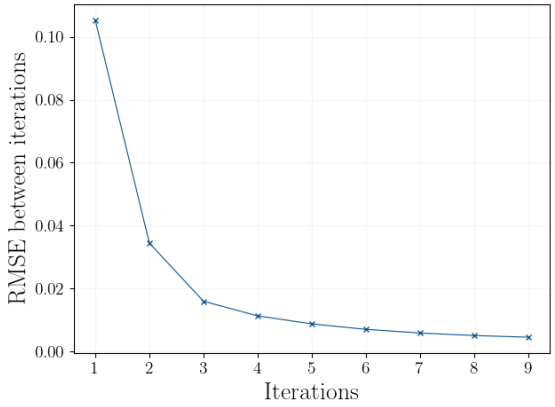

Figure 7.4: Example of stopping criterion in the scatter correction using CBCT images as prior information in the image of the µ-CT phantom with 13 mm phantom-to-detector distance as a function of iterations. The criterion for stopping has been set in such a way that the algorithm will stop if the RMSE between two consecutive iterations is less than 0.001.

In early heavy-ion radiotherapy treatment planning the dose for a single field is described as:

$$D(E_{\text{beam}}, \vec{x}) = d(E_{\text{beam}}, z)\ F(E_{\text{beam}}, \vec{r})\ , \tag{7.5}$$

with:

$$\vec{x} = \begin{pmatrix} x \\ y \\ z \end{pmatrix} \qquad \vec{r} = \begin{pmatrix} x \\ y \end{pmatrix} \tag{7.6}$$

with the significant simplification of neglecting lateral beam scattering and using the fluence F assumption of:

$$F(E_{\text{beam}}, \vec{r}) = \frac{N(E_{\text{beam}}, \vec{r})}{\Delta x \Delta y} \tag{7.7}$$

from Krämer et al., 2000, with Δx and Δy being the scanner step sizes in x and y, respectively. (The units were omitted for clarity.)
The aim of the treatment plan optimization is to calculate the incident particle number $N(E_{\text{beam}}, \vec{r})$ for each pencil beam that will accumulate to the prescribed dose distribution. In our case, the objective is to find the WET image, i.e., 2D arrangement of material thickness values along the beam direction, after which the addition of energy depositions (including the ones from scattered-in protons) reproduces the measured values for all probing energies (see figure 7.5).
The energy deposition E_d in one detector pixel (x,y) for a given incoming beam energy E_{beam} and after passing through a certain WET is the sum of: (i) The energy deposition from protons only passing through the segment of the object, that is laterally limited by

the projection of the pixel edges along beam direction. It is the WET of this segment that ideally should be assigned to the pixel $j = 0$ in the objective WET image. (ii) Energy depositions from protons that have (partly) traveled through adjacent parts of the object (pixels $j = 1, .., nn$ in the objective WET image):

$$E_{\mathrm{dep}}(E_{\mathrm{beam}}, \vec{r}, \mathrm{WET}) = \sum_{j=0}^{nn} E_{\mathrm{dep},j}(E_{\mathrm{beam}}, \mathrm{WET}_j) \ , \tag{7.8}$$

with nn being the number of nearest neighbours taken into account. The calculation of E_{dep} and the assumptions made in this work are explained in section 7.1.2.2.

7.1.2.1 Proposed Algorithm

Computationally, the scatter-free WET determination presented in this work was done along the following steps:

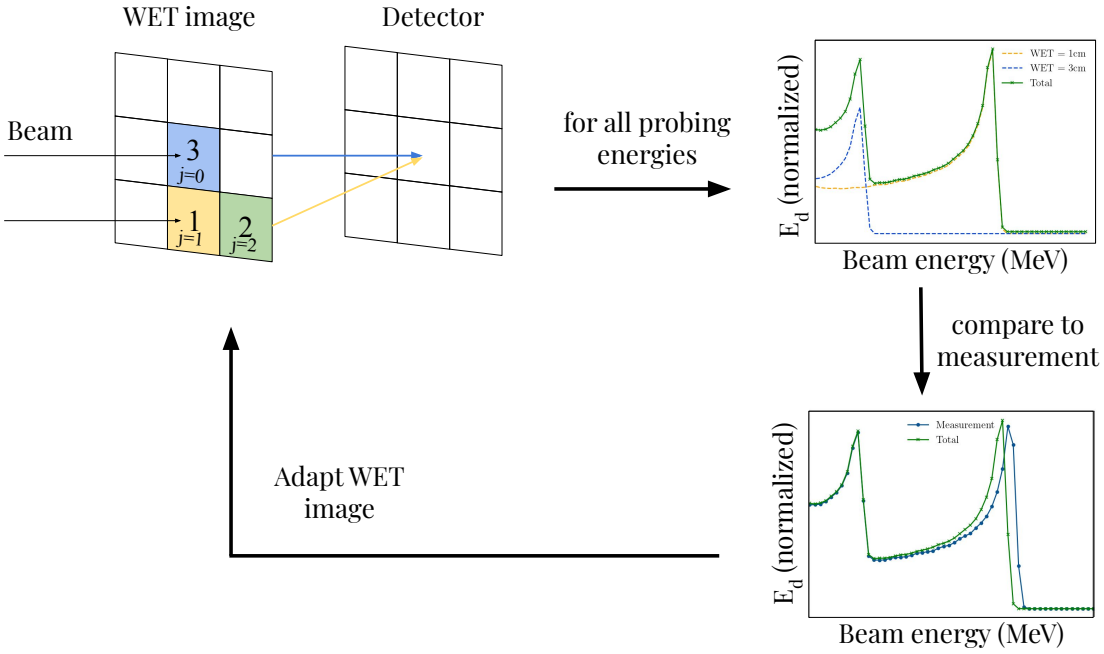

Figure 7.5: Schematic drawing of the iterative method for scatter correction. From the WET image, the relative energy depositions in a detector pixel are calculated and then compared to the measurement. Based on the outcome of that comparison, the WET image is adapted for the next iteration. For simplicity, a parallel beam is chosen.

Initialization Bragg Peak Decomposition as described in section 6.1.1.1 as first guess WET determination. The first guess could also be initialized with an array of the image shape and random values in the expected order of magnitude of the WET.

Optimization Minimize the objective function f_k by variation of the pixel values $j = 0, ..., nn$ in the objective WET image, i.e., repeat the steps a-c until convergence is reached.

Step a: Calculate the estimated energy deposition for one detector pixel k, denoted by $\vec{b}_{\text{est},k}(\vec{r}, \text{WET})$, from the WET image for the pixel at $j = 0$ directly "in front" of the detector pixel k and the adjacent pixels $j = 1, ..., nn$ for all probing energies $E_{\text{beam}} = E_i, ..., E_n$. See section 7.1.2.2 for the implementation of this step.

Step b: Calculate the objective function f_k for a pixel k,

$$f_k = \sum_{i=0}^{n} (b_{\text{est},k,i}(\vec{r}, \text{WET}) - b_{k,i})^2 \ , \tag{7.9}$$

with $b_{k,i}$ being the recorded signal in detector pixel k.

Step c: Make improved guess for WET image pixels $j = 0, ..., nn$.
This procedure is repeated for each detector pixel $k = 0...p$ and the corresponding pixels in the WET image that are taken into account for the calculation of the estimated signal.

Global comparison Evaluate total cost of image c by summing the objective function f over all pixels P:

$$c = \sum_{k=0}^{p} f_k \ , \tag{7.10}$$

which is a measure of difference between the calculated and measured energy deposition for all detector pixels and probing energies. If the total cost is higher than a defined threshold value, restart with the optimization step.

7.1.2.2 Forward Projection of Detector Signal

To approximate the energy deposition in one detector pixel, equation 7.8 needs a valid estimate of the 2D distribution of energy deposition in the detector plane for a certain beam energy and WET. This is similar to the matrix D_{ij} in radiotherapy treatment planning that gives the expected dose at voxel i from beam angle element (so-called *bixel*) j (Ziegenhein et al., 2008).
The lateral beam shape in the detector plane was assumed to be isotropic and described by a Gaussian function with amplitude of one and standard deviation σ being a function of probing energy E_i and WET_j. The energy deposition in a detector pixel $E_{\text{dep},j}(x_j)$ from the pixel j in the WET image is:

$$E_{\text{dep},j}(x_j) = E_{\text{dep}}(E_i, \text{WET}_j) \cdot e^{\frac{-x_j^2}{2\sigma(E_i, \text{WET}_j)^2}} \ . \tag{7.11}$$

with x_j being the distance between neighbour pixel j and the central pixel.

$E_{\text{dep}}(E_i, \text{WET}_j)$ and $\sigma(E_i, \text{WET}_j)$ were obtained from FLUKA MC simulations. In

a simulation model of the CM49 detector, the energy deposition of a parallel, quadratic beamlet with lateral size set to the image pixel size (99 µm) was scored. The 2D energy deposition for all combinations of probing energy and expected WET from the experiment (see section 6.2.6) was recorded in a 9.9 mm × 9.9 mm pixel grid with a resolution of 100 × 100. The initial energy spread was set to zero. The thickness of a simulated water column with density of $\rho_{\mathrm{w}} = 1.0\,\mathrm{g\,cm^{-3}}$ and $I_{\mathrm{pot,w}} = 78\,\mathrm{eV}$ was set to the WET values needed for the reconstruction and the distance to the sensor was 13 mm.

7.1.2.3 Test case

The algorith was tested with a ROI of 60 × 70 pixels behind the Cortical bone (SB3) tissue-equivalent insert from the data acquired at CAL with 13 mm phantom-to-detector distance. The number of nearest neighbors taken into account for each pixel was set to 15.

7.2 Results

7.2.1 Scatter Correction by Regularization of the LUT

For the evaluated cases of correcting a proton radiography of the µ-CT calibration phantom acquired at CAL with the CM49 detector, the threshold in the Bragg Peak Decomposition was set to 10 % and the margin to create the ROIs was 0.3 mm. The image without scatter correction was evaluated with a ROI margin of 1.1 mm due to blurring at the edges. WET error in the uncorrected case was (1.97 ± 2.98) % and spatial resolution was 0.52 mm. Evaluated with the 0.3 mm margin to the edge of the ROI, the WET accuracy is (11.4 ± 7.1) %, falsified by the consideration of pixels from the blurred edge.
The scatter correction method by regularization of the LUT for the phantom-to-detector distance of 13 mm yielded a WET error of (0.83 ± 0.19) % and spatial resolution of 0.03 mm in the first iteration, if ground truth was used as prior information. This values can be considered as the optimal result that is achievable in this method of scatter correction.
Using the CBCT image, which is considered the realistic prior, the achieved WET error was (1.43 ± 1.21) % and spatial resolution was 0.12 mm after 8 iterations. If the Bragg Peak Decomposition is used as first guess, the WET error was (1.11 ± 5.58) % and spatial resolution was 0.18 mm after 9 iterations.
Figure 7.6 shows the original and corrected proton images and figure 7.7 shows an example of improved spatial resolution as a function of iterations in the scatter correction. For the air gap of 33 mm, a WET error of 1.13 % and spatial resolution of 0.03 mm were achieved with the ground truth image as prior. With the CBCT prior information, WET error was 3.8 % and spatial resolution was 0.09 mm. For the 33 mm air gap, the scatter correction with the regularized LUT without prior information was not possible, as the energy deposition in a pixel from scattered-in protons is larger than the "straight line" signal. For the same reason, the scatter correction was stopped after the first iteration

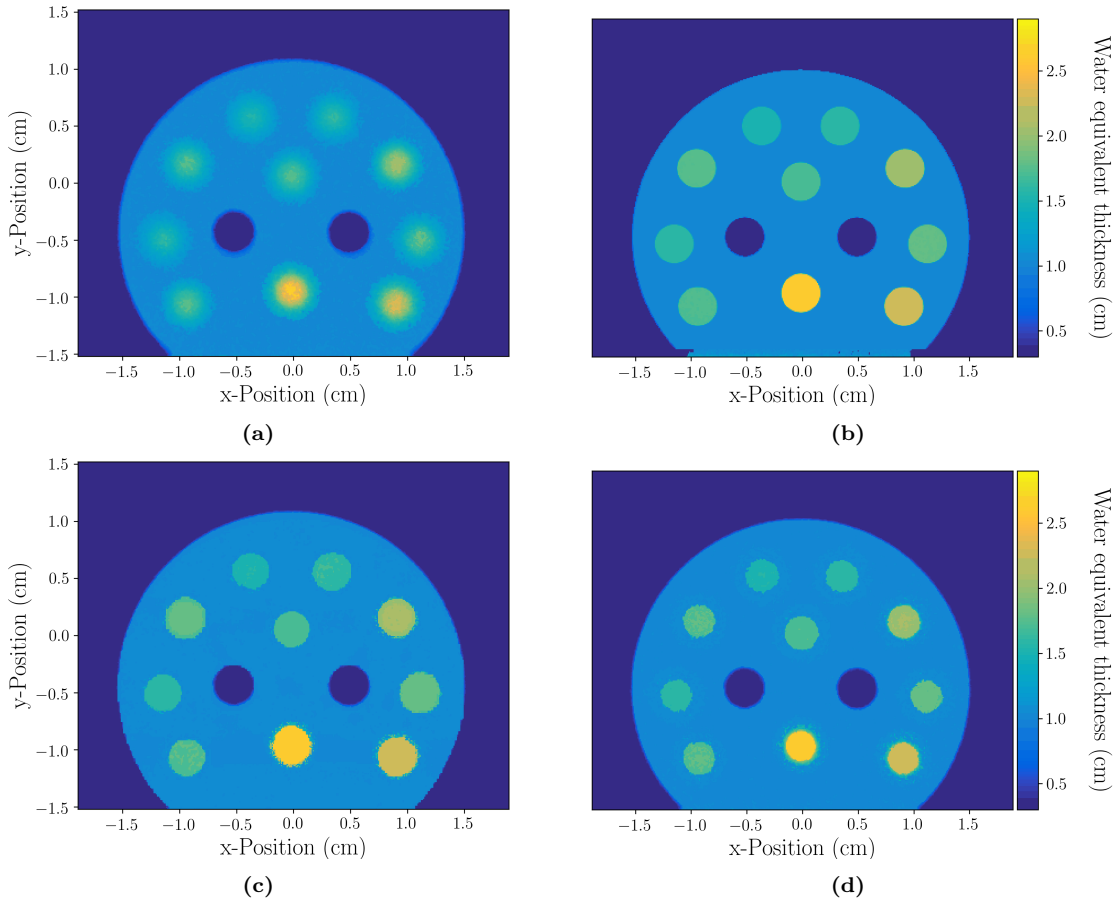

Figure 7.6: Results from the scatter correction with a regularized LUT for the radiography with 13 mm phantom-to-detector distance: (a) Bragg Peak Decomposition without scatter correction. (b) Corrected with ground truth WET as prior information. (c) Corrected with CBCT as prior information. (d) Corrected with (a) as prior information.

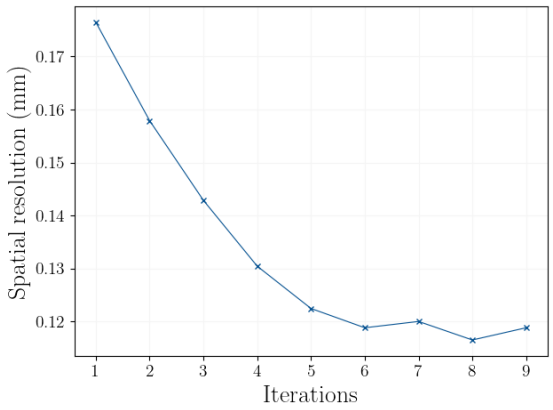

Figure 7.7: Spatial resolution evaluated on the radiography of the µ-CT phantom with 13 mm phantom-to-detector distance and scatter correction with prior knowledge from a CBCT as a function of iterations.

independent of the prior, as otherwise the pixel values would drift towards the largest WET component, which is always the scattered-in component of the baseplate. Prior knowledge from other imaging modalities or MC simulation of the phantom geometry is necessary in such cases (see discussion 7.3.1).
Figure 7.8 shows the original and attempted scatter corrected proton images.

7.2.1.1 Results for heterogeneous objects

The interest in imaging the plexiglas cylinder lies in the steep gradients in WET that are present in the radiography. As is visible in figures 7.9a to 7.9c, the Bragg Peak Decomposition fails in these pixels, as numerous WET components are found (and possibly eliminated by the threshold as in this case set at 20 %). The approach of a regularized LUT with or without a prior allows to identify the most probable WET value for the pixels (see figure 7.10).

As shown in section 6.4.6, the acquired images of the first generation multimodal mouse phantom present a lack of sharp contrast of the anatomical structures. Scatter correction without prior information allows to slightly increase the contrast (see figure 7.11b), and using CBCT information reveals anatomical structures in the correct position (see figure 7.11c).

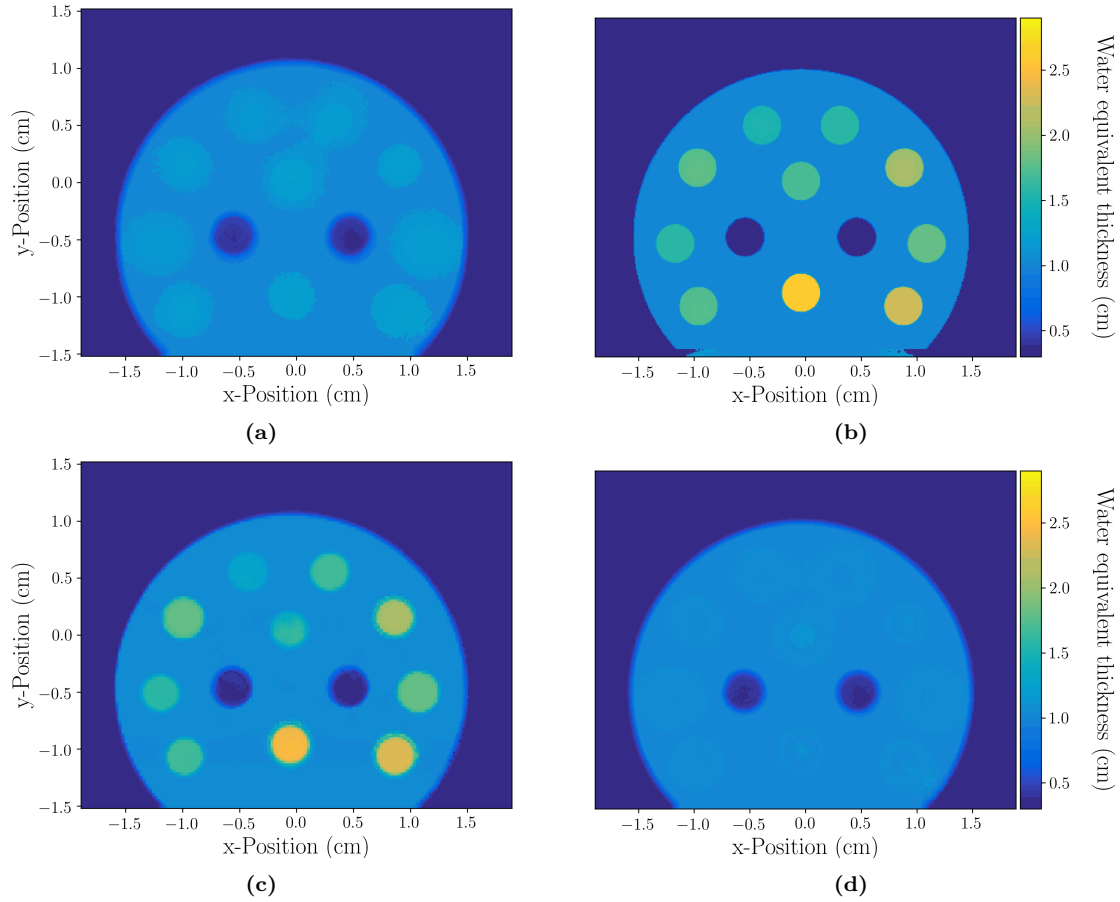

Figure 7.8: Results from the scatter correction with a regularized LUT for the radiography with 33 mm phantom-to-detector distance. a) Bragg Peak Decomposition without scatter correction. (b) Corrected with ground truth WET as prior information. (c) Corrected with CBCT as prior information. (d) Result from attempt to correct with (a) as prior information.

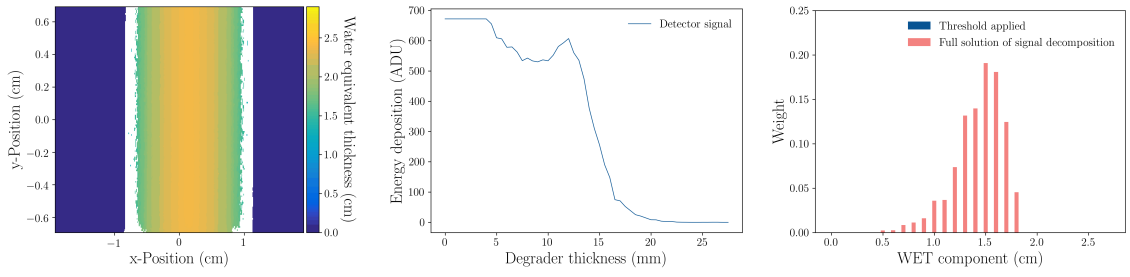

Figure 7.9: (a) WET image of cylinder from WET determination using only Bragg Peak Decomposition, but no scatter correction. (b) Corresponding energy deposition for probing energies (expressed as degrader thickness, see section 6.2.6) in one of the detector pixels where WET determination fails and (c) found solution WET components with weights which are all smaller than the threshold of 20 %.

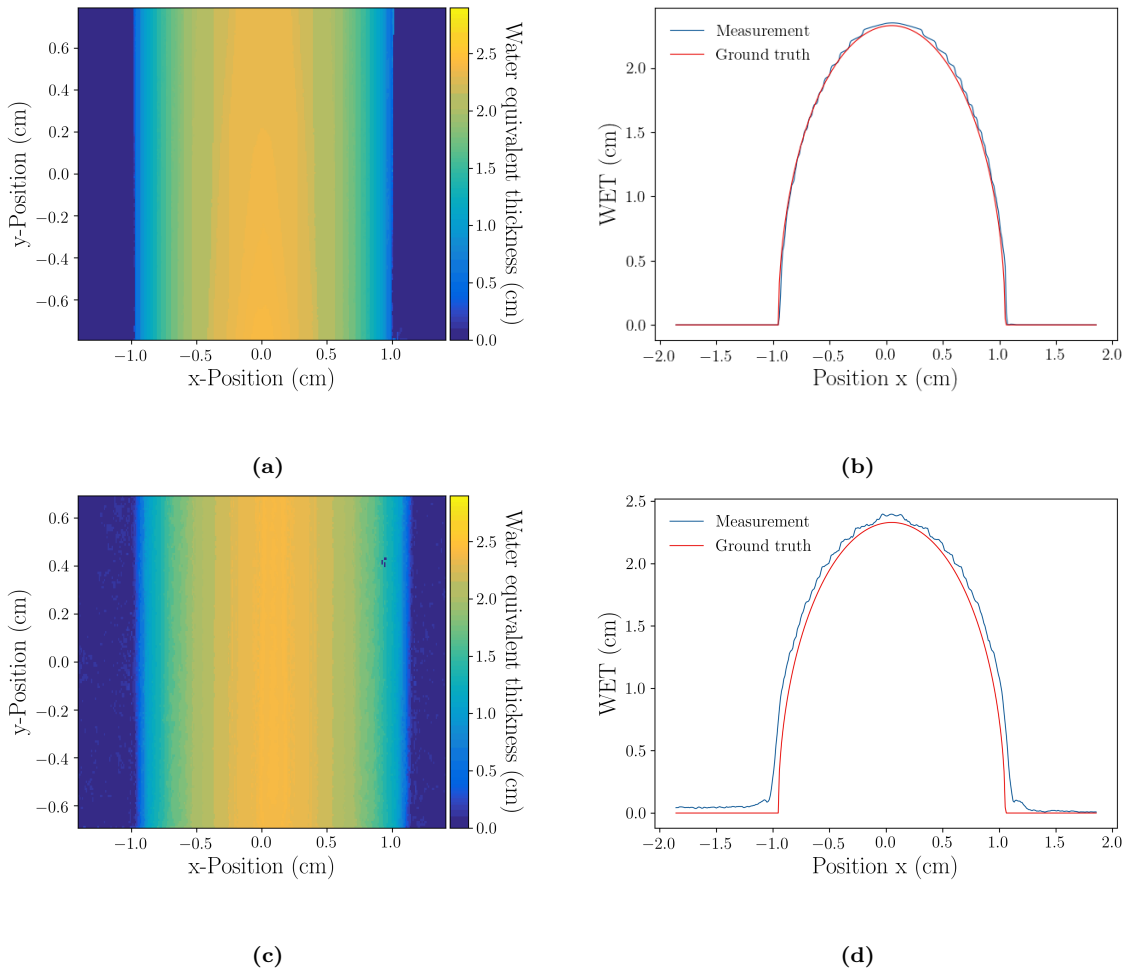

Figure 7.10: Images of cylinder from WET determination with scatter correction: (a), (b) using prior information, (c), (d) without prior informaiton.

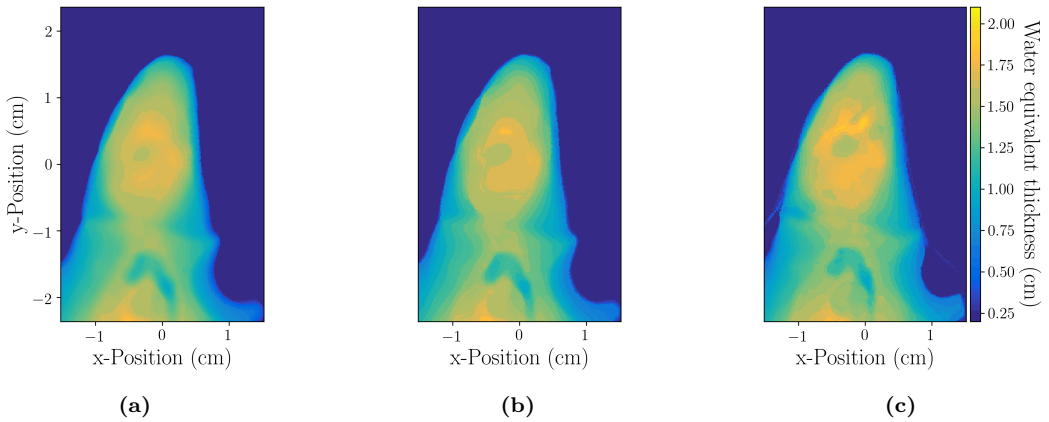

Figure 7.11: Results from scatter correction with regularized LUT of the radiography of the first generation multimodal mouse phantom in coronal projection: (a) Uncorrected WET image from Bragg Peak Decomposition. (b) Scatter correction without prior information (result after eight iterations) and (c) with prior information from CBCT after first iteration.

7.2.2 Inverse Optimization for Scatter Correction

With each iteration of the inverse algorithm for scatter correction, the amount of pixels with accurate WET of $\mathrm{WET}_{\mathrm{GT,SB3}} = 2.6\,\mathrm{cm}$ inside the Cortical Bone (SB3) insert increases (see figure 7.12). The results in figure 7.13 are evaluated for different ROI margins, to emphasize that finding. (Figure 7.13 also shows how scattering and choosing the ROI margin too small can falsify the assessment of the WET accuracy.)

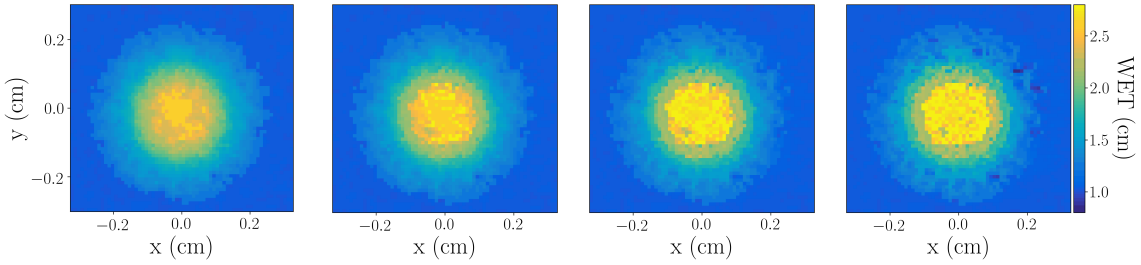

Figure 7.12: Results from inverse optimization for scatter correction for the ROI containing the Cortical Bone (SB3) insert ($\mathrm{WET}_{\mathrm{GT,SB3}} = 2.6\,\mathrm{cm}$) in the phantom baseplate ($\mathrm{WET}_{\mathrm{GT,base}} = 1.0\,\mathrm{cm}$): (a) First guess WET image from Bragg Peak Decomposition. (b) Iteration 1, (c) iteration 4 and (d) iteration 6.

The spatial resolution, evaluated on the edge from the Cortical Bone (SB3) insert improves from a value of 0.67 mm in the Bragg Peak Decomposition to a convergence value of 0.22 mm (see figure 7.14). The largest improvement is within the first two iterations to 0.57 mm after the first iteration and 0.50 mm after the second.

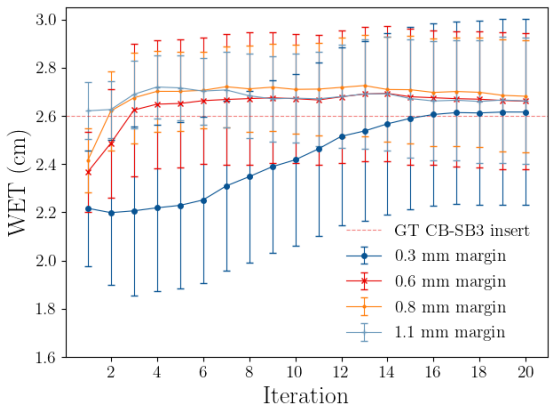

Figure 7.13: WET accuracy and precision of ROI in Cortical Bone (SB3) insert evaluated for different ROI margins as a function of the iterations of the scatter correction.

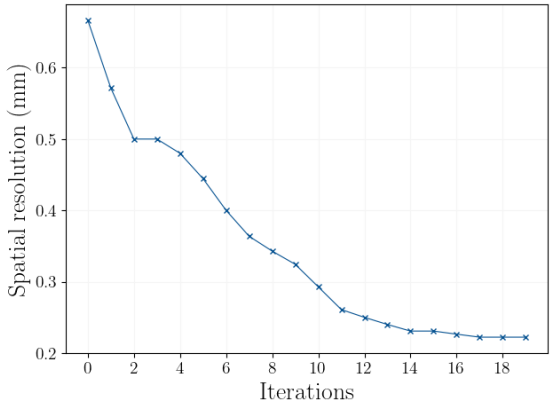

Figure 7.14: Spatial resolution evaluated at the edge of the Cortical Bone (SB3) insert as a function of the iterations of the scatter correction.

7.3 Discussion

In conventional volumetric CBCT, scattered radiation leads to severe degradation of the image quality. In this field, image correction methods have been developed that consist of hardware in the imaging setup to reduce scattering and scatter corrections software (Spies et al., 2001; Rührschopf et al., 2011). The scatter correction algorithms in general require an estimation of the scattering (e.g., measurements or mathematical models) as basis that is exploited in a subsequent correction step to remove the scattering from the image. In the presented approach of inverse optimization for scatter correction, the scatter estimation is obtained from MC simulation and correction is carried out by the minimization algorithm.

7.3.1 Scatter Correction by Regularization of the LUT

If the scattered-in component in the pixel signal is lower than the contribution from protons that went through the phantom with lateral deviation smaller than the pixel size (i.e., with relatively straight trajectory), then a first guess image from Bragg Peak Decomposition with the unaltered LUT is a valid choice.
Improved prior images could be obtained through ray tracing of the protons through the object and MC simulations, where particles with large lateral deviation can be excluded. A complete forward calculation including the scattered-in contributions for each pixel is also possible (Gianoli et al., 2019), but then subtracting or otherwise excluding the "scatter signal" from the image is error-prone.
The presented method works with one single parameter to be adjusted, which is the width of the Gaussian window around the prior components.
Also the image quality of the prior information is an error source for the scatter correction. As shown in figure 7.15, the beam hardening artefacts that are present in the CBCT image between the high-density inserts (see figure 7.15a) alter the correctly determined WET values in that region (see figure 7.6a) to a falsified, slightly lower value of WET (see figure

7.15b).

The scatter correction without prior information about the object is not possible if the signal in a pixel from scattered-in protons is larger than the contribution from protons with straight trajectory. In the context of this assessment, this is the case for the proton radiographies of the µ-CT phantom with 33 mm distance between phantom and detector (see figure 7.16). On the other hand, the use of prior information can considerably improve image quality for large phantom-to-detector separations or in the case of complex geometries of the object (see figures 7.8c and 7.11c).

7.3.2 Inverse Optimization for Scatter Correction

The method for scatter correction using inverse optimization presented in this work yielded correct results only for a limited amount of pixels and was very time-consuming with $\mathcal{O}(1\,\text{min})$ for each forward calculation with 15 neighbor pixels.

Improvements on computing time can be expected from parallel forward calcuation of the expected accumulated energy deposition for each pixel and its neighbors separately and for each probing energy.

To avoid extreme local variations in the optimization result, a boundary condition to ensure smoothness in homogeneous image regions needs to be implemented. Simple filtering procedures, e.g., mean or median filters, after each iteration have shown to introduce artefacts into the image. More sophisticated methods, like for example Total Variation Superization (TVS) or similar should be investigated.

Also the scatter kernel could be manipulated to include further effects in the experimental conditions by including e.g., the energy spread and beam divergence.

7.4 Conclusion and Outlook

Two methods of scatter correction for integration mode proton imaging are presented.

Scatter correction by regularization of the LUT for WET determination is possible within the limitations that are discussed in the previous section. Those considerations are in agreement with the prerequisites to achieve high accuracy integration mode proton images, e.g., reduced phantom-to-detector distance. This methodology is prepared for immediate implementation, e.g., for application to images acquired with the SIRMIO platform.

The scatter correction approach utilizing an inverse optimization algorithm has been demonstrated to reduce blurring in proton images, but further optimization and significant improvement in the use of computational resources are needed for the method to be applicable to meaningful image sizes.

Also methods employing artificial intelligence are promising candidates to reduce the image quality diminishing effect of proton scattering. Models could be trained on images acquired with proton irradiation and other imaging modalities as comparison, e.g., X-ray CT. Furthermore, MC simulated data could be exploited for training of AI models.

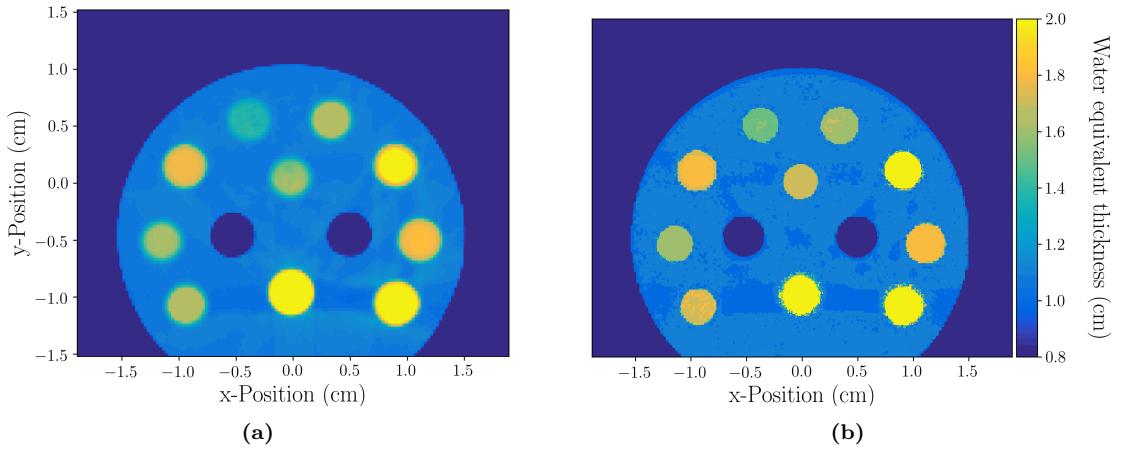

Figure 7.15: (a) CBCT image prior of the µ-CT phantom used for scatter correction with a regularized LUT. (b) Corrected radiography with 13 mm phantom-detector distance. The reconstruction artefacts present in (a) impact the correct WET determination, as shown in (b).

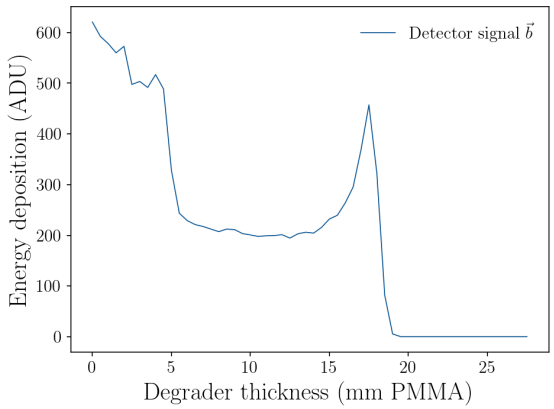

Figure 7.16: Detector signal as function of probing energies $E_d(E_i)$ for a pixel in the region behind the Cortical bone (SB3) tissue-equivalent insert. The peak on the left is from protons that have gone through the insert, the peak on the right is signal from scattered-in protons that have only traversed the baseplate of the phantom.

CHAPTER 8

Discussion

In this chapter, the approach of integration mode proton imaging with a CMOS in general is discussed and compared to methods of single-particle tracking.

8.1 General Considerations and Comparison to Single-Particle Tracking

The presented integration mode proton imaging setup for the SIRMIO platform has been developed to enable imaging in situations where high particle flux is necessary or inevitable, e.g., if ionoacoustic measurements are conducted at the same time, thus requiring a synchrocyclotron, or if the available space or time allocated for experiments require a compact and simple setup. The compromise that is made when not measuring individual particles is to accept that large-angle scattered energy deposition events can not be excluded from the WET determination. Furthermore, the remaining kinetic energy of each individual particle after the object is unknown. To deduce the WET from an integrated measurement, either energy stacking or a pixelated range telescope (or a mixture of these concepts) after the object are necessary. In the case of energy stacking, higher imaging time and dose, i.e., a minimum of a few 10 mGy of dose and duration from the optimal case of 30 s up to 1 min for a radiography, are of consequence. The development and use of a range telescope from multiple layers of pixelated detectors remains challenging (e.g., in terms of alignment and electronics), in particular regarding the pixel size of $< 200\,\mu m$ pursued in small animal imaging.

The superiority of Bragg Peak Decomposition in comparison to methods that rely only on the maximum of the measured signal has already been observed in (Krah et al., 2015; Meyer et al., 2017).

SPT imaging setups achieve better spatial resolution through the possibility to exclude

so-called "bad events" (e.g., large-angle scattered particles and particles that were registered in only one of the tracking detectors) and at acceptable dose levels, for example, values of 0.3 mm to 0.5 mm spatial resolution and less than 100 mGy dose were estimated for a tomography by Meyer, 2019 in a simulation of the small animal SPT setup for the SIRMIO platform. The main shortcoming of SPT setups is that they use more complex detectors of to-date limited rate capability.

Possible Improvements

Improvements related to the experimental setup and data processing are discussed in the respective chapters of this work.
A fundamental possible improvement to the integration mode imaging setup could be in the exploitation of **Pencil Beam Scanning Mode:** Analogous to the work described in (Meyer, 2019) and (Carriço, 2018), a treatment plan with raster points could be used in future version of the imaging setup. One proton radiography would be composed of several measurements for adjacent ROIs. The limited angular distribution of protons would lead to reduced blurring from scattering, but at the cost of increased imaging time and total dose exposure due to overlap of neighboring beam spots.

CHAPTER 9

Conclusion

9.1 CMOS Integration Mode Proton Imaging for Small Animals

In conclusion, a pixelated CMOS detector and dedicated post-processing methods can enable fast proton radiographic imaging for small animal studies in a simple and compact setup and achieve high WET accuracy and spatial resolution if phantom-to-detector distances are reasonable.
As the measurements on the CM49 detector revealed, it is imperative to choose a detector system that ensures reliable performance and allows the user to control the data acquisition according to experimental requirements.
In comparison to other methods of proton imaging, integration mode setups generally are easier in operation and require less space. CMOS detectors are produced in standardized manufacturing processes increasing the confidence in reliable performance and allowing for lower cost as compared to an accustomed solution.
The acquired small animal proton images can be used for pre-treatment position verification and DIR on a planning X-ray CT, or potentially also to obtain a patient specific HU to RSP conversion.

9.2 Scatter Correction

Two promising methods for post-acquisition proton scatter correction with and without prior imaging have been presented.
Scatter correction with regularization of the LUT for Bragg Peak Decomposition without using prior information is feasible in cases where the contribution from scattered particles to the signal is smaller than the signal from the true WET. When exploiting prior information, e.g., from other imaging modalities, proton radiographies can be considerably

improved for the cases of large phantom-to-detector separations and for complex geometries.
Further work is required for the inverse optimization method to decrease the calculation time and allow for realistically large images to be optimized.

APPENDIX A

Complementary Information

A.1 Hounsfield Values

Hounsfield values are defined after Hounsfield, 1973:

$$HU = 1000 \times \frac{\mu - \mu_{\text{Water}}}{\mu_{\text{Water}} - \mu_{\text{Air}}} \ , \tag{A.1}$$

with μ_{Water} and μ_{Air} being the linear attenuation coefficients of water and air respectively. Therefore HU_{Water} for distilled water at standard conditions are $HU_{\text{Water}} = 0$ and air $HU_{\text{Air}} = -1000$. The highest values naturally found in the human body $HU_{\text{bone,cortical}} \approx 3000$.

A.2 WET Values of the SMART µ-Calibration Phantom

The RSP of the materials of the phantom inserts, including the "solid water" material in the baseplate used for calibration, was measured for bigger samples of the same vendor in carbon ion beams (Hudobivnik et al., 2016) with an uncertainty of 0.2 % (see phantom description in 4.4.1).

Table A.1: Derivation of the ground truth WET of the µ-CT calibration phantom (SMART scientific solutions, The Netherlands) with the RSP measured in a carbon ion beam of 310.8 MeV u^{-1} (Hudobivnik et al., 2016) and length for each insert measured with a micrometer screw.

Tissue insert	RSP	length (cm)	WET (cm)
Adipose	0.94	1.598	1.51
Breast	0.97	1.598	1.55
Solid Water	1.00	1.593	1.59
Brain	1.06	1.596	1.70
Liver	1.08	1.597	1.72
Inner Bone	1.09	1.596	1.74
B200 Bone	1.10	1.598	1.76
CB2-30%	1.28	1.594	2.04
CB2-50%	1.43	1.596	2.29
SB3 Cort. Bone	1.62	1.599	2.60

A.3 WET measurements at HIT

Accurate knowledge of the WET of all elements in the beam reduces uncertainty in the calibration used for WET determination (see section 6.1.1) and enable to faithfully reproduce the experiment in MC simulations for further studies (e.g., on estimated dose deposition).
In the course of this work, a variety of PMMA pieces were utilized either as a degrader or as a reference WET for calibration. For different samples of the same material, the density and proton RSP can differ through the manufacturing process, in this case PMMA casting or extrusion.

The WET of different PMMA pieces used in the experimental campaigns was measured in a 107 MeV and 125 MeV beam at the HIT. The measurements at HIT were done with the PeakFinder^{TM} water column (PTW, Germany) that uses two parallel-plate ionization chambers with 4.08 cm radius to measure the laterally integrated IDD (Karger et al., 2010, Kurz et al., 2012, Sánchez-Parcerisa et al., 2012). The step size between measurement points was set to 0.1 mm. According to the manufacturer the achievable Bragg peak accuracy is 0.1 mm and Tessonnier et al., 2016 determined the reproducibility to be 0.05 mm. The geometrical length in beam direction of the pieces was measured with a micrometer gauge at multiple positions to calculate the RSP. The mass density ρ was assessed using a density scale (EMB-V, KERN & SOHN, Germany).

Table A.2: Different PMMA pieces used in the experiments at RPTC and CAL and their respective RSP measured at the HIT, as well as geometrical thickness assessed with a micrometer gauge and mass density measured with a density scale (EMB-V, KERN & SOHN, Germany). The parentheses give the standard deviation of the measurements.

Name	Thickness d in mm	Mass density ρ in g cm^{-3}	RSP
Degrader Block	34.564(10)	1.190(1)	1.166(4)
$PMMA_{Wheel}$	0.511(1)	1.154(2)	1.147(2)
Calib5	4.933(4)	1.190(4)	1.165(3)
Calib10a*	38.415(7)	1.188(3)	1.163(2)
Calib10b	10.142(63)	1.188(2)	1.164(8)
Calib20	19.578(5)	1.186(1)	1.165(1)
$PMMA_{Stair}$	27.656(2)	1.190**	1.161(1)

*WET determined for four pieces of the same material with nominal thickness of 10 mm each.

**Density could not be evaluated with the density scale due to the size of the PMMA pieces. The stated value is given by the vendor (Röhm, Switzerland).

Implementation of measured WET into the FLUKA MC simulation: In order to correctly model the calibration and degrader pieces, the respective FLUKA material cards were defined specific to each PMMA used, as the measurements showed differences in the RSP between the samples.

In a simulation reproducing the WET measurements conducted at HIT, the geometry of the PeakFinder was modelled as a water column with the entrance window positioned at isocenter. Density ρ_{w} and ionization potential $I_{\mathrm{pot,w}}$ for this water column were set to $\rho_{\mathrm{w}} = 0.998\,\mathrm{g\,cm^{-3}}$ and $I_{\mathrm{pot,w}} = 77.3\,\mathrm{eV}$ (Tessonnier et al., 2017). The initial proton beam energy was set to the nominal energy in the measurement and the beam is initiated in vacuum. This efficient approach is possible as the PeakFinder data is saved with a specific offset taking into account the nozzle of the beamline (Beam Application and Monitoring System (BAMS), vacuum window, and air in the nozzle), the standard air gap for WET measurements of 50 mm, and the parts in the PeakFinder that the beam has to pass through to get to the effective point of measurement of the ionization chamber.

The PMMA material to be adjusted was included from the standard material library in FLUKA and the density was set to the measured value. In an iterative process, the ionization potential of the PMMA was varied from the standard value of $I_{\mathrm{pot,PMMA}} = 74\,\mathrm{eV}$ to reproduce the measured Bragg peak position (see figure A.1).

The uncertainty of the MC reproduction of the PeakFinder range shift (including the uncertainty in reproducibility of the WET measurement itself) is 0.022 mm and needs to be propagated onto the final uncertainty in WET for each proton image.

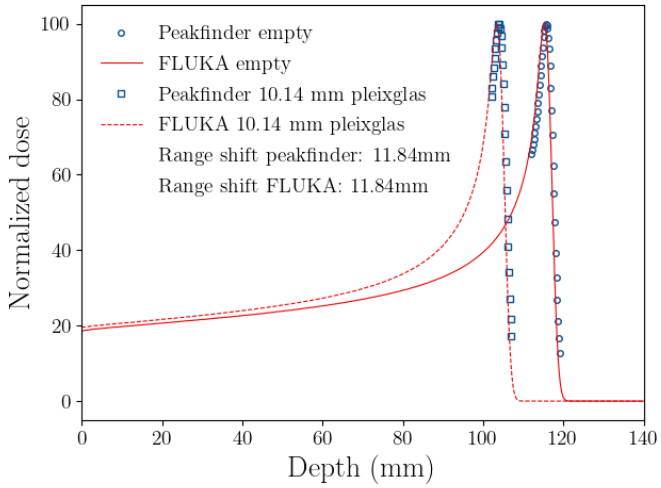

Figure A.1: The measured IDD of a 125 MeV proton beam and the same beam shifted by a 10.14 mm PMMA piece as well as the respective FLUKA simulations to determine the ionization potential $I_{\mathrm{pot,PMMA}}$ as described in section 6.2.3.

A.4 Beam size on the Detector for Open Field Configuration at RPTC

Table A.3: Beam size σ on the detector in the open field configuration at RPTC for measurement and simulation in x- and y-direction for the lowest used beam energy of 76 MeV and the highest beam energy of 96 MeV.

	x, 76 MeV	y, 76 MeV	x, 96 MeV	y, 96 MeV
Measured width (mm)	82	73	50	59
Simulated width (mm)	80	75	50	50

A.5 Imaging dose

In this section, the tabulated values for WET accuracy in relation to the image dose are presented as complementary data to section 6.4.3. Tables A.4 and A.5 show the values from radiographies acquired with the LASSENA detector at DCPT produced for one to ten averaged image frames for each probing energy, for phantom-detector separations of 0 mm and 10 mm, respectively.

Table A.4: WET accuracy for radiographies produced for one to ten averaged image frames for each probing energy and a phantom-detector separation of 0 mm.

Number of frames	Dose (mGy)	WET accuracy (%)	stat. uncertainty (%)
1	5.3	1.62	1.19
2	10.6	0.86	0.85
3	15.9	1.27	0.82
4	21.2	1.09	0.66
5	26.5	1.12	0.65
6	31.8	1.17	0.60
7	37.1	1.12	0.55
8	42.4	1.19	0.56
9	47.7	1.1	0.57
10	53	1.12	0.58

Table A.5: WET accuracy for radiographies produced for one to ten averaged image frames for each probing energy and a phantom-detector separation of 10 mm.

Number of frames	Dose (mGy)	WET accuracy (%)	stat. uncertainty (%)
1	5.3	2.15	1.55
2	10.6	1.53	1.18
3	15.9	1.09	1.13
4	21.2	0.81	1.02
5	26.5	0.76	1.14
6	31.8	0.92	1.18
7	37.1	0.84	1.06
8	42.4	0.82	1.17
9	47.7	0.86	1.03
10	53	0.78	1.00

Table A.6: WET accuracy for radiographies acquired with the LASSENA detector at DCPT produced for different granularity in probing energy of 1 MeV, 2 MeV, 3 MeV and 4 MeV and one, two, three and five averaged image frames for each probing energy. The phantom-detector separation was 0 mm.

Number of frames	Dose (mGy)	WET accuracy (%)	stat. uncertainty (%)
1 MeV granularity			
1	5.3	1.62	1.19
2	10.6	0.86	0.85
3	15.9	1.27	0.82
5	26.5	1.12	0.65
2 MeV granularity			
1	2.7	2.17	1.92
2	5.4	0.81	1.11
3	8.1	1.36	1.12
5	13.5	1.17	0.76
3 MeV granularity			
1	1.8	3.22	2.29
2	3.6	1.26	1.37
3	5.4	1.57	1.06
5	9	1.53	0.64
4 MeV granularity			
1	1.4	2.25	3.56
2	2.8	0.9	1.94
3	4.2	1.31	1.98
5	7	1.33	1.29

APPENDIX B

List of Scientific Contributions

Publications

2023

- K. Schnürle et al. (2023). "Development of integration mode proton imaging with a single CMOS detector for a small animal irradiation platform". *Frontiers in Physics*, 10(January): 1–11. ISSN: 2296424X. DOI: 10.3389/fphy.2022.1044156

- P. Palaniappan, Y. Knudsen, S. Meyer, C. Gianoli, K. Schnürle, M. Würl, J. Bortfeldt, K. Parodi, and M. Riboldi (2023). "Multi-stage image registration based on list-mode proton radiographies for small animal proton irradiation : A simulation study". *Zeitschift für Medizinische Physik*. DOI: 10.1016/j.zemedi.2023.04.003

2022

- J. Lascaud, P. Dash, K. Schnürle, J. Bortfeldt, K. Niepel, J. Maas, M. Würl, M. Vidal, J. Hérault, G. Landry, A. S. Savoia, K. Lauber, and K. Parodi (2022). "Fabrication and characterization of a multimodal 3D printed mouse phantom for ionoacoustic quality assurance in image-guided pre-clinical proton radiation research". *Physics in Medicine & Biology*: 0–12. DOI: 10.1088/1361-6560/ac9031Manuscript

- C. Gianoli, M. Zlatić, I. Butz, M. Würl, K. Schnürle, S. Meyer, J. Bortfeldt, F. S. Englbrecht, P. Palaniappan, M. Riboldi, and K. Parodi (2022). "Model-based and Data-driven Calibration of the X-ray CT Image based on Proton Radiographies". In: *2022 IEEE Nuclear Science Symposium and Medical Imaging Conference (NSS/MIC)*, pages 1–3. DOI: 10.1109/NSS/MIC44845.2022.10399089

2021

- J. Lascaud, R. Kowalewski, B. Wollant, H. Carmigniani, K. Schnürle, P. Dash, H.-P. Wieser, J. Bortfeldt, R. Kalunga, R. Rouffaud, A. Gérard, M. Vidal, J. Hérault, D. Certon, and K. Parodi (2021b). "Optimization of the backing material of a low frequency PVDF detector for ion beam monitoring during small animal proton irradiation". In: *2021 IEEE International Ultrasonics Symposium (IUS)*. URL: https://ieeexplore.ieee.org/abstract/document/9593703

2020

- S. Meyer, J. Bortfeldt, P. Lämmer, F. Englbrecht, M. Pinto, K. Schnürle, M. Wuerl, and K. Parodi (2020). "Optimization and performance study of a proton CT system for pre-clinical small animal imaging". *Physics in Medicine & Biology*. ISSN: 0031-9155. DOI: 10.1088/1361-6560/ab8afc

- M. Würl, K. Schnürle, J. Bortfeldt, C. Oancea, C. Granja, E. Verroi, F. Tommasino, and K. Parodi (2020a). "Proton Radiography for a Small-Animal Irradiation Platform based on a Miniaturized Timepix Detector". In: *2020 IEEE Nuclear Science Symposium and Medical Imaging Conference (NSS/MIC)*. IEEE, pages 1–6. DOI: 10.1109/nss/mic42677.2020.9508073

2019

- K. Parodi, W. Assmann, C. Belka, J. Bortfeldt, D. A. Clevert, G. Dedes, R. Kalunga, S. Kundel, N. Kurichiyanil, P. Lämmer, J. Lascaud, K. Lauber, G. Lovatti, S. Meyer, M. Nitta, M. Pinto, M. J. Safari, K. Schnürle, J. Schreiber, P. G. Thirolf, H. P. Wieser, and M. Würl (2019). "Towards a novel small animal proton irradiation platform: the SIRMIO project". *Acta Oncologica*, 58(10): 1470–1475. ISSN: 1651226X. DOI: 10.1080/0284186X.2019.1630752

Conference Contributions

2023

- **Poster:** Z. Huang, J. Bortfeldt, N. Kurichiyanil, K. Schnürle, F. S. Englbrecht, T. Rösch, S. Safai, M. Sitarz, K. Parodi, and M. Pinto (2023). *Monte Carlo simulation model of the SIRMIO beamline and experimental validation in clinical facilities*. Poster presented at the 61st Annual PTCOG Conference. Madrid, Spain. URL: https://www.ncbi.nlm.nih.gov/pmc/articles/PMC10698634/

2022

- **Oral:** K. Schnürle, J. Bortfeldt, F. S. Englbrecht, C. Gianoli, P. Hofverberg, S. Meyer, P. Poulsen, M. Sitarz, C. Sondergaard, M. Vidal, J. Herault, K. Parodi, and M. Würl (2022a). *CMOS Integration Mode Proton Imaging for a Small Animal Irradiator*. Edited by Katia Parodi, K. Lauber, G. Landry, F. Verhaegen, and P. Bartelds. Presentation at the 5th Conference on Small Animal Precision Image-Guided Radiotherapy. Munich, Germany. DOI: 10.5282/ubm/epub.92720

- **Oral:** K. Schnürle, J. Bortfeldt, F. S. Englbrecht, C. Gianoli, P. Hofverberg, S. Meyer, P. Poulsen, M. Sitarz, C. Sondergaard, M. Vidal, J. Herault, K. Parodi, and M. Würl (2022b). *CMOS Integration Mode Proton Imaging*. Presentation at the 23rd International Workshop on Radiation Imaging Detectors (iWoRiD2022). Riva del Garda, Italy. DOI: 10.5282/ubm/epub.92775

- **Oral:** J. Bortfeldt, O. Belker, A. Denker, A. Dittwald, F. S. Englbrecht, A. Frenzel, J. Gebhard, J. Gordon, G. Holthoff, G. Hu, Z. Huang, F. Kähler, P. Lämmer, A. Lange, M. Meurer, L. Marchfelder, S. Meyer, M. Pinto, O. Schackmann, S. Schinzel, D. Schmidt, K. Schnürle, M. Sitarz, C. Steinbrecht, M. Würl, and K. Parodi (2022). *Gaseous Detectors for Preclinical Proton Beam Monitoring, Characterization and Imaging*. Presentation at the 7th International Conference on Micro Pattern Gaseous Detectors

- **Oral:** G. Holthoff, F. S. Englbrecht, G. Hu, F. Kähler, P. Lämmer, A. Lange, L. Marchfelder, M. Meurer, S. Meyer, O. Schackmann, S. Schinzel, D. Schmidt, K. Schnürle, M. Sitarz, M. Würl, K. Parodi, and J. Bortfeldt (2022). *Entwicklung und Charakterisierung eines präklinischen Micromegas pCT-Systems*. Edited by U. Heinrichs, E. Beckers, and A. Bitz. Presentation at the 53. Jahrestagung der Deutschen Gesellschaft für Medizinische Physik. DOI: 10.5282/ubm/epub.103671

2021

- **Oral:** K. Schnürle, J. Bortfeldt, F. S. Englbrecht, C. Gianoli, J. Hartmann, P. Hofverberg, S. Meyer, M. Vidal, J. Schreiber, K. Parodi, and M. Würl (2021a). *Development of Integration Mode Proton Imaging with a Single CMOS Detector for a Small Animal Irradiation Platform*. Presentation at the Third European Congress of Medical Physics. Torinol, Italy & Virtual Conference. DOI: 10.5282/ubm/epub.92773

- **Oral:** K. Schnürle, J. Bortfeldt, F. S. Englbrecht, C. Gianoli, J. Hartmann, P. Hofverberg, S. Meyer, K. Niepel, I. Yohannes, M. Vidal, G. Landry, J. Hérault, J. Schreiber, K. Parodi, and M. Würl (2021b). *Small Animal CMOS Integration Mode Proton Imaging at Different Treatment Facilities The SIRMIO project*. Presentation at the

Seventh Annual Loma Linda Workshop on Particle Imaging and Radiation Treatment Planning. Loma Linda, California, USA & Virtual Conference

- **Oral:** K. Parodi, K. Schnürle, S. Meyer, G. Hu, B. Foglia, M. Würl, and J. Bortfeldt (2021). *Proton imaging for small animals*. Presentation at the Joint Conference of the ÖGMP, DGMP and SGSMP, Dreiländertagung der Medizinischen Physik. Virtual Conference. DOI: 10.5282/ubm/epub.103638

- **Oral:** J. Bortfeldt, O. Belker, A. Denker, A. Dittwald, A. Frenzel, K. Schnürle, M. Würl, and K. Parodi (2021). *Development of an Optical Micromegas Detector for Precision Particle Beam QA*. Presentation at the Joint Conference of the ÖGMP, DGMP and SGSMP, Dreiländertagung der Medizinischen Physik. Virtual Conference. DOI: 10.5282/ubm/epub.103640

- **Poster:** K. Schnürle, J. Bortfeldt, F. S. Englbrecht, C. Gianoli, J. Hartmann, P. Hofverberg, S. Meyer, M. Vidal, J. Hérault, J. Schreiber, K. Parodi, and M. Würl (2021c). *Development of scatter correction for integration mode proton imaging for a small animal irradiation platform*. Poster presented at the Joint Conference of the ÖGMP, DGMP and SGSMP, Dreiländertagung der Medizinischen Physik. Virtual Conference. DOI: 10.5282/ubm/epub.92774

- **Poster:** G. Hu, K. Schnürle, S. Meyer, G. Liubchenko, J. Bortfeldt, C. Gianoli, K. Parodi, and M. Würl (2021). *Expansion of a Small-Animal Proton CT Reconstruction Framework and Studies of Energy Dependence of Relative Stopping Power*. Poster presented at the Joint Conference of the ÖGMP, DGMP and SGSMP, Dreiländertagung der Medizinischen Physik. Virtual Conference. DOI: 10.5282/ubm/epub.103670

- **Poster:** J. Lascaud, R. Kowalewski, B. Wollant, H. Carmigniani, K. Schnürle, P. Dash, H.-P. Wieser, J. Bortfeldt, R. Kalunga, R. Rouffaud, A. Gérard, M. Vidal, J. Hérault, D. Certon, and K. Parodi (2021c). *Optimization of the backing material of a low frequency PVDF detector for ion beam monitoring during small animal proton irradiation*. Poster presented at the 2021 IEEE International Ultrasonics Symposium (IUS). URL: https://epub.ub.uni-muenchen.de/103645/1/IEEE%7B%5C_%7DIUS%7B%5C_%7DPVDF%7B%5C_%7DJL.pdf

- **Oral:** K. Schnürle, J. Bortfeldt, F. S. Englbrecht, C. Gianoli, J. Hartmann, P. Hofverberg, S. Meyer, K. Niepel, I. Yohannes, M. Vidal, G. Landry, J. Hérault, J. Schreiber, K. Parodi, and M. Würl (2021d). *Development of Integration Mode Proton Imaging with a Single CMOS Detector for a Small Animal Irradiation Platform*. Presentation at the Applied Nuclear Physics Conference 2021. Prague, Czech Republic & Virtual Conference. DOI: 10.5282/ubm/epub.92719

2020

- **Oral:** J. Bortfeldt, S. Schinzel, S. Meyer, O. Belker, F. Englbrecht, K. Schnürle, M. Würl, and K. Parodi (2020a). *Production and Test of an Aluminum Floating Strip Micromegas for Small Animal Proton Imaging*. Presentation at the RD51 Mini-Week February 10 - 13 2020, CERN

- **Oral:** K. Schnürle, J. Bortfeldt, F. S. Englbrecht, C. Gianoli, J. Hartmann, S. Meyer, K. Niepel, G. Landry, I. Yohannes, J. Schreiber, and K. P. und Matthias Würl (2020). *Entwicklung von Protonenbildgebung mit einem einzelnen integrierenden CMOS-Detektor für eine Kleintierbestrahlungsanlage*. Presentation at the 51. Jahrestagung der Deutschen Gesellschaft für Medizinische Physik. Virtual Conference. DOI: 10.5282/ubm/epub.74260

- **Poster:** M. Würl, K. Schnürle, J. Bortfeldt, C. Oancea, C. Granja, E. Verroi, F. Tommasino, and K. Parodi (2020b). *Proton Radiography for a Small-Animal Irradiation Platform based on a Miniaturized Timepix Detector*. Poster presented at the 2020 IEEE Nuclear Science Symposium and Medical Imaging Conference (NSS/MIC). Manchester, UK

- **Oral:** J. Bortfeldt, O. Belker, B. Haubmann, A. Lange, D. Lovric, K. Schnürle, M. Würl, and K. Parodi (2020b). *Status of Gaseous Detector R&D for a Small Animal Proton Irradiation System*. Presentation at the RD51 Collaboration Meeting. Santiago de Compostela, Spain. URL: https://indico.cern.ch/event/889369/contributions/4042751/

- **Oral:** G. Liubchenko, M. Würl, K. Schnürle, S. Meyer, J. Bortfeldt, C. Granja, C. Oancea, E. Verroi, F. Tommasino, and K. V. und Katia Parodi (2020). *Assessing the feasibility of high-Z metal (oxide) nanoparticles as contrast enhancement agents in proton imaging for a small animal irradiation platform (SIRMIO)*. Presentation at the 51. Jahrestagung der Deutschen Gesellschaft für Medizinische Physik. Virtual Conference

- **Oral:** M. Würl, K. Schnürle, J. Bortfeldt, K. Niepel, G. Landry, C. Oancea, C. Granja, E. Verroi, F. Tommasino, and K. Parodi (2020c). *Quantitative proton radiography for a small-animal irradiation platform based on a miniaturized Timepix detector*. Presentation at the 51. Jahrestagung der Deutschen Gesellschaft für Medizinische Physik. Virtual Conference. URL: https://epub.ub.uni-muenchen.de/74258/1/DGMP%7B%5C_%7D2020%7B%5C_%7DWuerl.pdf

- **Oral:** M. Würl, K. Schnürle, J. Bortfeldt, C. Oancea, C. Granja, E. Verroi, F. Tommasino, and K. Parodi (2020d). *Development of a setup for small-animal proton imaging based on a miniaturized Timepix detector*. Presentation at the 1st Workshop

Trento Proton Beam Line Facility, Trento. Trento, Italy. URL: https://agenda.infn.it/event/23198/book-of-abstracts.pdf

2019

- **Oral:** J. Bortfeldt, P. Lämmer, S. Meyer, F. Englbrecht, K. Schnürle, M. Würl, and K. Parodi (2019b). *Development of Novel Ultra-Thin Micromegas and a Time Projection Chamber for Animal Ion Transmission Tomography*. Presentation at the 6th International Conference on Micro Pattern Gaseous Detectors. URL: https://indico.cern.ch/event/757322/contributions/3402727/

- **Oral:** J. Bortfeldt, P. Lämmer, S. Meyer, F. Englbrecht, K. Schnürle, M. Würl, and K. Parodi (2019a). *Ultra-Thin Gaseous Detectors for for Small Animal Proton Transmission Imaging*. Presentation at the International Workshop on Detection Systems and Techniques in Nuclear and Particle Physics. URL: http://newcleo.unime.it/Events/DeSyT2019/talks/bortfeldt.pdf

- **Oral:** K. Schnürle, M. Würl, J. Esslinger, S. Meyer, J. Bortfeldt, F. S. Englbrecht, and K. Parodi (2019). *Monte-Carlo-Studie zur Protonenradiographie für die Positionsverifikation für Kleintierbestrahlungen an einem klinischen Protonen-Therapiezentrum*. Presentation at the 50. Jahrestagung der Deutschen Gesellschaft für Medizinische Physik. Stuttgart, Germany. DOI: 10.5282/ubm/epub.70700

- **Oral:** S. Meyer, J. Bortfeldt, P. Lämmer, F. Englbrecht, K. Schnürle, M. Würl, and K. Parodi (2019). *Optimierung und Performance Evaluierung eines Protonen Computertomographie Systems für präklinische Bildgebung*. Presentation at the 50. Jahrestagung der Deutschen Gesellschaft für Medizinische Physik. Stuttgart, Germany. DOI: 10.5282/ubm/epub.75413

- **Poster:** J. Bortfeldt, P. Lämmer, S. Meyer, F. Englbrecht, J. Gordon, K. Schnürle, M. Würl, and K. Parodi (2019c). *Novel Micropattern Gaseous Detectors for a Small Animal Proton Irradiation Platform*. Poster presented at the 2019 IEEE Nuclear Science Symposium (NSS) and Medical Imaging Conference (MIC). Manchester, UK

2018

- **Poster:** K. Schnürle, M. Vidal, C. Peucelle, A. Gérard, P. Hofverberg, and J. Hérault (2018a). *Monte Carlo Simulation of a Clinical Prototype 226MeV Protontherapy Beamline Using GATE Code*. Poster presented at the 57th Annual PTCOG Conference. Cincinnati, Ohio, USA. URL: https://www.ncbi.nlm.nih.gov/pmc/articles/PMC6874191/

- **Poster:** K. Schnürle, M. Vidal, C. Peucelle, A. Gérard, P. Hofverberg, and J. Hérault (2018b). *Monte Carlo Simulation of a Clinical Prototype 226MeV Proton-therapy Beamline Using GATE Code*. Poster presented ENLIGHT Annual Meeting and Training. London, UK

Further Scientific Contributions

- K. Schnürle (2018). *GATE Monte Carlo Simulation of a Proton Therapy Beamline for Water Luminescence Range Verification*. Master's thesis, Karlsruhe Institute of Technology (KIT), Germany
- K. Schnürle (2016). *Majorana Edge States on Toplogical Superconductors*. Bachelor's thesis, Karlsruhe Institute of Technology (KIT), Germany

Awards and Scholarships

- 2019: Finalist in the "Young Investigator Award" of the DGMP
- 2017: Award for exceptional student engagement at the Karlsruher Institut für Technologie (KIT)
- 2013-2018: Scholar of the German Academic Scholarship Foundation (Studienstiftung des deutschen Volkes)

Bibliography

Amaldi, U. and Kraft, G. (2005). "Radiotherapy with beams of carbon ions". *Reports on Progress in Physics*, 68(8): 1861–1882. ISSN: 00344885. DOI: 10.1088/0034-4885/68/8/R04 (cited on p. 1).

Amblard, R. et al. (2019). "A New Potential Method for Proton Radiography". *2019 IEEE Nuclear Science Symposium and Medical Imaging Conference (NSS/MIC)*: 1–5 (cited on p. 35).

Attix, F. H. (2004). *Introduction to Radiological Physics and Radiation Dosimetry*. WILEY-VCH Verlag GmbH & Co. KGaA. ISBN: 9780471011460. DOI: 10.1002/9783527617135 (cited on p. 12).

Battistoni, G. et al. (2016). "The FLUKA code: An accurate simulation tool for particle therapy". *Frontiers in Oncology*, 6(MAY). ISSN: 2234943X. DOI: 10.3389/fonc.2016.00116 (cited on pp. 37, 39).

Baumann, M. et al. (2016). "Radiation oncology in the era of precision medicine". *Nature Reviews Cancer*, 16: 234–249. ISSN: 1474-175X. DOI: 10.1038/nrc.2016.18 (cited on p. 2).

Beck, L. et al. (2023). "Suitability of Athena Monolithic Active Pixel Sensor for upstream monitoring of 6 MV, 6 FFF and 10 MV treatments". *Applied Radiation and Isotopes*, 198: 110799. ISSN: 09698043. DOI: 10.1016/j.apradiso.2023.110799 (cited on pp. 25, 61).

Bentefour, E. H., Schnuerer, R., and Lu, H. M. (2016). "Concept of proton radiography using energy resolved dose measurement". *Physics in Medicine & Biology*, 61(16): N386–N393. ISSN: 13616560. DOI: 10.1088/0031-9155/61/16/N386 (cited on p. 34).

Berger, M. J. et al. (1993). "Report 49". *Journal of the International Commission on Radiation Units and Measurements*, os-25(2): NP. DOI: 10.1093/jicru/os25.2.Report49 (cited on p. 13).

Berger, M. J. (1993). *Penetration of Proton Beams Through Water 1. Depth-dose Distribution, Spectra and LET Distribution*. Technical report. NIST (cited on p. 12).

Berghmans, F. et al. (2008). "An Introduction to Radiation Effects on Optical Components and Fiber Optic Sensors". In: *Optical Waveguide Sensing and Imaging*. Edited by W. J.

Bock, I. Gannot, and S. Tanev. Dordrecht: Springer Netherlands, pages 127–165. ISBN: 978-1-4020-6952-9 (cited on p. 19).

Berven, E. (1962). "The Development and Organization of Therapeutic Radiology in Sweden". *Radiology*, 79(5): 829–841. DOI: 10.1148/79.5.829 (cited on p. 30).

Bethe, H. (1930). "Zur Theorie des Durchgangs schneller Korpuskularstrahlen durch Materie". *Annalen der Physik*. DOI: 10.1002/andp.19303970303 (cited on p. 9).

Bichsel, H. (1988). "Straggling in thin silicon detectors". *Rev. Mod. Phys.*, 60(3): 663–699. DOI: 10.1103/RevModPhys.60.663 (cited on p. 15).

Bloch, F. (1933). "Zur Bremsung rasch bewegter Teilchen beim Durchgang durch Materie". *Annalen der Physik*, 408. DOI: 10.1002/andp.19334080303 (cited on p. 9).

Bock, R. K. (1998). *Neutron Fluence*. URL: http://arpg-serv.ing2.uniroma1.it/patera/didattica/fis%7B%5C_%7Dmod/trasp%7B%5C_%7Driv/Glossario/node123.html (visited on Apr. 14, 2024) (cited on p. 61).

Böhlen, T. T. et al. (2014). "The FLUKA Code: Developments and Challenges for High Energy and Medical Applications". *Nuclear Data Sheets*, 120: 211–214. ISSN: 0090-3752. DOI: https://doi.org/10.1016/j.nds.2014.07.049 (cited on pp. 11, 12, 28, 37).

Bopp, C. et al. (2014). "The impact of tracking system properties on the most likely path estimation in protonCT". *Physics in Medicine & Biology*, 59(23): N197–N210. ISSN: 13616560. DOI: 10.1088/0031-9155/59/23/N197 (cited on p. 34).

Borchert, H. J. et al. (2008). "Proton therapy with spot scanning: the Rinecker Proton Therapy Center in Munich Part 2: Technical and physical aspects". *Nowotwory Journal of Oncology*. Terapia protonowa z penetracja punktowa: Rinecker Proton Therapy Center w Monachium Czesc 2: Aspekty techniczne i fizyczne 58(2): 116–124. ISSN: 0029-540X. URL: http://inis.iaea.org/search/search.aspx?orig%7B%5C_%7Dq=RN:39110013 (cited on p. 44).

Bortfeld, T. (1997). "An analytical approximation of the Bragg curve for therapeutic proton beams". *Medical physics*, 24(12): 2024–33. DOI: 10.1118/1.598116 (cited on pp. 11–13).

Bortfeldt, J. et al. (2022). *Gaseous Detectors for Preclinical Proton Beam Monitoring, Characterization and Imaging*. Presentation at the 7th International Conference on Micro Pattern Gaseous Detectors (cited on p. 157).

Bortfeldt, J. et al. (2016). "Low material budget floating strip Micromegas for ion transmission radiography". *Nuclear Instruments and Methods in Physics Research, Section A: Accelerators, Spectrometers, Detectors and Associated Equipment*, 845: 210–214. ISSN: 01689002. DOI: 10.1016/j.nima.2016.05.003 (cited on p. 3).

Bortfeldt, J. et al. (2019a). *Ultra-Thin Gaseous Detectors for for Small Animal Proton Transmission Imaging*. Presentation at the International Workshop on Detection Systems and Techniques in Nuclear and Particle Physics. URL: http://newcleo.unime.it/Events/DeSyT2019/talks/bortfeldt.pdf (cited on p. 160).

Bortfeldt, J. et al. (2020a). *Production and Test of an Aluminum Floating Strip Micromegas for Small Animal Proton Imaging*. Presentation at the RD51 Mini-Week February 10 - 13 2020, CERN (cited on p. 159).

Bortfeldt, J. et al. (2021). *Development of an Optical Micromegas Detector for Precision Particle Beam QA*. Presentation at the Joint Conference of the ÖGMP, DGMP and SGSMP, Dreiländertagung der Medizinischen Physik. Virtual Conference. DOI: 10.5282/ubm/epub.103640 (cited on p. 158).

Bortfeldt, J. et al. (2019b). *Development of Novel Ultra-Thin Micromegas and a Time Projection Chamber for Animal Ion Transmission Tomography*. Presentation at the 6th International Conference on Micro Pattern Gaseous Detectors. URL: https://indico.cern.ch/event/757322/contributions/3402727/ (cited on p. 160).

Bortfeldt, J. et al. (2019c). *Novel Micropattern Gaseous Detectors for a Small Animal Proton Irradiation Platform*. Poster presented at the 2019 IEEE Nuclear Science Symposium (NSS) and Medical Imaging Conference (MIC). Manchester, UK (cited on p. 160).

Bortfeldt, J. et al. (2020b). *Status of Gaseous Detector R&D for a Small Animal Proton Irradiation System*. Presentation at the RD51 Collaboration Meeting. Santiago de Compostela, Spain. URL: https://indico.cern.ch/event/889369/contributions/4042751/ (cited on p. 159).

Bragg, W. H. and Kleeman, R. (1905). "On the α particles of radium, and their loss of range in passing through various atoms and molecules". *Philosophical Magazine Series 6*, 10(57): 318–340. DOI: 10.1080/14786440509463378 (cited on p. 13).

Bucciantonio, M. et al. (2013). "Development of a fast proton range radiography system for quality assurance in hadrontherapy". *Nuclear Instruments and Methods in Physics Research, Section A: Accelerators, Spectrometers, Detectors and Associated Equipment*, 732: 564–567. ISSN: 0168-9002. DOI: 10.1016/j.nima.2013.05.110 (cited on p. 34).

Carnicer, A. et al. (2012). "Study of the secondary neutral radiation in proton therapy: Toward an indirect in vivo dosimetry". *Medical Physics*, 39(12): 7303–7316. ISSN: 00942405. DOI: 10.1118/1.4765049 (cited on pp. 85, 86).

Carnicer, A. et al. (2013). "Development and validation of radiochromic film dosimetry and Monte Carlo simulation tools for acquisition of absolute, high-spatial resolution longitudinal dose distributions in ocular proton therapy". *Radiation Measurements*, 59: 225–232. ISSN: 13504487. DOI: 10.1016/j.radmeas.2013.06.011 (cited on pp. 85, 86).

Carriço, M. J. A. (2018). *Monte Carlo Investigations for a Novel Small-Animal Proton Radiographic Setup based on a Pixelated Silicon Detector and Energy Stacking*. Master's thesis, Ludwig-Maximilians Universität München (LMU), Germany (cited on pp. 69, 144).

Cavinato, M. et al. (1996). "Monte Carlo calculations using the Boltzmann Master Equation theory of nuclear reactions". *Physics Letters B*, 382(August): 1–5 (cited on p. 39).

Civinini, C. et al. (2013). "Recent results on the development of a proton computed tomography system". *Nuclear Instruments and Methods in Physics Research, Section A:*

Accelerators, Spectrometers, Detectors and Associated Equipment, 732: 573–576. ISSN: 01689002. DOI: 10.1016/j.nima.2013.05.147 (cited on p. 34).

Clarkson, R. et al. (2011). "Characterization of image quality and image-guidance performance of a preclinical microirradiator". *Medical Physics*, 38(2): 845–856. DOI: https://doi.org/10.1118/1.3533947 (cited on p. 2).

Cormack, A. M. (1963). "Representation of a Function by Its Line Integrals, with Some Radiological Applications". *Journal of Applied Physics*, 34(9): 2722–2727. ISSN: 0021-8979. DOI: 10.1063/1.1729798 (cited on p. 33).

DeJongh, E. A. et al. (2022). "Technical Note: A fast and monolithic prototype clinical proton radiography system optimized for pencil beam scanning". *Medical Dosimetry*, 48(3): 1356–1364. DOI: 10.1002/mp.14700.Technical (cited on p. 34).

Demtröder, W. (2017). *Experimentalphysik 4: Kern-, Teilchen- und Astrophysik*. 5th edition. Volume 4. 1. Springer Spektrum Berlin, Heidelberg. ISBN: 978-3-662-52883-9. DOI: 10.1007/978-3-662-52884-6 (cited on p. 24).

Deng, H. et al. (2007). "The small-animal radiation research platform (SARRP): Dosimetry of a focused lens system". *Physics in Medicine & Biology*, 52(10). ISSN: 00319155. DOI: 10.1088/0031-9155/52/10/007 (cited on p. 2).

Denker, A. et al. (2013). "STATUS OF THE HZB CYCLOTRON". In: *Proceedings of Cyclotrons 2013*. Vancouver, BC, Canada, pages 31–33. ISBN: 9783954501281 (cited on p. 47).

Deveaux, M. et al. (2011). "Radiation tolerance of a column parallel CMOS sensor with high resistivity epitaxial layer". *Journal of Instrumentation*. DOI: 10.1088/1748-0221/6/02/C02004 (cited on p. 61).

Dickmann, J. et al. (2020). "An optimization algorithm for dose reduction with fluence-modulated proton CT". *Medical Physics*, 47(4). ISSN: 00942405. DOI: 10.1002/mp.14084 (cited on p. 33).

Dickmann, J. et al. (2021). "An empirical artifact correction for proton computed tomography". *Physica Medica*, 86(2021): 57–65. DOI: 10.1016/j.ejmp.2021.05.018 (cited on p. 49).

Doolan, P. J. et al. (2015). "Patient-specific stopping power calibration for proton therapy planning based on single-detector proton radiography". *Physics in Medicine & Biology*, 60(5): 1901–1917. ISSN: 13616560. DOI: 10.1088/0031-9155/60/5/1901 (cited on p. 35).

Dössel, O. (2016). *Bildgebende Verfahren in der Medizin*. 2nd edition. Karlsruhe: Springer Vieweg. ISBN: 9783642544064. DOI: 10.1007/978-3-642-54407-1 (cited on p. 100).

Durante, M. (2014). "New challenges in high-energy particle radiobiology". *British Journal of Radiology*, (October 2013). DOI: 10.1259/bjr.20130626 (cited on p. 1).

Englbrecht, F. S. (2014). *Experimental based Monte Carlo modeling of a clinical proton beam*. Master's thesis, Ludwig-Maximilians Universität München (LMU), Germany (cited on pp. 64, 81, 82, 118).

Englbrecht, F. S. (2022). *Investigations of radiation shielding, diagnostic methods and imaging for conventional and laser-driven radiation sources*. PhD thesis, Ludwig-Maximilians Universität München (LMU), Germany (cited on pp. 42, 43, 54).

Esslinger, J. (2019). *Monte Carlo Implementation of a Realistic Beam Model for a Small Animal Proton Radiography Setup*. Bachelor's thesis, Ludwig-Maximilians Universität München (LMU), Germany (cited on p. 69).

Farace, P., Righetto, R., and Meijers, A. (2016). "Pencil beam proton radiography using a multilayer ionization chamber". *Physics in Medicine & Biology*, 61(11): 4078–4087. ISSN: 13616560. DOI: 10.1088/0031-9155/61/11/4078 (cited on p. 34).

Ferrari, A. et al. (1992). *An improved multiple scattering model for charged particle transport*. Technical report, pages 412–426 (cited on p. 39).

Ferrari, A. and Sala, P. (1993). "A new model for hadronic interactions at intermediate energies for the FLUKA code". In: *n Int. Conference on Monte Carlo Simulation in High Energy and Nuclear Physics (MC93)*. Tallahassee (Florida), pages 277–288 (cited on p. 39).

Ferrari, A. et al. (2005). "FLUKA: A multi-particle transport code". *Cern-2005-010, Infn/Tc 05/11, Slac-R-773*, (October) (cited on pp. 11, 12, 28, 37–39).

Flynn, S. et al. (2022). "Monitoring pencil beam scanned proton radiotherapy using a large format CMOS detector". *Nuclear Instruments and Methods in Physics Research, Section A: Accelerators, Spectrometers, Detectors and Associated Equipment*, 1033. ISSN: 01689002. DOI: 10.1016/j.nima.2022.166703 (cited on pp. 43, 44).

Ford, E. et al. (2017). "An image-guided precision proton radiation platform for preclinical in vivo research". *Physics in Medicine & Biology*, 62(1): 43–58. ISSN: 13616560. DOI: 10.1088/1361-6560/62/1/43 (cited on p. 2).

Gerlach, S. et al. (2020). "Beam characterization and feasibility study for a small animal irradiation platform at clinical proton therapy facilities". *Physics in Medicine & Biology*, 65(24). ISSN: 13616560. DOI: 10.1088/1361-6560/abc832 (cited on pp. 3, 27, 81).

Giacometti, V. et al. (2017). "Software Platform for Simulation of a Prototype Proton CT Scanner". DOI: 10.1111/ijlh.12426 (cited on p. 34).

Gianoli, C. et al. (2019). "Analytical simulator of proton radiography and tomography for different detector configurations". *Physica Medica*, 59(March): 92–99. ISSN: 1724191X. DOI: 10.1016/j.ejmp.2019.03.002 (cited on pp. 27, 73, 120, 139).

Gianoli, C. et al. (2020). "Patient-specific CT calibration based on ion radiography for different detector configurations in 1 H, 4 He and 12 C ion pencil beam scanning". DOI: 10.1088/1361-6560/aba319 (cited on p. 3).

Gianoli, C. et al. (2022). "Model-based and Data-driven Calibration of the X-ray CT Image based on Proton Radiographies". In: *2022 IEEE Nuclear Science Symposium and Medical Imaging Conference (NSS/MIC)*, pages 1–3. DOI: 10.1109/NSS/MIC44845.2022.10399089 (cited on p. 155).

Gottschalk, B. et al. (1993). "Multiple coulomb scattering of 160 MeV protons". *Nuclear Instruments and Methods in Physics Research, Section B: Beam Interactions with Materials and Atoms*, 74: 467–490. DOI: https://doi.org/10.1016/0168-583X(93)95944-Z (cited on p. 14).

Gottschalk, B. (2012). "Physics of Proton Interactions in Matter". In: *Proton Therpy Physics*. CRC Press, pages 19–60. ISBN: 9781138626508 (cited on pp. 1, 7, 12–14).

Grant, R. L. et al. (2014). "Relative stopping power measurements to aid in the design of anthropomorphic phantoms for proton radiotherapy". *Journal of Applied Clinical Medical Physics*, 15(2): 121–126 (cited on p. 14).

Groom, D. and Klein, S. (2020). "Passage of Particles Trough Matter". *Review of Particle Physiscs*, 01(August 2019): 1–37 (cited on pp. xx, xxvii, 9, 18).

Ha, S. et al. (2021). "Chapter 6 - Low-power integrated circuits for wearable electrophysiology". In: *Wearable Sensors (Second Edition)*. Edited by E. Sazonov. Second Edi. Oxford: Academic Press, pages 163–199. ISBN: 978-0-12-819246-7. DOI: https://doi.org/10.1016/B978-0-12-819246-7.00006-1 (cited on p. 25).

Harms, J. M. et al. (2020). "Flat-panel imager energy-dependent proton radiography for a proton pencil-beam scanning system". *Physics in Medicine & Biology*. ISSN: 0031-9155. DOI: 10.1088/1361-6560/ab9981 (cited on p. 35).

Hartmann, J. (2022). *Quantitative Ion Spectrometry and first laser-ion acceleration results at the Centre for Advanced Laser Applications*. PhD thesis, Ludwig-Maximilians Universität München (LMU), Germany (cited on p. 42).

Highland, V. L. (1975). "Some practical remarks on multiple scattering". *Nuclear Instruments and Methods*, 129(2): 497–499. ISSN: 0029554X. DOI: 10.1016/0029-554X(75)90743-0 (cited on p. 14).

Hilke, H. J. and Riegler, W. (2020). "Gaseous Detectors". In: *Particle Physics Reference Library: Volume 2: Detectors for Particles and Radiation*. Edited by C. W. Fabjan and H. Schopper. Cham: Springer International Publishing, pages 91–136. ISBN: 978-3-030-35318-6. DOI: 10.1007/978-3-030-35318-6_4 (cited on p. 23).

Hofverberg, P. et al. (2022). "A 60 MeV proton beam-line dedicated to research and development programs". *Applied Radiation and Isotopes*, 184(March): 110190. ISSN: 09698043. DOI: 10.1016/j.apradiso.2022.110190 (cited on p. 45).

Holthoff, G. et al. (2022). *Entwicklung und Charakterisierung eines präklinischen Micromegas pCT-Systems*. Edited by U. Heinrichs, E. Beckers, and A. Bitz. Presentation at the 53. Jahrestagung der Deutschen Gesellschaft für Medizinische Physik. DOI: 10.5282/ubm/epub.103671 (cited on p. 157).

Hounsfield, G. N. (1973). "Computerized transverse axial scanning (tomography): Part 1. Description of system". *The British Journal of Radiology*, 46(552): 1016–1022. DOI: 10.1259/0007-1285-46-552-1016 (cited on pp. 33, 147).

Hu, G. et al. (2021). *Expansion of a Small-Animal Proton CT Reconstruction Framework and Studies of Energy Dependence of Relative Stopping Power*. Poster presented at the

Joint Conference of the ÖGMP, DGMP and SGSMP, Dreiländertagung der Medizinischen Physik. Virtual Conference. DOI: 10.5282/ubm/epub.103670 (cited on p. 158).

Huang, Z. et al. (2023). *Monte Carlo simulation model of the SIRMIO beamline and experimental validation in clinical facilities*. Poster presented at the 61st Annual PTCOG Conference. Madrid, Spain. URL: https://www.ncbi.nlm.nih.gov/pmc/articles/PMC10698634/ (cited on p. 156).

Hudobivnik, N. et al. (2016). "Comparison of proton therapy treatment planning for head tumors with a pencil beam algorithm on dual and single energy CT images". *Medical Physics*, 43(1): 495–504. ISSN: 00942405. DOI: 10.1118/1.4939106 (cited on pp. 47, 49, 148).

Hynecek, J. (2006). *3T pixel for CMOS image sensors with low reset noise and low dark current generation utilizing parametric reset*. U.S. Patent (cited on p. 41).

Jee, K. W. et al. (2017). "Investigation of time-resolved proton radiography using x-ray flat-panel imaging system". *Physics in Medicine & Biology*, 62(5): 1905–1919. ISSN: 13616560. DOI: 10.1088/1361-6560/aa5a43 (cited on p. 34).

Johnson, R. P. (2018). "Review of medical radiography and tomography with proton beams". *Reports on Progress in Physics*, 81(1). ISSN: 00344885. DOI: 10.1088/1361-6633/aa8b1d (cited on pp. 2, 3, 33).

Johnson, R. P. et al. (2016). "A Fast Experimental Scanner for Proton CT: Technical Performance and First Experience with Phantom Scans". *IEEE Transactions on Nuclear Science*, 63(1): 52–60. DOI: 10.1109/TNS.2015.2491918.A (cited on p. 34).

Karger, C. P. et al. (2010). "Dosimetry for ion beam radiotherapy". *Physics in Medicine & Biology*, 55(21). ISSN: 00319155. DOI: 10.1088/0031-9155/55/21/R01 (cited on p. 149).

Kim, M. M. et al. (2019). "Design and commissioning of an image-guided small animal radiation platform and quality assurance protocol for integrated proton and x-ray radiobiology research". *Physics in Medicine & Biology*, 64(13). ISSN: 13616560. DOI: 10.1088/1361-6560/ab20d9 (cited on p. 2).

Kleeven, W. et al. (2013). "The IBA Superconducting Synchrocyclotron Project S2C2". *Proceedings of Cyclotrons2013, Vancouver, BC, Canada*: 115–119. URL: https://accelconf.web.cern.ch/AccelConf/CYCLOTRONS2013/papers/mo4pb02.pdf (cited on p. 45).

Koehler, A. M. (1968). "Proton Radiography". *Science*, 160(3825): 303–304. DOI: 10.1126/science.160.3825.303 (cited on p. 33).

Kozlowska, W. S. et al. (2019). "FLUKA particle therapy tool for Monte Carlo independent calculation of scanned proton and carbon ion beam therapy". *Physics in Medicine & Biology*, 64 (cited on p. 41).

Kraan, A. C. (2015). "Range Verification Methods in Particle Therapy: Underlying Physics and Monte Carlo Modeling". *Frontiers in Oncology*, 5: 150. DOI: 10.3389/fonc.2015.00150 (cited on p. 10).

Krah, N. et al. (2015). "An advanced image processing method to improve the spatial resolution of ion radiographies". *Physics in Medicine & Biology*, 60(21): 8525–8547. ISSN: 13616560. DOI: 10.1088/0031-9155/60/21/8525 (cited on pp. 73, 120, 143).

Krah, N. et al. (2018). "A comprehensive theoretical comparison of proton imaging set-ups in terms of spatial resolution". *Physics in Medicine & Biology*, 63(13). ISSN: 13616560. DOI: 10.1088/1361-6560/aaca1f (cited on pp. 3, 33, 35).

Krämer, M., Weyrather, W. K., and Scholz, M. (2003). "The Increased Biological Effectiveness of Heavy Charged Particles: From Radiobiology to Treatment Planning". *Technology in Cancer Research and Treatment*, 2(5): 427–436. ISSN: 15330346. DOI: 10.1177/153303460300200507 (cited on p. 1).

Krämer, M. et al. (2000). "Treatment planning for heavy-ion radiotherapy : physical beam model and dose optimization". 45: 3299–3317 (cited on pp. 128, 130).

Krischel, D. et al. (2007). "Design Aspects and Operation Experience With a Novel Superconducting Cyclotron for Cancer Treatment". *IEEE Transactions on Applied Superconductivity*, 17(2): 2307–2310 (cited on p. 44).

Krischel, D. (2012). "Advantages and Challenges of Superconducting Accelerators". In: *Ion Beam Therapy: Fundamentals, Technology, Clinical Applications*. Edited by U. Linz. Springer Berlin Heidelberg, pages 377–396. ISBN: 978-3-642-21414-1. DOI: 10.1007/978-3-642-21414-1_23 (cited on p. 44).

Kurz, C., Mairani, A., and Parodi, K. (2012). "First experimental-based characterization of oxygen ion beam depth dose distributions at the Heidelberg Ion-Beam Therapy Center". *Physics in Medicine & Biology*, 57(15): 5017–5034. ISSN: 00319155. DOI: 10.1088/0031-9155/57/15/5017 (cited on p. 149).

Lancaster, D. (1977). *CMOS cookbook*. Edited by G. Michael, J. Rounds, and F. N. Speights. Thatcher AZ, USA: Synergetics Press, page 414. ISBN: 0672213982 (cited on p. 24).

Landau, L. D. (1944). "On the energy loss of fast particles by ionization". *J. Phys. (USSR)*, 8(4): 201–205. DOI: https://doi.org/10.1016/B978-0-08-010586-4.50061-4 (cited on p. 15).

Lascaud, J. et al. (2021a). "Investigating the accuracy of co-registered ionoacoustic and ultrasound images in pulsed proton beams". *Physics in Medicine & Biology* (cited on p. 3).

Lascaud, J. et al. (2021b). "Optimization of the backing material of a low frequency PVDF detector for ion beam monitoring during small animal proton irradiation". In: *2021 IEEE International Ultrasonics Symposium (IUS)*. URL: https://ieeexplore.ieee.org/abstract/document/9593703 (cited on p. 156).

Lascaud, J. et al. (2021c). *Optimization of the backing material of a low frequency PVDF detector for ion beam monitoring during small animal proton irradiation*. Poster presented at the 2021 IEEE International Ultrasonics Symposium (IUS). URL: https:

//epub.ub.uni-muenchen.de/103645/1/IEEE%7B%5C_%7DIUS%7B%5C_%7DPVDF%7B%5C_%7DJL.pdf (cited on p. 158).

Lascaud, J. et al. (2022). "Fabrication and characterization of a multimodal 3D printed mouse phantom for ionoacoustic quality assurance in image-guided pre-clinical proton radiation research". *Physics in Medicine & Biology*: 0–12. DOI: 10.1088/1361-6560/ac9031Manuscript (cited on pp. 48, 99, 155).

Lawrence, E. O. and Livingston, M. S. (1932). "The Production of High Speed Light Ions Without the Use of High Voltages". *Phys. Rev.*, 40(1): 19–35. DOI: 10.1103/PhysRev.40.19 (cited on p. 31).

Lecoq, P. (2020). "Scintillation Detectors for Charged Particles and Photons". In: *Particle Physics Reference Library: Volume 2: Detectors for Particles and Radiation*. Edited by C. W. Fabjan and H. Schopper. Cham: Springer International Publishing, pages 45–89. ISBN: 978-3-030-35318-6. DOI: 10.1007/978-3-030-35318-6_3 (cited on p. 23).

Lehrack, S. et al. (2017). "Submillimeter ionoacoustic range determination for protons in water at a clinical synchrocyclotron". *Physics in Medicine & Biology*, 62(17): L20–L30. ISSN: 13616560. DOI: 10.1088/1361-6560/aa81f8 (cited on pp. 45, 93).

Liubchenko, G. (2021). *A Feasibility Study of High-Z Metal (Oxide) Nanoparticles as Contrast Agents for Proton Imaging at a Small Animal Irradiation Platform*. Master's thesis, Ludwig-Maximilians Universität München (LMU), Germany (cited on pp. 99, 126).

Liubchenko, G. et al. (2020). *Assessing the feasibility of high-Z metal (oxide) nanoparticles as contrast enhancement agents in proton imaging for a small animal irradiation platform (SIRMIO)*. Presentation at the 51. Jahrestagung der Deutschen Gesellschaft für Medizinische Physik. Virtual Conference (cited on p. 159).

Lovatti, G. et al. (2020). "An Advanced Simulation and Reconstruction Framework for a Novel In-Beam PET Scanner for Pre-Clinical Proton Irradiation". In: *2020 IEEE Nuclear Science Symposium and Medical Imaging Conference (NSS/MIC)*. IEEE, pages 1–3. ISBN: 978-1-7281-7693-2. DOI: 10.1109/NSS/MIC42677.2020.9508007 (cited on p. 3).

Lovatti, G. et al. (2023). "Design study of a novel geometrical arrangement for an in-beam small animal positron emission tomography scanner". *Physics in Medicine & Biology*. ISSN: 0031-9155. DOI: 10.1088/1361-6560/ad0879 (cited on pp. 3, 27).

Lu, H. M. (2008). "A potential method for in vivo range verification in proton therapy treatment". *Physics in Medicine & Biology*, 53(5): 1413–1424. ISSN: 00319155. DOI: 10.1088/0031-9155/53/5/016 (cited on p. 35).

Lutz, G. and Klanner, R. (2020). "Solid State Detectors". In: edited by C. W. Fabjan and H. Schopper. Geneva, Switzerland. ISBN: 9783030353186. DOI: 10.1007/978-3-030-35318-6_5 (cited on p. 25).

Lynch, G. and Dahl, O. (1991). "Approximations to Multiple Coulomb Scattering". *Nuclear Instruments and Methods in Physics Research B*, 58: 6–10. DOI: https://doi.org/10.1016/0168-583X(91)95671-Y (cited on p. 15).

Mandrillon, P. et al. (1989). "Commissioning and Implementation of the Medicyc Cyclotron Programme". *Proceedings of the Twelfth International Conference on Cyclotrons and their Applications, Berlin, Germany*, (3): 613–616 (cited on p. 45).

Mathieson, K. et al. (2002). "Charge sharing in silicon pixel detectors". *Nuclear Instruments and Methods in Physics Research, Section A: Accelerators, Spectrometers, Detectors and Associated Equipment*, 487(1-2): 113–122. ISSN: 01689002. DOI: 10.1016/S0168-9002(02)00954-3 (cited on p. 57).

Mattiazzo, S. et al. (2018). "iMPACT : An Innovative Tracker and Calorimeter for Proton Computed Tomography". 2(4): 345–352 (cited on p. 34).

Mayer, C., Gasalberti, D. P., and Kumar, A. (2022). *Brachytherapy*. Study Guide. URL: https://www.ncbi.nlm.nih.gov/books/NBK562190/ (cited on p. 29).

Metropolis, N. and Ulam, S. (1949). "The Monte Carlo Method". *Journal of the American Statistical Association*, 44(247): 335–341 (cited on p. 27).

Meyer, S. et al. (2017). "Tomographic imaging with Carbon ion beams". *2016 IEEE Nuclear Science Symposium, Medical Imaging Conference and Room-Temperature Semiconductor Detector Workshop, NSS/MIC/RTSD 2016, Strasbourg, France October 29-November 06, 2016*. DOI: 10.1109/NSSMIC.2016.8069538 (cited on pp. 73, 143).

Meyer, S. (2019). *On the Clinical Potential of Ion Computed Tomography with Different Detector Systems and Ion Species*. PhD thesis, Ludwig-Maximilians Universität München (LMU), Germany (cited on pp. 27, 120, 144).

Meyer, S. et al. (2019). *Optimierung und Performance Evaluierung eines Protonen Computertomographie Systems für präklinische Bildgebung*. Presentation at the 50. Jahrestagung der Deutschen Gesellschaft für Medizinische Physik. Stuttgart, Germany. DOI: 10.5282/ubm/epub.75413 (cited on p. 160).

Meyer, S. et al. (2020). "Optimization and performance study of a proton CT system for pre-clinical small animal imaging". *Physics in Medicine & Biology*. ISSN: 0031-9155. DOI: 10.1088/1361-6560/ab8afc (cited on pp. 3, 6, 33, 34, 156).

Micke, A., Lewis, D. F., and Yu, X. (2011). "Multichannel film dosimetry with nonuniformity correction". *Medical Physics*, 38(5): 2523–2534. ISSN: 00942405. DOI: 10.1118/1.3576105 (cited on p. 128).

Molière, G. (1948). "Theorie der Streuung schneller geladener Teilchen". *Zeitschrift für Naturforschung A*, 10(3): 133 (cited on p. 14).

Mori, I. and Machida, Y. (2009). "Deriving the modulation transfer function of CT from extremely noisy edge profiles". *Radiological Physics and Technology*, 2: 22–32. DOI: https://doi.org/10.1007/s12194-008-0039-9 (cited on p. 50).

Muraishi, H. et al. (2009). "Evaluation of spatial resolution for heavy ion CT system based on the measurement of residual range distribution with HIMAC". *IEEE Transactions on Nuclear Science*, 56(5): 2714–2721. ISSN: 00189499. DOI: 10.1109/TNS.2009.2023520 (cited on p. 34).

Newhauser, W. D. and Zhang, R. (2015). "The physics of proton therapy". *Physics in Medicine & Biology*, 60(8): R155–R209. DOI: 10.1088/0031-9155/60/8/R155 (cited on p. 16).

Niepel, K. et al. (2020). "Animal tissue-based quantitative comparison of dual-energy CT to SPR conversion methods using high-resolution gel dosimetry". *Physics in Medicine & Biology*: 0–31. DOI: 10.1088/1361-6560/abbd14 (cited on p. 47).

Nitta, M. et al. (2021). "Finalisation and performance evaluation of a novel PET detector for an in-beam small animal PET scanner". In: *Joint Conference of the ÖGMP, DGMP & SGSMP Dreiländertagung der Medizinischen Physik*. Edited by W. Birkfellner and D. Georg. September. ISBN: 9783948023164 (cited on p. 5).

Oancea, C. et al. (2018). "PO-0888: Comparison of x-ray CT and proton based CT planning in the presence of titanium dental implants". In: *Radiotherapy and Oncology*. Edited by M. Baumann. Volume 127. Barcelona, Spain: Elsevier, S470–S471. DOI: 10.1016/S0167-8140(18)31198-8 (cited on p. 33).

Overbo, I. (1977). "The Coulomb Correction to Electron Pair Production by Intermediate-Energy Photons". *Physics Letters B*, 71(2): 412–414 (cited on p. 15).

Paganetti, H. (2012a). *Proton Therapy Physics*. Edited by H. Paganetti. CRC Press. ISBN: 9781439836453 (cited on pp. 31, 83).

Paganetti, H. (2012b). "Range uncertainties in proton therapy and the role of Monte Carlo simulations". *Physics in Medicine & Biology*, 57(11): R99. ISSN: 0031-9155. DOI: 10.1088/0031-9155/57/11/R99 (cited on p. 33).

Paganetti, H. (2017). *Proton Beam Therapy*. IOP Publishing. ISBN: 978-0-7503-1370-4. DOI: 10.1088/978-0-7503-1370-4 (cited on p. 30).

Paganetti, H. et al. (2008). "Clinical implementation of full Monte Carlo dose calculation in proton beam therapy". *Physics in Medicine & Biology*, 53(17): 4825–4853. ISSN: 00319155. DOI: 10.1088/0031-9155/53/17/023 (cited on pp. 27, 31).

Palaniappan, P. et al. (2023). "Multi-stage image registration based on list-mode proton radiographies for small animal proton irradiation : A simulation study". *Zeitschift für Medizinische Physik*. DOI: 10.1016/j.zemedi.2023.04.003 (cited on pp. 3, 121, 155).

Parodi, K. (2014). "Heavy ion radiography and tomography". *Physica Medica*, 30(5): 539–543. ISSN: 1120-1797. DOI: https://doi.org/10.1016/j.ejmp.2014.02.004 (cited on p. 33).

Parodi, K. et al. (2007a). "Clinical CT-based calculations of dose and positron emitter distributions in proton therapy using the FLUKA Monte Carlo code". *Physics in Medicine & Biology*, 52(12): 3369–3387. ISSN: 00319155. DOI: 10.1088/0031-9155/52/12/004 (cited on pp. 27, 39).

Parodi, K. et al. (2012). "Monte Carlo simulations to support start-up and treatment planning of scanned proton and carbon ion therapy at a synchrotron-based facility". *Physics in Medicine & Biology*, 57(12): 3759–3784. DOI: 10.1088/0031-9155/57/12/3759 (cited on pp. 27, 40).

Parodi, K. et al. (2007b). "Patient Study of In Vivo Verification of Beam Delivery and Range, Using Positron Emission Tomography and Computed Tomography Imaging After Proton Therapy". *International Journal of Radiation Oncology Biology Physics*, 68(3): 920–934. ISSN: 03603016. DOI: 10.1016/j.ijrobp.2007.01.063 (cited on p. 16).

Parodi, K. et al. (2007c). "PET/CT imaging for treatment verification after proton therapy: A study with plastic phantoms and metallic implants". *Medical Physics*, 34(2): 419–435. ISSN: 00942405. DOI: 10.1118/1.2401042 (cited on p. 39).

Parodi, K. et al. (2019). "Towards a novel small animal proton irradiation platform: the SIRMIO project". *Acta Oncologica*, 58(10): 1470–1475. ISSN: 1651226X. DOI: 10.1080/0284186X.2019.1630752 (cited on pp. 2, 156).

Parodi, K. et al. (2021). *Proton imaging for small animals*. Presentation at the Joint Conference of the ÖGMP, DGMP and SGSMP, Dreiländertagung der Medizinischen Physik. Virtual Conference. DOI: 10.5282/ubm/epub.103638 (cited on p. 158).

Pearson, E. et al. (2013). "The new IBA superconducting synchrocyclotron (S2C2): from modeling to reality". *Proceeding of 11th International Topical Meeting on Nuclear Applications of Accelerators* (cited on p. 45).

Pelowitz, D. (2011). *MCNPX User's Manual. Version 2.7.0* (cited on p. 85).

Penfold, S. N. et al. (2011). "Geometrical optimization of a particle tracking system for proton computed tomography". *Radiation Measurements*, 46(12): 2069–2072. ISSN: 13504487. DOI: 10.1016/j.radmeas.2011.04.032 (cited on p. 34).

Pettersen, H. E. S. et al. (2017). "Proton tracking in a high-granularity Digital Tracking Calorimeter for proton CT purposes". *Nuclear Inst. and Methods in Physics Research, A*. ISSN: 0168-9002. DOI: 10.1016/j.nima.2017.02.007 (cited on p. 34).

Podgorsak, E. B. (2005). *Radiation Oncology Physics: A Handbook for Teachers and Students*. ISBN: 92-0-107304-6 (cited on pp. 11, 18, 20, 21).

Polf, J. C. et al. (2009). "Measurement and calculation of characteristic prompt gamma ray spectra emitted during proton irradiation". *Physics in Medicine & Biology*, 54(22): N519. DOI: 10.1088/0031-9155/54/22/N02 (cited on p. 16).

Poludniowski, G., Allinson, N. M., and Evans, P. M. (2015). "Proton radiography and tomography with application to proton therapy". *British Journal of Radiology*, 88(1053): 1–14. ISSN: 00071285. DOI: 10.1259/bjr.20150134 (cited on pp. 3, 33).

Presti, D. L. et al. (2016). "Design and characterisation of a real time proton and carbon ion radiography system based on scintillating optical fibres". *Physica Medica*, 32(9): 1124–1134. ISSN: 1120-1797. DOI: 10.1016/j.ejmp.2016.08.015 (cited on p. 34).

Puck, T. P. and Marcus, P. I. (1956). "Action of x-rays on mammalian cells". *Journal of Experimental Medicine*, 103(5): 653–666 (cited on p. 30).

Reinhardt, S. (2012). *Detection of laser–accelerated protons*. PhD thesis, Ludwig-Maximilians Universität München (LMU), Germany (cited on p. 42).

Rescigno, R. et al. (2016). "Pencil beam approach to proton computed tomography: A performance study". *2015 IEEE Nuclear Science Symposium and Medical Imaging Conference, NSS/MIC 2015*, 42(October): 6610–6624. DOI: 10.1109/NSSMIC.2015.7582189 (cited on p. 34).

Rinaldi, I. et al. (2013). "Experimental characterization of a prototype detector system for carbon ion radiography and tomography". *Physics in Medicine & Biology*, 58(3): 413–427. ISSN: 00319155. DOI: 10.1088/0031-9155/58/3/413 (cited on p. 34).

Rinaldi, I. et al. (2014). "Experimental investigations on carbon ion scanning radiography using a range telescope". *Physics in Medicine & Biology*, 59(12): 3041–3057. ISSN: 13616560. DOI: 10.1088/0031-9155/59/12/3041 (cited on p. 34).

Roesler, S., Engel, R., and Ranft, J. (2001). "The Monte Carlo Event Generator DPMJET-III". In: *Advanced Monte Carlo for Radiation Physics, Particle Transport Simulation and Applications*. Edited by A. Kling et al. Springer Berlin Heidelberg, pages 5–6. ISBN: 978-3-642-62113-0. DOI: 10.1007/978-3-642-18211-2_166 (cited on p. 39).

Rührschopf, E.-p. and Klingenbeck, K. (2011). "A general framework and review of scatter correction methods in x-ray cone-beam computerized tomography . Part 1 : Scatter compensation approaches". *Medical Physics*, 38(July): 4296–4311. DOI: 10.1118/1.3599033 (cited on p. 139).

Ryu, H. et al. (2008). "Density and spatial resolutions of proton radiography using a range modulation technique". *Physics in Medicine & Biology*. DOI: 10.1088/0031-9155/53/19/012 (cited on p. 34).

S'ng Ming Hao, M. (2019). *Characterisation of the CM49 CMOS detector for laser-driven ion acceleration*. Master's thesis, Ludwig-Maximilians Universität München (LMU), Germany (cited on pp. 42, 53, 54).

Sánchez-Parcerisa, D. et al. (2012). "Experimental study of the water-to-air stopping power ratio of monoenergetic carbon ion beams for particle therapy". *Physics in Medicine & Biology*, 57(11): 3629–3641. ISSN: 00319155. DOI: 10.1088/0031-9155/57/11/3629 (cited on p. 149).

Scaringella, M. et al. (2014). "A proton Computed Tomography based medical imaging system". *Journal of Instrumentation*, 9(12). ISSN: 17480221. DOI: 10.1088/1748-0221/9/12/C12009 (cited on p. 34).

Schaffner, B. and Pedroni, E. (1998). "The precision of proton range calculations in proton radiotherapy treatment planning: experimental verification of the relation between CT-HU and proton stopping power". *Physics in Medicine & Biology*, 43(6): 1579. DOI: 10.1088/0031-9155/43/6/016 (cited on p. 14).

Schneider, U., Besserer, J., and Hartmann, M. (2012). "Technical Note: Spatial resolution of proton tomography: Impact of air gap between patient and detector". *Medical Physics*, 39(2): 798–800. ISSN: 00942405. DOI: 10.1118/1.3676739 (cited on p. 34).

Schneider, U., Pedroni, E., and Lomax, A. (1996). "The calibration of CT Hounsfield units for radiotherapy treatment planning". *Physics in Medicine & Biology*, 41(111). DOI: 10.1088/0031-9155/41/1/009 (cited on pp. 33, 41).

Schneider, U. et al. (2004). "First proton radiography of an animal patient". *Medical Physics*, 31(5): 1046–1051. ISSN: 00942405. DOI: 10.1118/1.1690713 (cited on p. 34).

Schneider, W., Bortfeld, T., and Schlegel, W. (2000). "Correlation between CT numbers and tissue parameters needed for Monte Carlo simulations of clinical dose distributions". *Physics in Medicine & Biology*, 45(2): 459–478. ISSN: 00319155. DOI: 10.1088/0031-9155/45/2/314 (cited on p. 41).

Schnürle, K. (2016). *Majorana Edge States on Toplogical Superconductors*. Bachelor's thesis, Karlsruhe Institute of Technology (KIT), Germany (cited on p. 161).

Schnürle, K. (2018). *GATE Monte Carlo Simulation of a Proton Therapy Beamline for Water Luminescence Range Verification*. Master's thesis, Karlsruhe Institute of Technology (KIT), Germany (cited on pp. 94, 161).

Schnürle, K. et al. (2018a). *Monte Carlo Simulation of a Clinical Prototype 226MeV Protontherapy Beamline Using GATE Code*. Poster presented at the 57th Annual PTCOG Conference. Cincinnati, Ohio, USA. URL: https://www.ncbi.nlm.nih.gov/pmc/articles/PMC6874191/ (cited on p. 160).

Schnürle, K. et al. (2018b). *Monte Carlo Simulation of a Clinical Prototype 226MeV Protontherapy Beamline Using GATE Code*. Poster presented ENLIGHT Annual Meeting and Training. London, UK (cited on p. 161).

Schnürle, K. et al. (2019). *Monte-Carlo-Studie zur Protonenradiographie für die Positionsverifikation für Kleintierbestrahlungen an einem klinischen Protonen-Therapiezentrum*. Presentation at the 50. Jahrestagung der Deutschen Gesellschaft für Medizinische Physik. Stuttgart, Germany. DOI: 10.5282/ubm/epub.70700 (cited on pp. 120, 160).

Schnürle, K. et al. (2020). *Entwicklung von Protonenbildgebung mit einem einzelnen integrierenden CMOS-Detektor für eine Kleintierbestrahlungsanlage*. Presentation at the 51. Jahrestagung der Deutschen Gesellschaft für Medizinische Physik. Virtual Conference. DOI: 10.5282/ubm/epub.74260 (cited on p. 159).

Schnürle, K. et al. (2021a). *Development of Integration Mode Proton Imaging with a Single CMOS Detector for a Small Animal Irradiation Platform*. Presentation at the Third European Congress of Medical Physics. Torinol, Italy & Virtual Conference. DOI: 10.5282/ubm/epub.92773 (cited on p. 157).

Schnürle, K. et al. (2021b). *Small Animal CMOS Integration Mode Proton Imaging at Different Treatment Facilities The SIRMIO project*. Presentation at the Seventh Annual Loma Linda Workshop on Particle Imaging and Radiation Treatment Planning. Loma Linda, California, USA & Virtual Conference (cited on p. 157).

Schnürle, K. et al. (2021c). *Development of scatter correction for integration mode proton imaging for a small animal irradiation platform*. Poster presented at the Joint Confer-

ence of the ÖGMP, DGMP and SGSMP, Dreiländertagung der Medizinischen Physik. Virtual Conference. DOI: 10.5282/ubm/epub.92774 (cited on p. 158).

Schnürle, K. et al. (2021d). *Development of Integration Mode Proton Imaging with a Single CMOS Detector for a Small Animal Irradiation Platform*. Presentation at the Applied Nuclear Physics Conference 2021. Prague, Czech Republic & Virtual Conference. DOI: 10.5282/ubm/epub.92719 (cited on p. 158).

Schnürle, K. et al. (2022a). *CMOS Integration Mode Proton Imaging for a Small Animal Irradiator*. Edited by Katia Parodi et al. Presentation at the 5th Conference on Small Animal Precision Image-Guided Radiotherapy. Munich, Germany. DOI: 10.5282/ubm/epub.92720 (cited on p. 157).

Schnürle, K. et al. (2022b). *CMOS Integration Mode Proton Imaging*. Presentation at the 23rd International Workshop on Radiation Imaging Detectors (iWoRiD2022). Riva del Garda, Italy. DOI: 10.5282/ubm/epub.92775 (cited on p. 157).

Schnürle, K. et al. (2023). "Development of integration mode proton imaging with a single CMOS detector for a small animal irradiation platform". *Frontiers in Physics*, 10(January): 1–11. ISSN: 2296424X. DOI: 10.3389/fphy.2022.1044156 (cited on p. 155).

Schulte, R. et al. (2004). "Conceptual design of a proton computed tomography system for applications in proton radiation therapy". *IEEE Transactions on Nuclear Science*, 51(3): 866–872. DOI: 10.1109/TNS.2004.829392 (cited on p. 34).

Schulte, R. W. and Penfold, S. N. (2012). "Proton CT for Improved Stoppig Power Determination in Proton Therapy". *Trans Am Nucl Soc.*: 55–58 (cited on p. 33).

Schulte, R. W. et al. (2005). "Density resolution of proton computed tomography". *Medical Physics*, 32(4): 1035–1046. ISSN: 00942405. DOI: 10.1118/1.1884906 (cited on p. 33).

Schwandt, J. et al. (2013). "Design and first tests of a radiation-hard pixel sensor for the European X-ray Free-Electron Laser". In: *2013 14th European Conference on Radiation and Its Effects on Components and Systems (RADECS)*, pages 1–8. DOI: 10.1109/RADECS.2013.6937446 (cited on p. 26).

Seco, J. and Depauw, N. (2011). "Proof of principle study of the use of a CMOS active pixel sensor for proton radiography". *Medical Physics*, 38(2): 622–623. ISSN: 00942405. DOI: 10.1118/1.3496327 (cited on p. 34).

Seco, J. et al. (2013). "Characterizing the modulation transfer function (MTF) of proton / carbon radiography using Monte Carlo simulations". *Medical Physics*, 091717(2013). DOI: 10.1118/1.4819816 (cited on p. 50).

Sedgwick, I. et al. (2013). *LASSENA: A 6.7 Megapixel, 3-sides buttable, Wafer-Scale CMOS Sensor using a novel grid- addressing architecture*. Technical report, pages 3–6 (cited on pp. 42, 43, 119).

Selzner, D. (2021). *Development towards a Variable Calibration Water Phantom for a Small-Animal Proton Imaging Setup*. Bachelor's thesis, Ludwig-Maximilians Universität München (LMU), Germany (cited on p. 118).

Silari, M. (2011). "Applications of particle accelerators in medicine". *Radiation Protection Dosimetry*, 146(4): 440–450. ISSN: 01448420. DOI: 10.1093/rpd/ncr243 (cited on p. 44).

Snoeys, W. et al. (2000). "Layout techniques to enhance the radiation tolerance of standard CMOS technologies demonstrated on a pixel detector readout chip". *Nuclear Instruments and Methods in Physics Research, Section A: Accelerators, Spectrometers, Detectors and Associated Equipment*, 439: 349–360 (cited on p. 42).

Sommerer, F. et al. (2006). "Investigating the accuracy of the FLUKA code for transport of therapeutic ion beams in matter". *Physics in Medicine & Biology*, 51(17): 4385–4398. ISSN: 00319155. DOI: 10.1088/0031-9155/51/17/017 (cited on p. 40).

Sorge, H. and Stiicker, H. (1989). "Relativistic Quantum Molecular Dynamics Energies Approach to Nuclear Collisions at Ultrarelativistic Energies". *Nuclear Physics*, 498: 567–576 (cited on p. 39).

Spieler, H. (2005). *Semiconductor Detector Systems*. Oxford: Clarendon Press (cited on pp. 22–24).

Spies, L. et al. (2001). "Correction of scatter in megavoltage cone-beam CT". *Physics in Medicine & Biology*, 46(3): 821–833. ISSN: 00319155. DOI: 10.1088/0031-9155/46/3/316 (cited on p. 139).

Stark, P. B. and Parker, R. L. (1995). "Bounded-Variable Least-Squares: an Algorithm and Applications". *Computational Statistics*, 10 (cited on p. 73).

Tanabashi, M. et al. (2018). "Passage of particles through matter". *Physical Review D*, 98(030001): 1–40. URL: http://pdg.lbl.gov/2016/reviews/rpp2016-rev-passage-particles-matter.pdf (cited on p. 15).

Taylor, J. T. et al. (2016). "An experimental demonstration of a new type of proton computed tomography using a novel silicon tracking detector". 43(November): 6129–6136 (cited on p. 34).

Teledyne Dalsa (2014). *CM49 DST CMOS Image Sensor Data Sheet*. Technical report (cited on pp. 41, 43).

Teledyne Dalsa (2021). *Shad-o-Box High Speed Industrial X-Ray Detectors*. Technical report (cited on p. 41).

Telsemeyer, J., Jäkel, O., and Martišíková, M. (2012). "Quantitative carbon ion beam radiography and tomography with a flat-panel detector". *Physics in Medicine & Biology*, 57(23): 7957–7971. ISSN: 00319155. DOI: 10.1088/0031-9155/57/23/7957 (cited on p. 34).

Tessonnier, T. et al. (2017). "Dosimetric verification in water of a Monte Carlo treatment planning tool for proton, helium, carbon and oxygen ion beams at the Heidelberg Ion Beam Therapy Center". *Physics in Medicine & Biology*, 62(16): 6579–6594. ISSN: 13616560. DOI: 10.1088/1361-6560/aa7be4 (cited on p. 150).

Tessonnier, T. et al. (2016). "Experimental dosimetric comparison of 1H, 4He, 12C and 16O scanned ion beams". *Physics in Medicine & Biology*, 62: 3958–3982 (cited on p. 149).

Testa, M. et al. (2013). "Proton radiography and proton computed tomography based on time-resolved dose measurements". *Physics in Medicine & Biology*, 58: 8215–8233. DOI: 10.1088/0031-9155/58/22/8215 (cited on p. 34).

Tiffenberg, J. et al. (2017). "Single-Electron and Single-Photon Sensitivity with a Silicon Skipper CCD". *Phys. Rev. Lett.*, 119(13): 131802. DOI: 10.1103/PhysRevLett.119.131802 (cited on p. 24).

Trock Laegdsmand, P. (2020). *Monte Carlo Model for Scanning Proton Beam at the Danish Center for Proton Therapy*. Master's thesis, Aarhus University, Denmark (cited on p. 91).

Tsai, Y.-S. (1974). "Pair production and bremsstrahlung of charged leptons". *Rev. Mod. Phys.*, 46(4): 815–851. DOI: 10.1103/RevModPhys.46.815 (cited on p. 15).

Ulmer, W. (2007). "Theoretical aspects of energy – range relations , stopping power and energy straggling of protons". *Radiation Physics and Chemistry*, 76: 1089–1107. DOI: 10.1016/j.radphyschem.2007.02.083 (cited on p. 13).

Van De Walle, J. et al. (2014). "Dosimetry of pulsed beams in proton therapy". *Ibic2014*: 0–4 (cited on p. 45).

Van de Walle, J. et al. (2016). "The S2C2 : From Source To Extraction". *Proceedings of Cyclotrons 2016*: 285–289. URL: http://accelconf.web.cern.ch/AccelConf/cyclotrons2016/papers/thb01.pdf (cited on p. 45).

Vavilov, P. V. (1957). "Ionization Losses of High-Energy Heavy Particles". *Journal of Experimental and Theoretical Physics*, 5(4): 749–751 (cited on p. 15).

Verhaegen, F., Granton, P., and Tryggestad, E. (2011). "Small animal radiotherapy research platforms". *Physics in Medicine & Biology*, 56. DOI: 10.1088/0031-9155/56/12/R01 (cited on p. 35).

Vlachoudis, V. (2009). "Flair: A powerful but user friendly graphical interface for FLUKA". In: *International Conference on Mathematics, Computational Methods & Reactor Physics 2009*. Saragota Springs, New York, pages 790–800 (cited on p. 41).

Weick-Kleemann, M. (2013). *Dosimetrische Charakterisierung der Spotshape für zwei verschiedene Beamlines der selben Protonentherapieanlage*. Bachelor's thesis, Ludwig-Maximilians Universität München (LMU), Germany (cited on p. 44).

West, D. and Sherwood, A. (1973). "Proton-scattering radiography". *Non-Destructive Testing*, 6(5): 249–257. ISSN: 00291021. DOI: 10.1016/0029-1021(73)90072-8 (cited on p. 73).

Wilson, R. R. (1946). "Radiological Use of Fast Protons". *Radiology*, 47(5): 487–491. ISSN: 0033-8419. DOI: 10.1148/47.5.487 (cited on p. 31).

Würl, M. et al. (2016). "Dosimetric impact of the low-dose envelope of scanned proton beams at a ProBeam facility: Comparison of measurements with TPS and MC calculations". *Physics in Medicine & Biology*, 61(2): 958–973. ISSN: 13616560. DOI: 10.1088/0031-9155/61/2/958 (cited on p. 81).

Würl, M. (2014). *PET activation studies at a cyclotron-based proton therapy facility - Experiments and Monte Carlo simulations*. Master's thesis, Ludwig-Maximilians Universität München (LMU), Germany (cited on p. 81).

Würl, M. (2018). *On the Spectrometry of Laser-Accelerated Particle Bunches and Laser-Driven Proton Radiography*. PhD thesis, Ludwig-Maximilians Universität München (LMU), Germany (cited on pp. 54, 55).

Würl, M. et al. (2020a). "Proton Radiography for a Small-Animal Irradiation Platform based on a Miniaturized Timepix Detector". In: *2020 IEEE Nuclear Science Symposium and Medical Imaging Conference (NSS/MIC)*. IEEE, pages 1–6. DOI: 10.1109/nss/mic42677.2020.9508073 (cited on pp. 3, 156).

Würl, M. et al. (2020b). *Proton Radiography for a Small-Animal Irradiation Platform based on a Miniaturized Timepix Detector*. Poster presented at the 2020 IEEE Nuclear Science Symposium and Medical Imaging Conference (NSS/MIC). Manchester, UK (cited on p. 159).

Würl, M. et al. (2020c). *Quantitative proton radiography for a small-animal irradiation platform based on a miniaturized Timepix detector*. Presentation at the 51. Jahrestagung der Deutschen Gesellschaft für Medizinische Physik. Virtual Conference. URL: https://epub.ub.uni-muenchen.de/74258/1/DGMP%7B%5C_%7D2020%7B%5C_%7DWuerl.pdf (cited on p. 159).

Würl, M. et al. (2020d). *Development of a setup for small-animal proton imaging based on a miniaturized Timepix detector*. Presentation at the 1st Workshop Trento Proton Beam Line Facility, Trento. Trento, Italy. URL: https://agenda.infn.it/event/23198/book-of-abstracts.pdf (cited on p. 159).

Zhang, R. et al. (2019). "Iterative optimization of relative stopping power by single detector based multi-projection proton radiography". *Physics in Medicine & Biology*, 64 (cited on p. 34).

Zhang, R. and Newhauser, W. D. (2009). "Calculation of water equivalent thickness of materials of arbitrary density, elemental composition and thickness in proton beam irradiation". *Physics in Medicine & Biology*, 54(6): 1383–1395. ISSN: 15378276. DOI: 10.1088/0031-9155/54/6/001.Calculation. arXiv:NIHMS150003 (cited on p. 14).

Ziegenhein, P. et al. (2008). "Speed optimized influence matrix processing in inverse treatment planning tools". *Physics in Medicine & Biology*, 53(9). ISSN: 00319155. DOI: 10.1088/0031-9155/53/9/N02 (cited on p. 132).

Ziegler, J. F. (1999). "The Stopping of Energetic Light Ions in Elemental Matter". *Journal of Applied Physics*, 85(3): 281–287. ISSN: 00406090. DOI: https://doi.org/10.1063/1.369844 (cited on p. 10).

Zott, L. (2021). *A Computational Framework to Validate a Prototype Planning System for a Small Animal Proton Irradiatior*. Master's thesis, Ludwig-Maximilians Universität München (LMU), Germany (cited on p. 27).

Zygmanski, P. et al. (2000). "The measurement of proton stopping power using proton-cone-beam computed tomography proton-cone-beam computed tomography". *Physics in Medicine & Biology* (cited on p. 34).

Danksagung

Herzlichen Dank an alle, die mich bei dieser Dissertation unterstützt haben!
Mein besonderer Dank gilt meiner Doktormutter Prof. Dr. Katia Parodi für die besondere Erfahrung, an einem spannenden Thema und in diesem Team aus großartigen WissenschaftlerInnen - und vor allem Menschen - zu arbeiten. Danke für die Hingabe und die Zeit, mit der du diese Arbeit mit wissenschaftlicher Gründlichkeit und einem offenen Ohr für das Menschliche betreut hast. Danke auch für die Ermöglichung von Experimenten und Strahlzeiten und für die Gelegenheit, an zahlreichen Konferenzen teilzunehmen.
Danke an Matthias für die Betreuung und Unterstützung, die kritischen Fragen und die Hilfe bei der Fertigstellung dieser Arbeit, auch nach deiner Zeit am Lehrstuhl.
Danke an Beatrice, besonders für die Arbeit am LASSENA-Detektor. Danke an Jona für die große Unterstützung, insbesondere bei der Planung und Durchführung der Experimente. Danke an Chiara für die Hilfe bei Monte-Carlo-Simulationen und Bildrekonstruktionen.
Große Teile dieser Arbeit entstanden während der Covid19-Pandemie und vor dem Hintergrund der damit einhergehenden operativen und emotionalen Schwierigkeiten. Danke daher an alle (auch oben bereits genannte) KollegInnen und FreundInnen, dass wir in dieser besonderen Zeit stets einen Weg gefunden haben, dran zu bleiben und füreinander da zu sein. Danke an all die MitstreiterInnen im PhD: Juliana, Giulio, Giulia, Jannis, Franz, Sebastian M., Tim, EG, Pratik, Domenik, Bonny, Angelica, Guyue, Ze und Georg.
Danke auch an die bereits promovierten Mitglieder des SIRMIO-Teams: Julie, Mambo, George, Marco, Prof. Dr. Peter Thirolf, Mune und Prasanna. Danke auch an die "Laser Guys" und Prof. Dr. Jörg Schreiber für die Hilfe und die lustigen Momente: Jens, Martin, Lenny, Thomas, Felix, Johannes, Jannik und natürlich "Laser Girl" Sonja.
Danke an meinen ehemaligen Physiklehrer Dr. Torsten Tok, der mich ermutigt hat, Physik zu studieren.
Danke an Romy für deine Unterstützung. Danke Andrea! Danke an die Mitarbeitenden der Mechanischen Werkstatt der LMU in Garching unter der Leitung von Herrn Rolf Oehm für die Herstellung zahlreicher Bauteile für experimentelle Aufbauten.
Thanks to the team at CAL, Marie, Petter, Joël and Anaïs, that has set me on this path and continued to support me during this work.

Danke an Lukas, der die verrücktesten Dinge getanhat, um mich zum Lachen zu bringen. Danke für deine Liebe und Unterstützung.
Danke an meine Familie (aka die Famulle), dass ihr immer für mich da seid und mich unterstützt.